THERMO-ANEMOMETRY
IN
MAGNETOHYDRODYNAMICS

by

David G. Malcolm

A Thesis
submitted to the University of Warwick
for the Degree of Doctor of Philosophy
August, 1968

ABSTRACT

The problem of developing a reliable technique for measuring instantaneous velocities at an arbitrary point in a magnetohydrodynamic (MHD) flow of mercury is the primary concern of the thesis. The solution to this problem is urgently needed in order that measurements may be taken in practical MHD devices and in order that the interesting theoretical work which has emerged in the past decade may be substantiated by experimental evidence.

Much of the information on measurement techniques contained herein will be applicable to other liquid metal flows. The recent advances in the area of constant temperature hot-film anemometry have made this technique the best one for instantaneous measurements in low-temperature liquid metal systems.

The thesis is divided into two parts. The study of thermo-anemometry is described in chapter 2 and its application to some MHD experiments is described in chapter 3.

Chapter 2 is divided into two main sections, §2.2 and §2.3, which discuss the theory of thermo-anemometry in mercury and demonstrate its application in calibration exercises. The hot-film sensors tested are the tiny (0.030 mm diameter and 0.5 mm length) quartz-insulated platinum film sensors which are now made available for work in electrically conducting fluids by Thermo-Systems Inc., St. Paul, Minnesota, U.S.A. An account of our attempts to construct somewhat similar sensors in the laboratory is given in Appendix B.

In addition to discussing various calibration problems, such as MHD effects on free convective heat transfer from the hot-film and its dynamic response, chapter 2 develops, and demonstrates by experiment, new methods for the direct measurement of low turbulence intensities in low Prandtl number fluids. The simple formulae presented are likely to be more accurate in the majority of cases than more sophisticated methods involving linearization of the anemometer voltage with respect to velocity because of their lack of sensitivity to signal drift.

Chapter 3 discusses theoretical aspects in §3.2 and their experimental substantiation in §3.3 for two different types of MHD flow. The first of these is electrically driven flow in mercury between two circular, highly conducting electrodes which are placed opposite one another in insulating planes with a magnetic field normal to their surfaces. The steady flow is examined theoretically by an asymptotic analysis and experimentally using Pitot tubes and electric potential probes. The experiments give some insight into the behaviour of these probes in MHD situations. This same flow is studied using a hot-film sensor with good results. This experiment points to the need for an extensive study of the MHD effects on hot-film heat transfer and the associated MHD errors in measurements for various orientations of the sensor relative to the magnetic field.

Hot-film techniques are then used to examine the instability and subsequent wave-like secondary flow (when the Hartmann number, M, is very high) in this same electrically driven flow. These phenomena are interesting but very difficult to understand. It is shown that the transverse magnetic field, if strong enough, can control the stability of, and secondary flow in, the electrically driven shear layers through direct action on the most unstable three-dimensional disturbances even though most of the vorticity of these disturbances is parallel to the magnetic field. An attempt is made to discuss the physical mechanism involved.

The second type of MHD flow investigated is turbulent vorticity suppression behind a square-array wire grid in a transverse magnetic field. The experiment is of a preliminary nature but demonstrates some interesting phenomena which can be explained in order of magnitude terms.

Both of the MHD flows studied demonstrate various aspects of the behaviour of the hot-film sensors as well as being interesting in themselves.

The paper listed in the Table of Contents under Appendix A as "Malcolm (1968b)" may be read as an extended summary of the thesis.

PREFACE

The research presented in the thesis was carried out between October, 1965 and June, 1968 at the School of Engineering Science, University of Warwick. When my study of magnetohydrodynamics (MHD) began in September, 1965, it was suggested to me by Professor J.A. Shercliff that the development of techniques for measuring turbulence characteristics in MHD experiments using mercury, and the demonstration of these techniques in some interesting experiments, would be an important endeavour. Theoretical work pertaining to the behaviour of a turbulence field of electrically conducting fluid when acted upon by electromagnetic forces has occupied the minds of many applied mathematicians, but direct experimental evidence to test such work has been almost entirely lacking. This initial prompting led to my study of thermo-anemometry as applied to MHD experiments in mercury. The success of such a venture seemed hopeful because, firstly, Sajben (1964) had been successful in operating an insulated hot-wire in mercury and, secondly, an industrial firm, Thermo-Systems Inc., U.S.A., had recently been successful in producing very small, cylindrical, quartz-insulated, hot-film sensors which would operate in the constant temperature mode for reasonable periods of time in mercury.

After successfully developing the technique of constant temperature anemometry to a fairly reliable state, in both steady and turbulent mercury flows, I wished to test the technique still further by applying it to some relatively simple but interesting experiments in MHD. To this end, I have examined the structure of certain shear layers which occur in electrically driven flow between circular electrodes with the magnetic field normal to these electrodes, both in the steady primary flow and in the unsteady flow regime at the onset of instability. This study immediately suggested itself following the collaborative work using different experimental techniques on the same system by Hunt and Malcolm (1968). I have also examined another unsteady flow problem, that of vorticity suppression behind a conventional square mesh grid in a transverse magnetic field, as a preliminary attempt to examine experimentally the effect of electromagnetic forces on a field of turbulence.

My efforts have been frustrated to some extent by certain unfortunate

circumstances. A few months elapsed in 1966 while awaiting the long overdue anemometer equipment and the specially designed hot-film probes for mercury. Since then, more months have been anxiously spent awaiting the arrival of new and repaired hot-film probes. The cylindrical hot-film sensors are sufficiently fragile to make a certain amount of accidental breakage during the course of experiments unavoidable and to greatly enhance the probability of breakage during transit from the place of manufacture in the U.S.A. About 40% of all probes ordered new or returned for repair were broken either in transit or while clearing Customs. Since each repair and return journey involved a two-month wait, this situation led to some anxiety!

It was not possible to begin serious experimental work in mercury until the design and construction of the MHD Laboratory, a special building of plastic construction for MHD experimentation in mercury, was completed in the spring of 1967. Nevertheless, I value the experience gained through participation in this project.

No part of this thesis has been presented for a degree at any other university. Copies of three publications resulting from this work (including the collaborative study discussed below) have been included in Appendix A. One of these is a draft of a paper which is to be presented at the Sixth Symposium on Magnetohydrodynamics in Riga, Latvia, U.S.S.R., in September, 1968. This paper is an extended summary of the salient features of the thesis.

Some collaborative work was carried out on the problem of electrically driven flow between circular electrodes with Dr.J.C.R.Hunt between October, 1965 and March, 1966 in a temporary MHD laboratory located at Bristol Siddeley Engines Ltd., Coventry. This investigation led to the publication by Hunt and Malcolm (1968). I participated in the experiments and in the analysis of the results, but the theoretical analysis was carried out alone by Hunt. Except where references are given to the contrary, the remainder of the work described in the thesis is original.

I am very grateful to Professor Shercliff who originally suggested the work and introduced me to the subject of MHD, to my supervisor, Dr.C.J.N. Alty, for his constant interested in the project and many helpful discussions and to my colleagues, Dr.J.C.R.Hunt amd Mr.M.K.Bevir for various illuminating discussions on MHD in general. I gratefully acknowledge the help given by Mr.P.Bradshaw at the National Physical Laboratory and by Dr. D.L.Schultz at the University of Oxford who introduced me to the techniques

of thermo-anemometry.

It must be stated that, without the technical expertness, patience and keen interest of Mr.A.E.Webb in building and modifying apparatus, this work could hardly have been as successful. To him, and to his assistants, Mr.A.Ross and Mr.R.Coles, I am greatly indebted.

I would especially like to thank the members of the Royal Commission for the Exhibition of 1851 who have enabled me to continue my studies here through an Overseas Scholarship and whose encouragement and hospitality has been greatly appreciated. Thanks are also due to the National Research Council of Canada who provided part of the Schclarship during my first year.

I am grateful to the University of Saskatchewan, Saskatoon, Canada, who have graciously supported me during the final stages of thesis preparation, and who have provided a generous travel grant to enable me to present my paper in Riga next month.

Most of the anemometry equipment was purchased from a Royal Society Grant.

Finally, I would like to express my sincere appreciation to Miss Jennifer A. Green who prepared the typescript of the thesis.

The University of Warwick, Coventry,
August, 1968.

CONTENTS

INDEX OF FIGURES

INDEX OF TABLES

1. INTRODUCTION

The problem of devising and applying a sensing element to measure instantaneous local velocities in some interesting steady and unsteady MHD flows of mercury is the concern of this thesis. Many aspects of this problem are relevant in flows of other liquid metals such as sodium or NaK eutectic. With these examples, the difficulties are even greater because of the necessity of using higher operating temperatures.

The solution to this measurement problem is urgently required in order that the wide gaps between theoretical prediction and experimental verification can be closed. A clear understanding of the behaviour of liquid metal MHD flows in ducts is, of course, of considerable practical importance in designing electromagnetic pumping facilities to circulate liquid metal coolant in nuclear reactors, etc.

There are four conditions which must be satisfied by an ideal velocity sensing device in MHD whatever its mode of operation These are:

(i) The inherent response time of the sensing element to changing events at its surface must be much less than the shortest time which is characteristic of these changing events.

(ii) The interface region between the sensing element and the changing environment must cause negligible lag and attenuation of the changes as they are transmitted to the surface of the element.

(iii) The length scale of the sensing element must be much smaller than the smallest length scale which is characteristic of the changing environment.

(iv) Either the length scale of the sensing element must be sufficiently small to make the electromagnetic forces influencing the flow around it negligible compared to the forces of fluid mechanical origin, or the influence of the electromagnetic forces must be accurately calculable for the length scale employed.

As well as these stringent conditions on the operation of the sensing element, one is faced with deleterious effects due to the physical properties of the mercury environment. Amalgamation readily

takes place between mercury and most other metals, and mercury, being of high electrical conductivity, readily shorts out electrical signals so that direct contact must be prevented between the fluid and the sensing element if this is metallic and electrically operated.

The measurement device which comes closest to meeting the four desired conditions for accurate velocity measurement while still being sufficiently protected from the environment is a quartz-insulated, constant temperature platinum film mounted on a tiny (as small as .001 inch diameter) quartz fibre. This sensor is heated and kept at constant temperature electrically using conventional constant temperature anemometer equipment. The heat flux transferred by convection from the surface of the sensor is related to the local flow condition by idealised theoretical relationships or, more realistically, by a calibration. Sensors of this type are manufactured by only one firm, Thermo-Systems Inc., U.S.A. Attempts to make satisfactory hot-film sensors for mercury have also been made here at our School of Engineering Science as discussed in Appendix B of this thesis.

Only two publications are known of previous quantitative investigations of unsteady MHD flows. One is by Branover, Slyusarev and Shcherbinin (1965) who employed a strain gauge technique to measure the fluctuating drag on a tear-drop probe inserted in a turbulent mercury flow. The size of this tear-drop probe (2.15mm diameter) precludes the measurement of small scale turbulence. Due to interference by the probe stem, the quantitative relationship between the fluctuating drag force measured and the fluctuating flow velocity at the tear-drop is not at all clear. The authors do not, in fact, claim any great success as far as interpreting their results quantitatively is concerned.

In an introductory paragraph Branover et al make the rather curious and unqualified remark that the thermo-anemometer cannot be used in mercury owing to the smallness of the Prandtl number! Indeed, as will be discussed in section 2 of the thesis, the heat transfer characteristics of a fluid of small Prandtl number enable one to considerably simplify the problem of low intensity turbulence measurement by constant temperature anemometry. The only evident way in which a small Prandtl number could influence the turbulence measurement capability of thermo-

anemometry unfavourably is in lowering the frequency response through the thermal inertia effect of the thick thermal boundary layer. This effect is minimized by operating the sensor at constant temperature.

The other publication relating to quantitative turbulence measurements in mercury is by Sajben (1965) who employed a constant current thermo-anemometric technique. He used a lacquer-insulated tungsten wire in a turbulent jet, subjected to an axial magnetic field, with some success. Since the temperature of the sensor fluctuates in a fluctuating flow if the heating current is constant, the frequency response of the hot-wire is adversely effected by the thermal inertia of the thermal boundary layer and the insulating coating.

For a discussion of some simultaneous investigations at other institutions using Thermo-Systems quartz-insulated sensors, which have very recently been brought to the author's attention, refer to the introductory discussion in section 1 of Malcolm (1968b) in Appendix A of this thesis.

When testing a new experimental technique it is advisable to use relatively simple experimental arrangements. With this thought in mind the MHD studies given in section 3 of the thesis suggested themselves. The problem of steady electrically driven flow between circular electrodes had previously been investigated by Hunt & Malcolm (1968) (see Appendix A) using Pitot tubes and electric potential probes, thus providing comparable results for the steady flow case. In this investigation the control of the experiment was proven to be extremely easy.

The experiment on grid turbulence decay in a transverse magnetic field was considered the simplest possible since it required only minor alterations to apparatus already in existence.

It was hoped, of course, that these simple experiments would not only test the hot-film technique but would also extend our present understanding of MHD phenomena in liquid metals, particularly as regards the effects of electromagnetic forces on stability and on vorticity suppression in an unsteady flow.

2. THERMO-ANEMOMETERY IN MERCURY

2.1 General Introduction

Thermo-anemometry has long been a useful experimental technique in aerodynamics. At the root of all variations of this technique is the fundamental fact that the heat flux convected from a hot surface is a function of the physical properties and the flow velocity of the surrounding cooler fluid. In order that a hot surface can operate as a velocity measurement device when this function is known, its temperature or thermal dissipation must be controlled in some manner. The simplest way to do this is to choose an electrically conducting material for the hot surface and to provide the thermal dissipation and its control electrically.

The hot surface is usually represented in practice by a "hot-wire" or "hot-film". It is also possible to employ thermistor material, as reported by Lumley (1962), but problems of poor frequency response and low sensitivity have yet to be solved. The hot-wire sensor is composed of a wire, with a diameter usually less than 0.01mm and a length to diameter ratio of a few hundred, which is attached at its ends to electrically conducting supports. The hot-film sensor is composed of a thin metallic film deposited on a glass or quartz substrate and electrical connections to the film to supply the heating current.

For normal use in air the principal advantage of a hot-film sensor over a hot-wire sensor of similar electrical resistance is its superior strength and rigidity. When used in electrically conducting fluids it has the further advantage of being easier to insulate. In some cases it has proved possible to use a thin coat of lacquer for insulation purposes, but the most satisfactory method available at present is to use a coating of sputtered quartz. Thermo-Systems Inc., the firm supplying the quartz-insulated cylindrical hot-film sensors for the present research, report that they have not been successful in coating wires with sputtered quartz. It seems that the wires become brittle when coated in this manner. The difficulty associated with the insulation of wires by lacquer coatings is illustrated by the fact that, whereas Sajben (1964, 1965) was successful, Moreau (1967) had to abandon the attempt in spite of concerted effort.

Hot-film sensors may be constructed in the laboratory if the necessary equipment and technical skills are available. See Appendix B for a discussion of hot-film sensor manufacture.

The two common types of hot-film sensor are the wedge and cylinder as shown in Figure 2.1. The wedge type, first developed by Ling (1955, 1960) and Ling and Hubbard (1956) and further studied by Bankoff and Rosler (1962), is very robust and is without doubt the best sensor for work in low shear hydrodynamic flows where a small flow blockage is of minor importance. However, for minimizing flow blockage when traversing thin shear layers and for experimentation in MHD where MHD effects on the heat transfer from the sensor must be minimized, the smaller, more fragile cylindrical hot-film recently developed by Thermo-Systems must be employed. The cylindrical hot-film also has another advantage in turbulent flows since an X-array can be constructed (see Figure 2.1), as in conventional hot-wire anemometry, to measure turbulence intensities simultaneously in two perpendicular directions.

The two common modes of sensor operation are designated as "constant current" and "constant temperature". In both cases the voltage across the sensor is measured and related to flow velocity. In the constant current mode, the current through the sensor is maintained constant by using a large resistance in series with it. If the flow velocity in the neighbourhood of the sensor fluctuates, the surface temperature, and hence the resistance, of the sensor also fluctuates. Because of temperature fluctuation the constant current mode is unsatisfactory in hot-film anemometry; the thermal inertia of the substrate, insulation and boundary layer seriously impair the dynamic response of the hot-film element.

In the constant temperature mode a bridge and feedback system are used to maintain the sensor at constant resistance, and therefore at constant temperature. Constant temperature operation of thin film sensors is superior to constant current operation in allowing rapid response to rapid flow fluctuations.

Anyone who is interested in learning the basic principles of thermo-anemometry will find the publications of Kovásznay (1965) and Bradshaw and Johnson (1963) most helpful. Kovásznay's paper includes an excellent bibliography of hot-wire anemometry. Bradshaw and Johnson present a

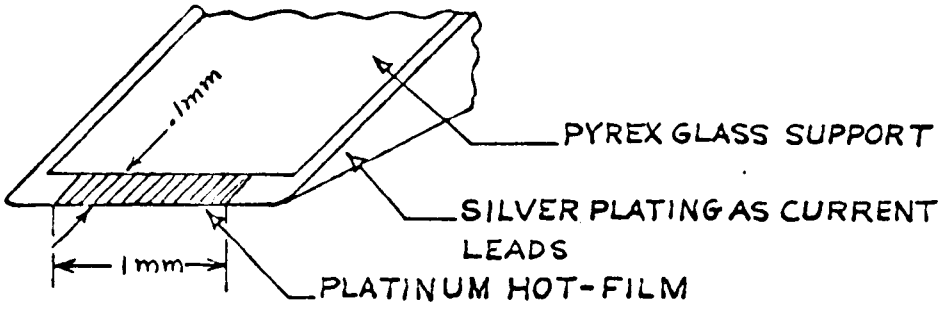

WEDGE-TYPE HOT-FILM SENSOR

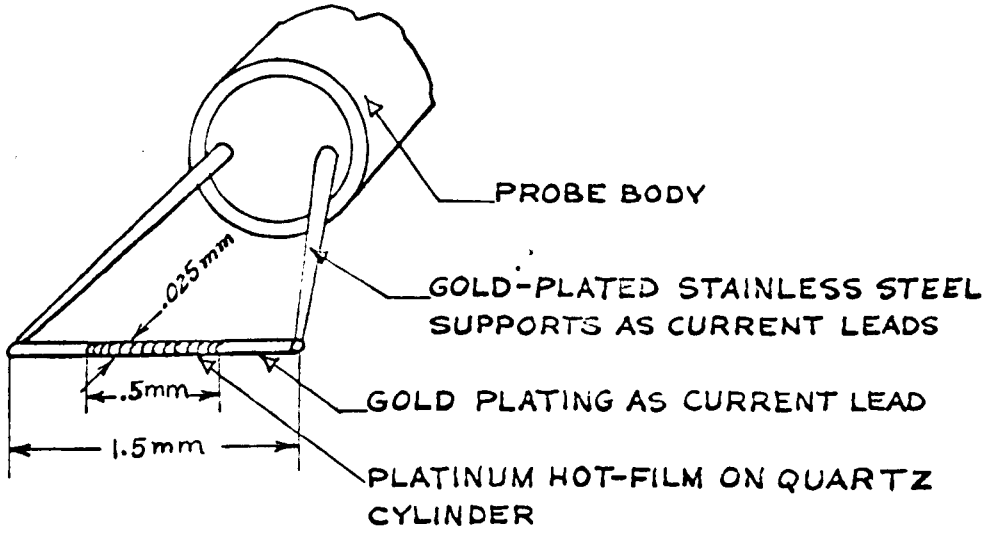

CYLINDRICAL-TYPE HOT-FILM SENSOR

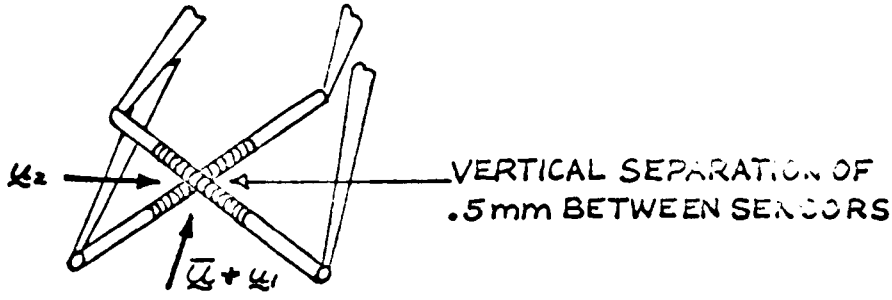

X-ARRAY HOT-FILM SENSOR

NOTE: FOR USE IN ELECTRICALLY CONDUCTING FLUIDS IT IS NECESSARY TO INSULATE THE HOT-FILM WITH SPUTTERED QUARTZ AND THE CURRENT LEADS WITH RESIN.

Figure 2.1 Types of hot-film sensors.

great deal of helpful information regarding the construction of hot-wire sensors and electronic apparatus for signal analysis. Other good reviews of hot-wire anemometry are given by Hinze (1959), Grant and Kronauer (1962) and Wieghardt and Kux (1967). Freymuth (1967) presents a clear and concise study of the operational behaviour of the constant temperature anemometer. Rasmussen (1966) discusses the ways by which turbulence characteristics, such as energy spectra and correlation functions, are calculated from the voltage output of a constant temperature anemometer. The present understanding of the dynamic behaviour of hot-film sensors is made clear by Bellhouse and Schultz (1967) and Bellhouse and Rasmussen (1968).

The first known attempt to apply a thermo-anemometric technique to mercury was by Lielpéteris (1960). He constructed a velocity measuring probe by positioning an electrically heated, semiconducting element in a small diameter glass tube adjacent to one end which was closed to exclude mercury. The probe was immersed in a mercury flow and attempts were made to calibrate it. It was found that the calibration curve changed from day to day in a peculiar manner and the technique was not developed further. The reasons for such strange behaviour would seem to be those discussed by Sajben (1964, 1965) to explain his similar results obtained using a constant current, lacquer-insulated tungsten-wire. He found an explanation by considering the changeable properties of the non-wetting layer which surrounds an insulated sensor in mercury. He also presented a calibration technique whereby this effect could be overcome. This technique is described later in section 2.2. and applied in section 2.3. Sajben used his constant current technique to measure the large turbulence intensities in a mercury jet which was subjected to an axial magnetic field (Sajben (1967)). This involved very complicated procedures of data analysis. By way of contrast, a very simple equation is derived in section 2.2 for measuring low turbulence intensities ($\sqrt{\overline{u^2}}/\overline{u} < 0.1$, say) by taking advantage of the constant temperature characteristic and the special convective heat transfer relations in a low Prandtl number fluid.

To complete this review of previous thermo-anemometric work in mercury, the work of Fraim (1966) and Fraim and Heiser (1968) should be mentioned. Fraim gained further experience with Sajben's system by using it as a qualitative instrument to study transition phenomena in a

circular pipe flow of mercury subjected to an axial magnetic field.

This chapter on thermo-anemometry is organised in the following manner. Section 2.2 presents the theory of constant temperature anemometry in mercury MHD systems. §2.2.1 reviews the relevant work on heat transfer from cylinders. §2.2.2 and 2.2.3 discuss MHD effects on heat transfer from finite length cylinders and the dynamic response of the cylindrical hot-film sensors to rapid flow changes. These topics are still not well understood and recommendations are made for their further study in chapter 4. The paper which is designated Malcolm (1968a), entitled "Some aspects of turbulence measurement in liquid mercury using cylindrical quartz-insulated hot-film sensors", forms an integral part of chapter 2 and is discussed in §2.2.4 to 2.2.7. This work was discussed more informally at the Tenth British Theoretical Mechanics Colloquium at Oxford in April, 1968.

Section 2.3 discusses the experiments. After a description of the apparatus and method in §2.3.1, §2.3.2 and 2.3.3 discuss some preliminary experiments on MHD heat transfer effects and frequency response. §2.3.4 and 2.3.5 discuss hot-film calibration results and results of the experiments designed to test the turbulence equation developed previously for the case of low Prandtl number fluids.

2.2 The theory of thermo-anenometry in mercury.

2.2.1 Heat transfer from cylinders in a steady flow of low Prandtl number fluid

Although no attempt has been made in this thesis to study in detail the heat transfer from finite-length cylinders in mercury, a few remarks are necessary in order to discuss the observed performance of the cylindrical hot-film sensors.

The fact that mercury has a low Prandtl number ($P \simeq .025$ at $20°C$) is of primary importance. Since P is the ratio of kinematic viscosity, $\nu = \eta/\rho$, to thermal diffusivity, $\alpha = k/\rho c_p$, a small Prandtl number signifies that the diffusivity of momentum is small compared to thermal diffusivity. A consequence of a low value of P in a flow situation is that the thermal boundary layer is thicker than the velocity boundary layer (eg. see Holman (1968)).

The competition between convective heat transport by momentum diffusion and conductive heat transport by thermal diffusion is characterised by the Prandtl-Reynolds number product, PR , known as the Péclet number, $Pé = ud/\alpha$, which represents the ratio of flow speed to thermal diffusion speed. In MHD flows of mercury one is often interested in measuring speeds of a few cm/sec. With such flow velocities normal to hot-film sensors of diameter 0.003 cm $Pé$ is less than one.

A theoretical expression for forced convection heat transfer, as described by the Nusselt number, Nu , which is valid at low $Pé$ and R for circular cylinders of <u>infinite</u> length has been derived by Cole and Roshko (1954) on the basis of the Oseen approximation and the assumption of uniform surface temperature. This expression is

$$\frac{1}{Nu} = \frac{(\ln 8 - \Gamma)}{2} - \frac{1}{2}\ln Pé \,, \qquad \text{(2.1)}$$

where Γ is Euler's constant. Note that $Nu \to 0$ as $Pé \to 0$. This is a result of the infinite length assumption. For cylinders of finite length, the situation is quite different. Nu for conduction alone is then of the same order of magnitude as that calculated from (2.1) with $Pé \sim 10^{-1}$. Cole and Roshko illustrated this by considering an ellipsoid as an approximation for a finite-length cylinder for which $Nu \simeq 2/\ln(2\ell/d)$ in steady conduction when the length to diameter ratio, ℓ/d , is large.

As $Pe \longrightarrow 0$, free convection effects also become important. For the small diameters and the temperature differences used in this work, Nu for free convection from infinite-length cylinders is again of the same order of magnitude as Nu from (2.1) (see Chapman (1967)). Free convection from cylinders of finite length is complicated by three-dimensional effects. The heat transfer from an insulated, cylindrical hot-film sensor is further complicated by end losses to the supports, a non-uniform temperature distribution, conduction through the insulating layer and the poorly understood effects of the non-wetting, contact resistance layer which surrounds the sensor in mercury.

It is evident, then, that (2.1) is an oversimplification of the practical situation. The experiments will show, however, that $1/Nu$ is a linear function of $-\ln Pe$ for $0.3 \leq Pe \leq 1.0$, although the slope of the line is less than $\frac{1}{2}$.

In a recently completed thesis, Hill(1968) has described experiments in which he examined the directional sensitivity of Thermo-Systems' cylindrical hot-film sensors in a steady mercury flow. The principal result of his work is that the proportion of the velocity component along the axis of a sensor inclined to the flow direction which contributes to the cooling rate varies considerably with flow velocity for a constant angle of inclination. This work should be studied before any attempt is made to use an X-array hot-film sensor in mercury.

2.2.2 MHD effects on convective heat transfer from cylinders of finite length.

MHD effects on the convective heat transfer from cylinders in mercury at low flow velocities are solely due to the modification of the flow field around the cylinder by electromagnetic forces. This modification takes place because vorticity components which are perpendicular to the magnetic field direction are suppressed (see Shercliff (1965)). The relative importance of electromagnetic forces to inertial forces in the flow is represented in the ratio M^2/R, where $M = B_o d (\sigma/\eta)^{1/2}$ is the Hartmann number. This ratio is referred to as the interaction parameter, N. M^2 represents the ratio of electromagnetic forces to viscous forces. It is not necessary that N be very large for significant alteration of the flow field around a cylinder to take place. Leibovich (1967) has shown theoretically that there can be no separation from a rear stagnation point when $N = 2$. This theory is

based on a magnetic field which is normal to the surface. Kalis et al (1965) studied the flow around a circular cylinder at low magnetic Reynolds number, R_m, in a transverse magnetic field numerically. They found separation to be prevented at $N = 0.5$ for $R = 40$. They found experimentally that separation was prevented at $N \simeq 2$ for $R \simeq 10^4$ in mercury. Another dimensionless ratio, M^2/G, where $G = \left(\frac{g d^3 \beta \Delta T}{\nu^3}\right)$ is the Grashof number, gives the relative importance of electromagnetic and buoyancy forces. This ratio is important in free convection.

When electromagnetic forces are similar in magnitude to other forces in the flow one would expect significant effects on the thermal dissipation of hot-film sensors in mercury, if they are orientated so that the vorticity of the free or forced convection around them is perpendicular to the magnetic field. Typical magnitudes, considering the .030 mm diameter sensors in mercury at $20°C$ flowing at 1 mm/sec with an applied magnetic field of $1\ wb/m^2$, are $N = 2.3$, $M^2 = 0.6$, $M^2/G = 8.5$. MHD effects must therefore be considered.

During the planning stage of the experimental work described herein it was decided to eliminate MHD effects by aligning the axes of the sensors, and hence the vorticity shed by them, with the magnetic field. It was not appreciated until the experiments were well under way that, in the free convection mode, it is not possible to eliminate <u>all</u> electromagnetic effects on the flow around finite-length cylinders in this way. The edge-effects at the ends of the heated film cause free convection currents with some of their vorticity perpendicular to the magnetic field. This vorticity is strongly damped by electromagnetic forces.

When vorticity in the wake of a heated cylinder is suppressed by the action of a magnetic field, the convective velocities are reduced. Consequently, the temperature gradients near the surface decrease and the thermal dissipation becomes less. It is expected then that MHD effects will cause a reduction in convective heat transfer.

2.2.3 <u>Dynamic response of constant temperature hot-film sensors in unsteady flow.</u>

In this discussion it is assumed that the hot-film sensor is heated by a feed back circuit with a gain sufficiently high to keep the hot-film at constant temperature throughout the frequency range of interest. (i.e. up to frequencies of $O(1)$ kHz).

The most important points to consider are, firstly, unsteady heat transfer between the film and its substrate material because of thermal feedback from the fluid to the substrate and, secondly, unsteady heat transfer between the film and the thermal boundary layer.

Bellhouse and Schultz (1967) have discussed the first aspect, with particular reference to wedge-type sensors, on the basis of a simple one-dimensional mathematical model. The results of their theoretical investigation are supported by experimental evidence and indicate that the thermal feedback effects are serious in air but not in water and mercury which have lower thermal impedances. These effects are expected to be unimportant in any fluid for cylindrical sensors in which the film surrounds the cylindrical quartz substrate for a length, ℓ, such that $\ell/d >> 1$, because direct feedback from the fluid to the substrate can only occur at the ends of the film. For practical sensors where $\ell/d \leq 20$ the thermal feedback at the ends may be noticeable in air but not in mercury.

The unsteady heat transfer between the film and the boundary layer involves the insulating quartz layer which is sandwiched between them. This protective coating adds 10 - 20% to the diameter of the sensors (.030 mm). If one approximates this coating by an infinite slab of similar material and thickness, the transient effect of a temperature jump on one side will decay in a time of $O(10^{-5})$ sec. The unsteady heat conduction across the insulating coating would therefore have negligible effects on the interaction between the film and the boundary layer.

The nature of the film-boundary layer interaction is not well understood. It may well be the most important factor influencing the dynamic response of the sensor. When R is $O(10)$ the velocity boundary layer around a cylinder is not thin compared to its diameter. When $P << 1$, the thermal boundary layer is much thicker than the velocity boundary layer. The effect of rapid flow oscillations on heat transfer in such a case has not been adequately studied. Strickland and Davis (1966) have used numerical techniques to study this effect in air ($P \simeq 0.7$) assuming constant physical properties, small velocity and temperature fluctuations and a constant surface temperature. They found the thermal inertia of the fluid at $R = 10$ to be twice as high as that predicted by Lighthill (1954) who solved the problem on the basis of

boundary layer approximations. This discrepancy was attributed to failure of the boundary layer assumption that the layer is very thin compared to the diameter of the cylinder. Obviously, boundary layer theory cannot be used to study the case of the much thicker thermal boundary layers in mercury. A numerical study along the lines of Strickland and Davis would be very helpful. The effects of the quartz insulation, the contact resistance layer and a non uniform and velocity dependent temperature distribution (see Davies and Fisher (1964)) should be taken into account, if possible.

The common method of checking frequency response in constant temperature anemometry is to introduce a small square-wave voltage across the bridge and to monitor the response of the bridge output voltage (i.e. the heating voltage). Whether or not this method of pulsing the temperature of a small diameter hot-film sensor adequately describes the response of the thermal boundary layer to fluctuations in free stream velocity is still open to speculation. Davies and Fisher (1964) have shown in their experiments with hot-wires in air that the axial temperature distribution on the wire varies with velocity when the mean temperature stays constant. This allows the possibility of unsteady heat transfer along the wire as the velocity changes. This effect would presumably be more serious in the case of cylindrical hot-films where such a changing temperature distribution would cause fluctuating heat transfer in the axial direction in the quartz substrate, in the quartz coating and in the thermal boundary layer. If velocity fluctuations are only small deviations from the mean (e.g. low intensity turbulence) these effects are probably negligible. The square-wave frequency response check does not take these effects properly into account since the mean temperature is made to fluctuate, but not the shape of the temperature distribution. This fluctuating mean temperature will cause unsteady interactions with the quartz substrate and quartz coatings which are unlike those met in practice.

It is expected that the square-wave test will give an approximate indication of the frequency response to be expected in unsteady flows with low intensity fluctuations. It should be noted that, because of lower freestream velocities being used with sensors of similar spacial resolution, the maximum frequency response necessary in liquids is much less than that required in air. In the low speed mercury flow considered here, for instance, one is interested in frequencies of up

to $O(10^2)$ Hz rather than $O(10^4)$ Hz as in air.

Before any definite conclusion can be drawn regarding the dynamic response of cylindrical hot-films in mercury, it will be necessary to conduct calibration experiments in which unsteady flows of known and variable amplitudes and frequencies can be accurately realised.

2.2.4 Introduction to Malcolm (1968a)

This paper is included in draft form in Appendix A. Its purpose is to discuss the application of constant temperature hot-film anemometry in mercury. After an introductory section, section 2 of the paper reviews Sajben's calibration theory (Sajben (1965)) and develops simple formulae for measuring low intensity turbulence in fluids of low Prandtl number. Section 3 describes and discusses the results of experiments which test these measurement theories. Section 4 draws some conclusions from the results. Two appendices are included, Appendix A on the effect of environmental temperature drift on measurement accuracy and Appendix B on the details of some special operational problems.

In the following subsections, §2.2.5 to 2.2.7, the measurement theories are briefly discussed.

The experimental section of the paper will be discussed later, in §2.3.4 and 2.3.5.

2.2.5 Sajben's calibration equation

Subsection 2.1. of the paper applies Sajben's analysis to develop the steady flow calibration equation for the cylindrical hot-film sensor. The hot-film sensor is approximated by a very long laminated cylinder. The thin lamination representing the platinum film is kept at constant temperature. The outermost "lamination" is the non-wetting contact resistance layer of unknown properties and thickness which surrounds the sensor and changes in properties each time the sensor crosses the mercury free surface. The basic heat transfer equation is simply that given in many heat transfer textbooks (e.g. Chapman (1967)) for radial heat conduction in a laminated cylinder combined with convective heat transfer at its surface. This equation, equation (1) in the paper, is rearranged in the following manner,

$$\frac{\pi k_f L \Delta T}{Q(Pé)} = \frac{1}{Nu(Pé)} + K, \qquad \text{(2.2)}$$

where K contains all velocity independent terms, including the term which describes the contact resistance layer.

The calibration equation, which eliminates velocity independent terms, is written as follows,

$$F(Pé) = \pi k_f L \Delta T \left(\frac{1}{Q(0)} - \frac{1}{Q(Pé)} \right) = \frac{1}{Nu(0)} - \frac{1}{Nu(Pé)} . \qquad \text{(2.3)}$$

In practice $Q(Pé)$ is the ohmic dissipation in the hot-film.

An important question is whether or not one would expect similar $F(Pé)$ curves, for a single sensor, at different values of ΔT. $Nu(Pé)$ is given by a temperature independent equation such as (2.1) in forced convection. One might expect, however, that $Nu(0)$ would have some temperature dependence since, in free convection,

$$Nu = f(P, G),$$

where $G \propto \Delta T$. One can calculate that, with a sensor diameter of 0.030 mm when ΔT is $O(10)^\circ C$, PG is $O(10^{-3})$. One then observes from heat transfer data for horizontal cylinders (e.g. see Chapman (1967)) that, at such low values of PG, $Nu(0)$ is a very weak function of temperature and will appear to be constant if changes in ΔT are not too great. Therefore one would expect $F(Pé)$ curves to be nearly similar.

2.2.6 Sensitivity of $F(Pé)$ to ambient temperature drift

When measuring velocities as low as a few mm/sec using the $F(Pé)$ calibration, a temperature drift as low as $0.1^\circ C$ during the course of an experiment can have disastrous effects on measurement accuracy. This problem is studied in Appendix A of the paper where the following error equation is developed to describe this effect.

$$\epsilon_F = \left(\frac{1}{z} - 1 \right) \left(1 - \frac{1}{\epsilon_T + 1} \right), \qquad \text{(2.4)}$$

where $\epsilon_T = (\Delta T_2 - \Delta T_1)/\Delta T_1$, the relative error in ΔT if ΔT drifts from ΔT_1 to ΔT_2, $z = \left(\frac{\Delta T_1}{Q_1(0)} - \frac{\Delta T_2}{Q_2(Pé)} \right) \Big/ \left(\frac{\Delta T_1}{Q_1(0)} \right)$ and

$\epsilon_F = (F_a - F_t)/F_t$, the relative error in $F(Pé)$ if ΔT_2 is mistakenly thought by the observer to have remained at ΔT_1 . Ξ may be given the alternative form,

$$\Xi = F_t(Pé) \Big/ \pi^2 \left(\frac{\Delta T_1}{Q(0)}\right)^2 ,$$

where $F_t(Pé)$ is the true value of $F(Pé)$ at either ΔT_1 or ΔT_2 .

Now, suppose that the particular measurement is being taken at which $\Xi = 0.02$ (this would correspond approximately to $F(Pé) = 0.1$), and that ΔT has drifted from $\Delta T_1 = 20.0°C$ to $\Delta T_2 = 20.1°C$ so that $\epsilon_T = 0.005$. Equation (2.4) then shows that $\epsilon_F = 0.24$. Thus, a 0.5 % error in ΔT has caused a 24% error in $F(Pé)$ which, when referred to the calibration curve, gives a correspondingly large error in $Pé$! It is advisable then to control the ambient temperature very carefully or to employ an electronic temperature compensator which follows the ambient temperature continuously and forces appropriate changes in R_S , the operating resistance of the sensor, to keep ΔT constant.

Note that ϵ_F <u>decreases</u> as ϵ_T <u>decreases</u> and Ξ <u>increases</u>. This shows that the temperature drift problem is less acute when measuring large $Pé$, since Ξ is larger, and when the operating ΔT is increased. In general it is advisable to keep ΔT low so as to encourage long sensor life.

2.2.7 <u>The measurement of small flow oscillations and low turbulence intensities</u>

In subsection 2.2 of the paper formulae are developed to enable the direct measurement of low intensity turbulence in mercury. The reader is referred to this subsection for details of the development. This consists of substituting an appropriate relationship for $Nu(Pé)$ and electrical quantities for $Q(Pé)$ in (2.2), differentiating the resulting equation with respect to the velocity, U , normal to the sensor, substituting the weak oscillations in measured voltage and velocity for the differentials and, finally, taking the rms of the equation in the usual manner, ignoring third order infinitesimals.

If (2.1) is used as the relationship for $Nu(Pé)$, the resulting equation for the intensity of the streamwise turbulent fluctuations is

$$4\left[\frac{\pi k_f L \Delta T (R_s+R^*)^2}{R_s}\right]\frac{\sqrt{\overline{e^2}}}{\overline{E}^3} = \frac{\sqrt{\overline{u^2}}}{\overline{u}}, \qquad (2.5)$$

where $\overline{E}$ is the mean voltage across the sensor resistance, R_s, and a resistance in series with it, R^*, and $\sqrt{\overline{e^2}}$ is the rms of the random voltage fluctuations corresponding to the rms of the velocity fluctuations, $\sqrt{\overline{u^2}}$. This theoretical equation would probably apply directly in the case of a very long sensor.

For finite-length sensors, where the slope of the $1/Nu(Pé)$ vs. $\ln Pé$ curve is not $-1/2$ but $-S$, which is determined experimentally from the calibration equation (2.3), the resulting formula is

$$\frac{2}{S}\left[\frac{\pi k_f L \Delta T (R_s+R^*)^2}{R_s}\right]\frac{\sqrt{\overline{e^2}}}{\overline{E}^3} = \frac{\sqrt{\overline{u^2}}}{\overline{u}}. \qquad (2.6)$$

A third formula may be developed for a low Prandtl number fluid at high $Pé$ by substituting for $Nu(Pé)$ the equation developed by Grosh and Cess (1958) under the assumptions of two-dimensional, inviscid flow, viz., $Nu = 1.015\, Pé^{1/2}$.

The formula becomes,

$$4(1.015\,\overline{Pé}^{1/2})\left[\frac{\pi k_f L \Delta T (R_s+R^*)^2}{R_s}\right]\frac{\sqrt{\overline{e^2}}}{\overline{E}^3} = \frac{\sqrt{\overline{u^2}}}{\overline{u}}, \qquad (2.7)$$

where $\overline{Pé}$ is the Péclet number at the mean velocity, $\overline{u}$.

Note that equations (2.5) and (2.6) possess the unique advantage of being independent, not only of the changeable properties of the contact resistance layer, but of any reference condition, such as $Q(0)$, so that the calculation of turbulence intensity is independent of signal drift, provided that the drift is on a slower time scale than the time necessary to read $\sqrt{\overline{e^2}}$ and $\overline{E}$. Note that (2.7) is not independent of signal drift since $\overline{Pé}$ must be determined using the calibration curve.

If one retraces the steps in the development of (2.6) to the point just prior to the rms operation, a relationship is found for the calculation of the amplitudes of small velocity fluctuations which may be caused by, say, a passing eddy, viz.,

$$\frac{2}{S}\left[\frac{\pi k_f L \Delta T (R_s + R^*)^2}{R_s}\right]\frac{e}{\bar{E}^3} = \frac{u'}{\bar{u}} \quad . \qquad \text{(2.8)}$$

Since $e << \bar{E}$ and $u' << \bar{u}$, E^3 and U have been approximated by $\bar{E}^3$ and $\bar{u}$. Equation (2.8) has no importance as far as turbulence measurement is concerned, but it becomes useful in calculating velocity fluctuations in the experiment on the stability of electrically driven flow.

2.3 Experiments and Discussion

2.3.1 Apparatus and measurement methods

2.3.1.1 Anemometer and auxiliary equipment

A Thermo-Systems Model 1010 constant temperature anemometer was used to operate the special hot-film sensors in mercury. Specifications and operating characteristics of this unit are described by Thermo-Systems Inc. (1966).

The d.c. component of the output voltage from the anemometer, corresponding to a particular mean flow condition, was read directly from a Solartron model LM 1440.3 digital voltmeter. The a.c. component of the output voltage, corresponding to a turbulent velocity fluctuation about the mean, was measured by a Hewlett Packard model H12-3400A true rms voltmeter with a frequency response extending down to 2Hz . The rms voltage is available at the back of this instrument as a (0 - 1) volt d.c. output (see Hewlett Packard (1966, 1967)). For low frequency work in liquids, this d.c. output is conditioned by switching the damping circuit from the normal 2 sec response to a 20 sec response. This amount of damping was still not sufficient to give a sufficiently steady mean rms reading. The d.c. output was therefore displayed on a Tektronix Model 565 Dual-Beam oscilloscope (containing two plug-in units, a Model 2A61 and a Model 3A3) and recorded by a photographic technique. The details of this technique are discussed in Appendix C and in Malcolm (1968a).

Before being fed into the rms meter the anemometer signal was usually passed through a 1kHz low-pass filter, thus limiting the noise-level to about 0.3 mv . This filtering was possible since the spatial resolution of the sensors and the flow speeds were such as to limit the measureable frequency range to less than 300 Hz .

To ensure correct operation of the anemometer system the anemometer output voltage was continuously displayed on the oscilloscope.

2.3.1.2 Hot-film sensors

Special quartz-coated platinum film probes for work in mercury were constructed by Thermo-Systems Inc. according to their standard procedures for cylindrical sensor construction and the specifications in Figure 2.2. A full scale photograph of the probe end containing the tiny sensor is shown in Figure 2.3.

A Nikon V-16 projecting microscope was used to measure the sensitive lengths and approximate diameters of the sensors. Table 2.1 gives descriptive data pertaining to the three hot-films used in the experiments. The temperature coefficients of resistance entered in the table were checked experimentally by immersing the sensors in a heated water bath and following the increases in resistance with increase in temperature. Resistance was measured using the resistance decks on the anemometer set.

No attempt was made to clean the sensors between runs. It was thought advisable to check the reproducibility of results obtained in this manner since, in practical MHD experiments, it is extremely hard to ensure cleanliness in the system.

2.3.1.3 The calibration tow tank

A special tow tank was designed and constructed for the purpose of calibrating hot-film sensors in mercury. This tank is formed of rigid pvc sheet, $^{3}/_{16}$-inch in thickness, to make a trough of internal dimensions, 4 x 4 x 54 inches. It is supported in a steel framework to eliminate deformation of the tank when it is filled with about 400 lb of mercury.

The hot-film probes are suspended from a 3 lb brass trolley so as to pass through the mercury free surface with the sensors horizontal. The trolley runs above the tow tank on two $\frac{3}{4}$- inch diameter stainless steel rails. It has three wheels, approximately $2\frac{1}{2}$ inches in diameter, which are formed from pvc material to assist in the damping of vibrations in the mechanism. Two wheels on one side resemble V-pulleys and serve to guid the trolley on one of the round rails. The third wheel has a flat running surface and rides freely on the other rail. This arrangement of guide wheels minimizes wheel chatter and eliminates the need for accurate positioning of the rails.

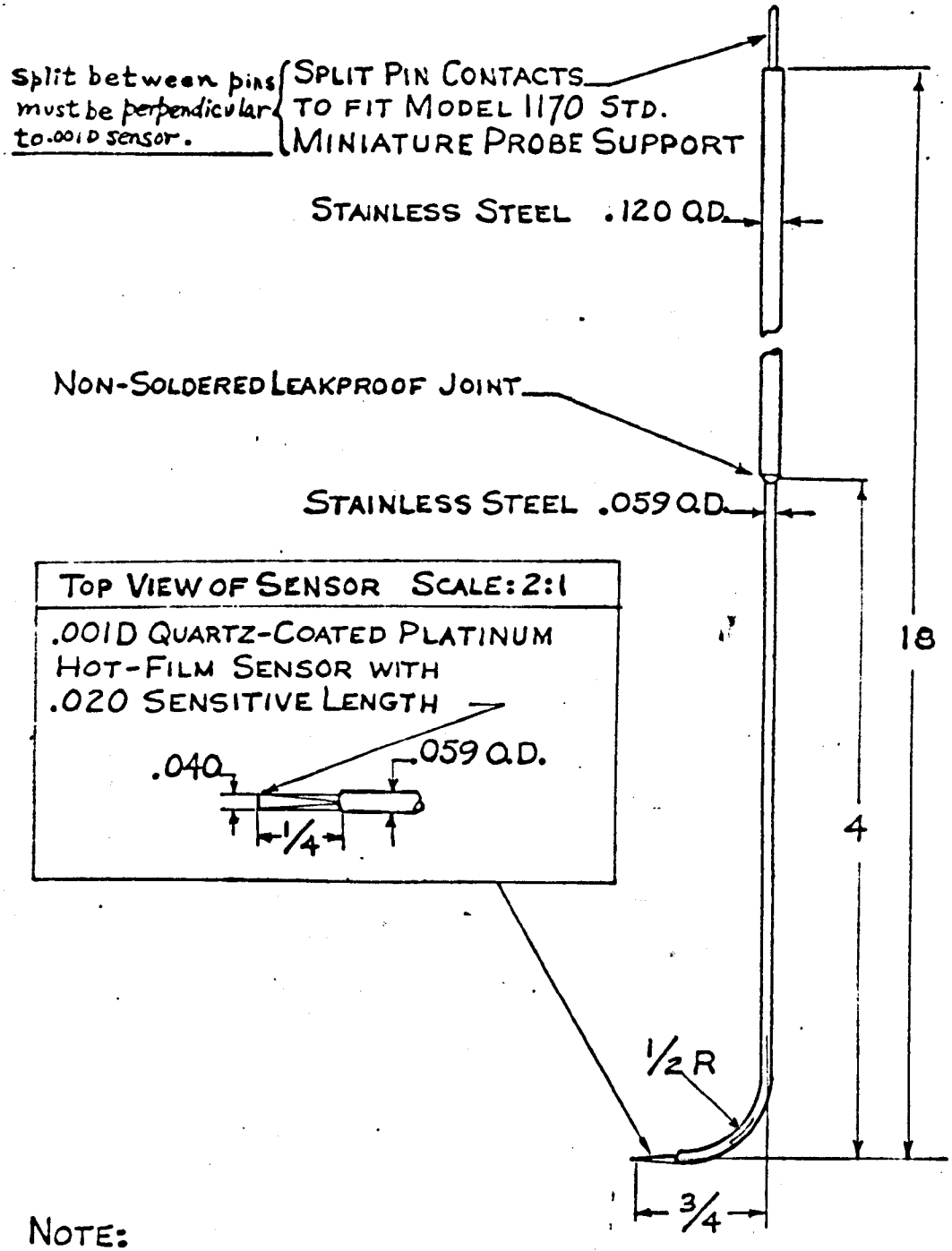

NOTE:

1. INSULATE PROBE FOR USE IN MERCURY.
2. PROBE MUST WITHSTAND OPERATION AT 100 °C.
3. ALL DIMENSIONS ARE IN INCHES.

U. OF WARWICK MHD LABORATORY	
DATE 3/5/66	SCALE 1:1
SINGLE SENSOR HOT-FILM PROBE	
D.G. MALCOLM	DWG. No. 1a

Figure 2.2 Specification drawing of special Thermo-Systems hot-film probe for mercury.

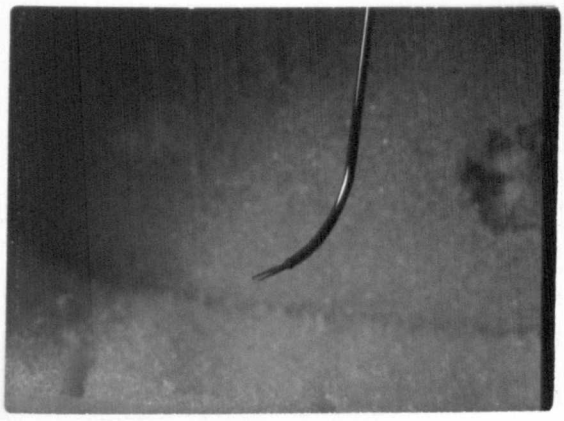

Figure 2.3 Full size photograph of probe showing hot-film sensor and mounting prongs.

Probe number	Approximate sensor diameter in mm	Sensitive length in mm	Approximate distance between tips of prongs in mm	Temperature coefficient of resistance in $^{\circ}C^{-1}$
1	0.030 ± 0.003	0.452 ± 0.015	1.13	0.00274
2	0.030 ± 0.003	0.495 ± 0.015	0.95	0.00236
6	0.028 ± 0.003	0.478 ± 0.015	1.42	0.00236

Table 2.1 Physical data of hot-film probes.

The trolley is towed via a system of pulleys and steel cables by a 2-inch O.D. hollow brass cylinder, with a sharp-edged orifice at one end, which descends vertically under gravity in an accurately machined stainless steel tube, 7 feet in length, through a mixture of water and common water-soluble machining lubricant. The rate of descent is fixed by the pressure drop across the 0.1-inch diameter orifice. Slower speeds are obtained by adding counterweights to a restraining cable which is attached to the rear of the trolley. The variation of speed with counterweight is shown in Figure 2.4. This method can be used to achieve trolley speeds as low as 0.2cm/sec. Higher speeds than 0.9 cm/sec are obtained by adjusting a by-pass valve to regulate a by-pass flow from the bottom to the top of the stainless steel tube during the descent of the brass cylinder. The trolley is timed over a 50 cm distance by a Griffin Centisecond Timer which is actuated by the tripping of microswitches situated on one guide rail at either end of the 50 cm length.

A similar towing technique was used by Lindgren and Chao (1967) who covered a range of speeds by installing orifices of various sizes, one for each speed, in the driving cylinder. The by-pass arrangement used in the present case seems a worthwhile simplification. The apparatus is capable of speed regulation from 0.3 to 14 cm/sec with $\pm$ 0.5% precision and with sufficiently low vibration in the mechanism to produce an equivalent turbulence intensity of 0.015 . Most of this vibration apparently arises from harmonic oscillations in the towing cables which are excited by a slight binding of the brass cylinder as it slides within the stainless steel tube. *

The two/tank was also used to produce a turbulence field in order to test the turbulence measurement formula which was developed in §2.2.7. This was accomplished by mounting a conventional square-mesh grid of round rods (0.028 in. diameter rods, 0.150 in. mesh spacing) on the trolley at a fixed distance ahead of the hot-film sensor and towing the entire assembly along the tank at constant speed.

Figure 2.5 shows the trolley traversing the 50 cm test length between the microswitches with the probe cable in place but without

---

* This binding problem can probably be corrected by skimming approximately 0.001 inch off the diameter of the brass cylinder before future use.

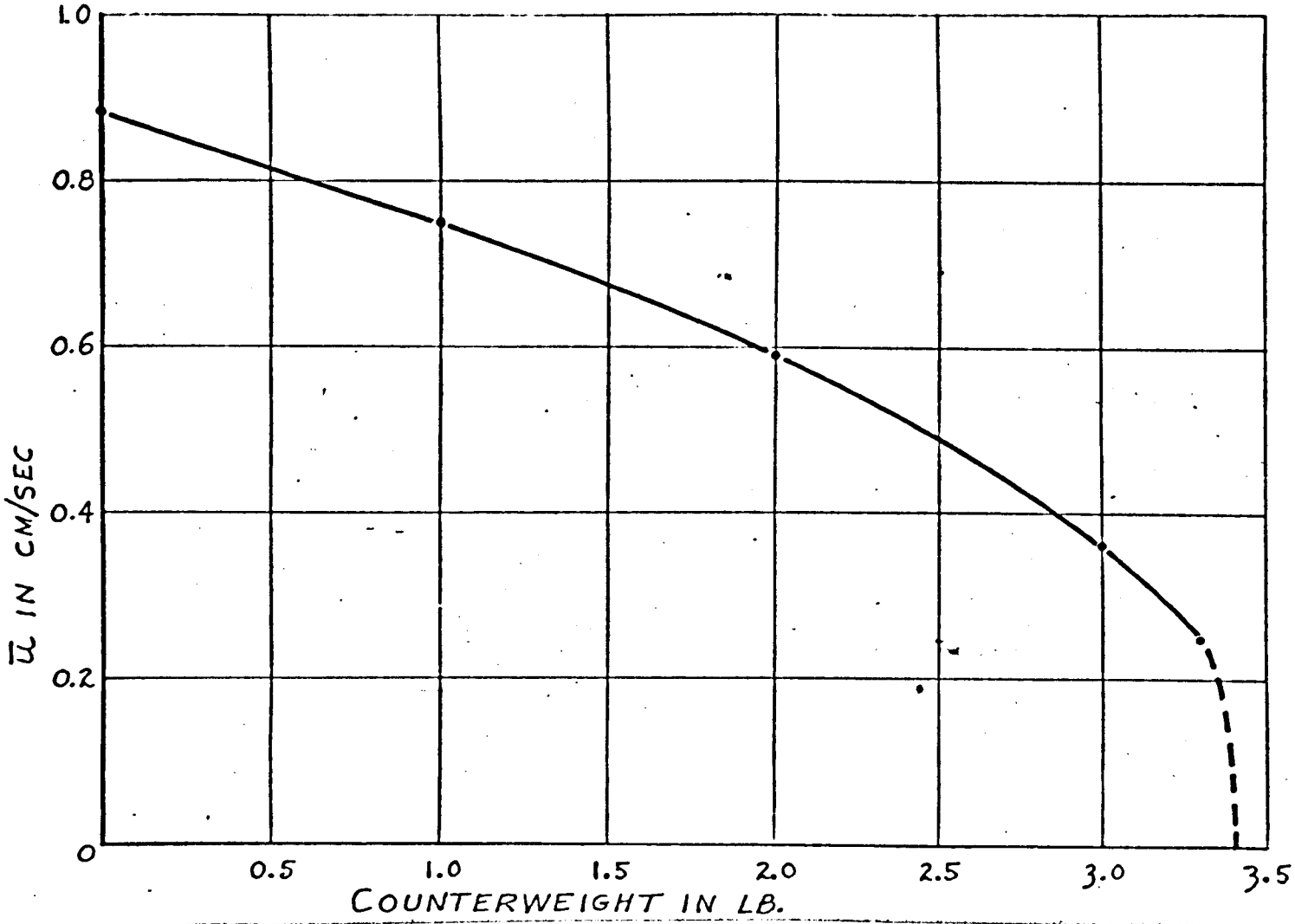

Figure 2.4 Tow tank calibration curve of towing velocity against added counterweight.

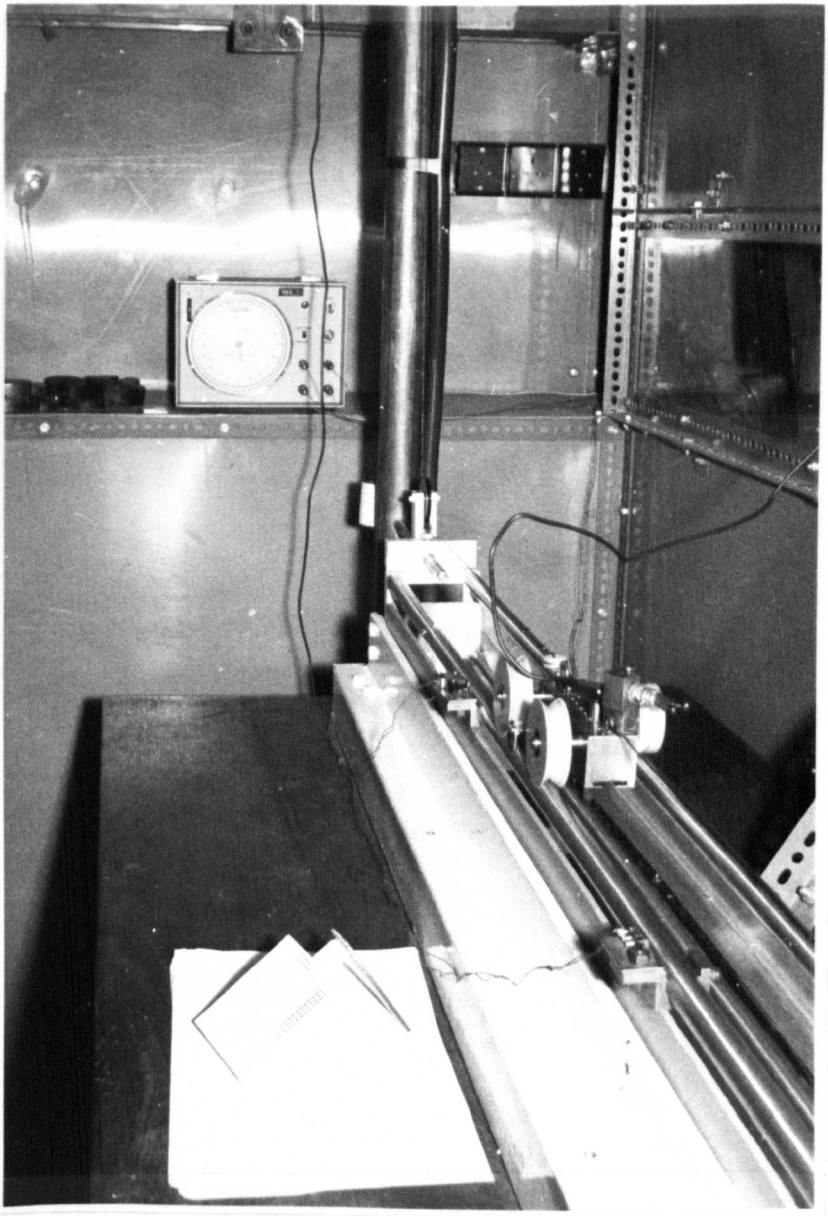

Figure 2.5. The calibration tow tank.

a hot-film probe attached. In the background is the timer and part of the vertical tube through which the driving cylinder descends. In the foreground is the grid attachment for producing turbulence.

2.3.1.4 Measurement methods

The operating procedure for velocity and turbulence intensity measurement and calculation methods are given in Appendix C. Property values for mercury as a function of temperature were obtained from Chapman (1967). They were evaluated at a temperature midway between that of the hot-film and that of the mercury environment.

The sensor runs exactly at the operating resistance only when the anemometer bridge is exactly balanced. This necessitates rebalancing of the bridge for each flow condition if a constant ΔT is to be obtained during a run. In the present case this procedure became very difficult and imprecise during calibration at high trolley speeds along the tow tank. For the highest values of Pe used here it was found that continual balancing of the bridge gave F values about 5% higher than when balancing at $Pe = 0$ only, but introduced a great deal of imprecision. The procedure was therefore dropped in favour of one where the bridge was balanced at the no flow condition prior to each run, the value of ΔT being calculated at this condition.

A discussion of various operational problems is contained in Appendix B of Malcolm (1968a). Of particular importance are problems associated with the thermal contact resistance layer (eg. very careful immersion of the sensor in the mercury to avoid a thick non-static layer), sensor operating lifetime and signal drift. Signal drift arises from gradually changing properties of the contact resistance layer (probably due to build up of impurities on the surface of the sensor) and to drifting ambient temperature. The use of electronic compensation equipment to keep ΔT constant as the ambient temperature changes is strongly advised to combat the latter problem. A Thermo-Systems 1025 Temperature Compensator with a constant voltage power source to drive it was purchased for this purpose late in the experimental programme, but a convenient season for its initiation never came. It was fortunate that in all but one of the experiments the ambient temperature drift was as low as $O(10^{-1})^{\circ}C/hr$. The exception was the experiment on turbulence decay using the flow circuit when temperature

changes of $O(10^{-1})^{\circ}C/min$ were encountered when the flow was stopped in order to measure $Q(0)$. Anyone doing future hot-film work in a flow circuit would be well advised to install a small calibration jet in the test channel to give an accurate reference of $Q(Pe)$ other than $Q(0)$ (eg. see Sajben (1965)), unless accurate temperature compensation is employed.

In the next subsection it will be shown experimentally that electromagnetic forces do significantly affect the heat transfer from the hot-films in free convection even when their axes are aligned with the magnetic field. The possibility of such an effect was discussed in §2.2.2.*

It becomes necessary, therefore, to make some allowance for MHD measurement errors caused by the effect of a magnetic field on $Q(0)$.

It will be shown in §2.3.4 that the calibration function, $F(Pe)$, varies linearly with $\ln Pe$ when $F > 0.3$ and $Pe > 0.25$, approximately. It is expected that free convection has been completely overpowered by forced convection in this range. Also, since N is no larger than $O(10^{-2})$ in this range, it is expected that MHD effects will be negligible. It is known, though, that MHD effects are significant in free convection (i.e. when $Pe = 0$). It would be expected then that the change in heat transfer due to MHD effects would vary from a maximum when $Pe = 0$ to zero at $Pe \simeq 0.25$. Since the detailed nature of this variation is unknown, it is assumed as a first approximation that the MHD effect varies linearly with F in the range $0 \leq F \leq 0.3$.

When electromagnetic forces are present let the measured calibration function be

$$F' = \pi k_f L \Delta T \left(\frac{1}{Q_B(0)} - \frac{1}{Q_B(Pe)} \right), \qquad \text{——— (2.9)}$$

where subscript B refers to the presence of a magnetic field. F' will not in general be equal to F, the calibration function outside the magnetic field. An approximate method of taking this error into account will now be sought. From equation (2.3) for F and equation (2.9) for F' the error in F is

---

* In the future it would be advisable to examine these effects in detail by calibrating the sensors in the presence of a uniform magnetic field.

$$\Delta F = F' - F = \pi k_f L \Delta T \left\{ \left(\frac{1}{Q_\beta(0)} - \frac{1}{Q(0)} \right) - \left(\frac{1}{Q_\beta(P\acute{e})} - \frac{1}{Q(P\acute{e})} \right) \right\} . \quad \text{—(2.10)}$$

From the defining equations of F and F', $F=0$ and $F'=0$ when $P\acute{e} = 0$ so that

$$\Delta F = 0,$$

in (2.10).

For $F \geq F_0$, where MHD effects are negligible, $Q_\beta(P\acute{e}) = Q(P\acute{e})$, so that from (2.10) the maximum ΔF is

$$(\Delta F)_m = \pi k_f L \Delta T \left(\frac{1}{Q_\beta(0)} - \frac{1}{Q(0)} \right) . \quad \text{——(2.11)}$$

This is the equation expressing MHD effects in free convection alone and is easily evaluated experimentally for different values of B_0.

For the correction in the range $0 \leq F \leq F_0$, let

$$\Delta F = \gamma (\Delta F)_m , \quad \text{——(2.12)}$$

where, according to the assumed first approximation,

$$\gamma \propto F. \quad \text{——(2.13)}$$

Thus, the corrected calibration curve may be represented by the expression,

$$F' = F + \gamma (\Delta F)_m , \quad \text{——(2.14)}$$

where $\gamma = 0$ for $F = 0$,
$\gamma \propto F$ for $0 \leq F \leq F_0$,
$\gamma = 1$ for $F \geq F_0$.

The adequacy of (2.13) for the correction factor is unknown. It should be adequate providing that $(\Delta F)_m / F_0$ is small. For the hot-films used in these experiments, $(\Delta F)_m / F_0 \simeq 0.1$.

2.3.2 MHD effects on free convection

These preliminary experiments were carried out using hot-film sensors numbered 1 and 6. These were immersed in mercury with their axes horizontal and parallel to a uniform magnetic field, B_0, which was provided by the magnet described later in §3.3.

The results of the experiments are expressed in the form of equation (2.11) and are plotted in Figure 2.6. For both sensors ΔF approaches a value of approximately 0.035 at $B_0 \simeq 0.5$ and remains constant thereafter. At $B_0 = 0.5$, $M^2/G \simeq 1.3$, which may have some theoretical

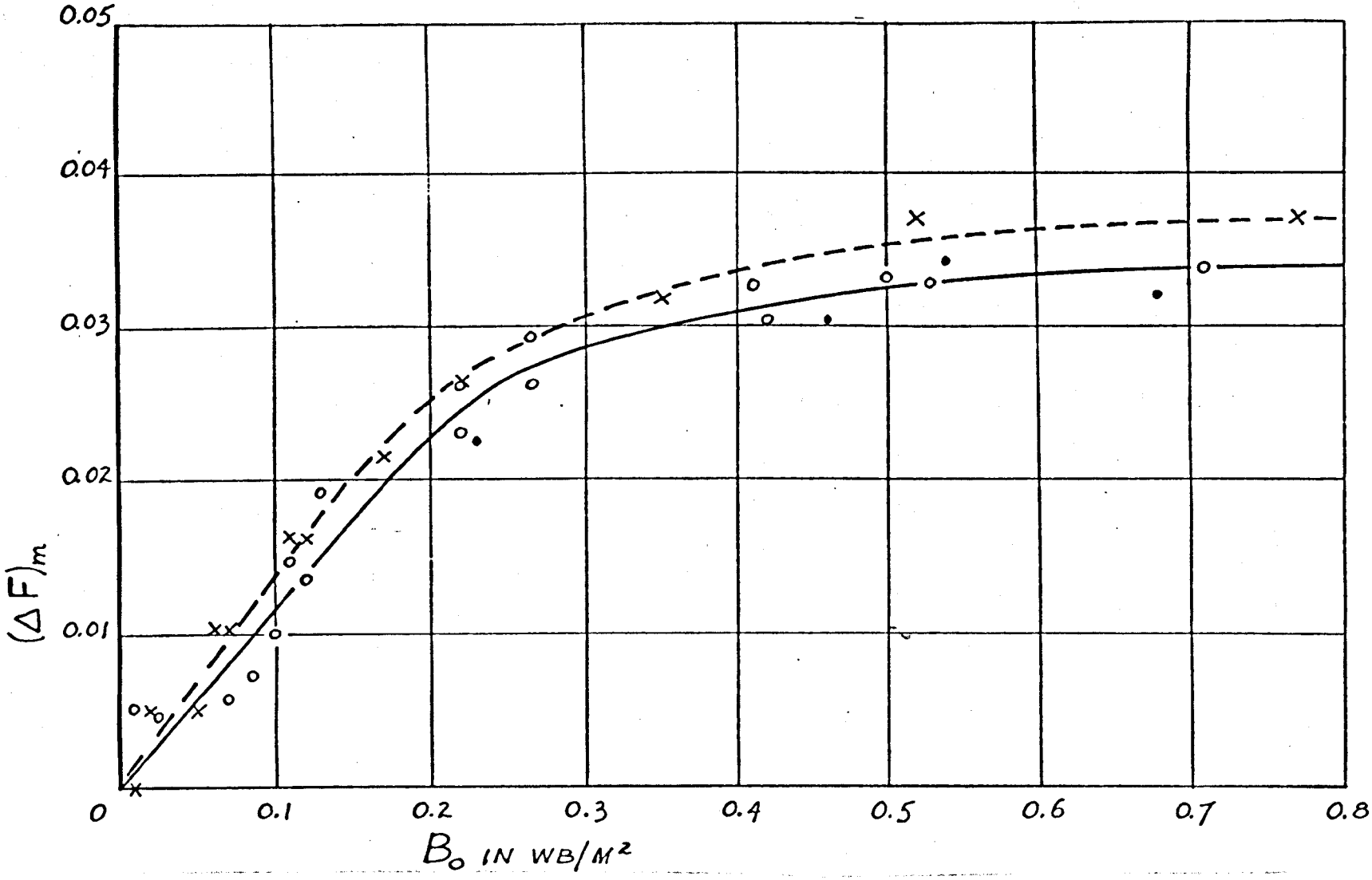

Figure 2.6 The effects of a magnetic field on free convection from field-aligned sensors (o• ———, sensor no.1, L/d = 15; x – – – –, sensor no.6, L/d = 17).

significance. Sajben (1964) examined the MHD effects on free convection in mercury with his enamel-coated hot-wire sensor positioned horizontally in a transverse magnetic field and found the MHD effects to reach a maximum at about the same value of M^2/G. A detailed study of MHD heat transfer from circular cylinders of finite length would make an important contribution to the understanding of the thermo-anemometry problem.

2.3.3 Frequency response checks

The routine square-wave test was applied to get some idea of the dynamic response of a Thermo-Systems cylindrical hot-film sensor to rapid flow fluctuations in mercury. As discussed in §2.2.3, the validity of the technique is questionable. Nevertheless, it is still possible to use this technique to optimize the frequency response of the system and to get a value of the response time which is likely to be within an order of magnitude of that which actually occurs.

Figure (2.7) shows a typical photograph of the response of the sensor in mercury. The pulse width is about 100μsec, which would indicate a frequency response of about 10kHz . It is thus very likely that the measurement system will respond sufficiently rapidly in the case of the frequencies of $O(10^2)$Hz which are of interest here.

2.3.4 Calibration of hot-film sensors

Raw data for the calibration of the three sensors used in the experiments is included in Appendix C.

The extensive calibration experiments on hot-film sensor no.2 are described in Malcolm (1968a) (see Appendix A). Sections 3 and 4 of the paper cover this experimental work and should be read in conjunction with this subsection and with the following subsection which discusses the tests of the turbulence measurement equation. In the paper the F vs $Pé$ and F vs $\ln Pé$ curves are plotted in Figures 2(a) and 2(b), the experimental conditions for the various runs are given in Table 1 and a low speed ($Pé < 0.06$) calibration is plotted in Figure 3.

Widely varying properties of the contact resistance - impurity layer around the sensor were obtained by repeated reimmersion through each of two types of interface, from air to mercury and from water to mercury. Accordingly, the free convection heat transfer, represented by $\pi k_f L \Delta T / Q(0)$ in Table 1, was observed to vary from 3.32 to 8.24. In spite of this wide variation, similar F vs $Pé$ curves were obtained

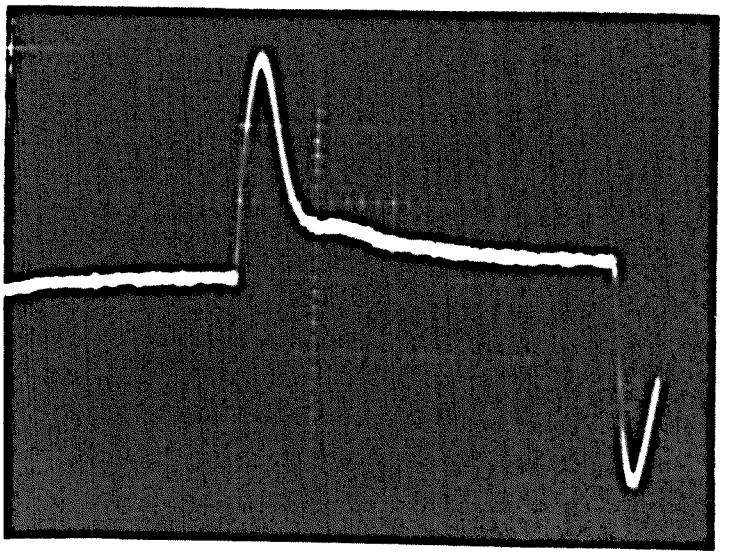

Figure 2.7 Frequency response test on a 0.030 mm diameter hot-film sensor by the square-wave test. Scales: 50 μsec/division, 10 mv/division.

so that Sajben's calibration method is indeed applicable.

The use of the water to mercury interface lessened the thermal contact resistance, and increased the sensitivity through improved surface wetting, at the expense of creating an unstable layer around the sensor which caused random drift effects. It is hoped that better methods can be found to improve the wetting of the sensor's surface by mercury. Hoff (1968), who is using larger diameter Thermo-Systems sensors (0.16mmdiameter) at large Pe, has attempted to solve the problem by depositing a thin gold film on the quartz insulation. He reports a significant improvement in operation of the sensors, especially as regards preventing the build-up of impurities on its surface, for as long a time as it takes the mercury to amalgamate with the gold film.

In the paper sensor no.2 was run at temperature differences from 11 to 34 ^{o}C. For this range, similar $F(Pe)$ curves were obtained (within experimental error). This was to be expected since $Nu(0)$ is a very weak function of temperature when GP is $0(10^{-3})$.

A great deal of scatter is evident in the F vs Pe curve, Figure 2(a). This is most important at larger values of Pe where a small change in F corresponds to a much larger change in Pe . The scatter may be attributed to impurity build-up on the sensor and would likely have been much less had stringent measures of cleanliness been observed. The only cleaning operation was to skim the free surface of the mercury in the two tank from time to time with a skimming probe, a stainless steel tube flattened slightly at one end, which was operated under vacuum.

The low speed calibration curve in Figure 3 of the paper shows that fairly reliable velocity measurements may be made when $\bar{u}$ is less than $1\ ^{cm}/_{sec}$($Pe < 0.06$) provided that the ambient temperature is constant during the measurement of a pair of $Q(0)$ and $Q(Pe)$ values.

Similar calibration curves for sensor no.1 are given on the following pages in Figures 2.8 to 2.10, and for sensor no.6 in Figures 2.11 and 2.12. Also shown are the F' curves which take MHD errors into account. These curves are calculated according to the method given in §2.3.1.4 which makes use of the values of $(\Delta F)_m$ from Figure 2.6.

It is not worthwhile to discuss the slight differences between the calibration curves for the three sensors. To do this it would be necessary to know the diameter of the sensors more exactly and the thicknesses of

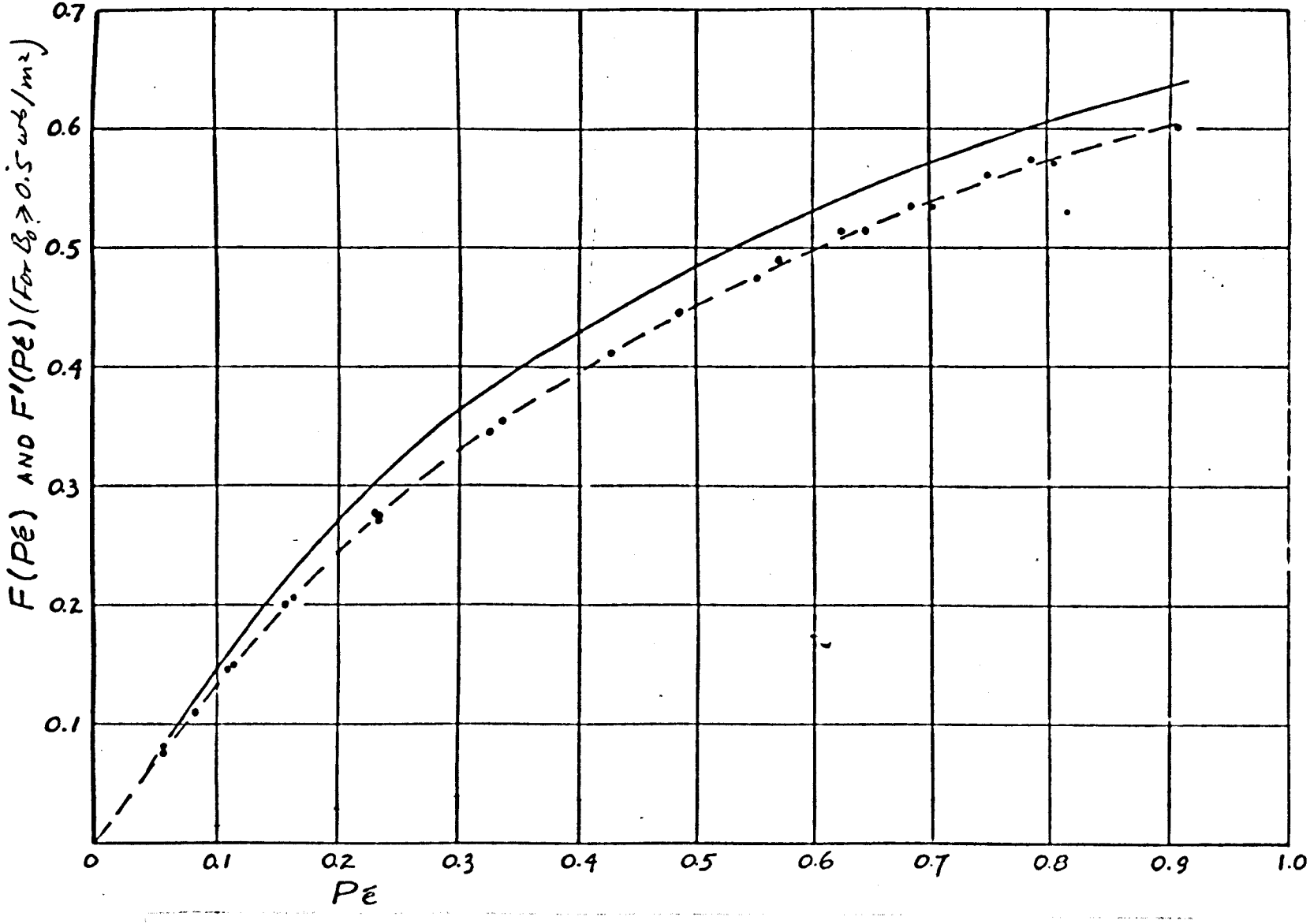

Figure 2.8 Hot-film probe no. 1 calibration curves: F(Pé) and F'(Pé) versus Pé (• — —, F vs Pé; ———, F' vs Pé).

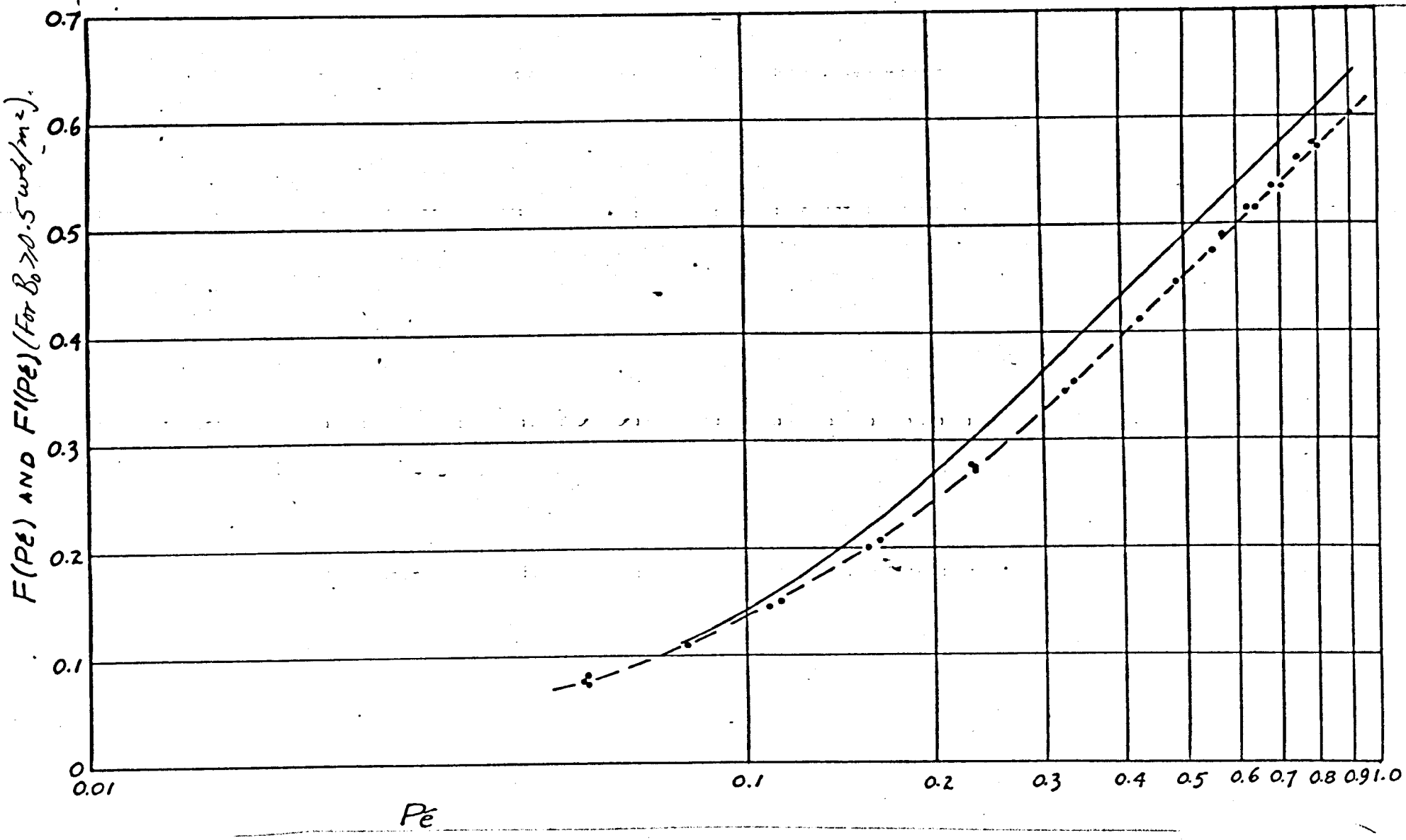

Figure 2.9 Hot-film probe no. 1 calibration curves: F(Pé) and F'(Pé) versus lnPé (• — —, F vs lnPé; ———, F' vs lnPé).

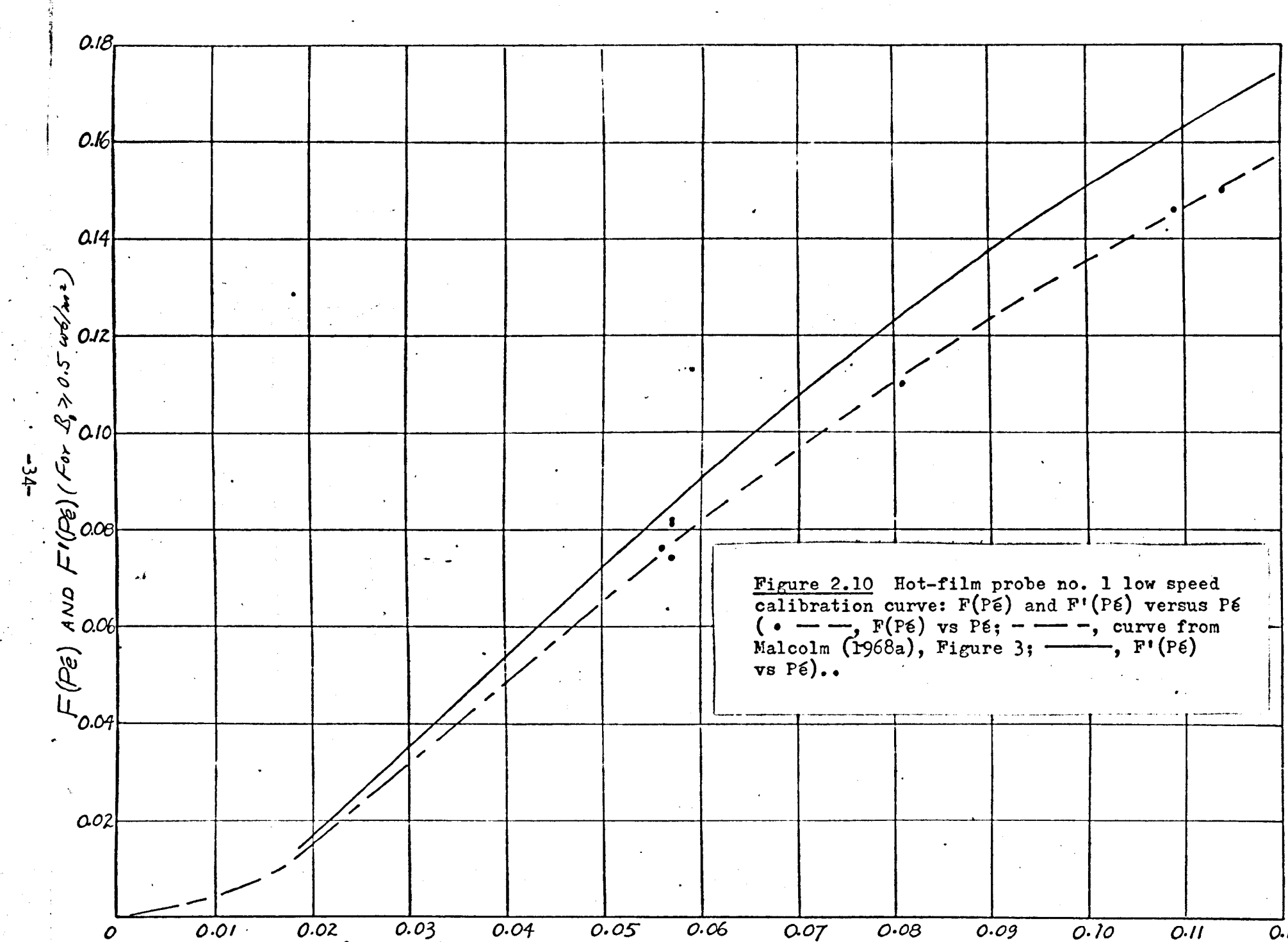

Figure 2.10 Hot-film probe no. 1 low speed calibration curve: F(Pé) and F'(Pé) versus Pé (• — —, F(Pé) vs Pé; - —— -, curve from Malcolm (1968a), Figure 3; ———, F'(Pé) vs Pé)..

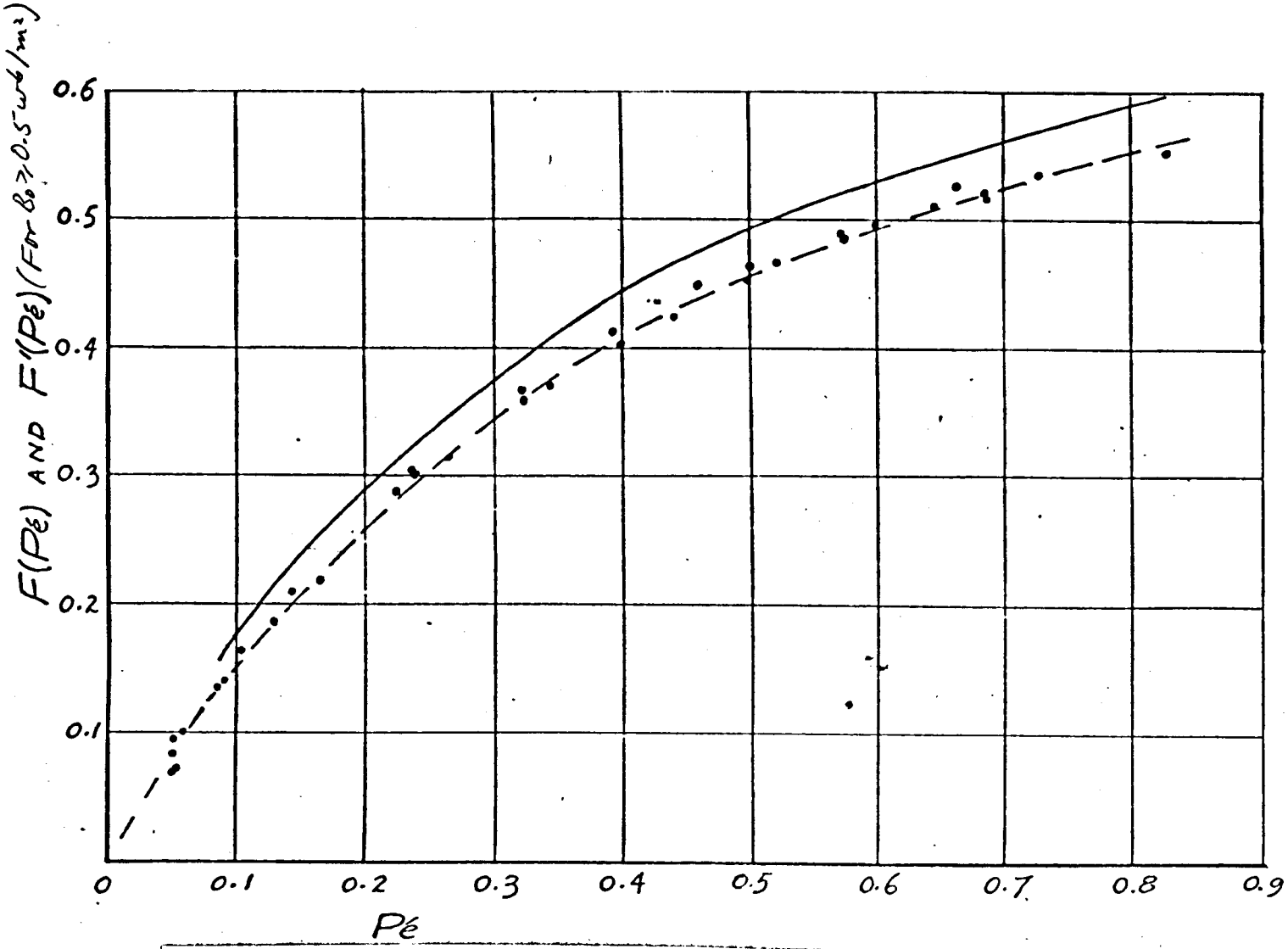

Figure 2.11 Hot-film probe no. 6 calibration curves: F(Pé) and F'(Pé) versus Pé (• — —; F vs Pé; ———, F' vs Pé).

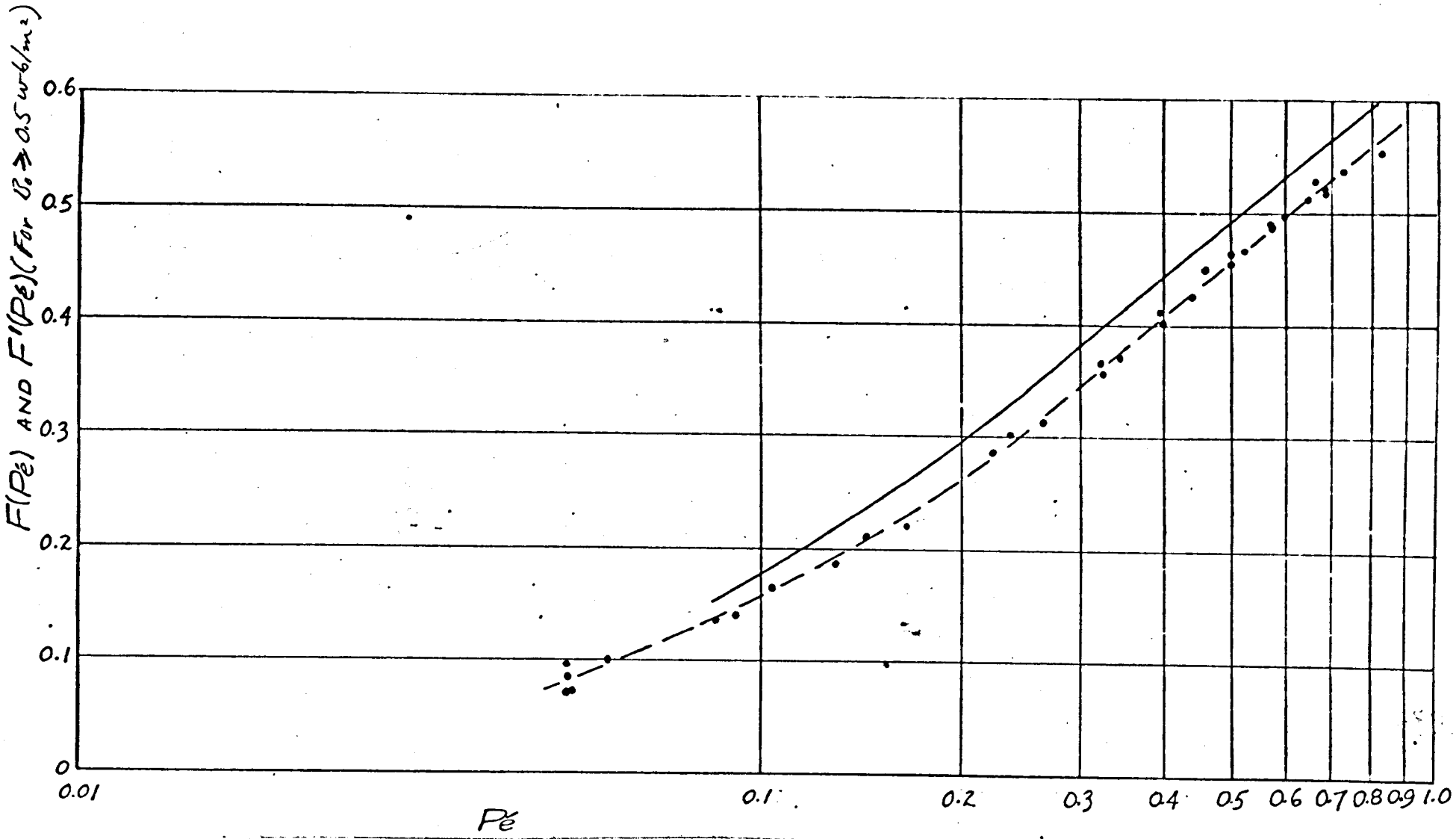

Figure 2.12 Hot-film probe no. 6 calibration curves: F(Pé) and F'(Pé) versus lnPé (• — —, F vs lnPé; ———, F' vs lnPé).

insulation, as well as to understand the complicated end effects.

The extension of the F vs Pe low speed calibration curve for sensor no.1 to lower values of Pe in Figure 2.10 requires some explanation. This extension was made out of necessity* in order to calculate some of the low velocities measured in the steady electrically driven flow experiment. The extended portion is identical to the low speed F vs Pe curve for sensor no.2 in Figure 3 of the paper. The physical similarity of the two sensors and the smooth way in which the F vs Pe curve for sensor no.1 in Figure 2.8 merged into the curve in Figure 3 was considered to provide sufficient justification for this extension.

Sensor no.2 was used only in the measurements described in Malcolm (1968a). Sensor no.1 was used in the electrically driven flow experiments and sensor no.6 was used in the grid turbulence decay experiment. These experiments will be discussed in §3.3 with reference to the calibration curves just described.

2.3.5 Tests of the turbulence measurement equation

The tests carried out to show the practicality of equation (2.6) for measuring the intensity of streamwise turbulent fluctuations in mercury are described in sections 3 and 4 of Malcolm (1968a). Only the main observations from these sections and a few extra details will be mentioned here.

The experiments were carried out using the tow tank with the grid attachment in place on the trolley (20 mesh lengths ahead of the hot-film position). The turbulence measured was a combination of the slight vibration of the mechanism and the actual grid turbulence.

The results of the experiments are presented in Table 2 of the paper. As in the calibration exercises, various reimmersions of the sensor through both a water to mercury and an air to mercury interface were tried over a fairly wide range of ΔT (i.e. from 11 to 44°C). Reynolds numbers, based on the grid mesh length, of 3050 and 4650 were tested.

Calculated values of $\sqrt{\overline{w^2}}/\overline{u}$ varied from 0.033 to 0.041 but

---

* Sensor no.1 was broken by accident during disassembly of the electrically driven flow apparatus so that no follow-up calibration at low speed could be attempted.

there doesn't seem to be any correlation between this variation and the variations in value of the independent experimental variables. The most likely cause of these variations is a slight change in the intensity of the mechanical vibration of the mechanism from one run to another. Although the equivalent turbulent intensity of these vibrations was generally about 0.015 when the trolley was run without the grid attachment, an unusually low or unusually high value was observed at times. For instance, see Figures 2.13(a) and (b) which represent two consecutive runs of the trolley with the grid detached. The amplitudes of the oscillations in the anemometer output voltage are observed to vary during a single run and also to vary from one run to the next.*

The dramatic effect of improving the wetting of the sensor by immersing the sensor through a water to mercury interface in place of an air to mercury interface is shown by comparing Figures 2.14 and 2.15 (i.e. the oscillographs from which Figures 4(a) and (b) in the paper were drawn). These figures display turbulent fluctuations of similar intensity in the form of typical e vs time variations. The two traces have identical time and voltage scales. However, the oscillation amplitudes are much greater where better thermal contact is achieved. This is because, at constant ΔT, $\sqrt{\overline{e^2}}$ must always increase in direct proportion to $\overline{E}^3$ to yield similar values of $\sqrt{\overline{w^2}}/\overline{u}$.

One advantage of improved thermal contact is to increase the hot-film's sensitivity to flow fluctuations and thereby increase the signal to noise ratio. This is very important when one is attempting to interpret a fluctuating anemometer signal. Refer to Figures 2.16 and 2.17. In Figure 2.16, representing the air to mercury interface case, the turbulent fluctuations are hidden behind a veil of weak electronic noise which has the appearance of a high frequency turbulence. On the other hand, in Figure 2.17 which represents the water to mercury interface case, the sensor is so sensitive to the flow fluctuations themselves that the electronic noise fluctuations are too small to be seen.

From the experiment as a whole it may be concluded that the turbulence intensity formula yields reliable measurements over a wide range of operating variables, provided only that in the range of Pe considered there is a linear dependence of F on $\ln Pe$.

---

*Suggestions as to the cause of this vibration and its possible cure were discussed in §2.3.1.3.

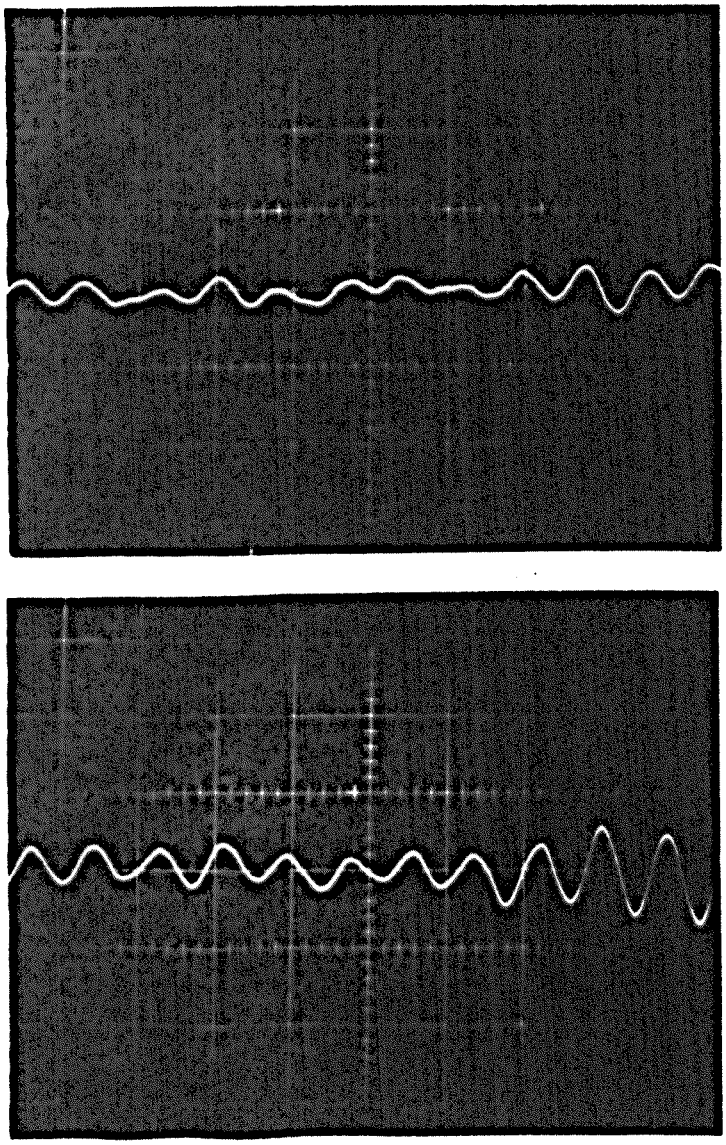

Figure 2.13 Trolley vibration.
(a) and (b): consecutive runs.
Scales: 0.02 sec/division, 50 mv/division.

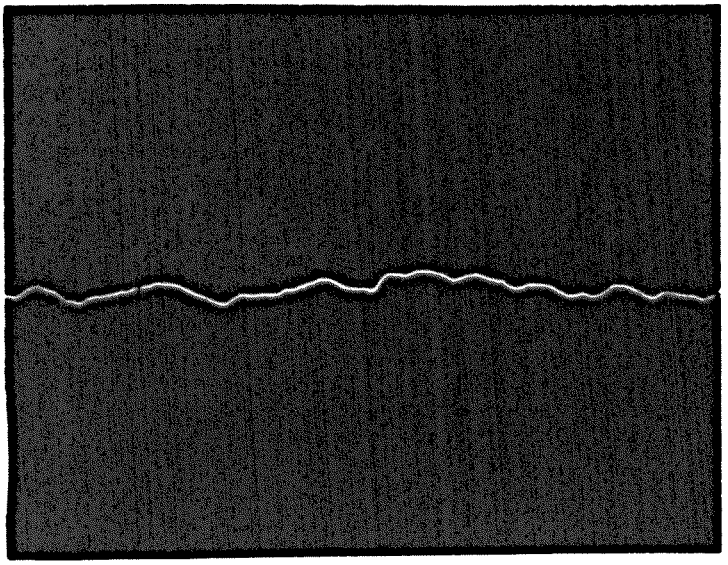

Figure 2.14 Hot-film turbulence signal: air-mercury interface.

Scales: 0.02 sec/division, 50 mv/division.

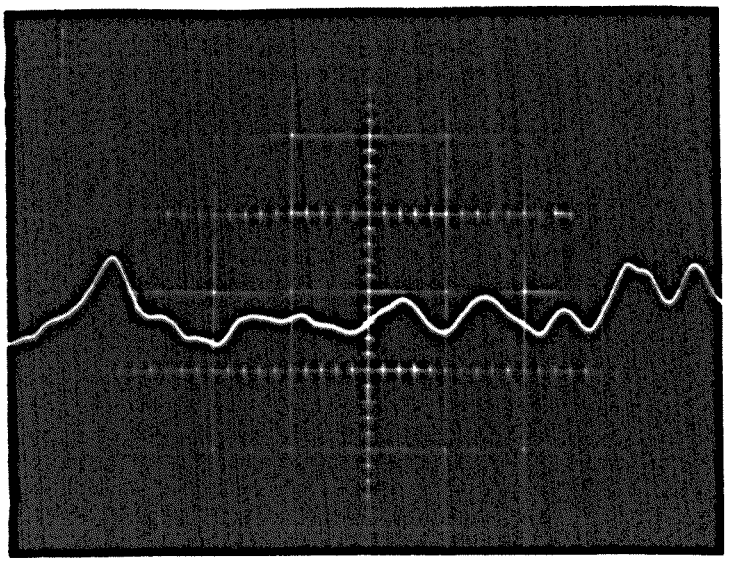

Figure 2.15 Hot-film turbulence signal: water-mercury interface.

Scales: 0.02 sec/division, 50 mv/division.

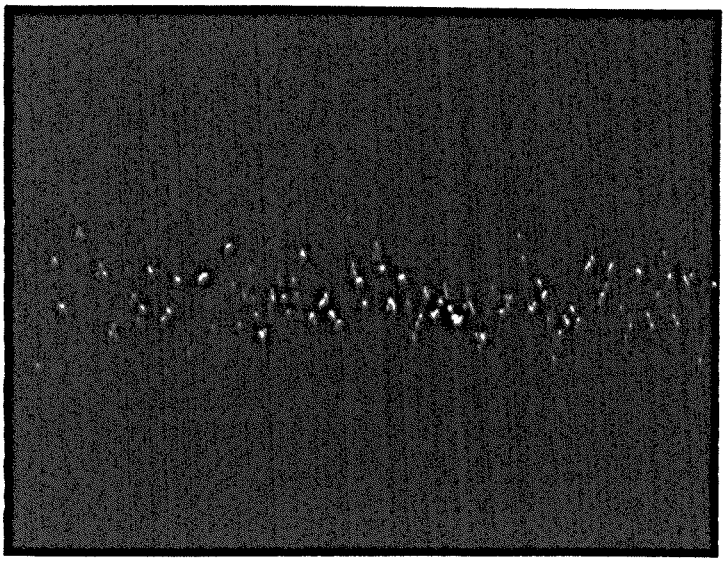

Figure 2.16 Hot-film turbulence signal: air-mercury interface.

Scales: 0.05 sec/division, 5 mv/division.

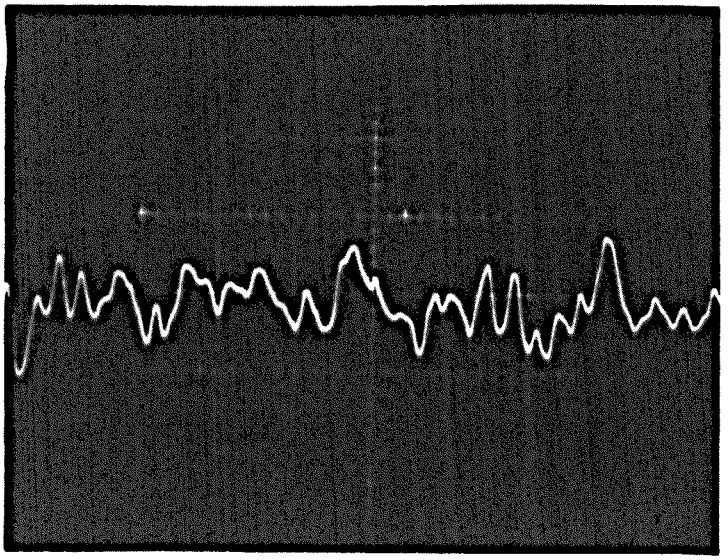

Figure 2.17 Hot-film turbulence signal: water-mercury interface.

Scales: 0.05 sec/division, 50 mv/division.

3. SOME MAGNETOHYDRODYNAMIC STUDIES

3.1 Introduction

The main purpose of this chapter is to show the practicality of the hot-film techniques discussed in chapter 2 by applying them to some typical MHD flows in mercury. Because of its small size and rapid dynamic response the cylindrical hot-film should have definite advantages over other probes as a measurement device in shear layers, unstable flows and turbulence fields. As will be seen, it nevertheless has its weaknesses.

It is hoped that the results obtained from the MHD experiments will be considered interesting in themselves since quantitative local measurements within MHD flows are seldom to be found in the literature. The art of measuring steady and unsteady MHD phenomena at an arbitrary point in a flow is still in an embryonic state.

The first concerted attempt to understand theoretically the behaviour of Pitot tubes and electric potential (e.p.) probes in an MHD situation was by Hunt (1967). The first known attempt to apply Pitot tubes and e.p. probes together in order to correlate their results and to compare these with theory was made by Hunt and Malcolm (1968) in the study of electrically driven flow (EDF) between circular electrodes. The results of these experiments serve to illustrate how little is presently understood of probe behaviour in MHD systems. However, they form a basis with which to compare the thermo-anemometric study of the same system. This hot-film study represents the first attempt to examine in detail experimentally the internal structure of an MHD shear layer and its stability.

The last experiment on grid turbulence decay in an MHD situation represents the first attempt in this direction. The study is very sketchy due to total depletion of two precious commodities, hot-film probes and time! It nevertheless provides some understanding of flow modification by electromagnetic forces downstream from a common square mesh grid.

This chapter is organised in the following way. §3.2 discusses the theory upon which the experiments are based. §3.2.1 summarises the work on steady circular EDF. §3.2.2 discusses a physical mechanism which may control the stability of the EDF shear layers. §3.2.3. summarises some of the theory applicable to MHD vorticity decay in mercury.

§3.3 covers the experimental work. §3.3.1 describes the new MHD laboratory which has been designed and built at the School of Engineering Science specifically for work with mercury. §3.3.2 describes the EDF apparatus, the flow system for the turbulence decay experiment and the thermo-anemometry system. §3.3.3 discusses the experiment on steady EDF between circular electrodes. §3.3.4 discusses the experiments on the stability of and subsequent secondary flow in the EDF case. §3.3.5 describes the experiment on turbulent vorticity decay downstream from a square mesh wire grid. To conclude the chapter, §3.3.6 compares the performance of Pitot tubes, e.p. probes and cylindrical hot-film sensors in MHD flows.

The research reported in this chapter is summarised in the last two sections of Malcolm (1968b) (see Appendix A). The study of the detailed structure of the EDF shear layers, their stability and the subsequent secondary flow will be published in more detail in the future (Malcolm (1969)).

3.2 Theory

3.2.1 Steady electrically driven flow (EDF) between circular electrodes

When two electrodes at different electric potentials are placed one in each of two parallel insulating planes, between which is an electrically conducting fluid, and when a magnetic field is applied normal to these planes, a flow is induced in thin layers which join the edges of the electrodes. This effect was first fully appreciated by Moffatt (1964). Some of the fluid mechanical and electrical phenomena which occur for different electrode geometries have been described in a paper in three parts by Hunt and Williams (1968), Hunt and Malcolm (1968) and Hunt and Stewartson (1969).

In Part 1, Hunt and Williams examined the specific cases of line and point electrodes theoretically. Of particular interest to the present research is part 2 by Hunt and Malcolm. This paper describes, both

theoretically and experimentally, the case where the electrodes are circular discs positioned directly opposite from one another. The arrangement (and the (r, θ, z) co-ordinate system) is shown, including the current lines when $M = 0$, in Figure 1(a) of the paper. When $M >> 1$ we found that the current was channelled or, in other words, confined to the cylinder of fluid joining the electrodes. This effect is accounted for by the action of the induced electric field, $\underset{\sim}{u} \times \underset{\sim}{B}$, owing to the velocity component, u_θ, which is induced by $\underset{\sim}{j} \times \underset{\sim}{B}$ forces in thin layers with thickness $O(M^{-1/2})$ at the circumference of the cylinder. Through the layers the electric potential, ϕ, falls and u_θ is induced in the manner shown in Figure 1(b) of the paper. The azimuthal velocity falls to zero on the centreplane between the discs and is of opposite sign on either side of this plane.

A complete solution to the analytical problems was not obtained in the paper. Conclusions of physical interest were drawn following and approximate asymptotic analysis when $M >> 1$. These conclusions were then substantiated by experiments using Pitot tubes and e.p. probes within the flow. For details of this work, refer to the paper in Appendix A of the thesis. The layout of the paper is as follows. An introductory section discusses the physical situation, section 2 presents the asymptotic analysis, sections 3 and 4 discuss the experimental apparatus and results and section 5 states the conclusions drawn from both theory and experiment. Appendix A of the paper describes in detail the experimental apparatus used and, in particular, summarises the theory of Hunt (1967) on the operation of the Pitot tube and the e.p. probe in MHD situations. Appendix B discusses the stability of the EDF system and secondary flow effects. These last aspects will be discussed in more detail in the next subsection.

The solution for the azimuthal velocity in the thin shear layers is given by the equation on p.6 of the paper, viz.,

$$u = \frac{1}{4\ell^2 M^{1/2}\sqrt{\pi}} \int_0^\infty g(t) \left\{ \frac{\exp\left(-(\tau-\bar{\tau})^2/4(1-\varsigma)\right)}{(1-\varsigma)^{1/2}} - \frac{\exp\left(-(t-\bar{\tau})^2/4(1+\varsigma)\right)}{(1+\varsigma)^{1/2}} \right\} dt, \qquad (3.1)$$

where $\bar{\tau} = (\varrho - \ell) M^{1/2}$, $\varrho = r/a$, $\varsigma = z/a$ and $\ell = b/a$. b and a are the radius of the electrode disc and the half-width of the space

between the electrodes respectively. $u = u_\theta/(I/2\pi a\sqrt{\sigma\eta})$ is a non-dimensional velocity in which I is the electric current, σ is the electrical conductivity and η is the viscosity.

In a forthcoming paper (part 3) Hunt and Stewartson (1969) present a complete asymptotic analysis in order to arrive at actual theoretical values for the velocity and electric potential. These values will be compared with the experimental results of Hunt and Malcolm, and with some of the hot-film measurements in §3.3.3 of this chapter.

For comparison with the hot-film measurements a graph of $u_\theta M^{1/2} b l \sqrt{\sigma\eta}/I$ against $(\rho - l) M^{1/2}$ for $\gamma = 0.50$, based on the above mentioned Hunt and Stewartson theory and kindly provided by Dr.J.C.R.Hunt, is plotted in Figure 3.1. In addition, the theoretical maxima of the curves at some values of γ are given in Table 3.1 for later reference.

γ	$u_\theta M^{1/2} b l \sqrt{\sigma\eta}/I$
0.50	0.059
0.905	0.137
0.922	0.142
0.97	0.166
1.00	0.226

Table 3.1: Maxima of radial velocity profiles in the EDF shear layer according to the theory of Hunt and Stewartson (1969).

3.2.2 The stability of some shear layers in MHD

3.2.2.1 Introduction

The three-dimensional character of the rotating EDF shear layer makes the physical mechanism which governs its stability very difficult to understand. The interesting outcome of the experimental study of this problem in §3.3 necessitates some attempt, however inadequate, to understand the ways in which electromagnetic forces affect the stability of this system.

There are three ways in which the presence of a magnetic field can affect the stability of an MHD flow. Firstly, it may affect the flow directly by altering the shape of the velocity profile. The effect may be stabilizing or destabilizing as discussed in the case of MHD duct flow by Hunt (1965). Secondly, the magnetic field may directly affect the growth or decay of the most unstable disturbances which occur when critical conditions are reached in some part of the flow. Hunt (1966)

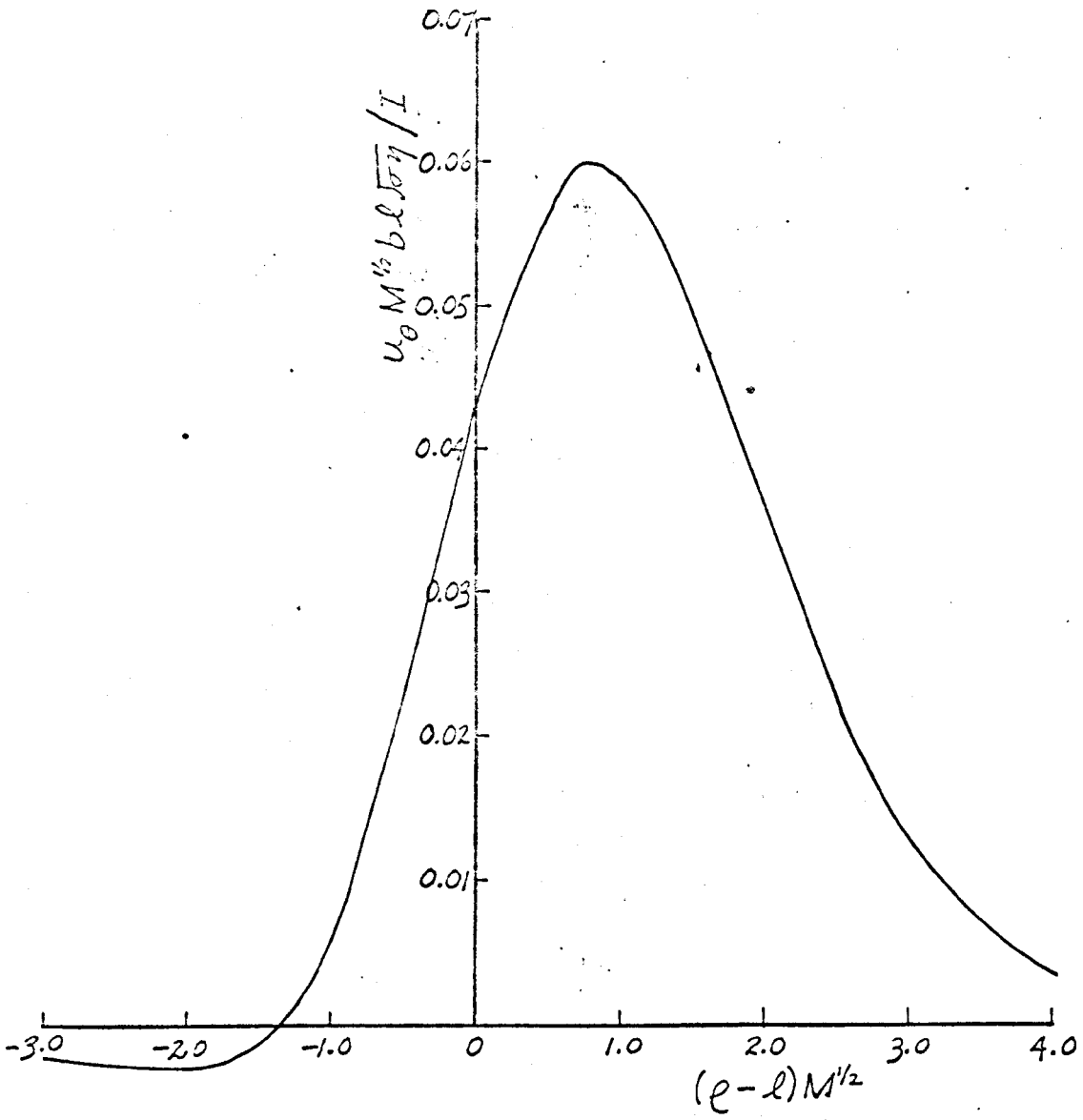

Figure 3.1 Theoretical radial profile of azimuthal velocity: provisional results from Hunt & Stewartson (1969) for $\mathcal{J} = 0.50$.

presented a lucid discussion of this effect. In particular he was able to deduce sufficient conditions for there to be no growth of perturbations in the magnetic field and the electric current. He also discussed the conditions for there to be no effect on a velocity disturbance by a magnetic field. Finally, through the direct action on the disturbances, the magnetic field may affect the interaction between these disturbances and the primary flow. This aspect has been dealt with by various writers, notably by Wooler (1961) and by Hunt (1966, 1967).

Following a statement of the relevant MHD equations this section discusses, in qualitative terms, the three aspects of MHD stability as applied to the rotating EDF shear layer. The remarks on the last two aspects, concerning the behaviour of an assumed velocity disturbance and its interaction with the primary flow, are conjectural because of the difficulty in understanding the three-dimensional effects.

A schematic sketch of the rotating EDF system, also showing the (r, θ, z) co-ordinates, is shown in Figure 3.2. The shear layer will under certain conditions be approximated by a three-dimensional, plane parallel flow in the (x, y, z) co-ordinate system shown in Figure 3.3. The angles ϕ_k and ϕ_B in the (x, z) plane refer to the inclination to the x -axis of the disturbance wave number vector, $\underset{\sim}{k}$, and of the applied magnetic field, $\underset{\sim}{B}_0$, respectively. In this co-ordinate system, x and y correspond to θ and $-r$, respectively, in the (r, θ, z) co-ordinate system (see Figure 3.2). The shear layer flows in the x-direction and the shape of its profile varies in the y and z -directions.

In the remainder of §3.2.2 the abbreviations "2-D " for "two-dimensional" and "3-D " for "three-dimensional" will be used.

3.2.2.2 MHD equations

The following equations of MHD will be referred to. They apply to incompressible fluids having uniform electrical conductivity, viscosity and density. See Shercliff (1965) for details of the derivations and for a discussion of the approximations made in these equations. The equations are:
the equation of motion,

$$\rho\left(\frac{\partial \underset{\sim}{u}}{\partial t} + (\underset{\sim}{u}\cdot\nabla)\underset{\sim}{u}\right) = -\nabla p + \underset{\sim}{J}\times\underset{\sim}{B} + \eta\nabla^2\underset{\sim}{u}, \qquad \text{——(3.2)}$$

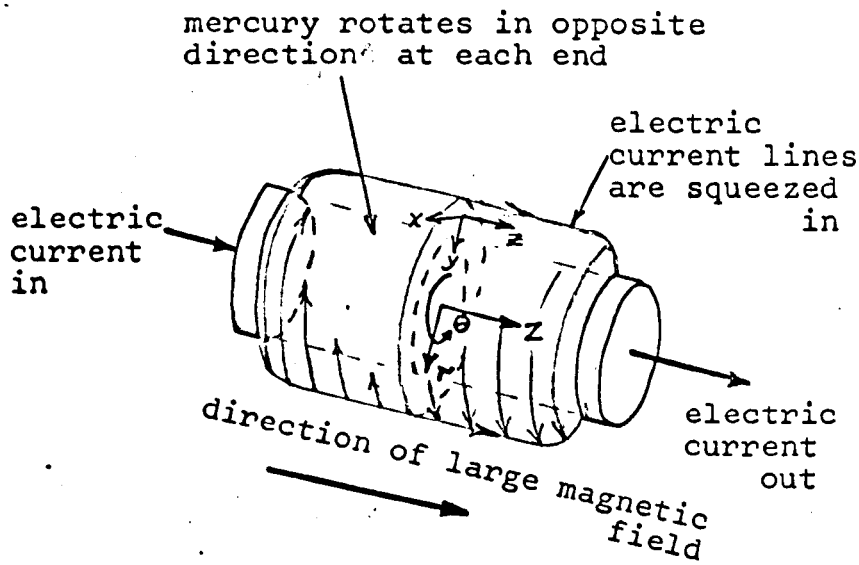

Figure 3.2 A sketch of the circular electrically-driven flow system with the systems of co-ordinates.

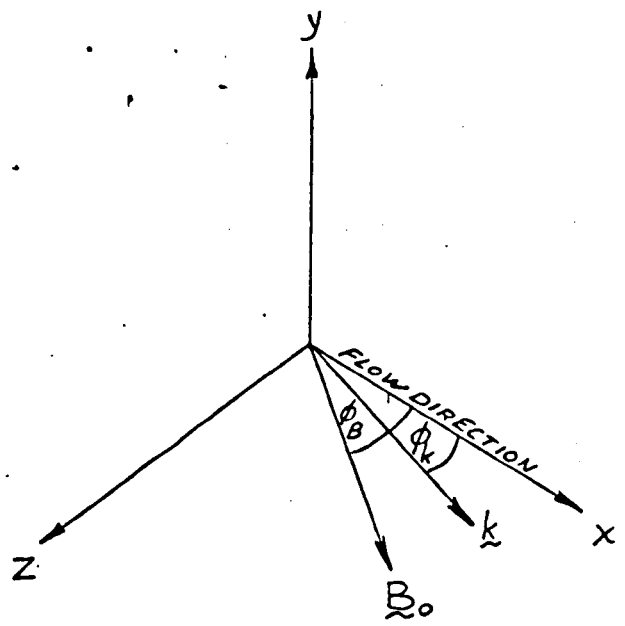

Figure 3.3 The (x,y,z) co-ordinate system, showing the directions of the wave number vector and the applied magnetic field relative to the flow direction.

Ohm's law,

$$\underset{\sim}{J} = \sigma(\underset{\sim}{E} + \underset{\sim}{u} \times \underset{\sim}{B}), \qquad \text{——— (3.3)}$$

$$\left.\begin{aligned} \mu\underset{\sim}{J} &= \nabla \times \underset{\sim}{B}, \\ -\partial\underset{\sim}{B}/\partial t &= \nabla \times \underset{\sim}{E}, \\ \nabla \cdot \underset{\sim}{B} &= 0, \end{aligned}\right\} \quad \text{Maxwell's equations,} \qquad \begin{aligned} &\text{——— (3.4)} \\ &\text{——— (3.5)} \\ &\text{——— (3.6)} \end{aligned}$$

the equation of continuity,

$$\nabla \cdot \underset{\sim}{u} = 0. \qquad \text{———(3.7)}$$

In these equations the symbols $\tilde{\rho}$, η, σ and μ represent the properties, density, viscosity, electrical conductivity and permeability, respectively. The fluid mechanical variables $\underset{\sim}{u}$ and p are the velocity vector and pressure. The electromagnetic variables $\underset{\sim}{J}$, $\underset{\sim}{B}$ and $\underset{\sim}{E}$ are the vectors of the current density, magnetic flux density and electric field, respectively.

In the following discussion it will be assumed that the magnetic Reynolds number, R_m ($R_m = \mu\sigma|\underset{\sim}{u}|\ell$, where ℓ is a typical length scale) is very small, i.e. $R_m << 1$. This implies that the induced magnetic field, $\underset{\sim}{B}_i$, as determined from (3.4), is very small compared to the externally applied field, $\underset{\sim}{B}_o$, and that the effects of $\underset{\sim}{B}_i$ on the fluid motion are correspondingly small. This assumption is usually valid when MHD flows of mercury are considered on the normal laboratory scale.

3.2.2.3 Direct stabilization of the EDF velocity profile by $\underset{\sim}{B}_o$

In Appendix B of H & M (Hunt and Malcolm (1968)) secondary flow in the rotating EDF system is discussed. The discussion is mainly based upon the experimental results obtained using Pitot tubes and electric potential probes, but also considers some preliminary hot-film measurements. That discussion will now be continued.

We concluded from experimental evidence in the H & M paper that the effect of an increase in the magnetic field on the flow at a given driving current was to stabilize it by lowering the Reynolds number. This effect becomes evident by considering the definition of a Reynolds number, R, based on the maximum azimuthal velocity, u_θ, which occurs in the shear layer of thickness $O(aM^{-1/2})$, viz.,

$$R = u_{\theta\,max}(aM^{-1/2})\tilde{\rho}/\eta. \qquad \text{———(3.8)}$$

From the asymptotic analysis which culminated in equation (3.1) it was observed that

$$u_\theta \propto I/M^{1/2}, \qquad \text{———(3.9)}$$

so that (3.8) and (3.9) may be combined in the following way:

$$R \propto I/M . \qquad \text{———(3.10)}$$

From (3.10) it may be stated that R decreases as M increases (i.e. the flow tends to be stabilized) at constant I.

If (3.10) is tested experimentally by increasing I at a constant value of M, a critical condition will eventually be reached in the region of maximum u_θ. At this condition the critical R and critical I are related by (3.10), i.e.,

$$R_c \propto I_c/M .$$

These critical conditions can be easily explored using the hot-film technique by measuring I_c as a function of M so that the dependence of R_c on M can be determined from the relationship,

$$R_c \propto f(M)/M . \qquad \text{———(3.11)}$$

It is evident from a comparison of (3.10) and (3.11) that the criterion of stability must be stated before it can be definitely decided whether or not a magnetic field is stabilizing or destabilizing. Although it is obvious from (3.10) that an increase in M is stabilizing at constant I it is not clear from (3.11), without further information about $f(M)$, whether or not R_c will increase with M. Tied up in $f(M)$ is the response of the system to both electromagnetic action on the most unstable disturbances and the interaction between these disturbances and the primary flow.

From the discussion of secondary flow in the H & M paper it might be expected that the centrifugal accelerations present in the rotating EDF system would adversely affect its stability. It is encouraging, however, that one of the direct effects of increasing $\underset{\sim}{B}_o$ is to make it appear more like a plane flow and less like a cylindrical flow. The condition for this to be so is that

$$\partial/\partial r >> 1/r .$$

In order of magnitude terms this condition can be given in the EDF case as

$$\ell M^{1/2} >> 1, \qquad \text{———(3.12)}$$

where $\ell = b/a$ is the ratio of the diameter of the electrodes to the distance between them. In the experimental apparatus described in §3.3 it was possible for M to reach a maximum value of about 640. Since $\ell = 0.502$, the maximum $\ell M^{1/2}$ is about 13 and the maximum $M^{1/2}$ is about 25. The $\ell M^{1/2}$ value is still not very large so that the effects of the centrifugal acceleration on the flow may be appreciable. The effects of small radial pressure gradients on the stability of the shear layers remain uncertain.

3.2.2.4 Direct electromagnetic effects on the growth of disturbances

Before discussing the growth or decay of the disturbances themselves, it is necessary to examine the 3-D EDF shear layer closely in order to postulate a type of velocity disturbance which could occur naturally.

In the H & M discussion it was reasoned that, since u_θ varies in the radial direction such that $\partial u_\theta/\partial r >> \partial u_\theta/\partial z$, i.e.,

$$M^{1/2} >> 1, \qquad \text{———(3.13)}$$

one might expect the shear layer to be unstable somewhat in the manner of a 2-D plane jet. This 2-D jet would have a velocity profile in the (x, y, z) co-ordinate system of the form

$$\underset{\sim}{u} = [u_x(y), 0, 0],$$

and would be situated in a coplanar, uniform magnetic field with $\phi_B = \pi/2$, i.e.,

$$\underset{\sim}{B_o} = [0, 0, B_o].$$

In any plane parallel flow, $u_x(y)$, without a magnetic field it was shown by Squire (1933) that the most unstable disturbances are those whose wave number vectors, $\underset{\sim}{k}$, are parallel to the flow direction (i.e. $\phi_k = 0$ in Figure 3.3). All the vorticity of these disturbances is in the z-direction. Therefore it is physically obvious that when a uniform, z-wise $\underset{\sim}{B_o}$ is applied, the vorticity of these disturbances cannot be affected by electromagnetic forces so that the magnetic field has no effect on the stability of the flow. This result was shown mathematically by Wooler (1961) and by Hunt (1966).

Therefore, if the conditions (3.12) and (3.13) are well satisfied one might expect the shear layer to resemble closely a 2-D parallel flow and to be susceptible to destabilizing 2-D disturbances which are

unaffected by $\underset{\sim}{B_o}$.

The velocity profile through the actual EDF shear layer has points of inflection on both sides of the peak velocity region (see Figure 3.1). As discussed by Lin (1966), points of inflection generally tend to decrease the ability of a parallel flow to damp out 2-D disturbances. It might be expected then that the EDF profile would be easily destabilized by 2-D disturbances.

Thus far in the discussion the sole claim for considering the EDF shear layer as 2-D has come from (3.13), the condition by which $\partial u_\theta/\partial r \gg \partial u_\theta/\partial z$. However, it is by no means clear how the most unstable, naturally occurring disturbances can ever be 2-D in a flow where the maximum $u_\theta(r, z)$ across the profile varies widely in the z -direction, even if (3.13) is well satisfied.

Consider the equivalent flow in (x, y, z) co-ordinates as shown in Figure 3.4. In this situation R_c would be reached at or near the point where $u_x = u_{x\,max}$ and when $u_{x\,max}$ reaches u_{xc} . If a 2-D disturbance were to be forced upon the system when $R = R_c$, it would grow where $u_x = u_{xc}$ but would be damped out elsewhere, where $R < R_c$, by viscous forces. Hence, a naturally occurring disturbance is likely to be 3-D even though $\partial u_x/\partial y >> \partial u_x/\partial z$.

A conceivable form of a 3-D naturally occurring disturbance would be one with its amplitude varying in the z -direction. It would probably still travel in the flow direction, i.e. $\phi_k = 0$, since in that way it could absorb the maximum amount of energy from the primary flow through the inertial stress, $\tilde{\rho}\,\overline{u'_x u'_y}$, while still keeping most of its vorticity parallel to $\underset{\sim}{B_o}$. Such a disturbance could possibly be of the form,

$$\underset{\sim}{u'} = \left[u'_x(y,z) \exp i(\alpha x - \beta t),\ u'_y(y,z) \exp i(\alpha x - \beta t),\ 0 \right], \qquad \text{———(3.14)}$$

where all the z -dependence is in the amplitudes of the fluctuation components. This disturbance would be superimposed upon the primary flow described by

$$\underset{\sim}{\bar{u}} = \left[u_x(y,z),\ 0,\ 0 \right]. \qquad \text{———(3.15)}$$

The usual assumption is made that $|\underset{\sim}{u'}| << |\underset{\sim}{\bar{u}}|$.

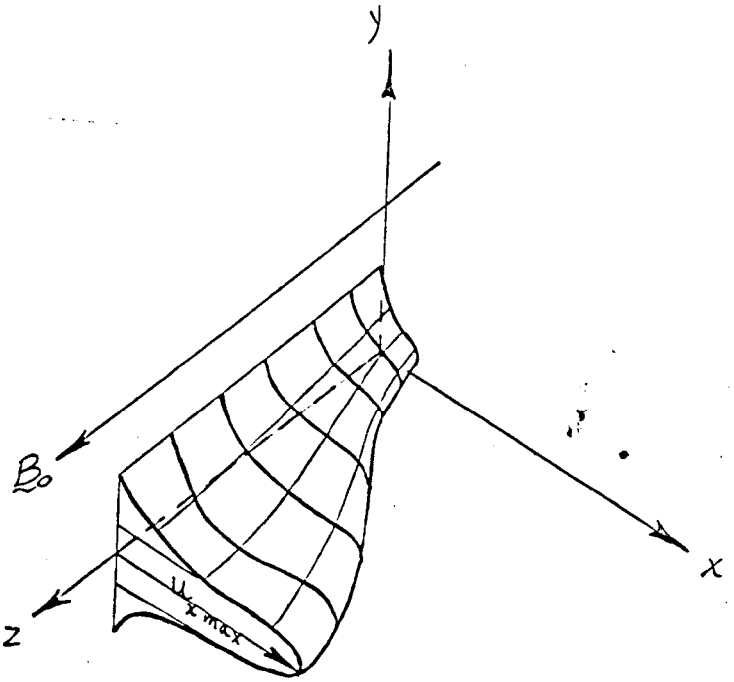

Figure 3.4 Sketch of three-dimensional MHD shear layer.

Since a perturbation in one variable usually brings about perturbations in the others, the list of instantaneous quantities includes the following:

the velocity, $\underset{\sim}{u} = \bar{\underset{\sim}{u}} + \underset{\sim}{u}'$, $|\underset{\sim}{u}'| << |\bar{\underset{\sim}{u}}|$,

the vorticity, $\underset{\sim}{\omega} = \bar{\underset{\sim}{\omega}} + \underset{\sim}{\omega}'$, $|\underset{\sim}{\omega}'| << |\bar{\underset{\sim}{\omega}}|$,

the magnetic field, $\underset{\sim}{B} = \underset{\sim}{B_0} + \underset{\sim}{b}$, $|\underset{\sim}{b}| << |\underset{\sim}{B_0}|$,

the electric field, $\underset{\sim}{E} = \underset{\sim}{E_0} + \underset{\sim}{e}$, $|\underset{\sim}{e}| << |\underset{\sim}{E_0}|$,

and the current, $\underset{\sim}{J} = \underset{\sim}{J_0} + \underset{\sim}{j}$, $|\underset{\sim}{j}| << |\underset{\sim}{J_0}|$,

where the perturbation quantities, $\underset{\sim}{u}'$, $\underset{\sim}{\omega}'$, $\underset{\sim}{b}$ and $\underset{\sim}{j}$ are functions of time as well as of the spatial co-ordinates.

It is possible to analyse qualitatively the effect of applying $\underset{\sim}{B_0}$ to the velocity disturbances (3.14) by examining the basic MHD equations in the manner adopted by Hunt (1966).

Under the assumption, $R_m << 1$, a good approximation of Ohm's law, (3.3), for the disturbances becomes

$$\underset{\sim}{j} = \sigma(\underset{\sim}{e} + \underset{\sim}{u}' \times \underset{\sim}{B_0}),$$

and it follows that,

$$\frac{1}{\sigma}(\nabla \times \underset{\sim}{j}) = \nabla \times (\underset{\sim}{u}' \times \underset{\sim}{B_0}). \qquad \text{——— (3.16)}$$

Hunt has deduced necessary and sufficient conditions for there to be no growth of the induced disturbances current, $\underset{\sim}{j}$. One of the necessary conditions, which is not by itself sufficient, is that, in (3.16),

$$\frac{1}{\sigma}(\nabla \times \underset{\sim}{j}) = \nabla \times (\underset{\sim}{u}' \times \underset{\sim}{B_0}) = 0 . \qquad \text{——— (3.17)}$$

It is not necessary to elaborate upon any other conditions because the necessary condition (3.17) cannot be met by disturbances of the type (3.14) and, hence,

$$\nabla \times \underset{\sim}{j} \neq 0, \quad \underset{\sim}{j} \neq 0 .$$

It is interesting to evaluate $\nabla \times \underset{\sim}{j}$ by substituting for $\underset{\sim}{u}'$ the components in (3.14) and making use of the continuity equation, (3.7). The result is

$$\nabla \times \underset{\sim}{j} = \left[B_0 \frac{\partial u_x'(y,z)}{\partial z} \exp i(\alpha x - \beta t),\ B_0 \frac{\partial u_y'(y,z)}{\partial z} \exp i(\alpha x - \beta t),\ 0 \right]. \qquad \text{——— (3.18).}$$

From (3.18) it is evident that currents can circulate in the (y, z) and (x, z) planes but that current circulation in the (x, y) plane is zero.

The $\underset{\sim}{j}$ components which exist may interact with $\underset{\sim}{B_0}$ to affect the growth of the velocity disturbance. This interaction depends upon

the nature of the electromagnetic body force, $\underset{\sim}{j} \times \underset{\sim}{B}_o$, in the equation of motion, (3.2). As discussed by Shercliff (1965), the $\underset{\sim}{j} \times \underset{\sim}{B}_o$ force only affects the velocity distribution in an incompressible, homogeneous fluid medium when it is rotational, i.e. when

$$\underset{\sim}{\nabla} \times (\underset{\sim}{j} \times \underset{\sim}{B}_o) \neq 0. \qquad \text{———(3.19)}$$

As discussed by Hunt (1966), the condition (3.19) can be tested by taking the curl of the equation of motion, (3.2), and, ignoring second order infinitesimal quantities, arriving at an equation of motion for the vorticity, $\underset{\sim}{\omega}'$, of the disturbance. If $\underset{\sim}{\nabla} \times (\underset{\sim}{j} \times \underset{\sim}{B}_o) = 0$ in this equation then the vorticity of the disturbance will be unaffected by $\underset{\sim}{B}_o$. If $R_m << 1$ and $\underset{\sim}{B}_o$ is uniform, the term, $(\underset{\sim}{B}_o \cdot \underset{\sim}{\nabla})\,\underset{\sim}{j}$ in $\underset{\sim}{\nabla} \times (\underset{\sim}{j} \times \underset{\sim}{B}_o)$ is much larger than the others. To a good approximation then, the rate of growth or decay of the vorticity of the disturbances is unaffected by $\underset{\sim}{B}_o$ if the condition,

$$(\underset{\sim}{B}_o \cdot \underset{\sim}{\nabla})\,\underset{\sim}{j} = 0, \qquad \text{———(3.20)}$$

is met. In the present case (3.20) becomes

$$B_o \frac{\partial \underset{\sim}{j}}{\partial z} = 0. \qquad \text{———(3.21)}$$

However, $\underset{\sim}{j}$ does vary in the z-direction since $\underset{\sim}{\omega}' \times \underset{\sim}{B}_o$ varys in the z-direction. Therefore the condition (3.21) cannot be met and one concludes that the growth or decay of disturbances of the type proposed will indeed be affected by the magnetic field, although the magnitude of the effect is uncertain.

The exact pattern of current circulation is very difficult to imagine. Current will circulate so as to suppress the vorticity components of the disturbance which are perpendicular to $\underset{\sim}{B}_o$. A disturbance which begins to move outward in the y-direction, in the region where critical conditions exist, will find its progress impeded by the damping action of the $\underset{\sim}{j} \times \underset{\sim}{B}_o$ forces. Figure 3.5 represents schematically a single disturbance of the periodic ensemble at a certain instant during its development. Some schematic current lines and directions of the forces are also shown. Note that the $\underset{\sim}{j} \times \underset{\sim}{B}_o$ force is <u>amplifying</u> rather than damping where the current lines return across the disturbance. This situation suggests a possible electromagnetic coupling mechanism (somewhat similar to the wave generating mechanism described in Alfvén and Fälthammar (1963)) whereby the disturbance is directly damped in the critical region of its origin and is amplified in other parts of the flow where conditions are below critical.

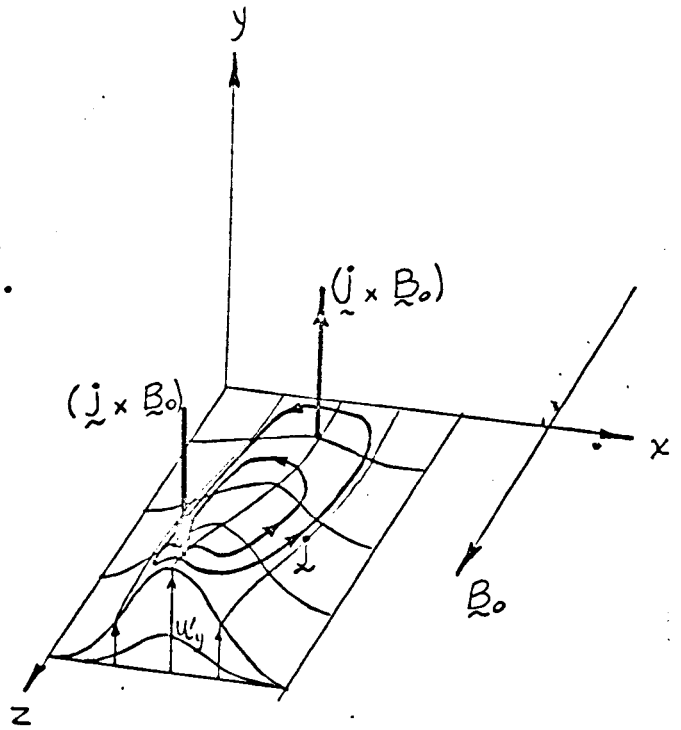

Figure 3.5 Sketch of three-dimensional velocity disturbance showing circulating disturbance currents and directions of $\underset{\sim}{j} \times \underset{\sim}{B}$ forces.

3.2.2.5 Electromagnetic coupling between the disturbance and the primary flow

A physical mechanism is now presented whereby the stability of a 3-D shear layer of the type, (3.15), in which $\partial u_x/\partial y >> \partial u_x/\partial z$, may be affected by fluid mechanical and electromagnetic interactions with a 3-D disturbance of the type (3.14). The disturbance, which originates in the critical flow region where $u_x = u_{xc}$ derives its energy from the primary flow by means of the inertial stress, $\rho \overline{u'_x u'_y}$. By the electromagnetic coupling effect just described this energy is transmitted to the region of the flow where conditions are not critical and where the energy can be dissipated by viscous and ohmic means.

Whether the disturbance will continue to grow or not in these circumstances depends on whether the rate of energy transfer into the disturbance from the main flow in the critical region is greater or less than the rate of energy dissipation by viscous and ohmic means throughout the length of the disturbance. If, at some stage in the growth of the disturbance, these energy transfer rates are balanced it might be possible for the disturbance to maintain a constant amplitude and to behave as a steady wave-like secondary flow in which the waves are carried along by the flow but lag behind the critical velocity, u_{xc}, owing to drag forces.

To stretch an analogy to its limit, the conjectured situation in which a wave-like secondary flow might remain steady shows some resemblance to the wake problems studied by Hasimoto (1960) or to flow over conducting cylindrical bodies of finite length as studied by Ludford and Singh (1964). If each wave in the flow profile at the position where $u_x = u_{xc}$ were replaced by a finite-length cylinder with its axis parallel to $\underset{\sim}{B}_0$, Ludford and Singh's work suggests that the fluid far in the z-direction, away from the ends of the cylinders, would be constrained to flow around "phantom" extensions of these cylinders. Thus, the velocity disturbance created by the short cylinder is transmitted to other parts of the flow in the direction of $\underset{\sim}{B}_0$.

3.2.2.6 Conclusion

It is concluded that the following phenomena may occur at the onset of instability in the 3-D rotating EDF shear layer when $M^{1/2}$; $\ell M^{1/2} >> 1$.
(i) The critical Reynolds number, R_c, is related to the critical driving current, I_c, through the relationship, $R_c \propto I_c/M$.

(ii) The most unstable disturbances are likely to extend parallel to $\underset{\sim}{B}_o$. and to have an amplitude which varies with z, even when $\partial u_\theta/\partial r >> \partial u_\theta/\partial z$.

(iii) A tendency exists for the magnetic field to introduce an electromagnetic coupling effect whereby the energy fed into the disturbance from the primary flow, at the position where $u_\theta = u_{\theta c}$, is transmitted to other non-critical parts of the flow along the length of the disturbance. This energy is dissipated by viscous dissipation throughout the length of the disturbance and by ohmic dissipation which is due to the circulation of the disturbance currents.

(iv) The most unstable 3-D disturbances may be damped out, amplified until the primary flow is disrupted, or grow to a constant amplitude and then resemble travelling waves, depending on whether the rate of energy transfer into the disturbance by inertial stresses is less than, greater than, or balanced by the rate of energy dissipation through viscous and ohmic effects.

3.2.3 Decay of MHD grid turbulence in mercury

The preliminary experiment on turbulent vorticity decay in §3.3 is of greater value as a study of hot-film anemometric techniques in mercury than as a study of the MHD aspects. Nevertheless, it illustrates the MHD effects that one would expect for flow through a conventional square mesh grid in the presence of a strong transverse magnetic field. These effects will now be briefly discussed in order of magnitude terms.

Consider a square array of wires which is placed in a steady mercury flow in the x-direction, $\underset{\sim}{\bar{u}} = [\bar{u}, 0, 0]$, in the presence of an applied magnetic field $\underset{\sim}{B}_o = [0, 0, B_o]$, with the wires extending parallel to the y and z co-ordinate axes. The mesh is characterised by the ratio L_o/d_o, where L_o is the distance between wire centres and d_o is the wire diameter. The energy containing turbulent eddies generated by the grid also have the length scale, L_o. The nature of the damping of this turbulence as it passes downstream depends upon the value, $|\underset{\sim}{B}_o|$.

In the hydrodynamic case, $|\underset{\sim}{B}_o| = 0$, vorticity is shed from the wires with components in the y and z-directions, such that the rms intensities of the y and z fluctuations, $\sqrt{\overline{v'^2}}$ and $\sqrt{\overline{w'^2}}$, are equal. This vorticity provides the velocity fluctuations in the x-direction, u', which are measurable by a hot-film sensor orientated with its axis

normal to the flow. As the fluid passes downstream, the y and z - vorticity mixes to produce x -vorticity, although this x -vorticity remains less than in the other directions so that $\overline{v'^2} = \overline{w'^2} < \overline{u'^2}$. Experimental results have shown that $\overline{w'^2}/\overline{v'^2} \simeq 1.3$ (see Uberoi and Wallis (1967)). Thus, grid turbulence is never truly isotropic, although it is usually assumed to be, and may not be homogeneous (see Grant and Nisbet (1957)).

When $|\underset{\sim}{B}_0| \neq 0$, the turbulence generated never reaches an approximate state of isotropy because of the tendency for vorticity perpendicular to $\underset{\sim}{B}_0$ to be suppressed. The turbulence generating capability of the grid is altered to an extent which depends upon two magnetic interaction parameters, $N_d = \sigma B_0^2 d_0/\rho \bar{u}$ and $N_L = N_d L_0 \bar{u}/d_0 \sqrt{\overline{u_0^2}}$. N_d represents the effect of electromagnetic forces on the flow around the grid wires whose axes are perpendicular to $\underset{\sim}{B}_0$ and N_L represents the effect of electromagnetic forces on the energy containing eddies which have length and fluctuating velocity scales, L_0 and $\sqrt{\overline{u_0^2}}$.

If $N_d << 1$ and $N_L >> 1$, the flow around the grid wires will not be significantly affected but the mixing process by which their wakes are combined to form the energy containing eddies will be drastically altered. The turbulence thus produced is damped out before any degree of homogeneity can be attained. The damping time will be $O(\sigma B_0^2/\rho)^{-1}$, the characteristic time for the suppression of vorticity (see Shercliff (1965)). It is thus concluded that the convertional square mesh grid will be of little assistance in producing interesting turbulence fields under the influence of an applied magnetic field.

When $N_d \geq 2$, approximately, separation of the flow will be prevented from the cylinders with axis perpendicular to $\underset{\sim}{B}_0$ (see Kalis et al (1965) and Leibovich (1967)). Therefore when $N_d = O(1)$, $R_d >> 1$, it would be expected that the flow behind the grid would contain only the vortices which separate from the wires whose axes run parallel to $\underset{\sim}{B}_0$. These vortices will be carried downstream and dissipated mainly by viscous action.

It is worthy of note that Moffatt (1967) has studied the suppression of initially isotropic turbulence by the sudden application of a strong uniform magnetic field under the assumptions, $N_L >> 1$, $R_L >> 1$, $R_m << 1$. Included in his paper is a critical review of previous work in this field. He has produced theoretical results for turbulence decay which suggest

some very interesting experiments using hot-films in liquid mercury. The most difficult experimental problem is the task of applying a strong magnetic field suddenly to the turbulence field. Moffatt has suggested two possibilities, the sudden switch-on of an electromagnet and the sweeping of an isotropic turbulence field, created elsewhere, into the region of strong, uniform field. These proposals are not easy to carry out since, from the basic assumption, $N_L >> 1$, the application of B_0 must be completed before the turbulent eddies have time to turn around! Note that the assumption, $N_L >> 1$, implies that the characteristic vorticity decay time for the eddies, $(\sigma B_0^2/\rho)^{-1}$, must be much less than their characteristic turn-over time, $l_0/\sqrt{u_0^2}$. The technical problem of switching on a large electromagnet in a small fraction of a second is formidable. The technique of "sweeping in" requires high flow rates to bring the turbulent eddies into the magnetic field quickly but is more practicable. It might also prove possible to use grids of special design within the magnetic field to produce a fairly homogeneous turbulence of high intensity.

3.3 Experiments and Discussion

3.3.1 Notes on the new MHD laboratory

A special, small laboratory has been designed and built at the School of Engineering Science for the specific purpose of accommodating MHD experiments which use mercury as the working fluid. The design and construction of the building, hereinafter referred to as the MHD lab, was carried out under the supervision of Dr.C.J.N.Alty during seven months beginning in October, 1966. On the working committee, in addition to the author, were Mr.A.E.Webb, Mr.M.K.Bevir and Mr.W.J.Boulton. A photo of the completed unit is shown in Figure 3.6.

The mercury lab was built upon a sloping concrete slab of basic dimensions, 12 x 32ft. The floor slopes $\frac{1}{2}$ in. downward per ft. horizontal from front to back over the 12ft. dimension. The lower edge of the floor is 6in. above the floor of the main laboratory (i.e. the larger room in which the MHD lab is situated) to facilitate the positioning of a seam-welded, mercury collecting trough, manufactured from 3/16-in. thick rigid pvc sheet, of dimensions 6in. x 6in. x 32ft. The purpose of the sloping floor is to allow free movement of spilled mercury down to the collecting trough.

An external Dexion framework was erected. An external framework was chosen because of the need of having a smooth, easy to clean interior.

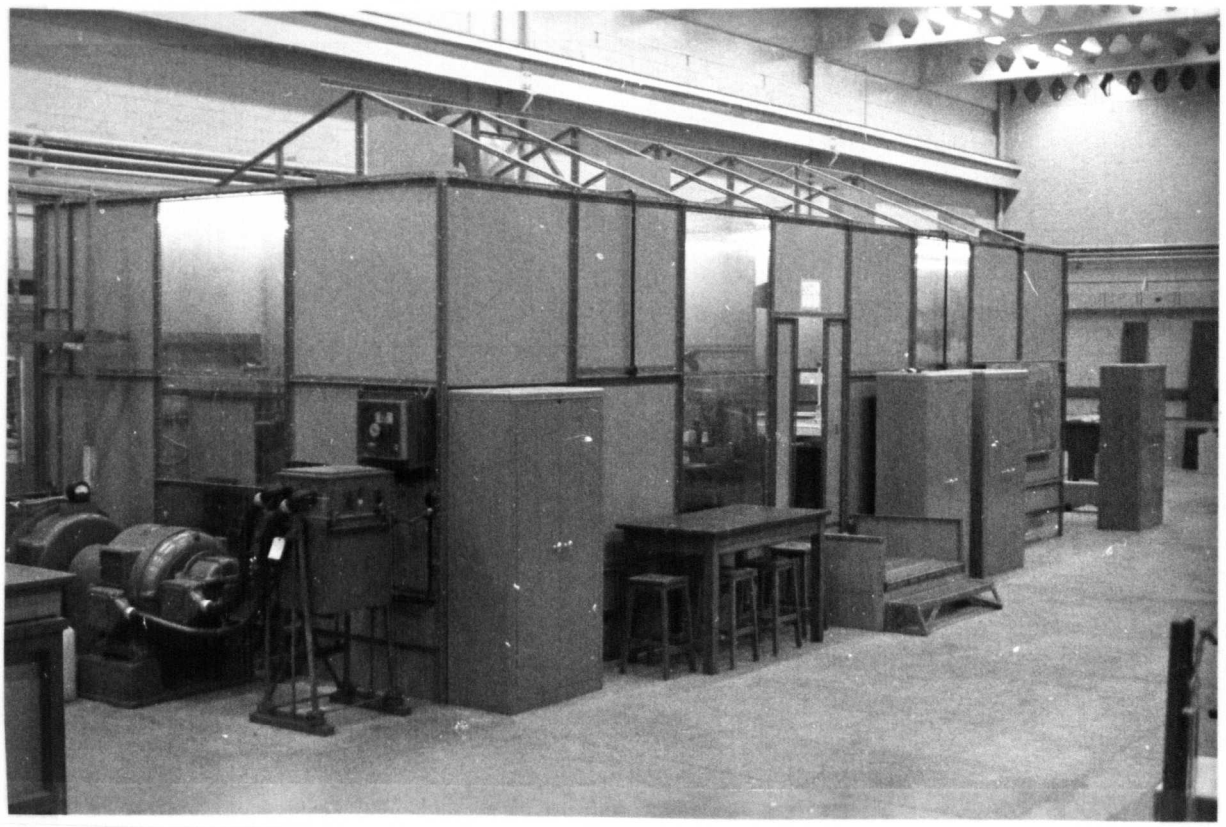

Figure 3.6 The new mercury - MHD laboratory.

All wall and roof panels are 4 x 8 ft. sheets of 1/8-in. rigid pvc material. The windows seen in the photo are actually clear sheets of this same material. A continuous sheet of 3/16-in. flexible pvc covers the floor and is welded all around to the wall panels. All internal pvc seams are welded (except around the removable roof panels and the door) and the protruding Dexion bolt heads are sprayed with liquid pvc to prevent mercury corrosion. The door, also made of pvc, is hung from a track and, when pulled to, overlaps the door opening. Outside the door is a step of Dexion construction with a pvc under-tray. The strange looking truss framework on top of the lab is necessary to provide a strong, rigid support for the removable roof panels.

The special needs which governed the entire project were:
(i) the containment of enough mercury and experimental equipment to allow at least four separate experiments to proceed simultaneously,
(ii) complete protection of the experimentalist during prolonged occupation of the MHD lab, especially through the provision of ample ventilation, mercury vapour detection equipment and protective rubber clothing to be worn in the event of an emergency,
(iii) the prevention of contamination, by mercury fumes or spillage, in the surrounding main laboratory,
(iv) the facility for installing and removing heavy pieces of apparatus, such as electromagnets, by overhead crane through the roof,
(v) provision for mercury cleaning,
(vi) provision for easy collection of spilled mercury within the lab, and for cleaning up following such a catastrophe,
(vii) 60 kw. d.c. power installations to drive two electromagnets at one time.

A few additional notes to accompany the enumerated items above now follow. To satisfy (i) the mercury lab was divided internally into five compartments using removable partitions. The centre compartment houses a stainless steel sink, mercury storage facilities and mercury cleaning apparatus. The other four compartments are intended to be used for experiments. The two end compartments contain two large electromagnets, the Lintott transverse field magnet, which was used in the experiments described in this thesis, and a radial field magnet. Benches and cupboards have been installed to contain all experimental equipment which is normally used in the lab.

The importance of ventilation was mentioned in (ii). The responsibility for designing a suitable system and obtaining the necessary

equipment was allotted to the author. The heart of the system is a quiet running fan unit which is capable of withdrawing 3000 cfm at 910 rpm (approximately one air change per minute) with a system pressure drop of 1 in. of water. It is a size 200 Anguline model supplied by Axia Fans Ltd. and is painted within and without to prevent corrosion by mercury vapour. The quietness of the unit is ensured by the low rotational speed and the large inlet ($27\frac{1}{2}$ in. diameter) and outlet ($20\frac{1}{4}$ in. square). Air is drawn into the MHD lab through four shrouded inlets on the roof, sweeps down through the room toward the mercury collecting trough and is withdrawn there through a 4 in. x 32 ft. opening by pvc trunking which is open at the bottom to overhang the trough. The back wall of the MHD lab forms one wall of the trunking. The circular fan inlet is led directly into the trunking half way along its length through this wall. The air withdrawn by the fan is passed upward about 12 ft. through a one piece circular pvc duct and out into the atmosphere through the wall of the main laboratory.

Contamination of the surrounding main laboratory (item (iii)) is prevented by the leakproof exhaust duct leading from the fan to atmosphere, the continuous heavy duty ventilation system which takes air in through splash proof inlets, the spillproof welded seams used throughout and the 8 ft^3 collecting trough which can contain all the mercury stored within in the event of the maximum catastrophe.

The mercury cleaning facilities mentioned in (v) are minimal. Mercury is cleaned by passing it in a fine spray through successive columns of dilute nitric acid and distilled water. Very dirty mercury is returned to the supplier for redistillation. No provision has yet been made for the installation of an elaborate filtration system for "in line" operation. This may be necessary in the future to increase the precision of the hot-film technique in a flow system.

The mercury collecting trough and sloping floor make the collection of spilled mercury a simple undertaking (item (vi)). The walls and floor may be hosed down with water when necessary. The water runs down to the collecting trough and may be readily pumped off into the sink. Water is not dumped from the sink to the sewer until it has passed trhough a glass trap and a polythene settling tank.

To satisfy (vii) two (0 - 60) volt, 1000 amp d.c. motor-generator sets are installed, one at each end of the MHD lab. The power is fed to the various compartments within by three copper buss bars which run the full length of the lab. One of the buss bars is common to both generating sets.

A (0-60) volt supply is thus available to any two compartments simultaneously. By operating both sets together any one compartment can have a supply variable from 0-120 volts.

3.3.2 Apparatus

3.3.2.1 The electromagnet

The transverse field, iron core electromagnet was obtained from Lintott Engineering. Water cooled coils are used and are designed to take up to 60 volts and 1000 amps, d.c. The dimensions of the pole faces are 9 x 66 in. and the gap between them is 3 in. This magnet was used in previous experiments by Hunt (1967). According to his measurements, when $B_o = 0.78$ wb/m^2 the field was uniform to 0.5% over a central volume of dimensions 3 x 3 x 60 in., and when $B_o = 1.24$ wb/m^2 the field was uniform to 0.6% over the 3 x 3 x 60 in. volume.

The electromagnet was calibrated as follows. The magnetic flux density, B_o, near the centre of the pole faces was measured using a Cambridge fluxmeter and search coil. At the same time, the current to the magnet coils was read on a current meter. B_o was plotted against the current meter reading, for B_o increasing and decreasing, to obtain a calibration curve. No measureable hysteresis was evident. This calibration curve was used thereafter to find values of B_o from readings taken off the dial of the current meter. The readings in B_o are likely to be in error by about ± 0.01 wb/m^2 due to imprecision in reading the magnet current.

3.3.2.2 Hot-film anemometry equipment

Detailed descriptions of this equipment and the methods of measurement were presented earlier in §2.3.1. A Thermo-Systems model 1010 constant temperature anemometer was employed to run the Thermo-Systems quartz-insulated hot-film sensors. The design features of the hot-film sensors were shown previously in Figures 2.2 and 2.3 and their physical data were given in Table 2.1. The probe bodies were made of nonmagnetic stainless steel tubing. The calibration curves for these sensors were presented in Figures 2.8 to 2.12. Probe no.1 has been employed in the EDF experiment and probe no.6 in the experiment on MHD suppression of vorticity behind a grid.

The screened cable supplying the heating current to the sensors was attached to them by split pin contacts. Once connected, the supply cable was usually clamped, or taped to a convenient portion of the apparatus to

prevent the connector rotating about the pins and either changing the resistance of contact slightly, and hence changing the anemometer reading, or else shorting the signal altogether.

The d.c. level of the anemometer voltage, $\overline{E}$, corresponding to the mean flow velocity, $\overline{u}$, was read on a Solartron LM1440.3 digital voltmeter. A mean voltage could be read on this instrument in the presence of low intensity turbulence and unstable flow oscillations providing that the filters on the instrument were switched in.

To measure $\sqrt{\overline{e^2}}$, the rms of the voltage fluctuations about the mean corresponding to the turbulence, $\sqrt{\overline{u^2}}$, the d.c. output from a Hewlett-Packard H12-3400A true rms voltmeter, with frequency response down to 2Hz, was displayed on a Tektronix 565 oscilloscope and photographed by the procedure outlined in Appendix C and in §3.1 of Malcolm (1968a).

The Tektronix 565 oscilloscope was fitted with two plug-in differential amplifiers, a 2A61 and a 3A3. The 2A61 became a very important piece of equipment in the EDF stability experiment. Its filtering facilities enabled the rejection of all frequencies in the anemometer output signal above 50Hz, while at the same time sensing frequencies as low as 0.06Hz, so that the detection of slow changes in the primary flow at the onset of instability could be easily detected.

Two Farnell C2 power supplies, with the combined features of constant current (0-2 amps, d.c.) or constant voltage (0-30 volts, d.c.) were used. One of these was used to supply d.c. current to the EDF apparatus. The other was used as a constant d.c. voltage supply as follows. The 2A61 amplifier mentioned above would not accept the large d.c. voltage level (approximately 10v.) in the anemometer output signal. It was therefore necessary to introduce a constant d.c. level of nearly the same magnitude so that the small difference between the two signals could be accepted by the 2A61.

A photograph of the anemometer and auxiliary equipment as set up for the EDF experiments is shown in Figure 3.7. This compact arrangement was chosen so that the anemometer output could be observed on the digital voltmeter and oscilloscope while changes in operating variables were being made. The EDF apparatus installed in the electromagnet was also close enough to this group of instruments for changes in anemometer output to be seen immediately upon adjusting the position of the hot-film probe. The major instruments in Figure 3.7 are, beginning in the upper left hand corner of the picture: electromagnet current meter, oscilloscope camera,

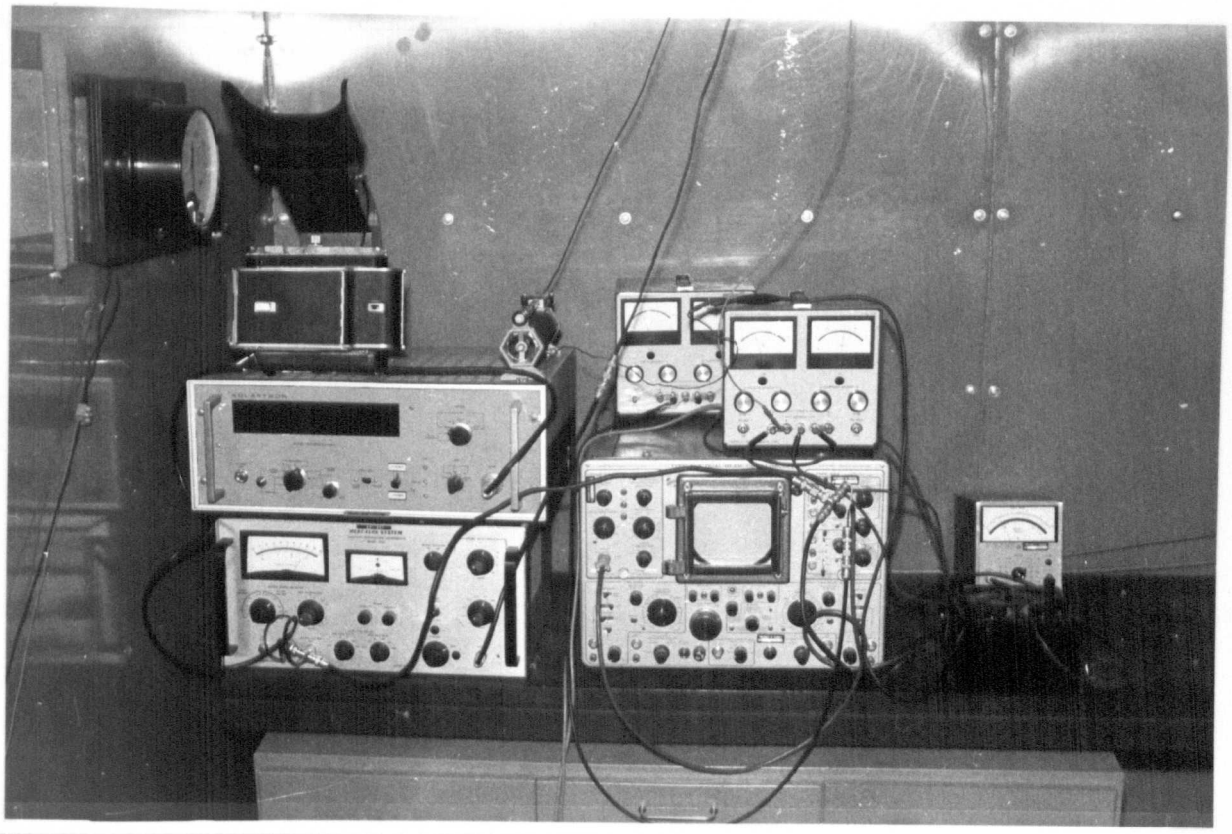

Figure 3.7 Constant-temperature anemometer and auxiliary equipment as set up for the electrically-driven flow experiment.

digital voltmeter, constant temperature anemometer, the two Farnell power supplies, the oscilloscope and the true rms voltmeter.

3.3.2.3 The EDF apparatus

This apparatus is described in detail in section 3 of Hunt and Malcolm (1968). In particular refer to the detailed drawings in Figures 3(a), (b) and (c) on pp. 8-9 of the paper.

The following changes were made prior to the new experiments. The distance between the discs was changed to 1.495 in. so that $\ell = b/a = 0.502$. To allow more freedom of probe movement, the perspex spindle, S, and the crank bar mechanism in Figure 3(c) were removed from the perspex block and replaced by a different probe traversing mechanism. The hot-film probe was suspended through the vertical spindle well to a position near the electrodes by attaching it to a vertically orientated vernier depth gauge (adjustable to 0.001 in.). This depth gauge was attached to an aluminium probe traversing device which was mounted on the top of the perspex block. The probe traversing device was fitted with two one-inch micrometers (adjustable to 0.001 in.) to facilitate adjusting the probe co-ordinates in a horizontal plane. The two micrometers and the depth gauge together provided adjustments in an (x , y , z) co-ordinate system. This co-ordinate system is shown in relation to one of the electrode discs and the hot-film probe in Figure 3.8. The origin of the co-ordinate system (for purposes of tabulating data) is midway along the line which joins the centres of the two discs.

An adjustable stop was installed to limit probe movement in the z-direction near the discs, and so to prevent accidental collision between the hot-film sensor and the electrode disc or duct wall.

Figure 3.9 shows the EDF apparatus in place in the gap of the electromagnet. The orientation of the two micrometers relative to the depth gauge may be seen in this figure. The apparatus was filled with mercury, to at least the bottom edge of the vertical well, by pouring into one of the pvc tubes in the picture. These tubes were then simply tied above the apparatus as shown to prevent spilling. The current leads to the electrodes are fed down through one of the pvc tubes. The connector to the split pins on the hot-film probe is clamped to the depth gauge to prevent any rotation about the pins which could cause small alterations in contact resistance or shorting.

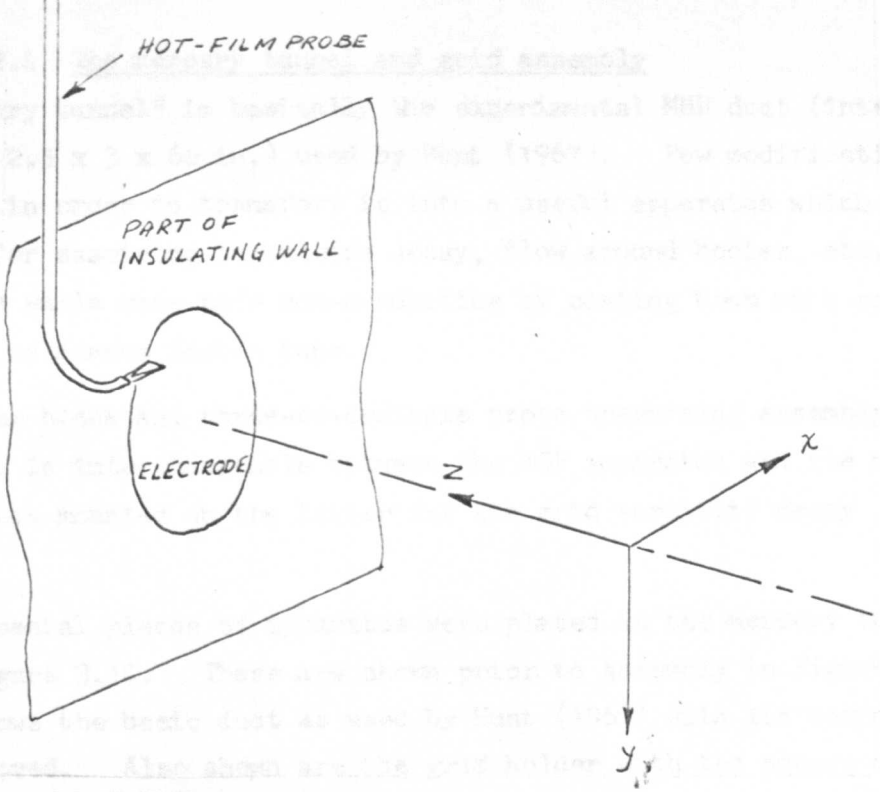

Figure 3.8 Sketch of probe-positioning co-ordinate system.

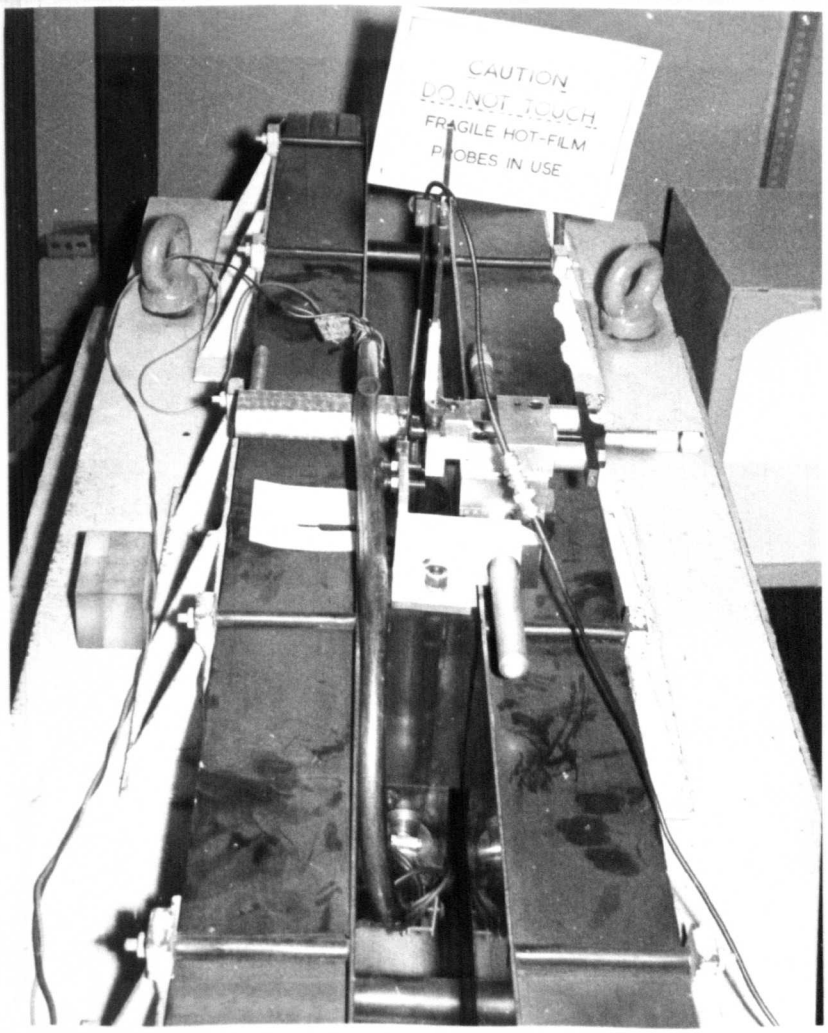

Figure 3.9 The electrically-driven flow apparatus installed in the transverse-field electromagnet.

3.3.2.4 The mercury tunnel and grid assembly

The "mercury tunnel" is basically the experimental MHD duct (internal measurements: 2.5 x 3 x 66 in.) used by Hunt (1967). Few modifications were necessary in order to transform it into a useful apparatus which could be used for examining turbulence decay, flow around bodies, etc. The copper side walls were made non-conducting by coating them with continuous layers of common Scotch tape.

The perspex block and three-co-ordinate probe traversing assembly just described is interchangeable between the EDF apparatus and the mercury tunnel and so was mounted on the latter for the grid vorticity decay experiment.

Various special pieces of apparatus were placed in the mercury tunnel as shown in Figure 3.10. These are shown prior to assembly in Figure 3.11. This figure shows the basic duct as used by Hunt (1967) with its copper side walls removed. Also shown are the grid holder with the square mesh grid in place, a plate grid with circular holes (which was never used) and and electromagnetic flowmeter* insert. A detailed description of these pieces of apparatus follows.

Directly following the diverging inlet to the tunnel (see Figure 3.10) are two nylon scrubbers and the electromagnetic flowmeter with grids at either end, the purpose of which are to smooth out the flow and shorten the entry length. It was hoped that the flowmeter would provide an approximate check on the centreline velocities measured by the hot-film probe. Unfortunately, it did not function properly during this experiment so that the check could not be made.

Still further downstream from the flowmeter insert is the test section. At this section the flow should be completely developed and the core flow should be uniform, if $M >> 1$, with Hartmann boundary layers on the side walls of thickness $O(M^{-1})$ and boundary layers on the top and bottom walls of thickness $O(M^{-1/2})$, providing that R/M is not high enough for the flow to become unstable. Instability was not evident over the range of parameters given in Table 3.2. This table lists the experimental ranges of relevant

---

* The flowmeter is of "perfect" design, i.e., the potential difference, $\Delta\phi$, and the flow rate, Q, are directly related by $\Delta\phi = QB_0/w$, where w is the channel width, for arbitrary parallel electrode cross sections and velocity profiles, providing only that B_0 is uniform and w is constant for a meter length which encloses most of the current (say 99%) (see Bevir (1969)).

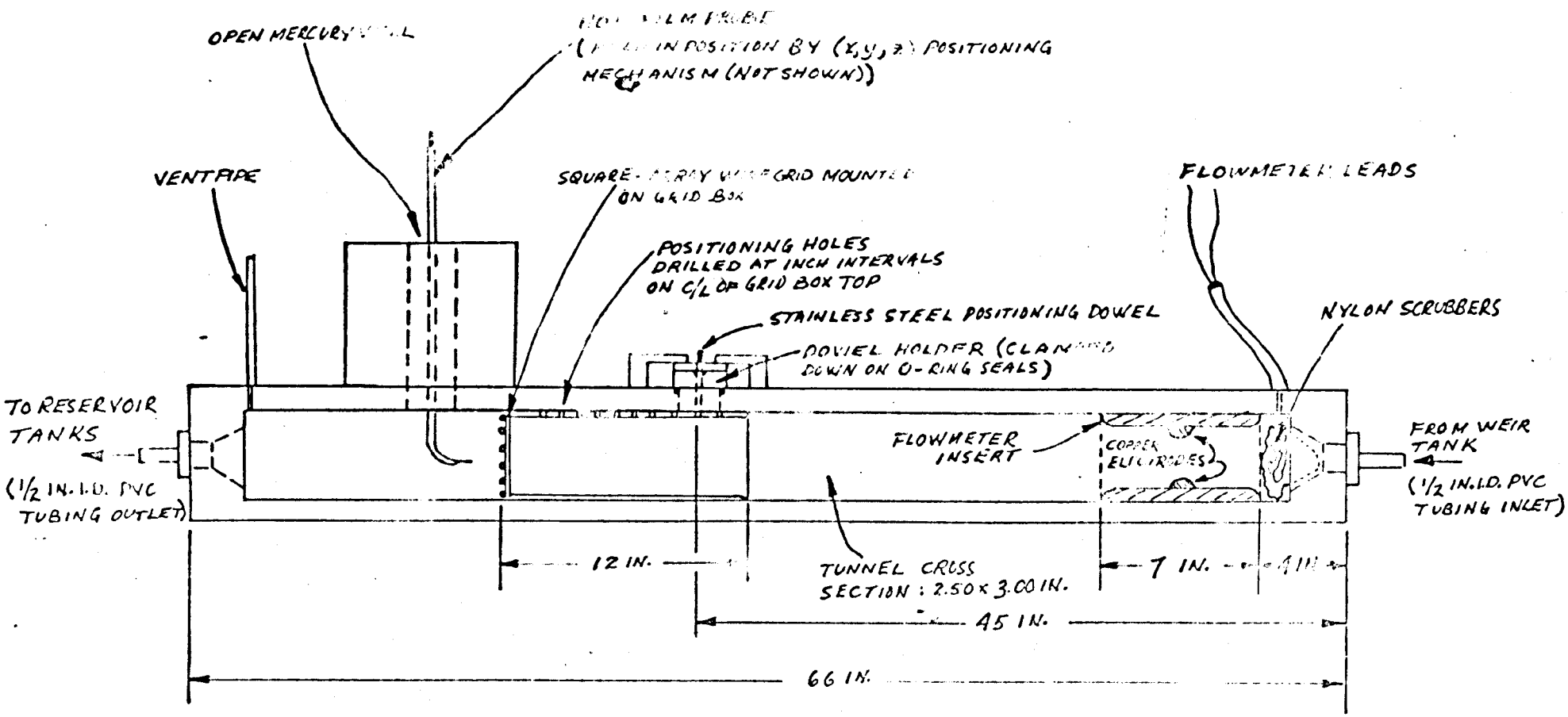

Figure 3.10 Sketch of the mercury tunnel (similar to duct of Hunt(1967)) with one side wall removed

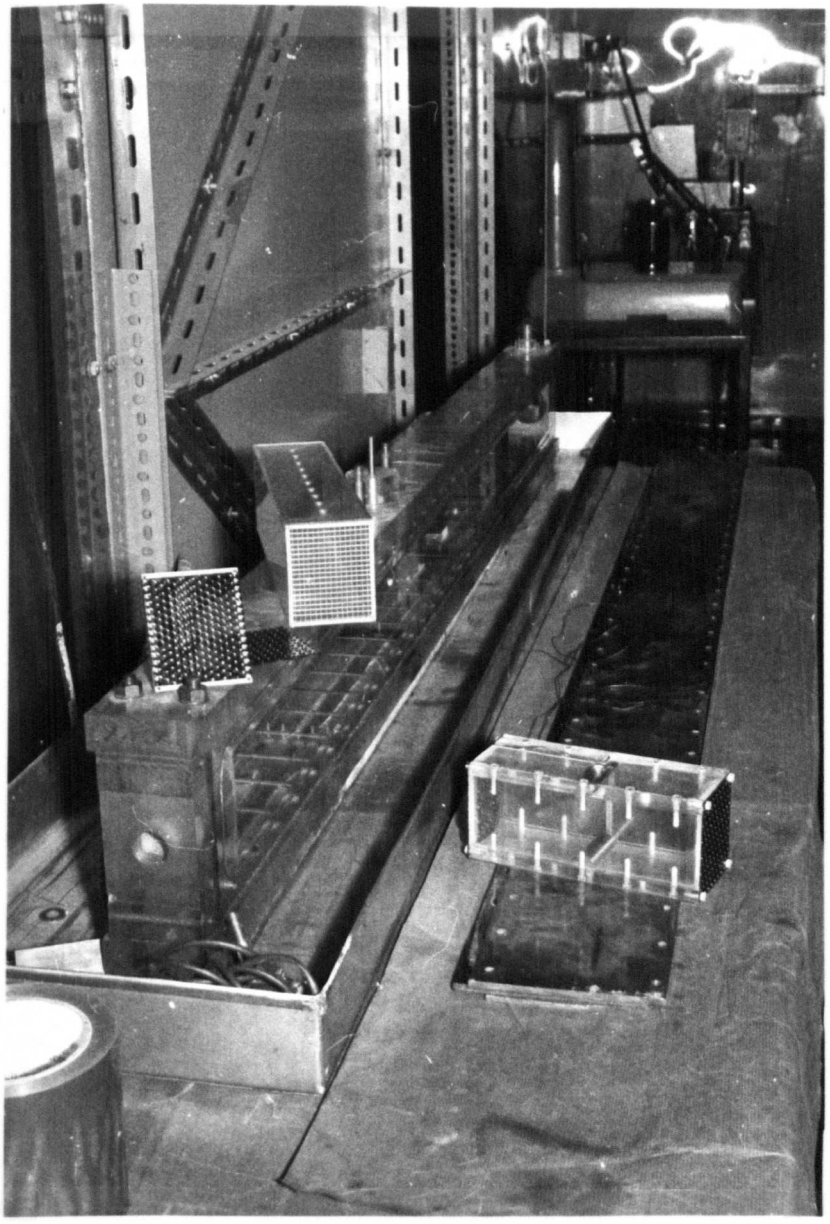

Figure 3.11 The disassembled mercury tunnel and turbulence generating apparatus.

U_{max} (cm/sec)	$\dot{Q}_{max}$ (litres/sec)	B_o (wb/m^2)	Mercury tunnel (2a=6.35cm)		Square-array grid (L_o=0.18cm, d=0.071cm)		
			R	R/M	R_d	N_d	N_L
3.2	0.15	0.275	8800	39	200	0.13	7.0
		0.50		11		0.43	23
		1.22		8.8		2.6	140

Table 3.2 Flow parameter magnitudes for the mercury tunnel and square-array grid.

dimensionless parameters for both the mercury tunnel and the grid mesh.

The uniform core flow enters the box-like grid holder, where it speeds up slightly due to the slight convergence of the inlet, and then passes through the turbulence generating grid toward the hot-film probe.

The grid holder is formed of pieces of 1/8 in. perspex sheet, which are bonded together with perspex cement, and has outside dimensions slightly less than the inside dimensions of the tunnel so as to allow a free sliding movement within it. The top of the grid holder is drilled at 1.000 in. intervals for a length of 9 in. along its centreline to facilitate positioning by the stainless steel dowel shown in Figure 3.10. After the tunnel has been assembled, the distance of the hot-film sensor from the grid can be varied over a distance, 0-10in., by the combined adjustment of one of the one-inch micrometers and the grid holder position. In order to move the grid holder to the desired 1-inch position, the experiment must be momentarily stopped, the mercury level lowered, the 1.875 in. diameter dowel holder removed from the top of the tunnel and the dowel inserted in this large hole to pull the grid holder along until the desired position is reached (the hole positions are numbered and the numbers etched into the top of the grid holder to avoid confusion). In the preliminary experiment described in §3.3.5 this positioning procedure was unnecessary because all measurements were taken within one inch of the grid.

The grid itself is a square array of lengths of 0.028 in. O.D. non-magnetic stainless steel tubing positioned 0.150 in. between centres. The L_o/d_o ratio is thus 5.36, the same value as used in the grid turbulence measurements in the tow tank experiment of Malcolm (1968a). The square array of tubes is held in position by a pvc frame which is attached to the grid holder by four nylon screws, one at each corner.

In the photo, Figure 3.11, another grid drilled with circular holes was shown. This grid was expected to generate a more intense and (perhaps) more homogeneous turbulence but, unfortunately, accidental breakage of the last hot-film probe occurred during disassembly of the tunnel to install this new grid and the experimental programme ended abruptly.

The mercury tunnel was operated with the spindle well nearly full of mercury. The extent to which the open bottom end of this well disturbed the flow in front of the grid was shown to be negligible experimentally, at least over the centre square inch of the channel where all readings were taken. For more sophisticated experiments it was planned to insert a

slotted perspex plate at the bottom of the well to fit flush with the upper wall of the tunnel. This arrangement would limit probe movement to vertical and streamwise directions only but would eliminate the disturbances which are created when the well is open-ended at the bottom.

3.3.2.5 The flow circuit

To save time the flow circuit was built up from existing pieces of apparatus which were used originally by Hunt (1967). This posed some problems since the existing apparatus was originally designed to operate at flow rates below 0.05 litres/sec. A few simple alterations enabled the system to run at flow rates up to 0.15 litres/sec. The details of the circuit are shown in Figures 3.12 and 3.13. Larger diameter pvc tubing, a larger weir tank, and baffles in the reservoir tanks to diffuse the incoming mercury jets would be necessary to obtain still higher flow rates with this type of system. When operating at 0.15 litres/sec, the surface of the mercury in the modified constant head weir tank (Figure 3.13) was rather rough showing turbulent flow beneath, but fluctuations in head were negligibly small.

The flow rate through the mercury tunnel was varied by a micrometer controlled conical seated valve on the outlet of the weir tank. The supply of mercury to the weir tank was controlled at high flow rates by adjusting the rotational speed of a gear pump (Stainless Steel Pumps Ltd.) with the adjustment provided on a Kopp variable speed drive, and at low rates by adjusting the throttle valve on the pump bypass line. Before reaching the weir tank the flow passed through an inverted Aerox filter, having a stainless steel body with a ceramic porous pipe filter element.

Beside the bypass throttle valve and the weir tank throttle valve, two more controls proved necessary to balance the flow properly. First, it was necessary to constrict the outlet line from the mercury tunnel using a simple adjustable clamp, when operating it at low flow, to keep the tunnel running full. It was also necessary to constrict the weir overflow line in a similar manner to prevent its becoming completely empty and allowing air to be sucked into the system.

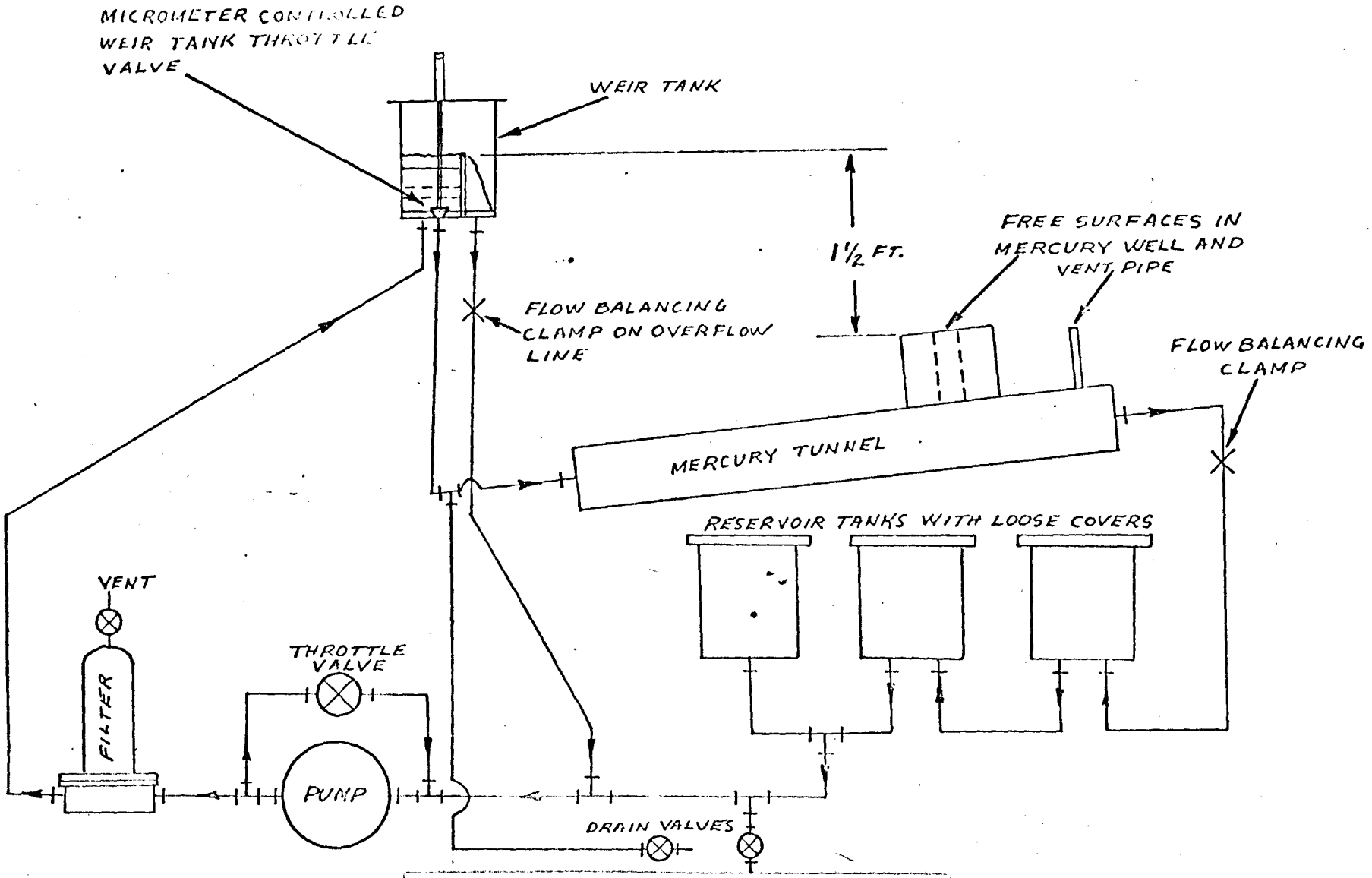

Figure 3.12 The flow circuit.

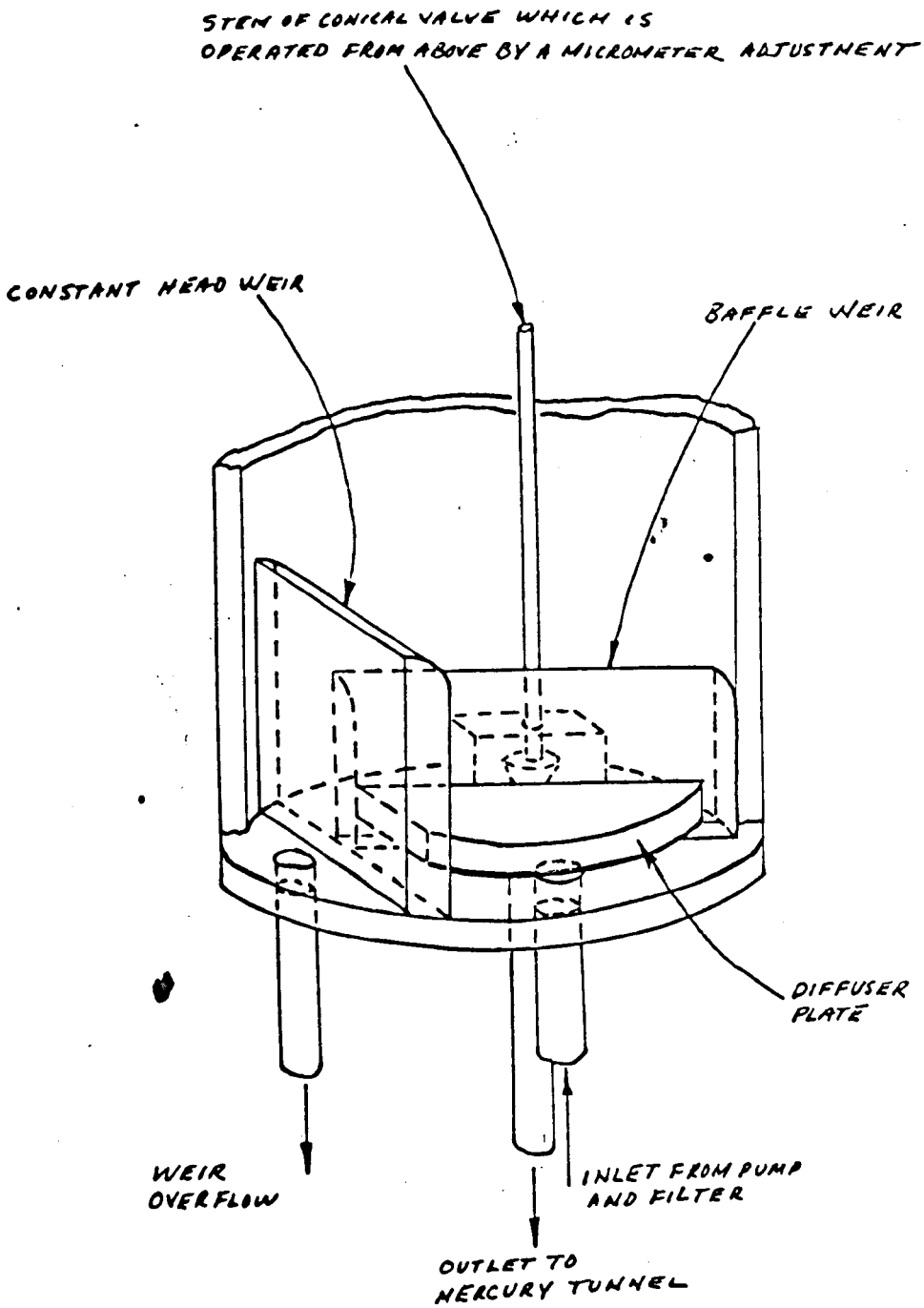

Figure 3.13 A sketch of the weir tank.

3.3.3. Steady electrically driven flow between circular electodes

3.3.3.1 The experiment

Measurements were made in the EDF shear layer with the apparatus set up and installed in the transverse-field magnet as described previously. The mercury in the apparatus was held at earth potential by strapping one of the current supply terminals to earth. The flow was controlled by varying the driving current, I, and the magnetic field, B_o . The flow direction could be reversed simply by reversing the relative directions of I and B_o. The hot-film sensor was operated at an "overheat" resistance ratio of 1.075, corresponding to a ΔT of about 30°C. The F' vs Pé curve in Figure 2.10 was used to find velocities from measured values of F'. The hot-film probe was traversed across the shear layer in the half space which is associated with the disc at $\zeta = 1$.

To measure the variation of velocity through the shear layer the probe was traversed in the (y, z) plane at x = 0 (the (x, y, z) co-ordinate system was shown in Figure 3.8) where the flow is nearly horizontal, and corresponds to the flow direction in the tow tank calibration. Less flow blockage would have been caused by the probe had the sensor been brought through the shear layer from the side (i.e. traversed in the (x, z) plane at y = 0), but the original calibration would not hold for vertical flow where the interaction between free and forced convection is quite different. Free convection effects will be discussed shortly.

The reference value of the heat transferred from the sensor, Q(0), was obtained beyond the outward edge of the shear layer rather than on the axis of symmetry. Although $u_\theta = 0$ on this axis, the presence of small u_z components renders a Q(0) measurement there subject to error.

Before beginning the experiment the following checks were made. First, the resistance of the fluid between the discs was measured at M = 0 by passing a current between the discs and measuring the potential between them with a Pye precision potentiometer. The resulting resistance of 42 $\mu\Omega$ checked well with the measurements by Hunt and Malcolm (1968) which had been taken in the same apparatus about two years previously (see Figure 5 of the paper). Then, the hot-film was operated in the region between the discs while the current was varied up to about 2 amps at M = 0. As was expected, this low density current had no measurable effects on the operation of the hot-film. Finally, the effect of the magnetic field on the free convection from the sensor was

checked at various M for I = 0. These results were discussed previously and were plotted in Figure 2.6.

3.3.3.2 Results

Some raw data for the measurements taken during this experiment are included in Appendix C so that new calculations can be done in the future if a better understanding is obtained of the effect of MHD errors on hot-film readings. Also included in Appendix C are the raw data for traverses at $\zeta = 0$, where $u_\theta = 0$, and along the flow axis, $r = 0$, where $u_\theta = 0$ also. These data show the presence of some radial and axial secondary flow in the system, which is caused by small radial pressure gradients that vary with ζ.

The most important results are shown in Figures 3.14 to 3.22. Figures 3.14 and 3.15 show velocity profiles across the EDF shear layer for ζ values of 0.25 and 0.5, respectively, by plotting $u_\theta b \ell M^{1/2}\sqrt{\sigma\eta}/I$ against $\xi = (\rho - \ell)M^{1/2}$. The measurements were taken while descending through the layer in the (y, z) plane at x = 0.

To show the effects of free convection, Figure 3.16 presents the variation of $(E-E_o)$ against (r-b) for three cases, where E is the anemometer voltage corresponding to u_θ at the point of measurement and E_o is the voltage at r = 0. In the first case, curve A plots the $(E-E_o)$ values which were obtained in the y-direction traverse at $\zeta = 0.50$, M = 212 as shown previously in Figure 3.15. For comparison, curve B shows the effects when the hot-film is traversed through the layer in the x-direction, at y = 0, in the presence of an updraft velocity past the sensor and curve C shows the effects in a similar traverse in the presence of a downdraft velocity.*

Figures 3.17 and 3.18 show velocity profiles for ζ values of 0.75 and 0.9, respectively. Figure 3.19, compares the velocity profiles for all ζ at M = 588.

Figure 3.20 shows the variation with ζ of $(u_\theta b \ell M^{1/2}\sqrt{\sigma\eta}/I)_{max}$, the peak value of the nondimensional velocity in each profile. The experimental values and the theoretical results of H & S (Hunt and Stewartson (1969)) from Table 3.1 are plotted together. Figure 3.21 compares the experimental velocity profile at $\zeta = 0.50$, M = 390 with the theoretical curve of H & S from Figure 3.1.

*The direction of flow is reversed by changing the relative directions of I and B_o.

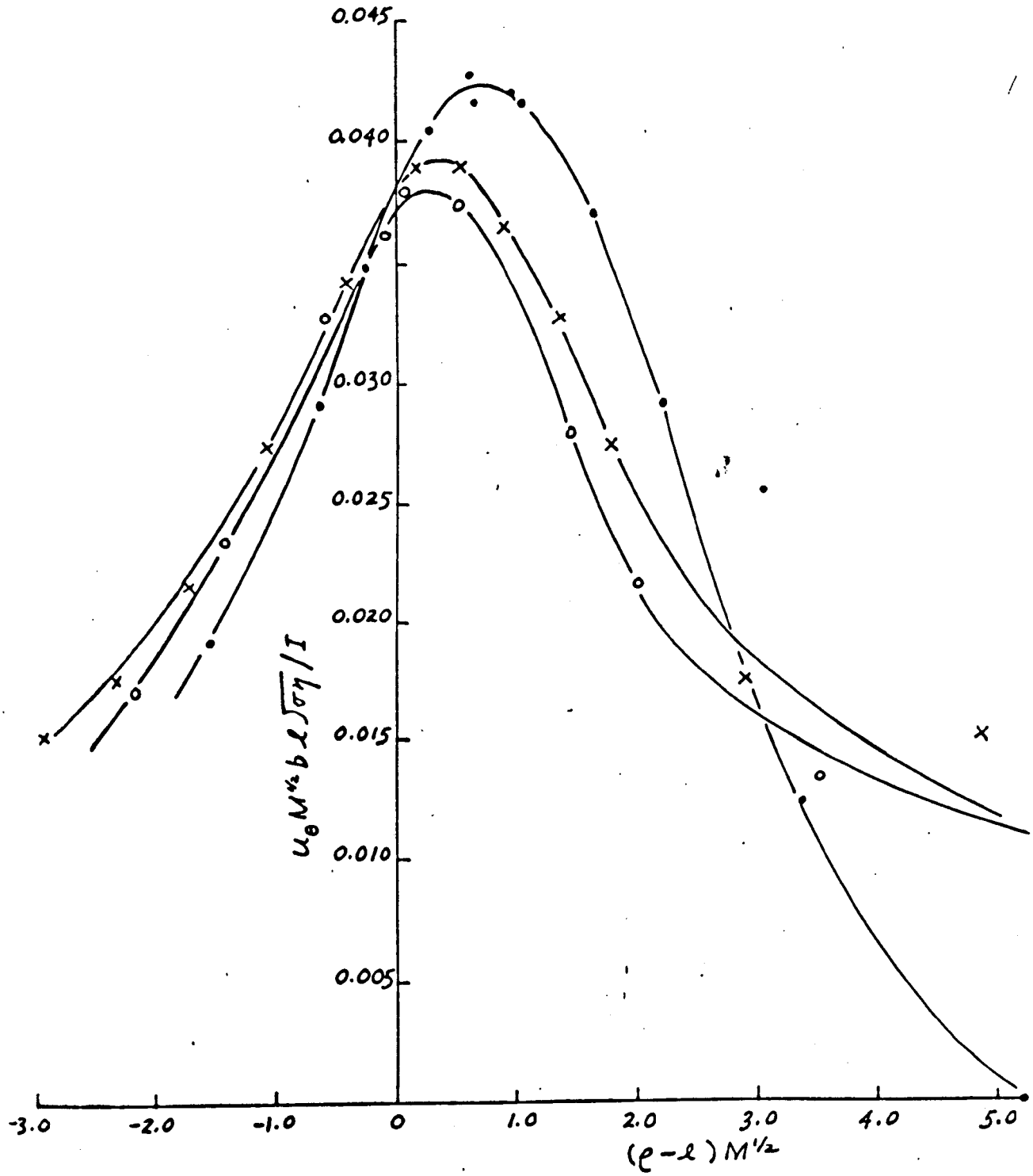

Figure 3.14 Radial profiles of azimuthal velocity, $\zeta = 0.25$ (•, M = 212, ζ = 0.250; ×, M = 390, ζ = 0.250; •, M = 588, ζ = 0.272).

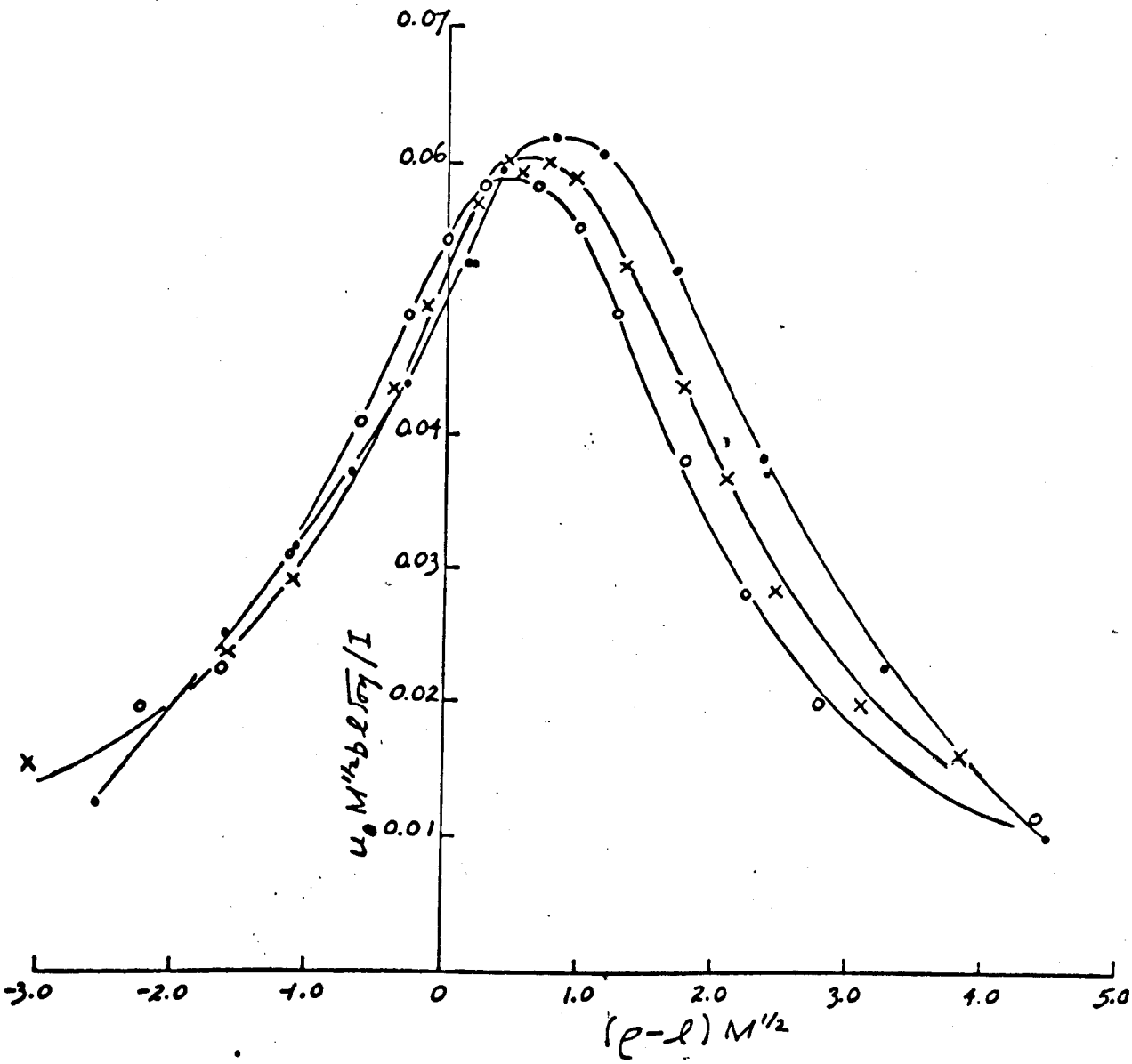

Figure 3.15 Radial profiles of azimuthal velocity, $\zeta \sim 0.5$ (•, M = 212, ζ = 0.500; x, M = 390, ζ = 0.500; ∘, M = 588, ζ = 0.522).

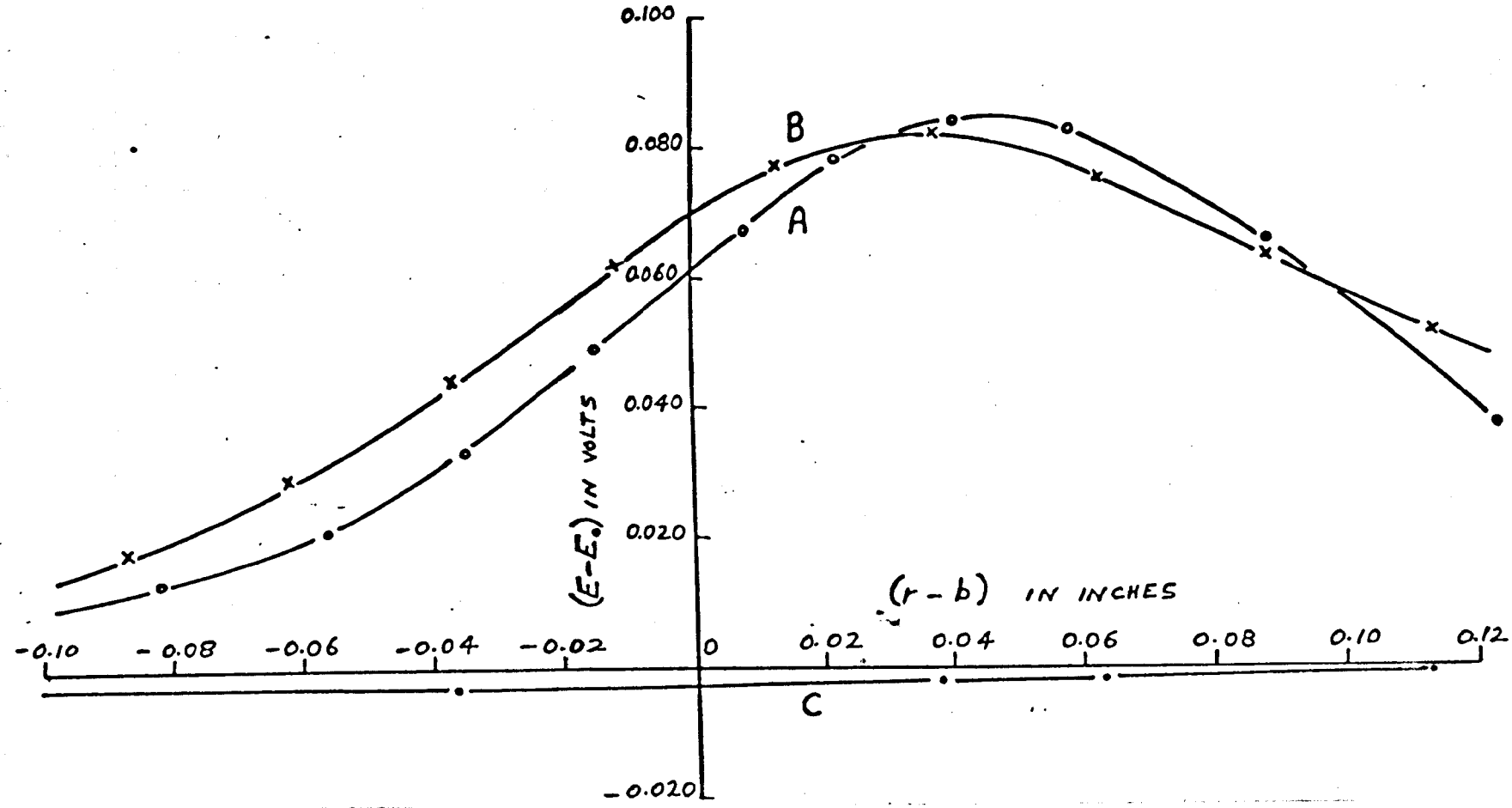

Figure 3.16 Effects of flow direction on hot-film sensitivity (f = 0.52, M = 212; curve A: horizontal flow; curve B: updraft flow; curve C: downdraft flow).

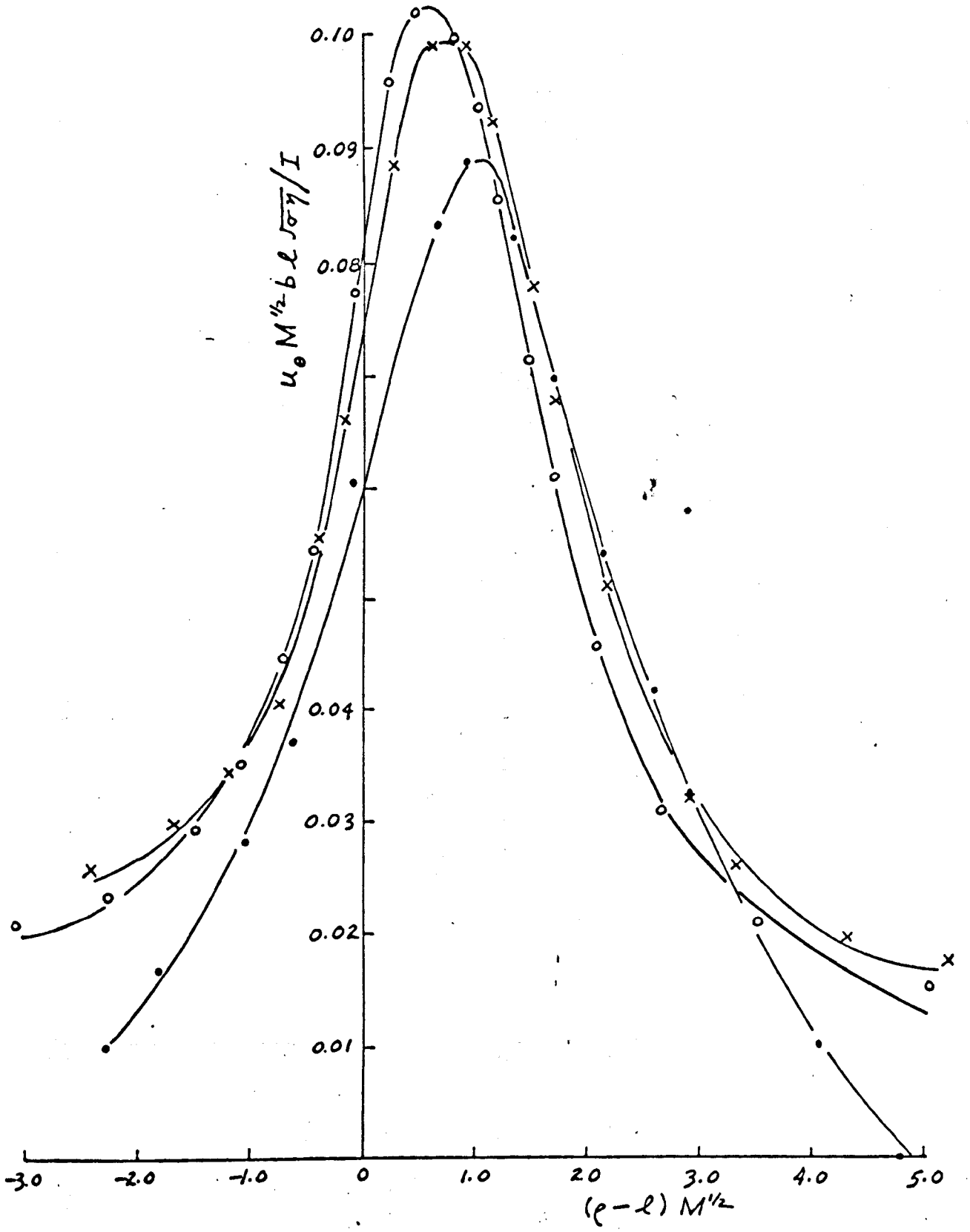

Figure 3.17 Radial profiles of azimuthal velocity, $f = 0.75$ (•, M = 212, f = 0.750; x, M = 390, f = 0.750; ∘, M = 588, f = 0.770).

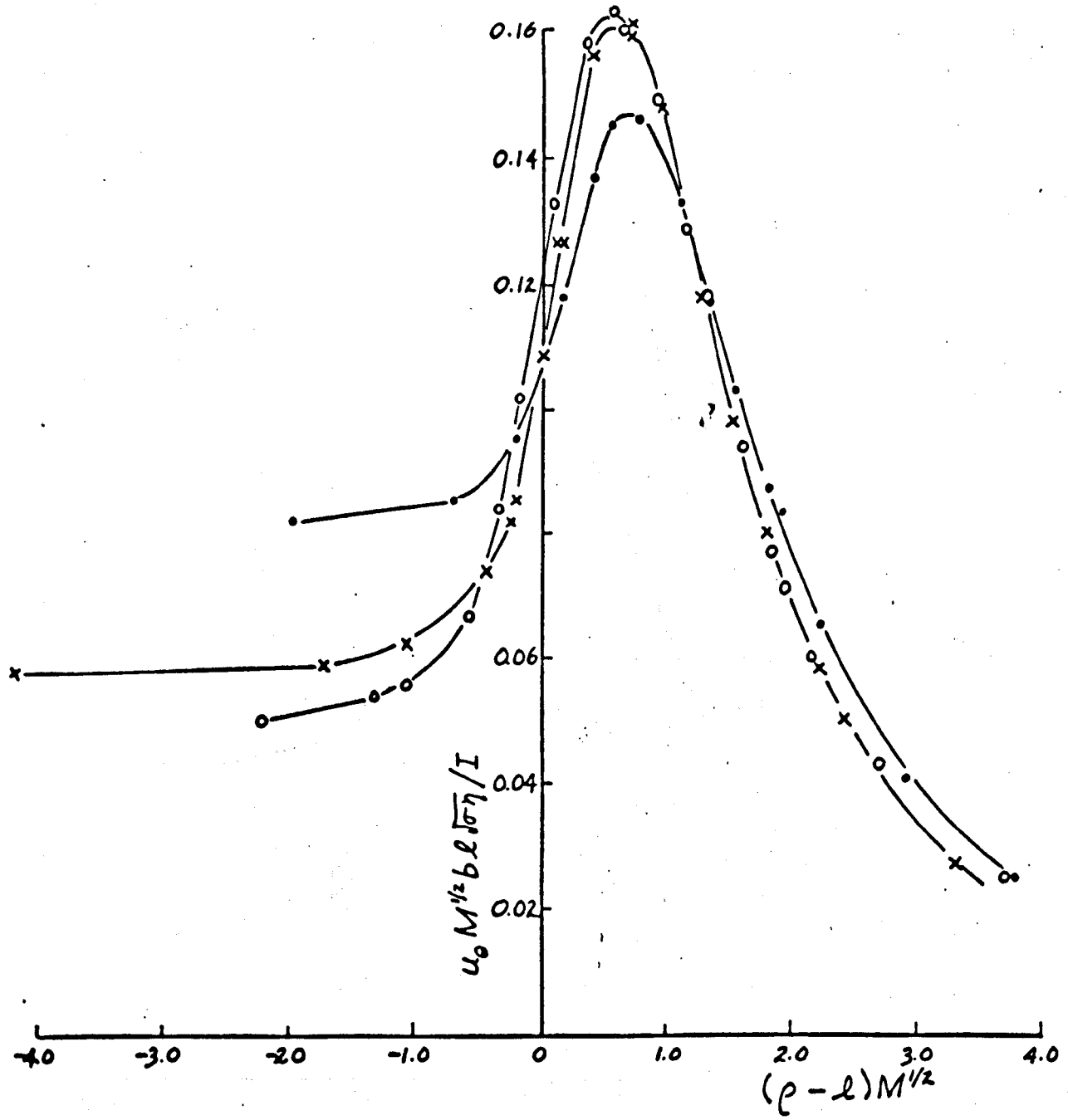

Figure 3.18 Radial profiles of azimuthal velocity, $\mathcal{J} \approx 0.9$ (•, M = 212, $\mathcal{J}$ = 0.922; ×, M = 390, $\mathcal{J}$ = 0.922; ○, M = 588, $\mathcal{J}$ = 0.905).

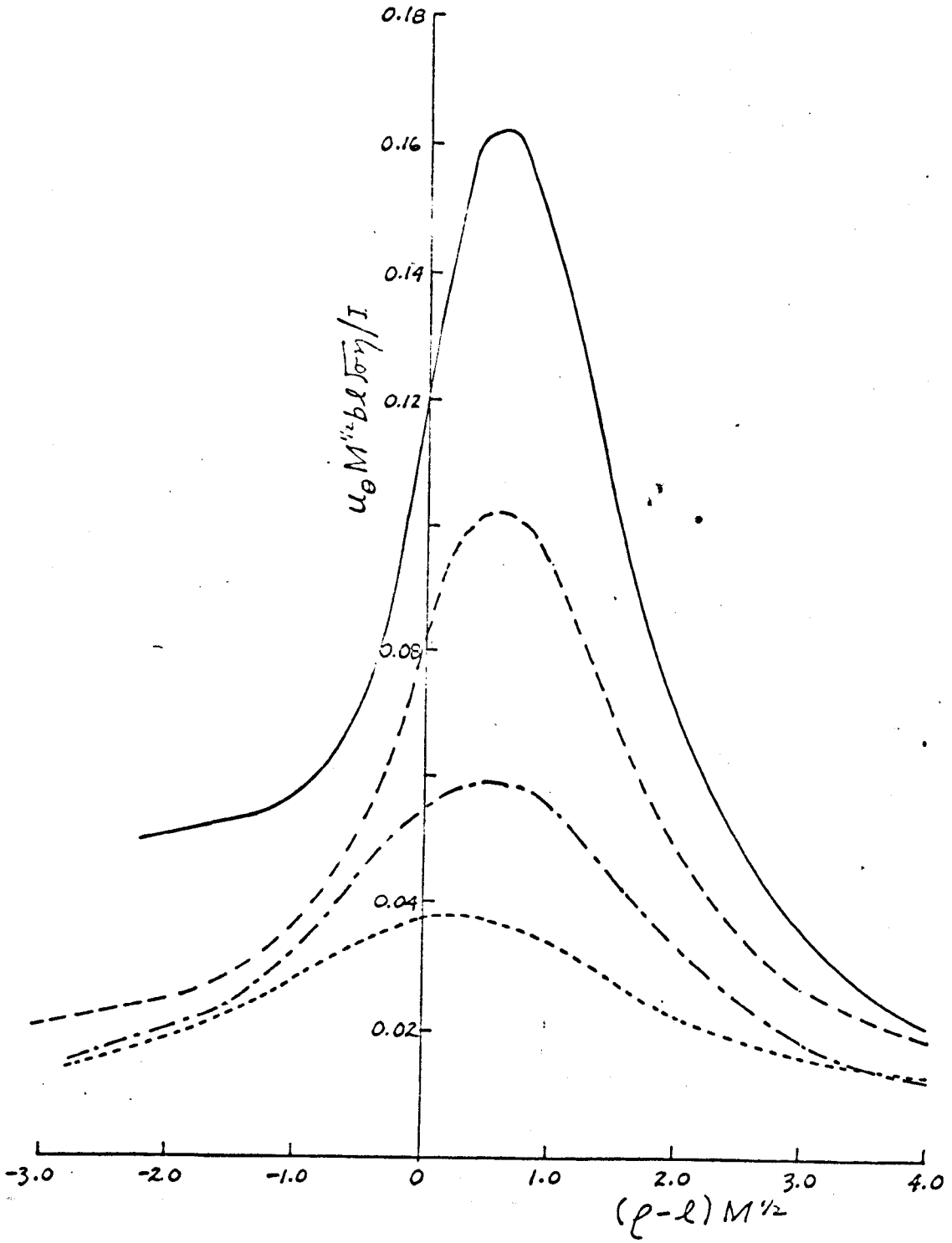

Figure 3.19 Radial profiles of azimuthal velocity at M = 588 at various distances from the electrode (————, ρ = 0.905; - - - -, ρ = 0.770; —·—·—, ρ = 0.522; -------, ρ = 0.272).

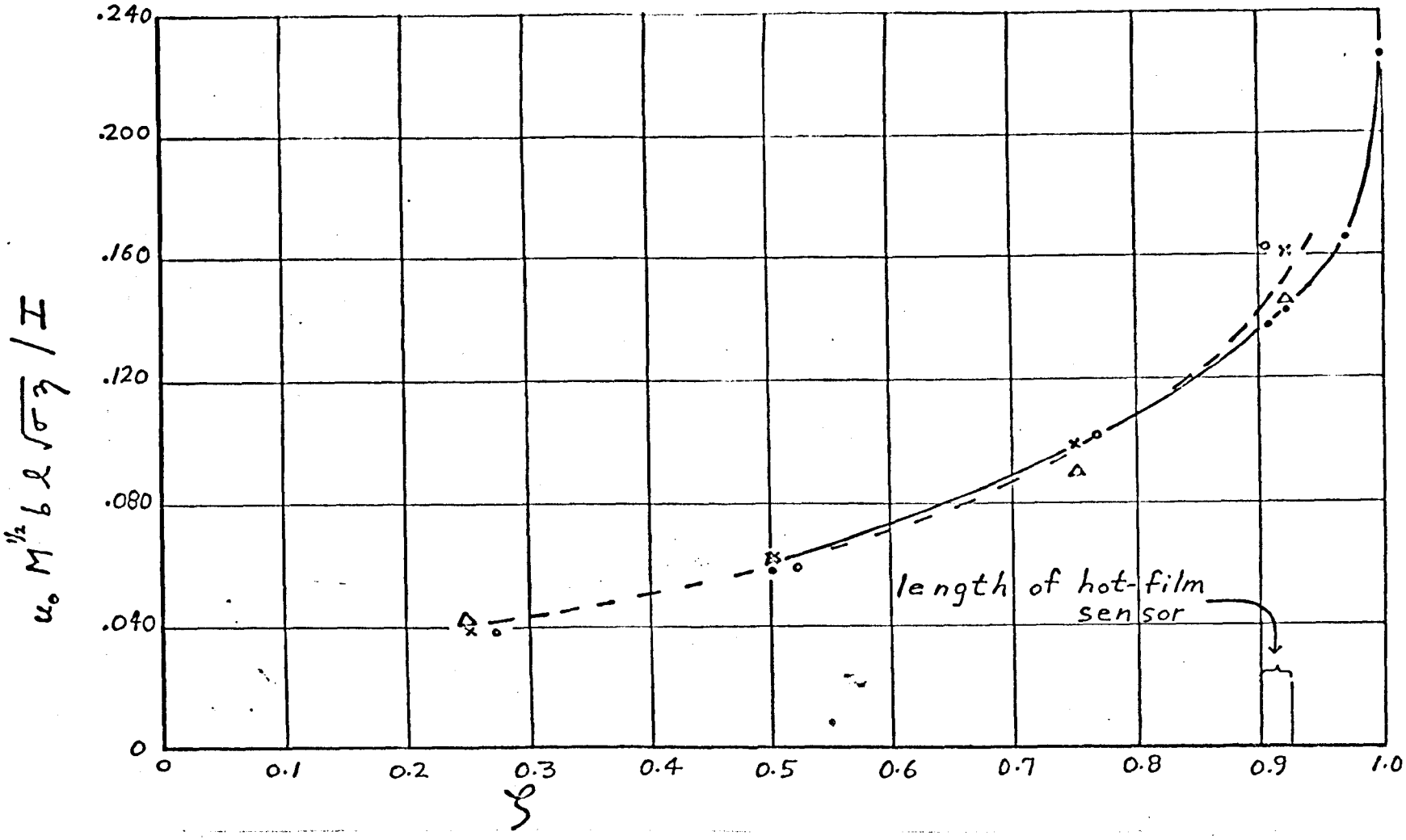

Figure 3.20 Variation of the maximum azimuthal velocity in the shear layer with distance from the electrode (• ———, theoretical curve from the theory of Hunt & Stewartson (1969); △×○ — —, experimental curve for the three values of M: 212, 390, 588).

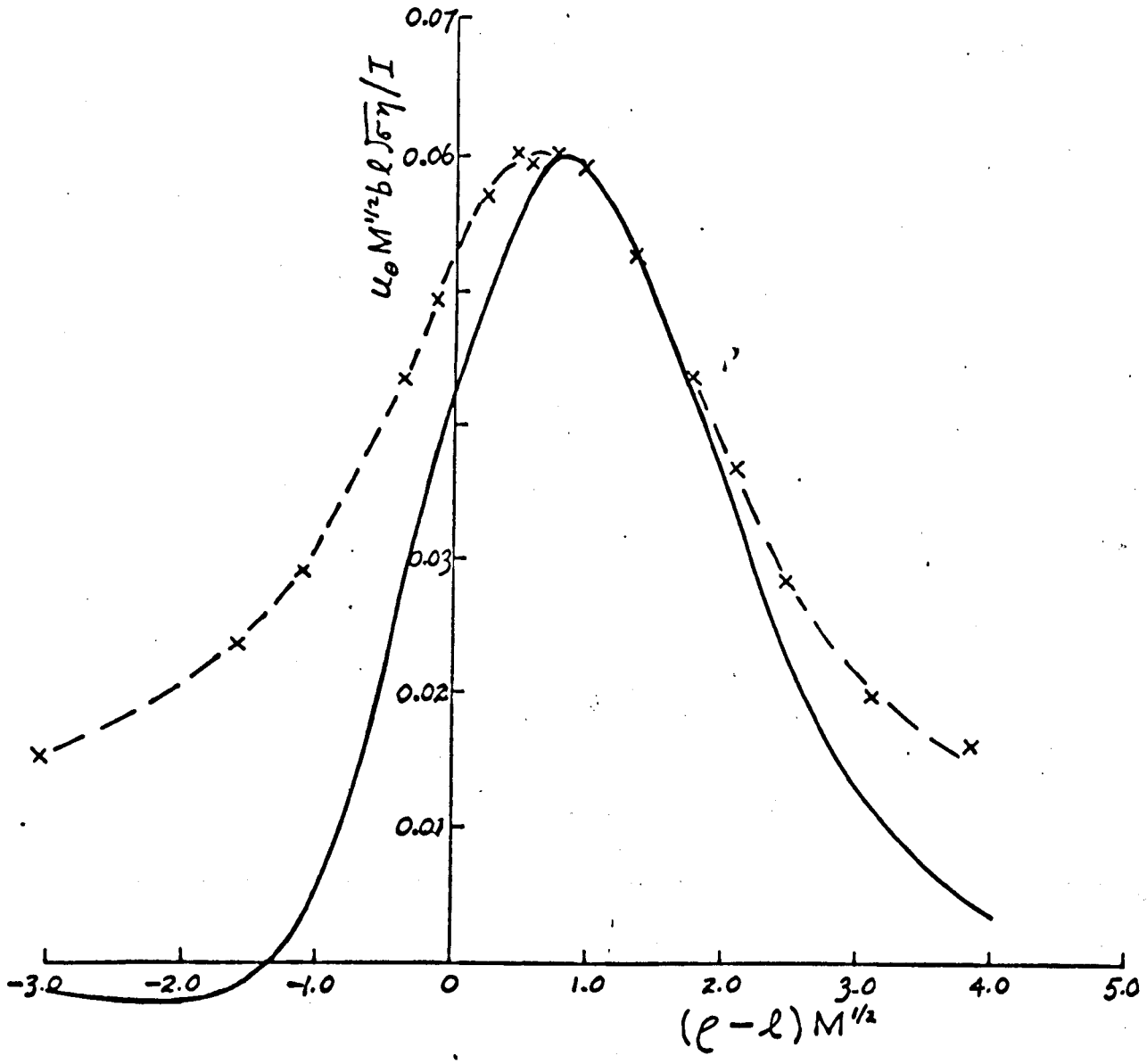

Figure 3.21 Radial profiles of azimuthal velocity: experimental versus theoretical, $\gamma = 0.50$, $M = 390$ (× — —, hot-film measurements; ————, theoretical results of Hunt & Stewartson).

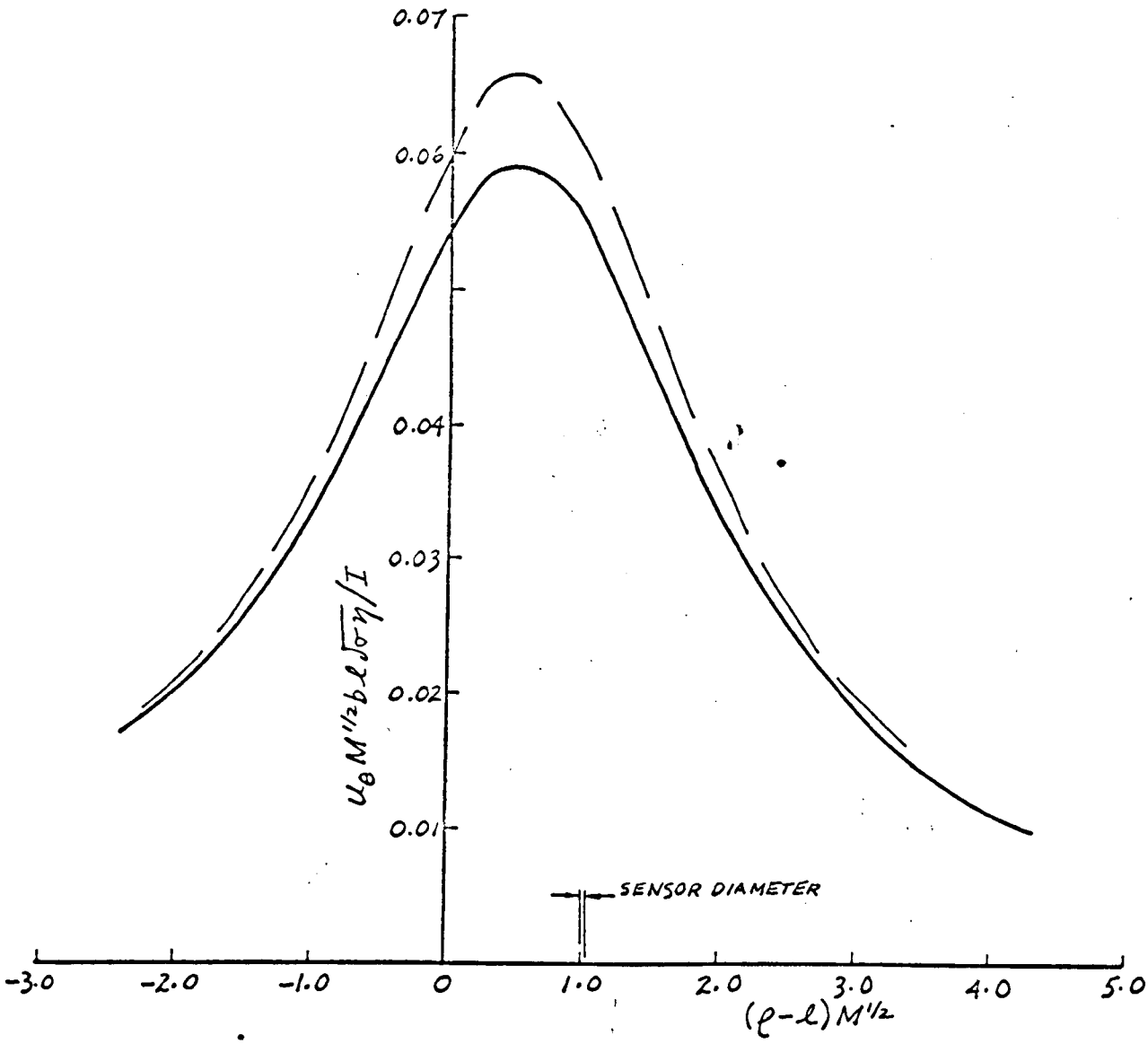

Figure 3.22 Radial profiles of azimuthal velocity at $\beta = 0.52$, M = 588, showing magnitudes of the corrections for MHD errors (—— ——, uncorrected curve; ————, corrected curve).

Figure 3.22 shows the magnitudes of the corrections for MHD heat transfer effects, which have been applied to the calculation of velocity, in the case of the profile at $\zeta = 0.52$, M = 588. Also shown is the small sensor length scale which corresponds to the hot-film diameter.

3.3.3.3 Discussion

In all the foregoing results one should expect the measurements at the highest M to correspond most closely to the asymptotic theory of H & S since $M^{\frac{1}{2}}$ and $\ell M^{\frac{1}{2}}$ then attain their maximum values. For M = 588, these values are $M^{\frac{1}{2}} = 24.2$ and $\ell M^{\frac{1}{2}} = 12.2$. Significant changes are noted in the velocity profiles as M increases from 212 to 588. The fact that these changes are much less pronounced between M values of 390 and 588 than between M values of 212 and 390 leads one to conclude that the flow, as described by the nondimensional variables $u_\theta b \ell M^{1/2} \sqrt{\sigma\eta}/I$ and $\bar{\zeta}$, is approaching an asymptotic state which is independent of M as M increases and that this asymptotic state is nearly reached at $M \simeq 600$.

At $\zeta \simeq 0.9$, the closest position to the disc, an "apparent" velocity is evident for $\bar{\zeta} < 0$ in Figure 3.18. This is likely due to the presence of some radial flow which exists because of the condition, $\ell M^{\frac{1}{2}} >> 1$, not being satisfied well enough. One would expect therefore, as is indeed seen in Figure 3.18, that the apparent velocity owing to radial flow would decrease as M increases.

In Figure 3.19 it is observed that the values of $\bar{\zeta}$ which correspond to the values of $(u_\theta b \ell M^{1/2} \sqrt{\sigma\eta}/I)_{max}$ decrease as ζ decreases. It is not known whether or not the H & S theory will show this to be a real effect.

The experimental values of u_θ at the maxima of the velocity profiles are seen to correspond fairly well with the theoretical predictions in Figure 3.20. The agreement is best at $\zeta = 0.50$, which may be due to the fact that the u_r secondary flow is least in this region of the flow.

In Figure 3.21 the experimental and theoretical velocity profiles correspond fairly well for $\bar{\zeta} > 0$. The reason for the large discrepancy for $\bar{\zeta} < 0$ is not clear. It may be due to a complicated interaction between the buoyant plume of free convection and the forced convection velocity, since $\bar{\zeta} < 0$ represents the "underside" of the shear layer in the experimental set up. There may be some secondary flow effects as well. It is unfortunate that no experimental check could be made on the theoretical prediction by H & S that a reversal of flow should take place in the region of $\bar{\zeta} = -2$.

Some comment on the accuracy of the data is necessary. The measurements could be repeated at any point in the flow with a precision of about ±2%. Perhaps the most serious effects on accuracy are due to the basic limitations of the hot-film sensor. As positioned in this flow it cannot distinguish between the u_θ and u_r components. Also, it is not entirely insensitive to flow along its length. This means that each measurement includes the effects of the smaller u_r and u_z components as well as u_θ, the component of interest. Another effect, which is not yet understood, is that of the interaction between free and forced convection from the sensor as it passes through a thin, low velocity shear layer. If the free convection velocity is of the same order of magnitude as the flow velocity being measured, then this interaction may be very complicated indeed. That the free convection velocities may be appreciable is illustrated by Figure 3.16 in the case of the downwash velocity curve. Throughout the high velocity region the hot-film is observed to be completely insensitive. It would seem that the updraft of the free convection plume tends to balance the downward forced convection so that the net result is a complete loss of sensitivity. In contrast, the updraft velocity gives an $(E-E_o)$ curve which is somewhat similar to that in which the flow is horizontal. From these results one would infer that the free convection velocities are of the same order of magnitude as the flow velocity at $\zeta = 0.5$, i.e., $O(10^{-1})$ cm/sec. This is rather surprising since one ordinarily expects free and forced convection velocities to be similar in magnitude only when $GP \sim Pe$; GP is $O(10^{-3})$ in these experiments and, at $\zeta = 0.50$, the maximum Pe is $O(10^{-2})$. The more pronounced free convection may be caused by three-dimensional heat transfer from the sensor owing to finite length effects. Another point to note is that the free convection is being suppressed by MHD effects in this experiment so that the free convection velocity must be lower than if the magnetic field were absent. In conclusion, the velocity measurements are expected to be most accurate at the highest values of M, where radial and axial flow is at a minimum, and in the regions of highest velocity, where the free convection effects are least.

To conclude this discussion, the most important observations are recapitulated as follows. The hot-film technique has enabled a detailed examination of the structure of an MHD shear layer, the results of which compare reasonably well with the theory of Hunt and Stewartson (1969). The velocity profiles at each value of ζ are quite similar at high M

when plotted in the nondimensional form, $u_\theta\, b\, \ell\, M^{1/2}\sqrt{\sigma\eta}/I$ versus $(\ell - \ell)M^{\frac{1}{2}}$.

The results serve to illustrate the basic limitation of the cylindrical hot-film, which is its lack of directional sensitivity. On the other hand, the chief advantage of the hot-film, its small size, is utilised to the full. The results also show that, contrary to expectations, free convection effects for a finite length ($L/d \simeq 20$) sensor may be significant up to $Pé = O(10^{-1})$.

3.3.4 Unsteady electrically driven flow between circular electrodes

3.3.4.1 The experiment

In order to study stability and secondary flow in the EDF shear layer the driving current was increased while holding the magnetic field constant, for each of a large range of magnetic field values, until critical conditions were reached. The onset of instability was observed by positioning the hot-film sensor in the outer, low velocity region of the shear layer and following the anemometer output signal on the oscilloscope while the current was being increased. The accurate determination of critical conditions was facilitated by using the 2A61 oscilloscope amplifier which contained the facility for filtering out all noise frequencies above 50 Hz while sensing frequencies as low as 0.06 Hz. The first sign of unsteadiness in the flow could thus be detected. The determination of a critical current was very tedious because of the necessity of approaching critical conditions very slowly and not forcing the onset of instability. When the current value was near critical it was necessary to observe the system for about 3 min. before making the next very small increase. After reaching critical conditions, a return to stable flow could be effected by either increasing B_e slightly at constant I or decreasing I slightly at constant B_e.

At the onset of instability, interesting phenomena observed on the oscilloscope were recorded using Polaroid film. From the information contained in these oscillograms at various probe positions, and from the measured values of I_c and M, it was possible to describe the phenomena involved in instability and secondary flow both qualitatively and quantitatively and to substantiate the physical mechanism proposed earlier in §3.2.2.

3.3.4.2 Results and Discussion

Figures 3.23 and 3.24 show the I_c vs M results, from which it appears that the data may be adequately described by the following empirical relationships:

$$I_c = 2.07M \times 10^{-3}, \quad 150 \leq M \leq 350, \qquad \text{———(3.22)}$$

and $$I_c = 2.95M^{4/3} \times 10^{-4}, \quad 350 \leq M \leq 650. \qquad \text{———(3.23)}$$

In Appendix B of Hunt and Malcolm (1968) some preliminary hot-film results were given as:

$$I_c \propto M, \quad M > 200.$$

The data plotted in Figure 3.23 have been obtained in more carefully controlled experiments over a much wider range of M. The result stated in H & M, i.e. $I_c \propto M$, still appears to hold, although over a more limited range of M. Equation (3.11) of the thesis gave the relationship of R_c to M as,

$$R_c \propto f(M)/M, \qquad \text{———(3.11)}$$

where f(M) is the functional relationship, to be obtained experimentally, between I_c and M. By combining (3.22) and (3.23) with (3.11) it is seen that,

$$R_c = \text{a constant}, \quad 150 \leq M \leq 350, \qquad \text{———(3.24)}$$

and $$R_c \propto M^{\frac{1}{3}}, \quad 350 \leq M \leq 650. \qquad \text{———(3.25)}$$

The fact that R_c is a constant, independent of M, in (3.24) suggests that the magnetic field is not strong enough to have an observable effect on the growth of the most unstable three-dimensional disturbances. Its effect on the stability is through changing the shape of the velocity profile, i.e., at constant I, $U_\theta \propto M^{-\frac{1}{2}}$ and $\delta \propto M^{-\frac{1}{2}}$, so that R decreases as M increases. On the other hand, the dependence of R_c on M in (3.25) suggests that when the magnetic field becomes sufficiently high, it has an observable, direct effect on the growth of the most unstable disturbances. It will be seen shortly, when the oscillograms are discussed, that for values of M higher than 300 the magnetic field markedly alters the manner of disturbance growth.

The critical Reynolds numbers in (3.24) and (3.25) may be approximately evaluated from the following definition of R_c, viz.,

$$R_c = U_{\theta c}(6aM^{-\frac{1}{2}})\tilde{\rho}/\eta, \qquad \text{———(3.26)}$$

where $U_{\theta c}$ is the critical velocity which occurs near the electrode edge in the region of highest velocity and $6aM^{-\frac{1}{2}}$ is the approximate shear layer width as shown previously in the velocity profiles (e.g., see Figure 3.21). Although it was not possible to come

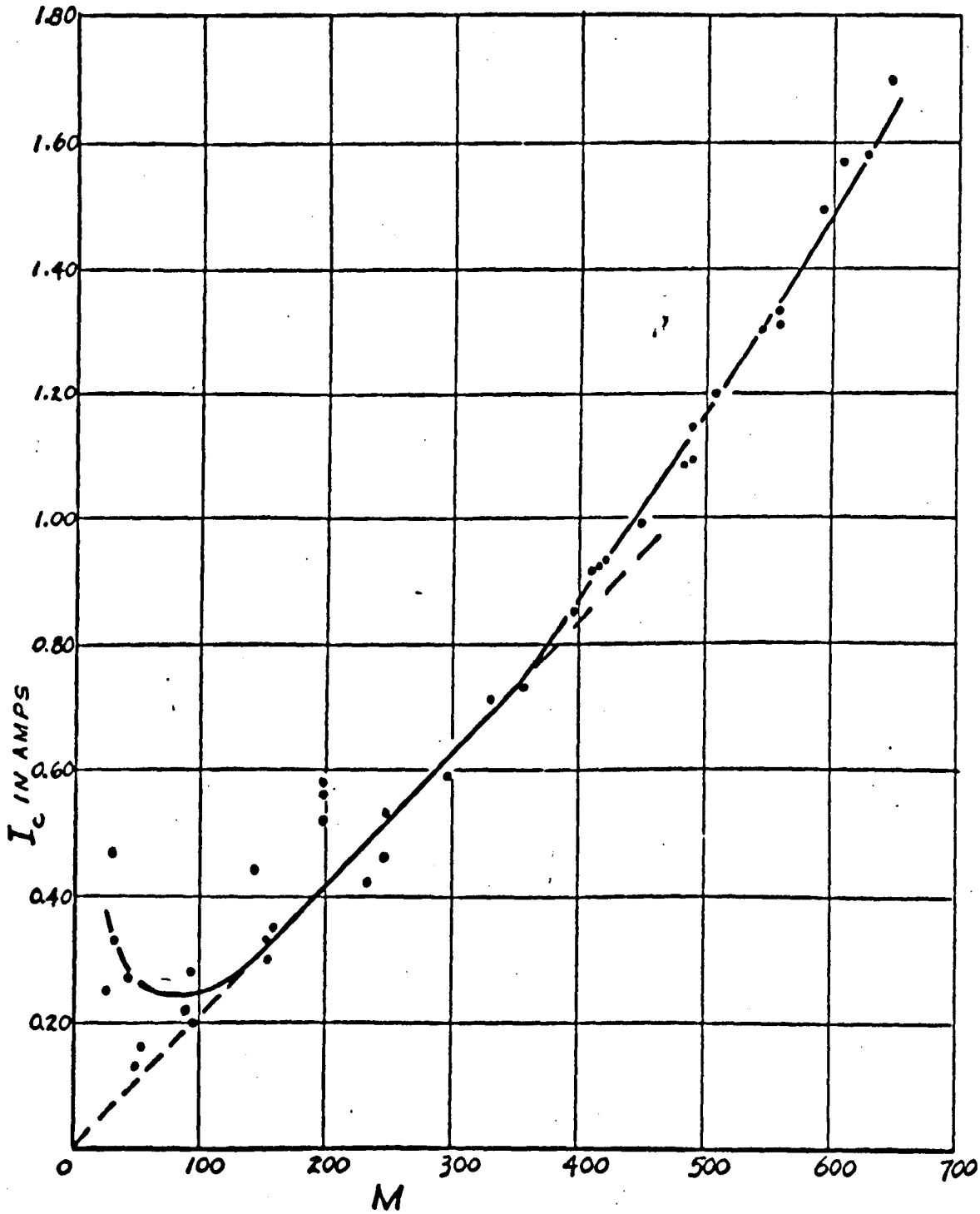

Figure 3.23 The dependence of critical driving current on Hartmann number in circular electrically driven flow, $\ell = 0$.

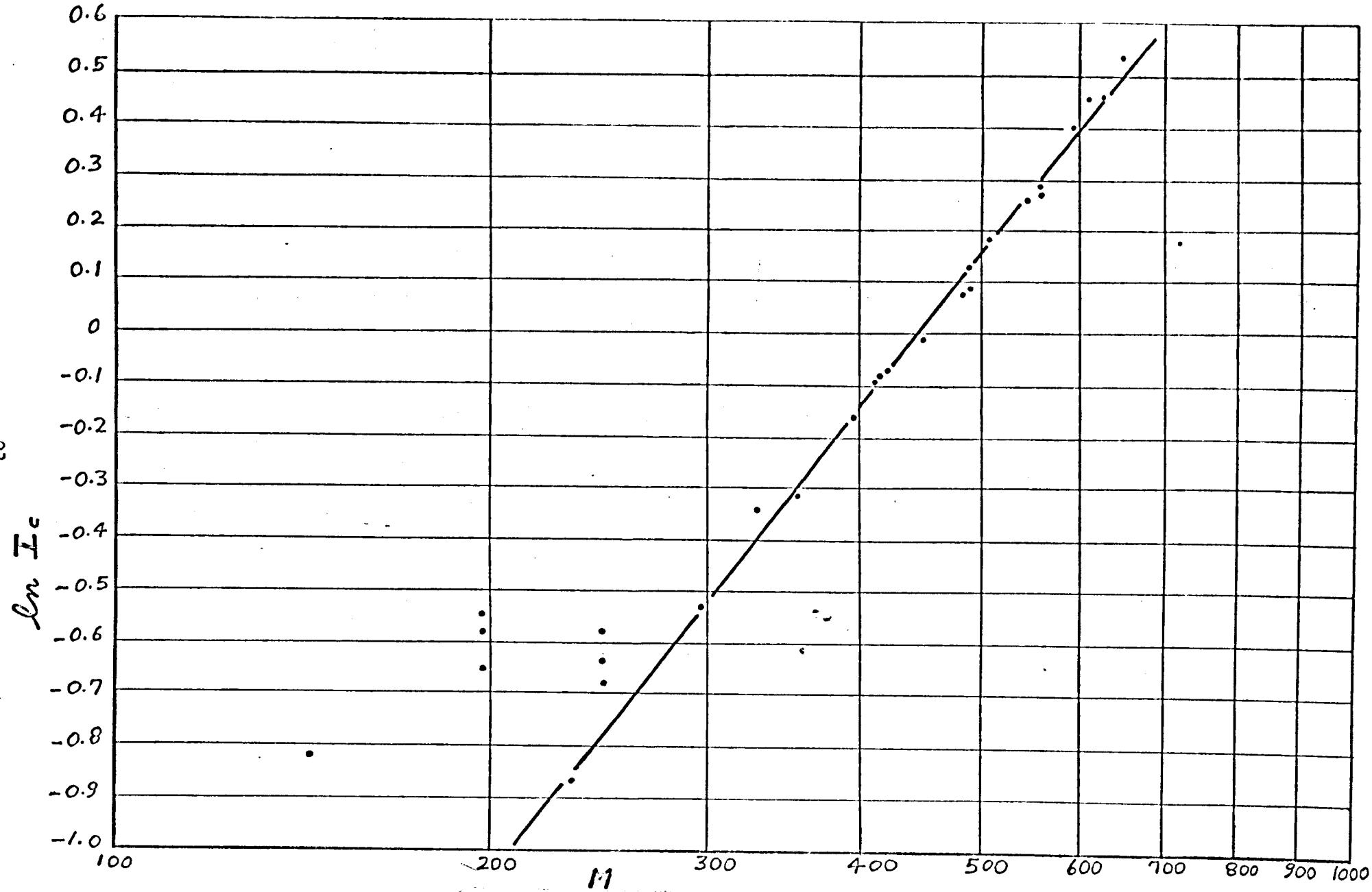

Figure 3.24 A plot of $\ln I_c$ versus M.

close enough to the wall to measure velocities in the region of highest velocity with the hot-film sensors, since that region occurs at a distance of approximately aM^{-1} away from the wall, use can be made of the theoretical predictions of Hunt and Stewartson (1969). As given in Table 3.1, the theoretical maximum velocity in the shear layer occurs near $\zeta = 1.00$ and is given by:

$$u_\theta b \ell M^{1/2} \sqrt{\sigma\eta} / I = 0.226 \, .$$

From this information, and the fact that Figure 3.20 showed reasonable agreement between theory and experiment, the critical velocity can be determined as follows,

$$u_{\theta c} = \left(\frac{0.226}{a \ell^2 \sigma^{1/2} \eta^{1/2}} \right) \frac{I_c}{M^{1/2}} \, . \qquad \text{——(3.27)}$$

Now, (3.27) can be substituted in (3.26) to give,

$$R_c = \left(\frac{1.36 \tilde{\rho}}{\ell^2 \sigma^{1/2} \eta^{3/2}} \right) \frac{I_c}{M} \, . \qquad \text{——(3.28)}$$

If I_c in (3.28) is replaced by (3.22) or (3.23) the critical Reynolds numbers can be calculated and are given as follows, using properties of mercury at 20°C,

$$\begin{aligned} R_c &= 2420 \, , \quad 150 \leq M \leq 350, \\ R_c &= 345 M^{\frac{1}{3}} \, , \quad 350 \leq M \leq 650. \end{aligned} \qquad \text{——(3.29)}$$

R_c, from (3.29), is plotted against M in Figure 3.25 along with the experimental data. In figures 3.23 and 3.25 it is observed that the experimental values of I_c and R_c become much more reproducible once M becomes large enough to exert control on the growth of disturbances. As will be seen in the following oscillograms, the manner in which the shear layer goes unstable is not reproducible when M is less than 300, whereas when $M \geqslant 300$ instability always sets in in the same manner and ultimately produces a wave-like secondary flow.

The oscillograms in Figure 3.26 are a sequence (top to bottom) of three observations taken one after another in a single run. They demonstrate the very unstable nature of the flow when M is low; in this case, M = 94. The observed oscillations, with a period of about 7 sec, are likely caused by either an "out of balance" rotation of the cylinder of fluid between the electrode, or a pulsating radial flow which is driven out by centrifugal forces.

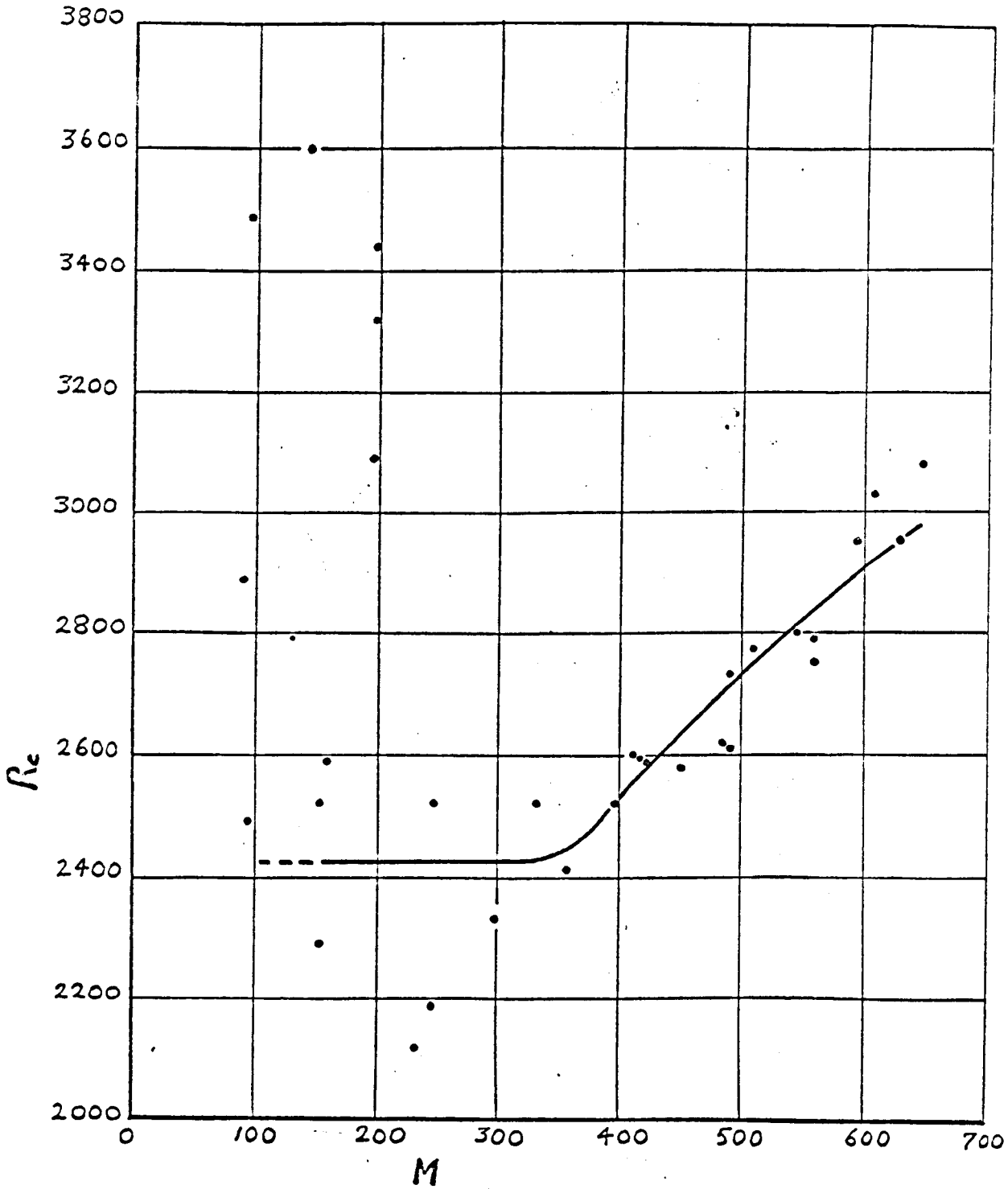

Figure 3.25 The dependence of R_c on M.

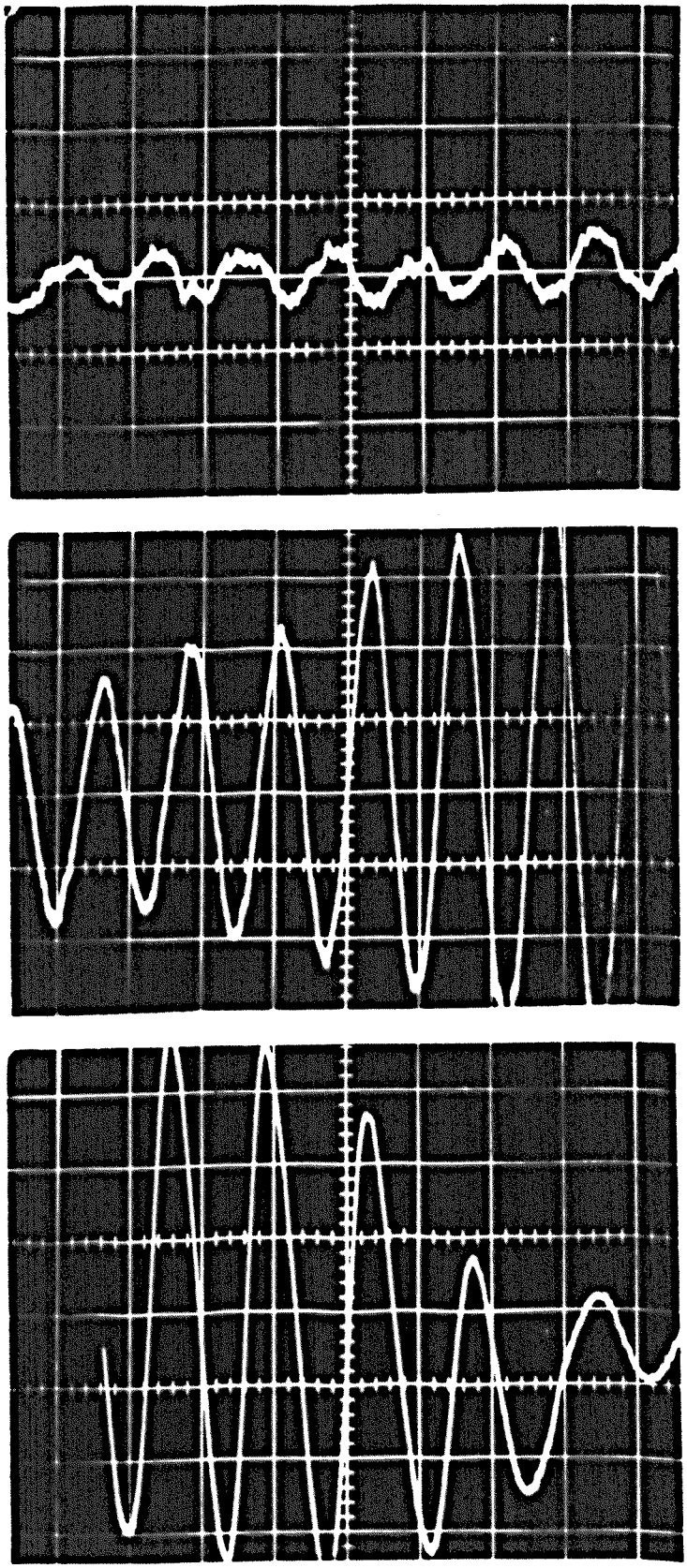

Figure 3.26 Secondary flow at critical conditions, M = 94, I_c = 0.28 amps.
Scales: 5 sec/division, 2 mv/division except for bottom oscillogram which is 5 mv/division.

A predominant characteristic of the onset of instability for M lower than about 300 was the lack of reproducibility of the results under identical experimental conditions. For instance, Figure 3.27 shows two separate runs at M $\simeq$ 150. In Figure 3.27(a), the flow became weakly turbulent at the onset of instability, whereas in Figure 3.27(b) the flow became oscillatory with a period of about 8 sec, which is probably caused by the same physcial phenomenon that gave rise to the results observed in Figure 3.26. Figure 3.28 shows three separate runs at critical conditions when M $\simeq$ 250. In Figures 3.28(a) and (c), instability has given rise to similar oscillatory secondary flows having a period of about $3\frac{1}{2}$ sec. In Figure 3.28(b), however, the onset of instability proceeded in a much more erratic fashion and did not settle down to a more regular pattern of flow. Note that the oscillation period is much longer in this case, being about 16 sec.

For values of M $\geq$ 300 the magnetic field was able to control the stability so that the destabilizing disturbances always developed into a non-axisymmetric flow having a wave-like form, with a definite and reproducible wave number corresponding to each value of M. The significance of this phenomenon will be discussed later. As an example of this predictable nature of the flow, Figure 3.29 shows three separate observations at M $\simeq$ 500. In these three oscillograms the wave period is between 1.5 and 1.6 sec.

Thus far, the oscillograms have described the flow situations a long time after the onset of instability. Figure 3.30 shows the actual onset of instability when M = 450. It takes place very gradually and without disrupting the main flow. The final result is simply a wave-like secondary flow superimposed on the steady primary flow. Upon witnessing this phenomenon for the first time it was tempting to consider these oscillatory signals as being caused by vortices rather than by waves. It will be shown later to be unlikely, although the idea cannot be completely ruled out. For an example of a somewhat similar non-axisymmetric secondary flow which occurs in a rotating system of free hydrodynamic shear layers, see Hide and Titman (1967).

After examining the phenomena which occur at critical conditions, an attempt was made to find out the effect of a further increase in the driving current. These effects are illustrated in Figures 3.31 and 3.32. Figure 3.31(a) represents the case, M $\simeq$ 485, I_c = 1.08 amps, when I is increased from I_c to 1.17 amps. The effect is to slightly increase the frequency of the initial oscillations and to introduce another mode of

(a)

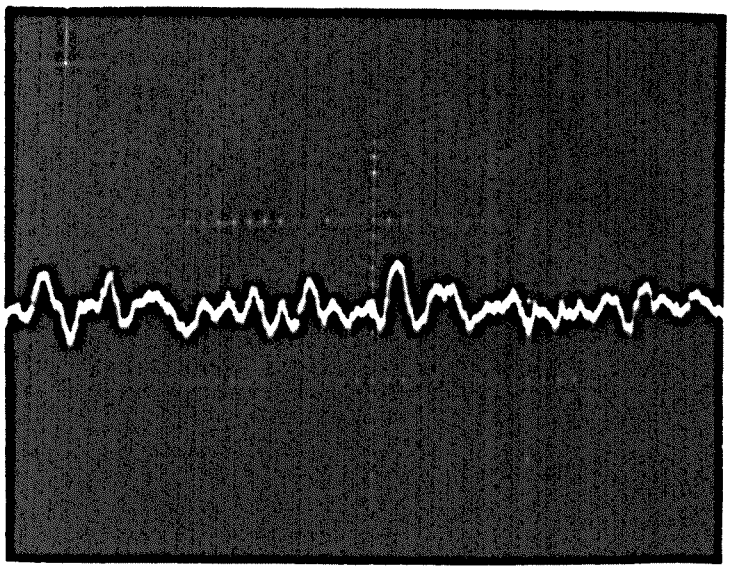

(b)

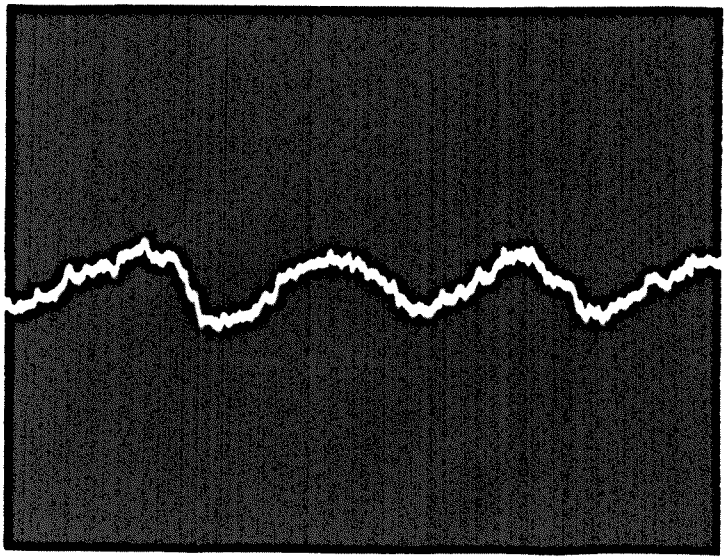

Figure 3.27 Secondary flow at critical conditions,
(a) M = 143, I_c = 0.44 amps,
(b) M = 153, I_c = 0.30 amps.

Scales: 5 sec/division, 2 mv/division.

(a)

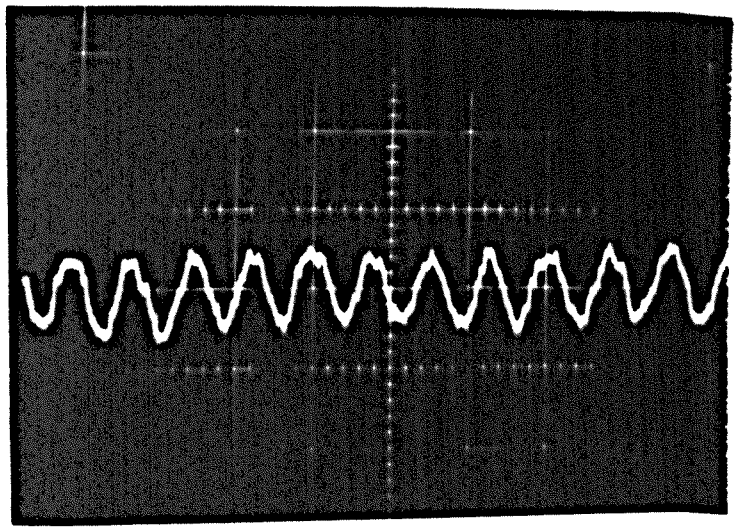

(b)

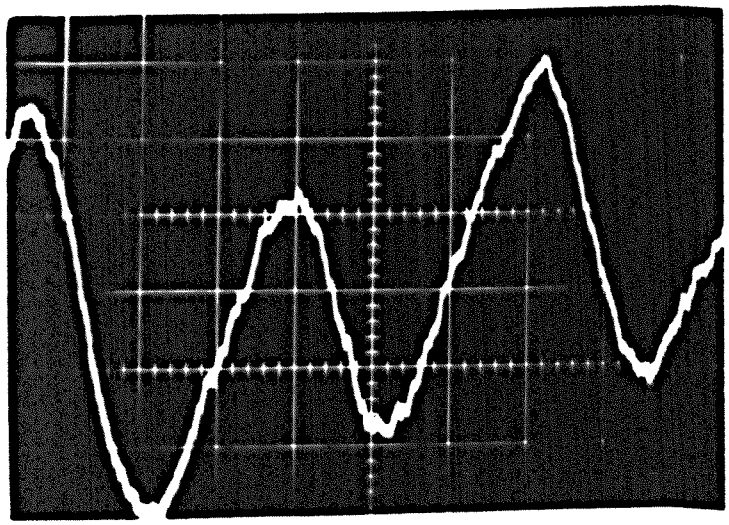

(c)

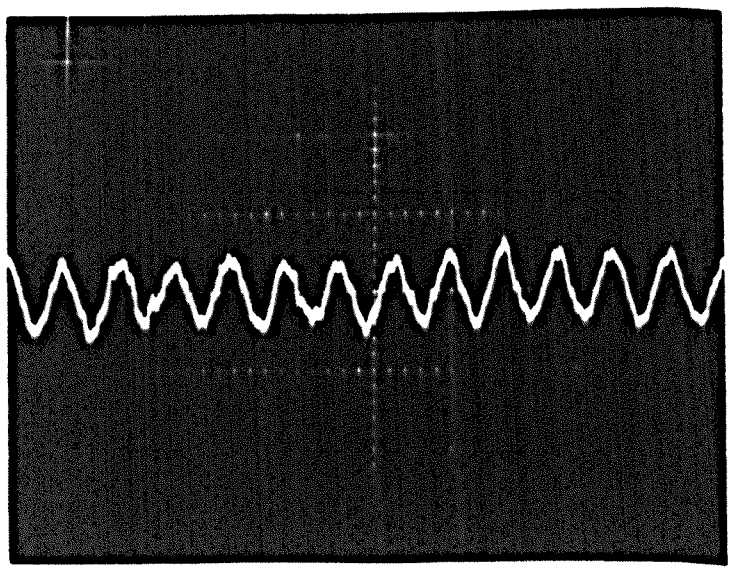

Figure 3.28 Secondary flow at critical conditions,
(a) M = 232, I_c = 0.42 amps,
(b) M = 247, I_c = 0.53 amps,
(c) M = 247, I_c = 0.46 amps.

Scales: 5 sec/division, 2 mv/division.

(a

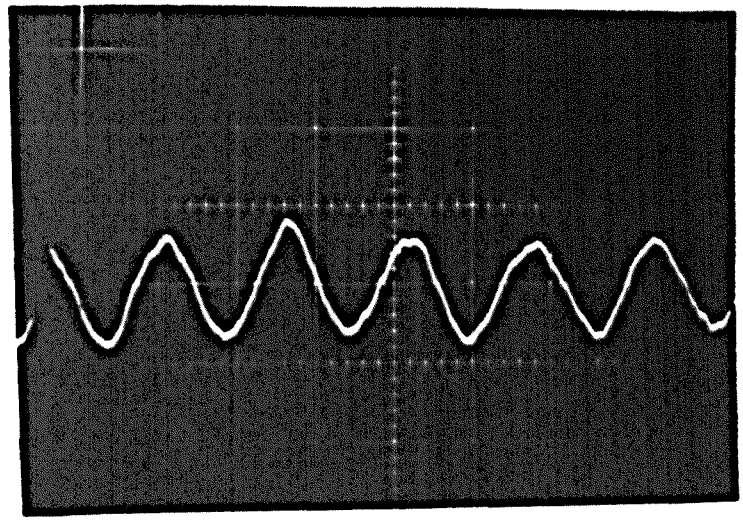

(b

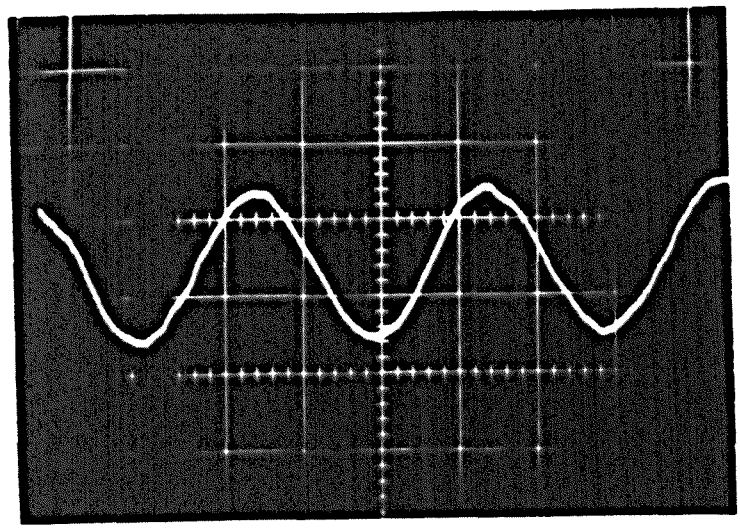

(c

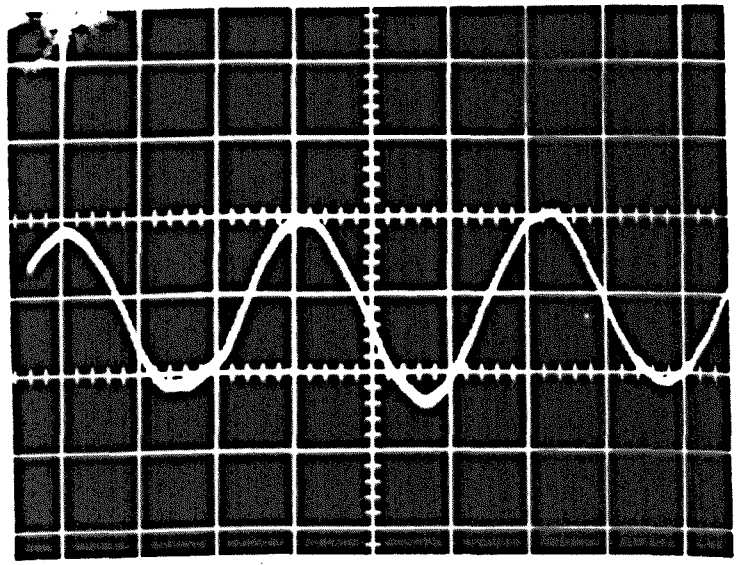

Figure 3.29 Secondary flow at critical conditions,
(a) M = 484, I_c = 1.08 amps (1 sec & 2 mv /division),
(b) M = 508, I_c = 1.20 amps (0.5 sec & 2 mv /division),
(c) M = 490, I_c = 1.14 amps (0.5 sec & 2 mv /division).

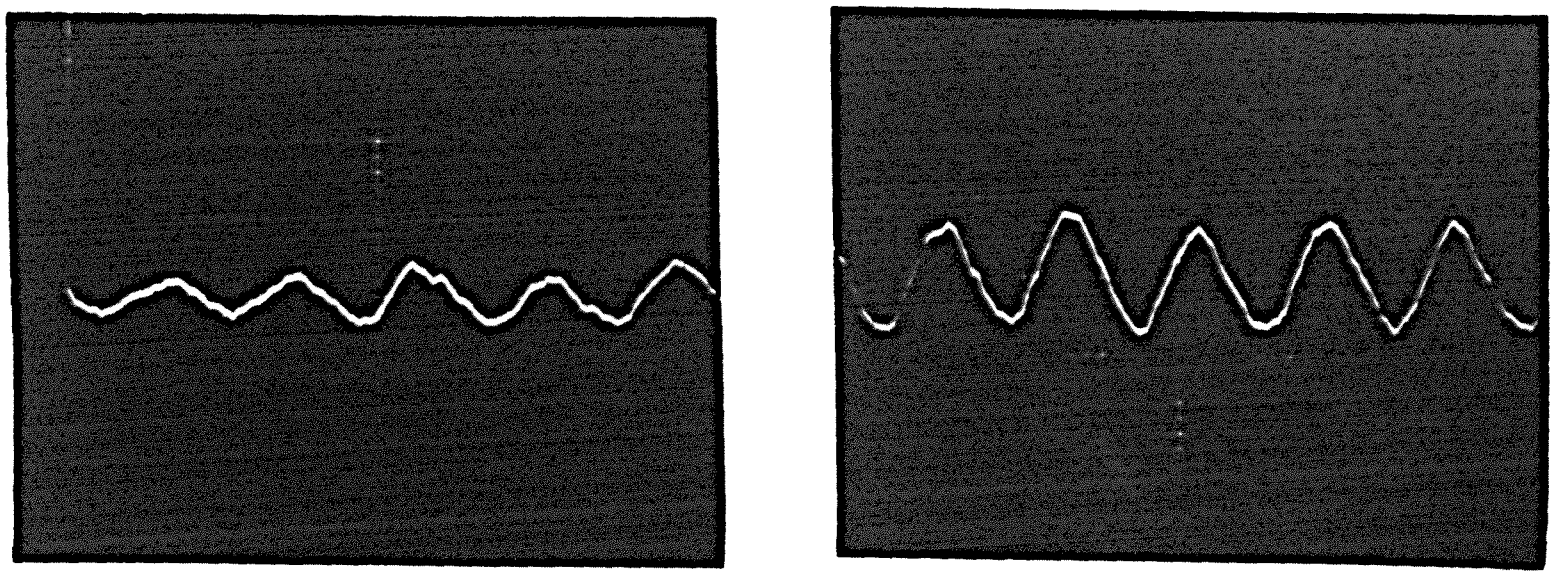

Figure 3.30 The onset of instability at M = 450, I_c = 0.99 amps.

(a)

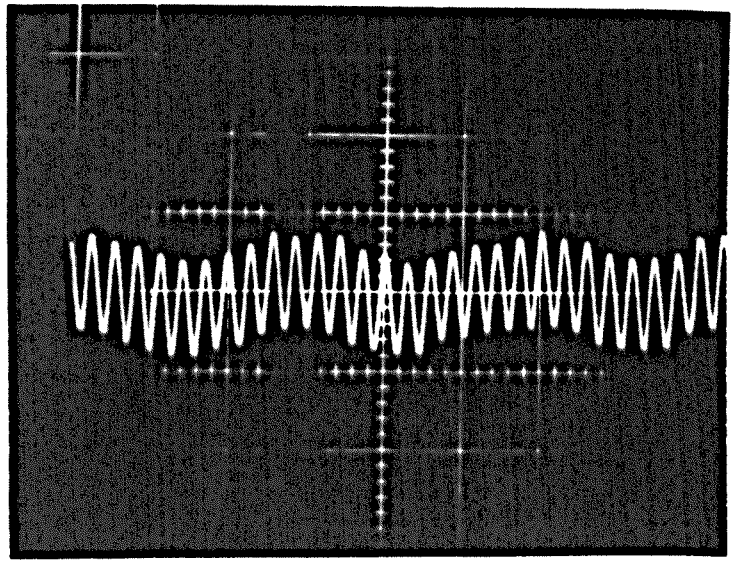

(b)

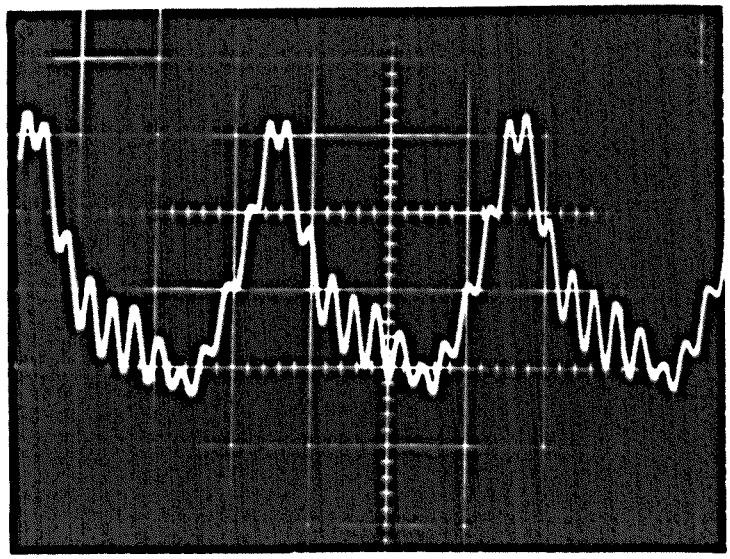

Figure 3.31 Secondary flow when $I > I_c$, M = 484,
(a) I = 1.17 amps.
Scales: 5 sec/division, 5 mv/division.
(b) I = 1.20 amps.
Scales: 5 sec/division, 10 mv/division.

(a)

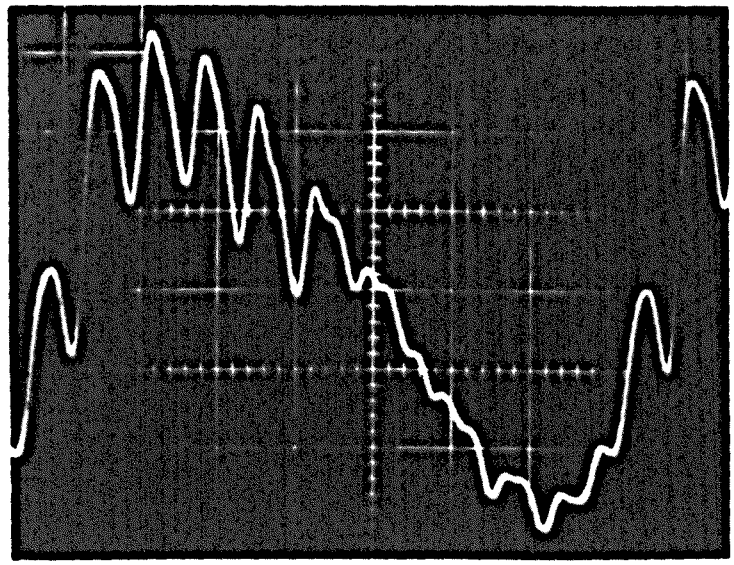

(b)

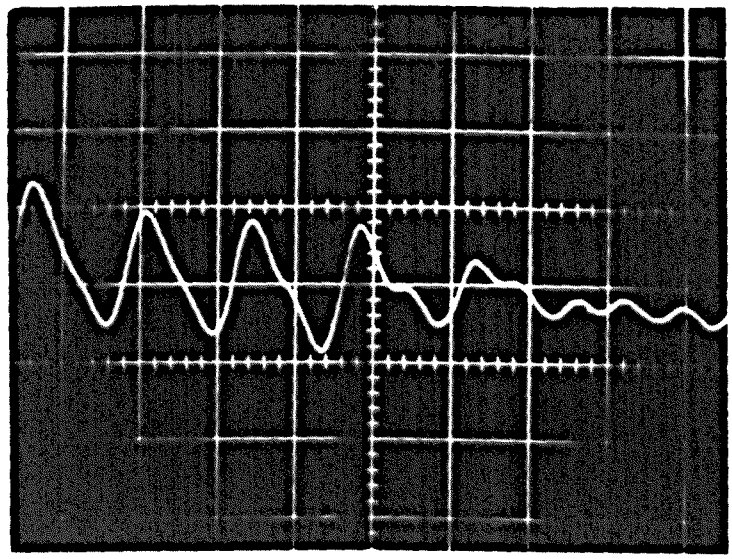

Figure 3.32 Secondary flow when $I > I_c$, M = 490, I = 1.30 amps,
(a) using 0.06 Hz high pass filter.
Scales: 2 sec/division, 10 mv/division.
(b) using 0.6 Hz high pass filter.
Scales: 1 sec/division, 10 mv/division.

oscillation having a period about 10 times as long as that of the initial one. This new mode probably represents an "out of balance" rotation of the whole cylindrical flow system. When the current is further increased from 1.17 to 1.20 amps this new low frequency oscillation grows in amplitude until the situation in Figure 3.31(b) is observed. The amplitude of the original higher frequency mode has now began to oscillate as well. When the flow is pushed still faster by increasing I to 1.30 amps, the situation is somewhat similar to that in Figure 3.31(b), and is shown in Figure 3.32(a) and (b). The notable new change is the peculiar frequency doubling effect. Figure 3.32(b) shows this effect more clearly by filtering out the lowest frequency oscillation. It may be caused by the formation of waves of twice the original frequency, or by the beginnings of vortex formation behind the crests of the primary waves, as usually takes place when a hydrodynamic free shear layer goes unstable. A somewhat similar frequency doubling effect was noted by Klebanoff, Tidstrom and Sargent (1962) in a hot-wire study of the three-dimensional characteristics of boundary layer instability. At M = 500, the system could not be driven turbulent by increasing the current to as high as 2.00 amps, the limit of the constant current supply.

Thus far, the results of the experiment confirm the conclusions drawn in §3.2.2 concerning the influence of a coplanar magnetic field, in a direction perpendicular to that of the flow, on the stability of a three-dimensional, approximately-parallel shear layer. The proposed physical mechanism seems to exist, viz., the energy fed into the growing disturbances from the critical region of the primary flow may be transmitted by an electromagnetic coupling action to other parts of the flow, in the direction of $\mathbf{B}_0$, where conditions are below critical. The situation is decidedly different to the similarly orientated MHD shear flow studied by Lehnert (1956), which was very nearly two-dimensional, in which the onset of instability was marked by the appearance of trains of vortices which were aligned with and apparently unaffected by the magnetic field.

If the above electromagnetic coupling mechanism were truly in operation, one would expect the fully-developed waves to travel in the flow direction and to lie parallel to $\mathbf{B}_0$. An experiment was therefore designed to provide more detailed information concerning the physical structure of the waves. In this experiment it was desired to determine, firstly, whether or not each of the waves was symmetrical about a line

joining its peak and the flow axis, secondly, whether or not the waves were aligned with $\underset{\sim}{B}_o$ and, finally, whether or not the waves were truly travelling in the flow direction and, if so, at what speed.

Figure 3.33 indicates that the waves are symmetrical. To obtain this information the hot-film was first positioned in the outer portion of the shear layer at $\zeta = 0.52$, $\bar{\xi} = 1.97$ (in a flow characterised by M = 607, I = 1.60 amps). Then the oscilloscope sweep rate was synchronized with the wave signal so that the wave pattern was stationary on the screen. A photograph was then taken, corresponding to one of the large amplitude signals in the figure. The sensor was then moved out in the radial direction from $\bar{\xi} = 1.97$ to $\bar{\xi} = 2.79$ where another exposure was taken, corresponding to the low amplitude signal in the figure. As a check on the synchronization of the wave pattern, the sensor was returned to its original position and a third exposure taken, corresponding to the other large amplitude trace in the figure. The lack of any discernible phase shift between the signals indicates that the waves were symmetrical.

Figure 3.34 illustrates that the waves lie parallel to $\underset{\sim}{B}_o$. The corresponding flow conditions were, M = 410, I = 0.95 amps. The sensor was positioned at $\zeta = 0.50$, $\bar{\xi} = 2.30$, and the sweep rate was again synchronized with the wave signal. The wave signal was photographed at constant $\bar{\xi}$ at various stations in the z-direction in the range $0.50 \leq \zeta \leq 0.90$. The lack of any discernible phase shift in the resulting oscillogram is convincing evidence that the waves were aligned with $\underset{\sim}{B}_o$.

In order to determine an approximate wave speed, a similar synchronization procedure was used, the results of which are observed in Figure 3.35. The sensor was positioned in a flow (described by M = 509, I = 1.24 amps) at $\bar{\xi} = 2.33$, directly above the z-axis, and an exposure was taken, represented by one of the large amplitude traces which are superimposed in Figure 3.35(a). The sensor was then traversed in the (x, z) plane (referring to the probe traversing co-ordinates), in the direction of u_θ , a distance of 0.125 in. where another exposure was taken. When referred to the cylindrical co-ordinate system this represents a movement out in the r-direction as well as in the θ -direction so that the trace, as photographed in Figure 3.35(a), is of lower amplitude. The original position was then returned to for a check exposure, represented by the other of the large amplitude, superimposed traces in the figure.

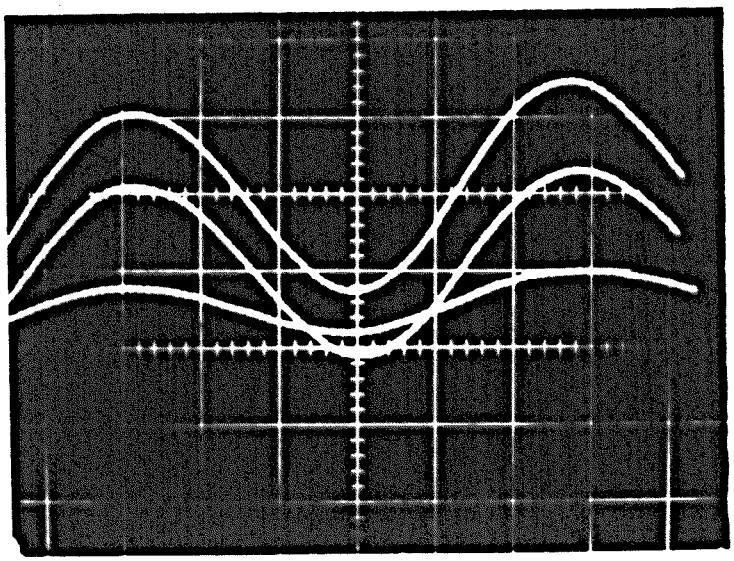

Figure 3.33 Evidence of wave symmetry.

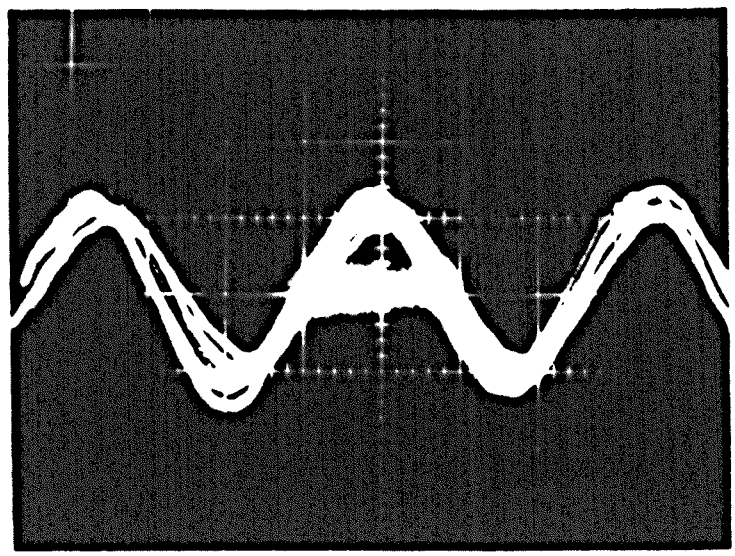

Figure 3.34 Evidence of alignment between the waves and the applied magnetic field.

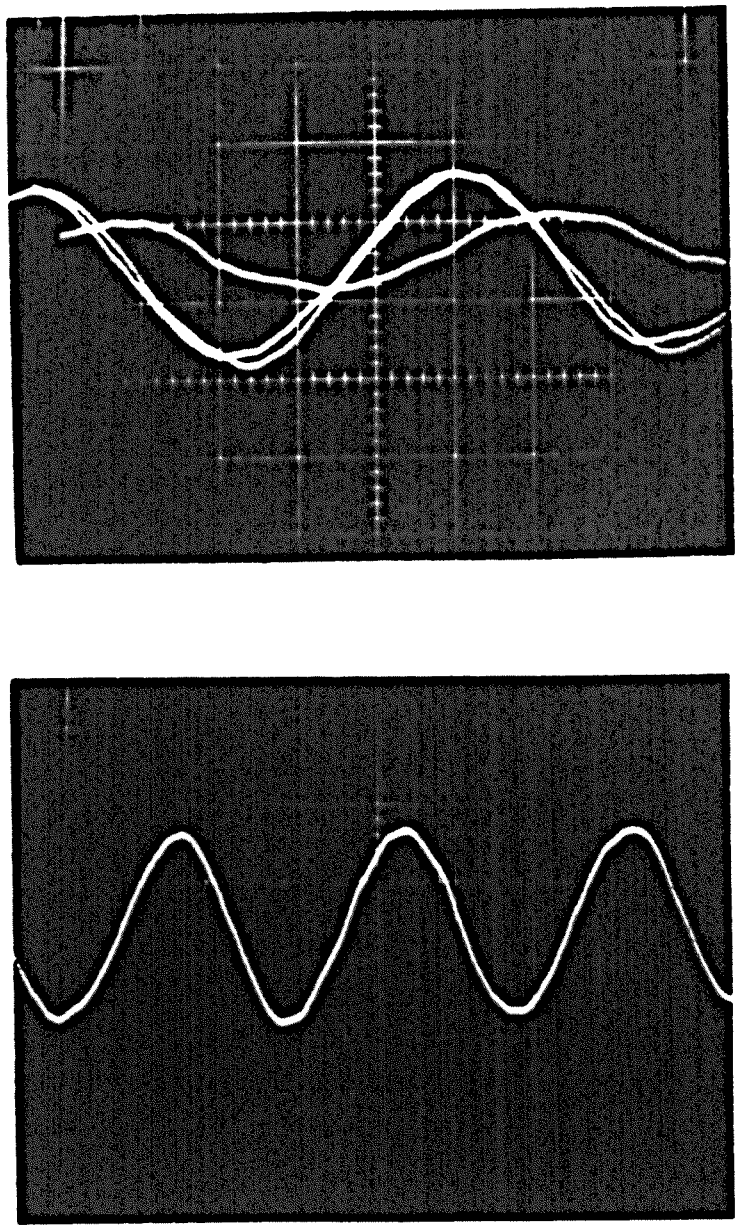

Figure 3.35 Determination of wave speed,
(a) speed determination procedure using a synchronized sweep rate.
(b) reference trace in real time: 0.5 sec/division.

With this figure and Figure 3.35(b) to give an accurate value of the actual wave period, it is a simple matter to calculate the lag time brought about by moving the sensor the given distance in the flow direction, and hence the corresponding wave speed. When referred to the edge of the electrode, i.e. $\bar{\ell} = 0$, this speed is about 0.74 cm/sec.

From the above approximate wave speed it is possible to estimate the wave number, which in this context will be taken to mean the actual number of waves, n, spaced around the EDF shear layer, i.e.,

$$\frac{1}{n} = \frac{t_w u_w}{2\pi b}, \qquad \text{———(3.30)}$$

where t_w is the wave period. For the case illustrated in Figure 3.35 it appears that $n \simeq 5.4$, i.e., n must be 5 or 6. The experimental error does not allow a more exact calculation of n.

By using equation (3.27) it is calculated that the above wave speed is 10 - 15% of the critical velocity. Throughout most of the EDF system, then, the fluid particle velocity is greater than the wave velocity. At each value of ℓ the phase velocity between the fluid particles and the wave will be different.

A similar calculation for n, using experimental results at M = 415, shows that in this case also n must be either 5 or 6. Upon increasing M to 603 it is found that the corresponding n is now 7 or 8. It seems therefore that the wave number is some function of M. Since the cylindrical geometry of the flow allows an integral wave number only, each n must hold over a certain range of M. The fact that n must be constant over a range of M allows the interesting observation that u_w is a constant proportion of $u_{\theta c}$, i.e. $u_w \propto u_{\theta c}$, over this same range of M. To demonstrate, let it be assumed that, for each value of n,

$$u_w \propto u_{\theta c} \qquad \text{———(3.31)}$$

From (3.27) and (3.23) it is observed that,

$$u_{\theta c} \propto \frac{I_c}{M^{1/2}} \propto M^{5/6}, \quad 350 \leq M \leq 650. \qquad \text{———(3.32)}$$

Now, combining (3.30) to (3.32), it is expected that,

$$\frac{1}{n} \propto t_w M^{5/6}. \qquad \text{———(3.33)}$$

The wave numbers at two values of M can be compared directly from this relationship. Table 3.3 applies the data from various runs at critical conditions to (3.33) in order to test (3.31). The fact that $t_w M^{5/6}$ is constant, within 3%, as M varies from 355 to 509 is convincing

Run	M	$M^{5/6}$	t_w sec.	$t_w M^{5/6}$	From (3.33) n_1 / n_2	From (3.30) n	Probable n
1	296	115	3.12	359	0.74		4 - 5
2	355	134	1.97	264	1.00		5 - 6
3	395	146	1.80	263	1.00		5 - 6
4	415	153	1.75	268	0.98	5 - 6	5 - 6
5	449	163	1.62	264	1.00		5 - 6
6	509	181	1.50	272	0.97	5 - 6	5 - 6
7	603	208	0.96	200	1.32	7 - 8	7 - 8
8	607	209	0.97	203	1.30		7 - 8

Table 3.3 Integral wave number determinations in secondary EDF.

evidence that the assumption, $u_w \propto u_{\theta c}$, is valid so that, for each n, u_w is a constant proportion of $u_{\theta c}$. The relationship (3.33) does not likely hold for two values of M when n is different for each because the proportionality constant may be influenced by wave drag, etc. The column of probable n's in the table has been filled in assuming that this proportionality constant is little influenced by such effects.

Finally, an attempt was made to determine the variation in the intensity of the velocity disturbance associated with the travelling wave by traversing across the shear layer at M = 603 under critical conditions for two values of ζ, 0.522 and 0.770. Most of the data for this study has not been reduced as yet but any valuable information will be reported later in Malcolm (1969). The maximum peak to peak fluctuations in the streamwise direction have been estimated however. These occur near $\zeta = 1.51$ (very near to the outer point of inflection on the steady velocity profile). With the help of equation (2.8), the intensity of these peak to peak fluctuations is estimated to be about 0.05 at both values of ζ. From this calculation, since u_θ falls as ζ decreases, it would seem that the peak to peak fluctuations become less as ζ decreases. This is in qualitative agreement with

the observation that both the fluctuations and the mean value of u_θ die out when the centreplane is reached, i.e. when $\zeta = 0$.

This section is now concluded by a summary of the main observations and conclusions. The conclusions based on physical reasoning in §3.2.2 have been substantiated by experimental evidence. The growth of the most unstable disturbances are controlled in some way, most likely by the electromagnetic coupling effect, when M is sufficiently great. The critical Reynold's number for the onset of instability has been shown to vary, in this range of very high M, in the manner,

$$R_c = 345\, M^{1/3}, \quad 350 \leq M \leq 650. \tag{3.29b}$$

For somewhat lower values of M, the electromagnetic forces seem too weak to exert an observable controlling action on the stability and R_c is a constant, being approximately equal to 2420 as given in (3.29a). For the higher range of M where electromagnetic control is observed, the most unstable disturbances grow to produce an integral number of travelling waves which are positioned periodically around the cylindrical shear layer. These waves lie parallel to the magnetic field and die out on the centreplane. There is evidence to suggest that the wave velocity is directly proportional to the critical velocity in the layer. The fully developed secondary flow as viewed from outside the flow system resembles a rotating, fluted cylinder (rotating in opposite directions on either side of the centreplane) with the flutes, or waves, lying in an axial direction but travelling at a velocity less than that of the fluid particles throughout most of the shear layer. An attempt to sketch this complicated situation is made in Figure 3.36.

The interesting outcome of this study of the stability of a three-dimensional MHD free shear layer poses the question as to whether or not the stability of other similarly orientated shear layers, such as those occurring in the duct flows studied by Alty (1969), might be similarly affected by the magnetic field. If the shear layers are very nearly two-dimensional, such as those studied experimentally by Lehnert (1956), it is unlikely that an observable effect of the magnetic field on the growth of disturbances will be observed.

3.3.5 Magnetohydrodynamic suppression of vorticity downstream from a square-mesh wire grid

3.3.5.1 The experiment

A description of the grid and the mercury tunnel used in this

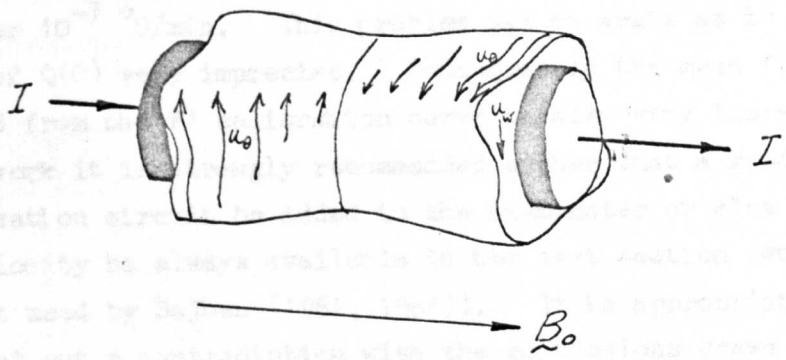

Figure 3.36 Sketch of probable wave-like secondary electrically-driven flow which occurs after critical conditions have been reached in the primary flow.

experiment was given in §3.3.2. The procedure was simply to traverse hot-film probe no.6 downstream from the square-mesh grid in a steady mean flow while applying various magnetic field strengths. It was intended that this experiment should be of a preliminary, qualitative nature, to be followed by a study in greater detail of turbulence decay downstream from a plate grid having circular holes. As already mentioned, this latter study was prevented by accidental breakage of probe no.6. Accordingly, the results for vorticity decay presented in this section are meagre.

The experiment showed how discomfiting the presence of signal drift can be during startup and shutdown, owing simply to temperature drift of order 10^{-1} °C/min. This problem was so acute as to make the measurement of Q(0) very imprecise. Consequently the mean flow rate as determined from the F' calibration curve is also very imprecise. For further work it is strongly recommended either that a good temperature compensation circuit be added to the anemometer or else that a reference velocity be always available in the test section (such as the reference jet used by Sajben (1964, 1965)). It is appropriate at this point to point out a contradiction with the conclusions drawn by Sajben as a result of severe signal drift in his experiment. He experienced severe, erratic signal drift during a period of about two hours after startup and found that temperature drift effects could not account for the phenomenon. He concluded that minute amounts of impurities present in the mercury, which might arise from chemical action between mercury and the stainless steel walls of his system, could change the heat transfer coefficient significantly. This conclusion is contradicted in the present experiment where there was enough chemical action between the mercury and the pvc tubing, perspex channel walls and stainless steel apparatus to give rise to a continual fresh collection of dark scum on the surface of the mercury in the reservoir tanks. Because the stainless steel pump had only recently been installed oil droplets also continued to appear on the free surfaces. In contrast to Sajben's experience, a period of about thirty minutes was sufficient for signal drift to be reduced to a low level, which could easily be accounted for by small temperature drift, in the present experiment. It may be that the differences between the sensor insulation used in the two cases, i.e. enamel vs quartz, has a significant effect on the complicated heat transfer characteristics of the contact resistance-impurity layer surrounding the sensor.

The mean velocity downstream from the grid was measured to be about 3.2 ± 0.5 cm/sec for the vorticity suppression tests. Although not accurately determined, the flow rate was very constant during any set of conditions.

3.3.5.2 Results and Discussion

The qualitative results will be discussed first, followed by the few reliable quantitative results. These confirm the expected behaviour of flow through a square mesh grid as discussed in order of magnitude terms in §3.2.3.

When the highest magnetic field was applied, $B_o = 1.22$ wb $/m^2$, the interaction parameter based on the wire diameter was very high, viz., $N_d \simeq 2.6$. As expected, no measureable flow separation was allowed from those grid wires which were orientated vertically, perpendicular to B_o. The wake of the grid was then filled with the combined oscillating wakes of the field-parallel grid wires. At a distance of about 8 wire diameters downstream of the grid, no trace could be detected of any effects on the flow caused by the vertical wires; an oscillogram of the anemometer output is shown in Figure 3.37, taken at a position midway between two of the field-parallel wires. The sensor was then traversed in the stream direction to see how the vortex system decayed with time. As will be seen in the quantitative results this vortex system decayed quite rapidly, whether due to MHD effects at the vortex ends or to intense viscous action in the close-packed vortex array is not known.

When the magnetic field was lowered to 0.50 wb/m^2, with N_d now falling to 043, the presence of the vertical wires could just be detected at the 8 wire diameter station downstream. Also, the velocity fluctuations in the oscillating grid wake were more intense. The decay of this wake system was also examined.

When B_o was still lower, 0.275 wb $/m^2$, N_d had fallen to 013 and, as expected, the wakes of the two sets of wires now combined strongly enough to produce some turbulence. This turbulence had a maximum intensity at $x/L_o \simeq 1.3$ and at the centre of a mesh square. The distance x was measured from the rear edge of the field-parallel wires which were nearest to the hot-film sensor. The sensor was traversed in the flow-direction, along a line through a mesh-square centre, to study the decay of this turbulent vorticity. The oscillograms in Figure 3.38 show the suppression qualitatively.

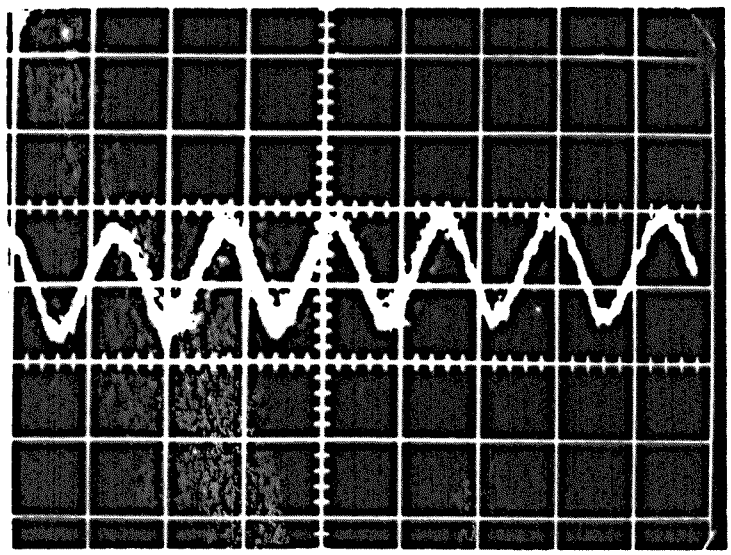

Figure 3.37 Periodic wake behind a square-mesh grid, $N_d = 26$, $\bar{u} = 3.2 \pm 0.5$ cm/sec.

Scales: 0.1 sec/division, 5 mv/division.

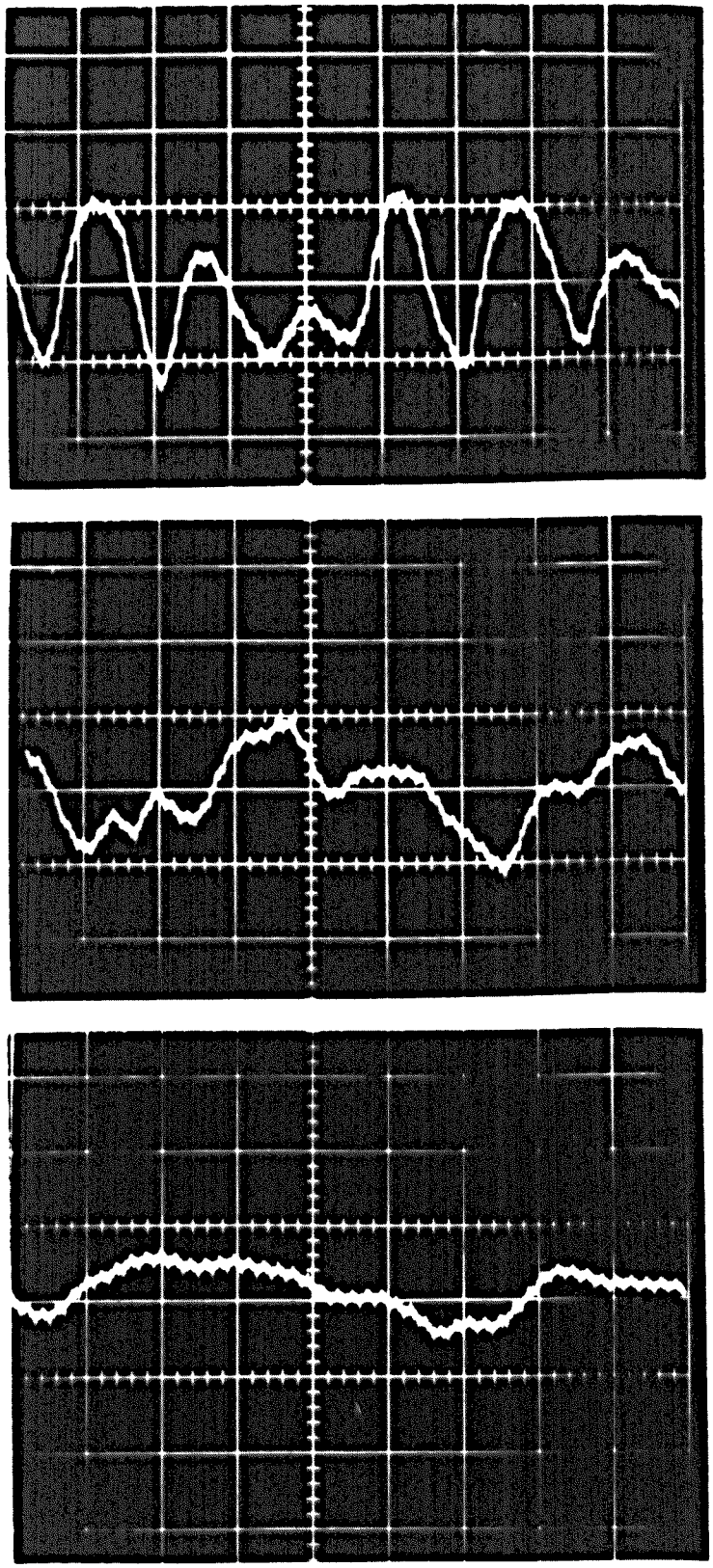

Figure 3.38 Vorticity suppression behind a square-mesh grid, $N_d = 0.13$, $N_L = 70$.

Top to bottom: $x/L_o = 1.3$, 3.3 and 6.0.

Scales: 0.1 sec/division, 5 mv/division.

The turbulence intensities were calculated using the measurement techniques described in chapter 2 of the thesis. It was rather unfortunate that the F'(Pé) corresponding to the mean flow was only about 0.28, corresponding to $\overline{Pé} \simeq 0.18$, and was somewhat too low to be in the straight line portion of the F' vs $\ln Pé$ curve in Figure 2.12. The local value of the slope, -s, was taken to be -0.20.

The vorticity decay results are plotted as $\sqrt{\overline{\omega'^2}}/\bar{u}$ vs x/L_o in Figure 3.39. Note that the fluctuation intensities, $\sqrt{\overline{\omega'^2}}/\bar{u}$, are highest when B_o is lowest, indicating that both y and z-vorticity are present in the grid wake. Accordingly, the $\sqrt{\overline{\omega'^2}}/\bar{u}$ values are lowest when B_o is highest and only z-vorticity is present. It seems rather strange, as already mentioned, that the vorticity decays so quickly in this situation. The intensity of the vortex trails decays to approximately zero at $x/L_o = 5.0$, $x/d_o = 27$.

The most interesting curve in Figure 3.39 is the upper one, since it represents the only part of the study which could be termed "MHD turbulence decay". The interaction parameter of the eddies, N_L, is equal to 70, i.e., $N_L >> 1$. The characteristic suppression time, $(\sigma B_o^2/\rho)^{-1}$, is in this case approximately 0.18 sec. For comparison, the characteristic "eddy turnover time", $L_o/\sqrt{\overline{u_o^2}}$ is about 1.2 sec (where $\sqrt{\overline{u_o^2}} \simeq \sqrt{\overline{\omega'^2}}$ at $x/L_o = 1.3$). Consequently, each eddy newly formed behind the grid may be expected to decay in a time which is much less than the time taken for it to revolve and interact with surrounding eddies. The appropriate data plotted in Figure 3.39 are obviously not varying linearly with time as in the case of the largest B_o. The presence of such large scatter and the small number of data points requires caution in interpreting the results. The results are plotted as $\ln\left(\sqrt{\overline{\omega'^2}}/\bar{u}\right)$ vs time, $t = x/\bar{u}$, in Figure 3.40 and they appear to follow a straight line. Zero time is taken to be at $x/L_o = 1.33$ where $\sqrt{\overline{\omega'^2}}/\bar{u}$ was observed to be greatest. The equation of the line, drawn in by eye is,

$$\frac{\sqrt{\overline{\omega'^2}}}{\bar{u}} = 0.10\, e^{-2.44\, t} = 0.10\, e^{-0.44\left(\frac{\sigma B_o^2}{\rho}\right) t}$$

It is seen therefore that the eddies newly formed behind the grid seem to decay as $e^{-\beta t}$ and that the damping time is indeed $O(\sigma B_o^2/\rho)^{-1}$.

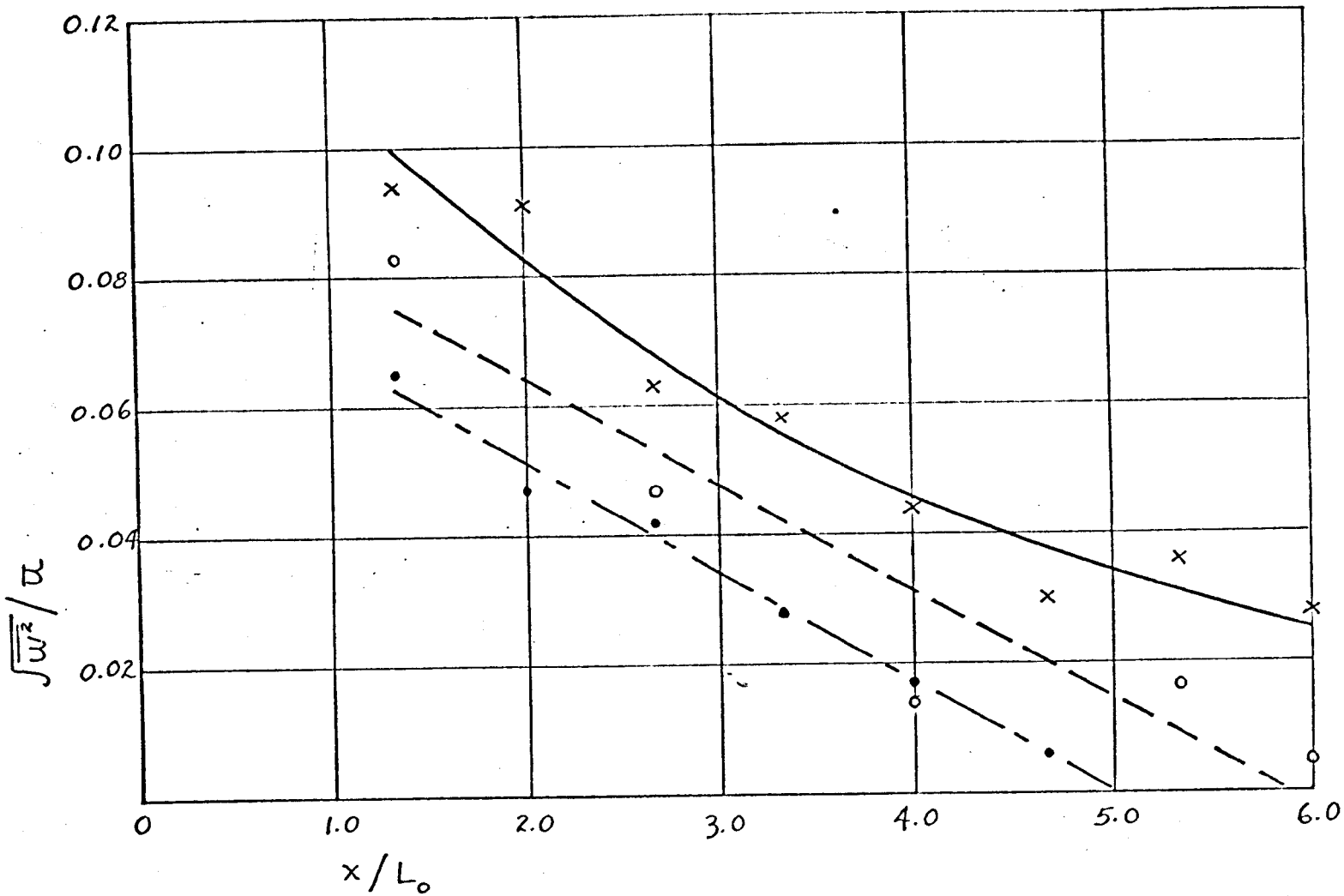

Figure 3.39 Vorticity suppression behind a square-mesh grid of circular cylinders ($\bar{u}$ = 3.2 cm/sec, L_o = 0.38 cm; • ——— –, B_o = 1.22 wb/m^2; ° — —, B_o = 8.50 wb/m^2; × ———, B_o = 0.275 wb/m^2).

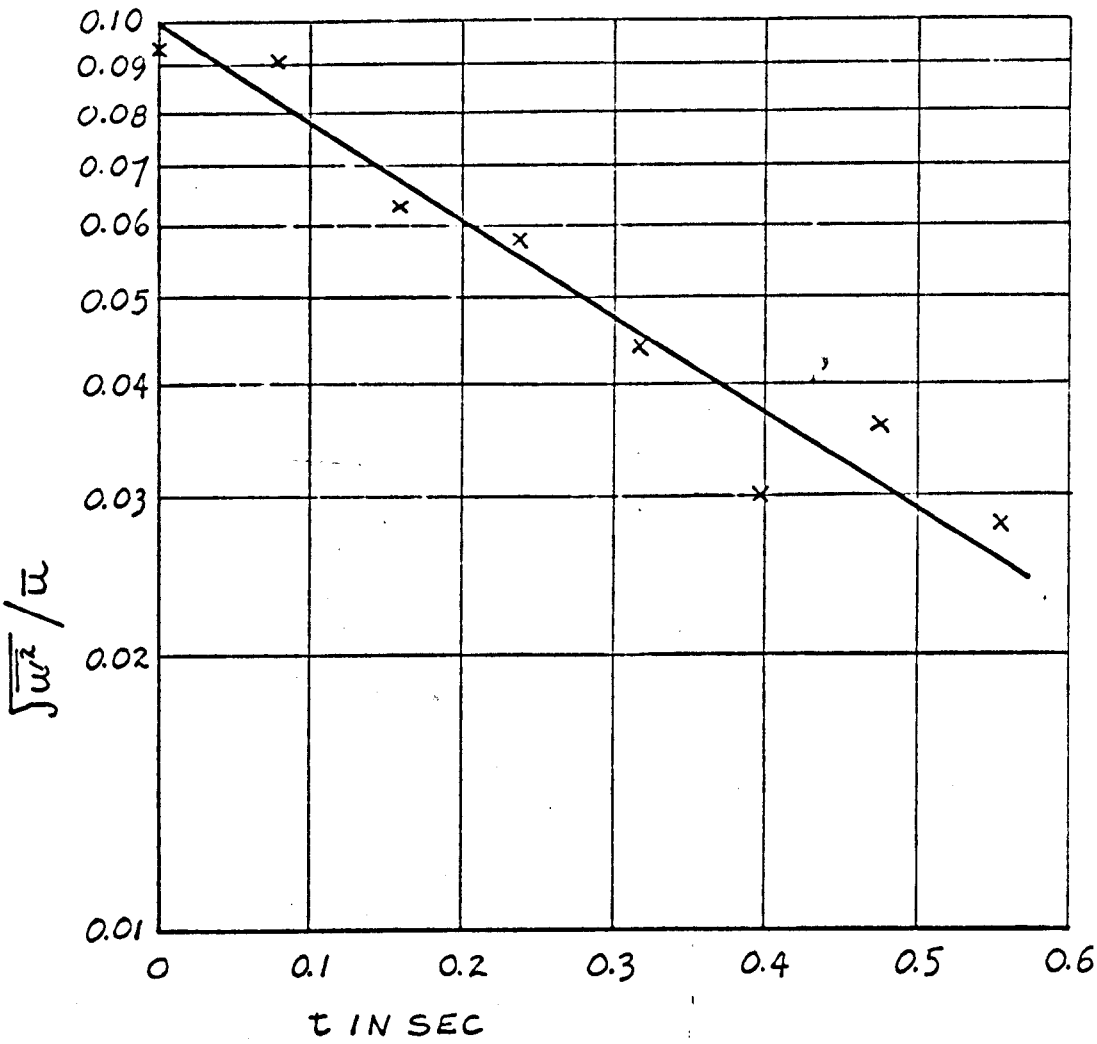

Figure 3.40 Turbulent vorticity suppression behind a square-mesh grid of circular cylinders, N_L = 70, t = 0 at x/L_o = 1.3.

3.3.6 A comparison of local velocity measurement techniques in magnetohydrodynamics

To conclude this chapter the hot-film velocity measuring techniques used in most of the thesis will be compared with the alternative techniques studied by Hunt and Malcolm (1968) using Pitot tubes and e.p. (electric potential) probes. Convenient measures of comparison are dynamic response, spatial resolution, sensitivity and measurement precision and accuracy.

In the area of dynamic response the cylindrical, constant temperature hot-film is unsurpassed, although the upper limit of its response in liquid metals still needs a careful investigation. It would seem that a well designed e.p. probe should also stand out well in this regard. The response of a Pitot tube is practically nil.

The hot-film is certainly capable of the best spatial resolution and, if constructed carefully, introduces the smallest flow blockage effects. The tip of an e.p. probe can be made smaller than that of the Pitot tube which must be sufficiently large to prevent fouling and to keep waiting time between measurements to a reasonable limit.

As far as sensitivity is concerned the hot-film and e.p. probe both stand out well in measurements at low velocities where the pressure across a Pitot-static tube is too low to measure accurately. At higher velocities, however, the Pitot tube comes into its own since the measured pressure difference rises as the square of the velocity. At high velocities the sensitivity of the hot-film decreases, as seen in the calibration curves.

A comparison of the techniques according to relative precision and accuracy is difficult. As far as precision is concerned, little can be concluded because precision in measurement depends to a large extent on the control of the experiment, particularly as regards the design of the apparatus and the care taken by the observer. The hot-film technique in mercury suffers in being somewhat imprecise because of uncontrolled variables, such as thermal contact resistance at the sensor-fluid interface, and because the calibration function, F, is obtained by subtracting two large quantities which are nearly equal.

As far as accuracy is concerned the great problem is to be able to accurately relate a measured variable to its corresponding velocity for all experimental conditions. In MHD flows the Pitot tube and e.p. probe both suffer because of large MHD errors (see Hunt and Malcolm (1968)

and Hunt (1967)). The e.p. probe can seldom be used to measure velocity because the current field surrounding it is generally unknown. It was possible to use it in the case of EDF only because the velocity could be related directly to the electric potential gradient with fair accuracy. The cylindrical hot-film is potentially the most accurate measurement device in MHD for velocities which are high enough for forced convection to completely dominate free convection, if the sensors are aligned with B_o, or for the interaction parameter based on the sensor diameter to be very small, if the sensors are perpendicular to B_o. For low speeds, however, the MHD effects are not well understood and the only way to achieve reasonable accuracy is to calibrate the device over the range of B_o employed. MHD errors persist to much higher velocities when a Pitot tube is used, compared to a cylindrical hot-film, because the interaction parameter is proportional to the much larger probe diameter.

4. CONCLUSION

In the thesis the constant temperature, cylindrical, quartz-insulated, hot-film sensor has proved its worth as a device for obtaining qualitative and quantitative information on the detailed structure of steady and unsteady MHD flows in mercury. In this final chapter recommendations are made which follow from the discussion and conclusions drawn in chapters 2 and 3.

There is much room for further study of the hot-film technique in mercury. Particular areas concern, firstly, the improvement of the measurement sensitivity by improving the wetting at the sensor-fluid interface, secondly, the development of accurate temperature compensation equipment*, thirdly, a better understanding of dynamic response at low speeds in a low Prandtl number fluid such as mercury where the thermal boundary layer is not thin compared to the diameter of the sensor and, finally, a better understanding of MHD measurement errors for various sensor orientations relative to the applied magnetic field. It may be possible to develop a technique for using an X-array sensor in mercury, but the results of Hill (1968) on directional sensitivity of hot-films in mercury give some insight into the great difficulty of this task.

As regards MHD shear layer stability, there are interesting experiments waiting in the area of flows in rectangular ducts which are subjected to inclined, transverse magnetic fields (see Alty (1969)). Other interesting experiments remain to be done in MHD flows in diverging channels and in MHD flows around bodies where peculiar shear layers are also expected to exist (e.g. see Hunt (1967)). The hot-film techniques which have been developed in this thesis should be used to probe these shear layers in steady flow and to examine their stability.

As regards the suppression of MHD turbulence, it may be possible to

---

* Thermo-Systems Inc. provide temperature compensation equipment with which it may be possible to correct for ambient temperature changes as small as 0.1°C if a regulated power supply is used.

sweep a field of isotropic turbulence (created by a square-mesh grid outside a magnetic field, for instance) into a magnetic field and to examine its decay using hot-film techniques. The results of such an experiment could be compared with the theoretical study of Moffatt (1967). The creation of an intense field of turbulence in a flow within a magnetic field using specially designed grids and the examination of its decay would provide another interesting study. The turbulence measurement hot-film technique developed in this thesis should be extended to determine the effects of the magnetic field on the turbulent energy spectrum as well as examining the changes in the overall turbulence intensity.

The field of MHD duct flow turbulence is wide open for the application of hot-film techniques. The results may be compared with the large amount of published literature on the subject. Until now, measurements in turbulent duct flows have been limited to static pressure measurements on the boundaries and the measuring of mean velocity profiles using Pitot tubes. The detailed structure of the turbulence has been left untouched.

REFERENCES

Alfvén, H. and Fälthammar, C.-G. (1963). Cosmical Electrodynamics, second ed., Oxford.

Alty, C.J.N. (1969). Magnetohydrodynamic duct flow, to be published in J.Fluid Mech.

Bankoff, S.G. and Rosler, R.S. (1962). Constant-temperature hot-film anemometer as a tool in liquid turbulence measurements, Rev. Sci. Inst., 33, 11, 1209.

Bellhouse, B.J. and Rasmussen, C.G. (1968). Low-frequency characteristics of hot-film anemometers, DISA Information, 6, 3.

Bellhouse, B.J. and Schultz, D.L. (1967). The determination of fluctuating velocity in air with heated thin film gauges, J.Fluid Mech., 29, 2, 289.

Bevir, M.K. (1969). Ph.D. thesis, to be submitted to the University of Warwick.

Bradshaw, P. and Johnson, R.F. (1963). Turbulence Measurements with Hot Wire Anemometers, N.P.L. Notes on Applied Science, No.33, H.M.S.O., London.

Branover, G.G., Slyusarev, N.M. and Shcherbinin, E.V. (1965). Some results of measurements of turbulent velocity pulsations in a mercury flow in the presence of a transverse magnetic field, Magnetohydrodynamics, 1, 1, 23.

Chapman, A.J. (1967). Heat Transfer, second ed., Macmillan.

Cole, J. and Roshko, A. (1954). Heat transfer from wires at Reynolds numbers in the Oseen range, Heat Transfer and Fluid Mechanics Institute, University of California, Berkeley, 13.

Davies, P.O.A.L. and Fisher, M.J. (1964). Heat transfer from electrically heated cylinders, Proc. Roy. Soc., A, 280, 486.

Fraim, F.W.(1966). D.Sc. thesis, Mass. Inst. Tech., Cambridge, Mass.

Fraim, F.W. and Heiser, W.H. (1968). The effect of a strong longitudinal magnetic field on the flow of mercury in a circular tube, to be published in J.Fluid Mech.

Freymuth, P. (1967). Feedback control theory for constant-temperature hot-wire anemometers, Rev. Sci. Inst., 38, 5, 677.

Grant, H.P. and Kronauer, R.E. (1962). Fundamentals of hot wire anemometry, Symposium on Unsteady Flow, A.S.M.E., 44.

Grant, H.L. and Nisbet, I.C.T. (1957). The inhomogeneity of grid turbulence, J.Fluid Mech., 2, 263.

Grosh, R.J. and Cess, R.D. (1958). Heat transfer to fluids with low Prandtl numbers for flow across plates and cylinders of various cross section, Trans. A.S.M.E., 80, 667.

Hasimoto, H. (1960). Steady longitudinal motion of a cylinder in a conducting fluid, J.Fluid Mech., 8, 61.

Hewlett-Packard (1966). Operating and service manual, Model 3400A rms voltmeter.

Hewlett-Packard (1967). Operating and service manual modifications, Spec. H12-3400A rms voltmeter.

Hide, R. and Titman, C.W. (1967). Detached shear layers in a rotating fluid, J.Fluid Mech., 29, 1, 39.

Hill, J.C. (1968). The Directional Sensitivity of a Hot-Film Anemometer in Mercury, Ph.D. thesis, University of Washington, Seattle, Wash.

Hinze, J.O. (1959). Turbulence, McGraw-Hill.

Hoff, M. (1968). Private communication.

Holman, J.P. (1968). Heat Transfer, second ed., McGraw-Hill.

Hunt, J.C.R. (1965). Magnetohydrodynamic flow in rectangular ducts, J.Fluid Mech., 21, 4, 577.

Hunt, J.C.R. (1966). On the stability of parallel flows with parallel magnetic fields, Proc. Roy. Soc., A, 293, 342.

Hunt, J.C.R. (1967). Some Aspects of Magnetohydrodynamics, Ph.D. thesis, University of Cambridge.

Hunt, J.C.R. and Maclolm, D.G. (1968). Some electrically driven flows in magnetohydrodynamics. Part 2. Theory and experiment, accepted for publication in J.Fluid Mech.

Hunt, J.C.R. and Stewartson, K. (1969). Some electrically driven flows in magnetohydrodynamics. Part 3. The asymptotic theory for flow between circular electrodes, to be published.

Hunt, J.C.R. and Williams, W.E. (1968). Some electrically driven flows in magnetohydrodynamics. Part 1. Theory, J.Fluid Mech., 31, 4, 705.

Kalis, Kh.E., Tsinober, A.B., Shtern, A.G. and Shcherbinin, E.V. (1965). Flow of a conducting fluid past a circular cylinder in a transverse magnetic field, Magnetohydrodynamics, 1, 1, 11.

Klebanoff, P.S., Tidstrom, K.D. and Sargent, L.M. (1962). The three-dimensional nature of boundary-layer instability, J.Fluid Mech., 12, 1, 1.

Kovásznay, L.S.G. (1965). The hot-wire anemometer, Acta Tech. Hung., 50, 131.

Lehnert, B. (1956). An instability of laminar flow of mercury caused by an external magnetic field, Proc. Roy. Soc., A, 233, 299.

Leibovich, S. (1967). Magnetohydrodynamic flow at a rear stagnation point, J.Fluid Mech., 29, 2, 401.

Lielpéteris, J.J. (1960). Electromagnetic and Hydrodynamic Processes in the Channel of the Induction Pump, Thesis, Moscow Power Institute.

Lighthill, M.J. (1954). The response of laminar skin friction and heat transfer to fluctuations in the stream velocity, Proc. Roy. Soc., A, 224, 1.

Lin, C.C. (1966). The Theory of Hydordynamic Stability, Cambridge University Press.

Lindgren, E.R. and Chao, J.-L. (1967). Application of the hot-film technique on flow of high-polymer solutions, Phys. of Fluids, 10, 3, 667.

Ling, S.C. (1955). Measurement of Flow Characteristics by the Hot-Film Technique, Ph.D. thesis, University of Iowa, Ames, Iowa.

Ling, S.C. (1960). Heat-transfer characteristics of hot-film sensing element used in flow measurement, Trans. A.S.M.E., J.Basic Eng., D82, 629.

Ling, S.C. and Hubbard, P.G. (1956). The hot-film anemometer, J.Aero. Sci., 23, 890.

Ludford, G.S.S. and Singh, M.P. (1964). The hydromagnetics of an ellipsoid moving in a cross-field, Proc. Camb. Phil. Soc., 60, 341.

Lumley, J.L. (1962). The constant temperature hot-thermistor anemometer, Symposium on Unsteady Flow, A.S.M.E., 75.

Malcolm, D.G. (1968a). Some aspects of turbulence measurement in liquid mercury using cylindrical quartz-insulated hot-film sensors, submitted for publication to J.Fluid Mech.

Malcolm, D.G. (1968b). Unsteady magnetohydrodynamic flow measurement in liquid metals using thermo-anemometry with applications of insulated platinum films in mercury, Sixth Symposium on Magnetohydrodynamics, Inst. of Phys., Acad. of Sci., Riga, Latv. S.S.R., Sept.3-6, (eventually to appear in Magn. Gidro.).

Malcolm, D.G. (1969). An experimental investigation of the stability of a magnetohydrodynamic shear layer, to be published.

Moffatt, H.K. (1964). Electrically driven steady flows in magnetohydrodynamics, Proc. 11th Int. Cong. Appl. Mech., Munich, 946.

Moffatt, H.K. (1967). On the suppression of turbulence by a uniform magnetic field, J.Fluid Mech., 28, 3, 571.

Moreau, R. (1967). Contribution à l'Étude des Écoulements Hydromagnetiques, D.Sc. thesis, University of Grenoble.

Rasmussen, C.G. (1966). Measurement of turbulence characteristics, DISA Information, 3, 9.

Sajben, M. (1964). Hot Wire Measurements in a Liquid Mercury Jet Subject to an Axial Magnetic Field, D.Sc. thesis, Mass. Inst. Tech., Cambridge, Mass.

Sajben, M. (1965). Hot wire anemometer in liquid mercury, Rev. Sci. Inst., 36, 7, 945.

Sajben, M. and Fay, J.A. (1967). Measurement of the growth of a turbulent mercury jet in a coaxial magnetic field, J.Fluid Mech., 27, 1, 81.

Shercliff, J.A. (1965). A Textbook of Magnetohydrodynamics. Pergamon.

Squire, H.B. (1933). On the stability for three-dimensional disturbances of viscous fluid flow between parallel walls, Proc. Roy. Soc., A, 142, 621.

Strickland, W.T., Jr. and Davis, S.H., Jr. (1966). Transient response of the fluid surrounding a hot wire, I & EC Fundamentals, 5, 1, 38.

Thermo-Systems Inc. (1966). Heat Flux System Model 1010 Instruction Manual, Thermo-Systems Inc., St.Paul, Minnesota.

Uberoi, M.S. and Wallis, S. (1967). Effect of grid geometry on turbulence decay, Phys. of Fluids, 10, 6, 1216.

Wieghardt, K. and Kux, J. (1967). Experimental Methods in Wind Tunnels and Water Tunnels, with Special Emphasis on the Hot-Wire Anemometer, N.A.T.O., AGARD Report 558.

Wooler, P.T. (1961). Instability of flow between parallel planes with a coplanar magnetic field, Phys. of Fluids, 4, 1, 24.

"It is a difficult and never ending road upon which man proceeds in his quest for further and further pieces of knowledge, from which he combines the mosaic called an image of the universe."

Milan Marvan.

Appendix A. Publications

A.1 Some electrically driven flows in magnetohydrodynamics. Part 2. Theory and experiment

by J.C.R. Hunt
and D.G. Malcolm
- to appear in J. Fluid Mech., 1968.

Some electrically driven flows in magnetohydrodynamics Part 2. Theory and experiment

By J. C. R. HUNT

Central Electricity Research Laboratories, Leatherhead, Surrey

AND D. G. MALCOLM

School of Engineering Science, University of Warwick

(Received 4 July 1967 and in revised form 10 January 1968)

In this part we first extend the theory of part 1 to analyse the distribution of velocity and electric current in an electrically conducting liquid between two circular electrodes of finite diameter, when a current is passed between them. The electrodes are set opposite to each other in insulating planes and a magnetic field is applied perpendicular to these planes. When the Hartmann number $M \gg 1$ we find that the current is confined to the cylinder of fluid joining the electrodes. This effect is accounted for by the velocity which is induced in thin layers of thickness $O(M^{-\frac{1}{2}})$, at the circumference of the cylinder. In our analysis we concentrate on these interesting layers and, amongst other results, we find that in the limit $M \to \infty$ the resistance of the fluid between the electrodes becomes that of the cylinder of fluid joining the electrodes.

We then describe some experiments to test the validity of this theory. In these experiments we measured, as a function of the magnetic field, (*a*) the potential difference between the copper electrodes, the fluid being mercury, (*b*) the electric potential distribution in the fluid between the disks and in the thin layers between the electrode edges, by means of an *electric potential probe*, and (*c*) the velocities induced in the layers using a *Pitot tube*. Our conclusions were: (i) the overall predictions of the theory were correct; (ii) the results of the two probes approximately correlated with each other; despite the theory still having some limitations and the behaviour of these probes still being somewhat uncertain.

1. Introduction

Part 1 of this paper (Hunt & Williams 1968) was an analysis of the flows induced in an electrically conducting fluid by passing current between electrodes placed in non-conducting planes surrounding the fluid, a magnetic field being applied perpendicular to the planes. The analysis was largely concentrated on the interesting physical phenomena which occur when the Hartmann number $M = B_0 a(\sigma/\eta)^{\frac{1}{2}} \gg 1$. ($B_0$ is the applied magnetic flux density, a is a typical length, σ is the fluid's conductivity and η is its viscosity.) The solutions to the problems analysed in part 1 demonstrated some of the basic physical effects very clearly and were simple mathematically. However, to contrive those situations

experimentally proves very difficult, particularly those involving point or line electrodes.

In part 2 we examine the effects of passing an electric current between circular electrodes of finite diameter under the action of a magnetic field, B_0. The geometry of the situation is depicted in figure 1*a*; in this figure is also sketched the pattern of electric current streamlines when $|\mathbf{B}_0| = 0$, the characteristic feature being the spreading of these streamlines. When a magnetic field is applied in the z direction, i.e. parallel to the direction of current, the $j \times B$ force has, for $z > 0$, a positive component, $(-j_r B_z)$, in the θ or azimuthal direction. A velocity v_θ results, which in turn leads to a reduction in $|j_r|$ because of the induced electric field, $\mathbf{v} \times \mathbf{B}$, being opposed to the original applied electric field. Ultimately a steady flow is created in which the viscous forces, $O(\eta v_\theta/\delta^2)$, are balanced by the $\mathbf{j} \times \mathbf{B}$ forces, $-j_r B_z = O(\delta j_0 B_0/a)$, where δ is the thickness of the layers emanating from the edges. From the curl of Ohm's law, since $\delta \ll a$, $v_\theta = O(j_0 a/\sigma \delta B_0)$, where j_0 is the value of j_z near $r = 0$. Then it follows that $\delta = O(aM^{-\frac{1}{2}})$ and a layer must exist joining the edges of the electrodes through which the electric potential, ϕ, falls and a velocity is induced as shown in figure 1*b*. This effect was first fully appreciated by Moffatt (1964).

In §2 we analyse such a situation, assuming (*a*) that the electrodes are highly conducting relative to the fluid, (*b*) that $M \gg 1$, (*c*) that the fluid is uniform and incompressible, and (*d*) that the radius of the electrodes b is very much greater than δ, the thickness of the layers between the electrode edges, i.e. $b \gg aM^{-\frac{1}{2}}$. From this highly approximate analysis we obtain some quantitative results and provide a theoretical basis for explaining the results of the experiments. In a forthcoming paper Hunt & Stewartson (1968) deduce a more rigorous asymptotic solution to this problem.

We then describe experiments in which we investigated the effects of a magnetic field on (*a*) the potential difference between the electrodes (copper), (*b*) the potential distribution in the fluid (mercury) between the disks and in the layers between the electrode edges, by means of an electric potential probe, and (*c*) the velocities induced in the layers, using a Pitot tube. These experiments were unlike most MHD experiments in that measurements were made *in* the fluid, as well as at its confining walls. Furthermore, although velocities have recently been measured in MHD flows with Pitot tubes, e.g. Branover & Lielausis (1962) and Moreau (1966), there have been no previous attempts to use Pitot tubes with electric potential probes, to correlate their results, and to compare these results with theory. These experiments are also interesting in that the probe measurements provide a rough check on the theory of MHD probes developed by Hunt (1967).

In §3 the experimental apparatus is described briefly, a more detailed description of the probes and the mechanism for moving the probe being given in appendix A. An outline of the measurement theory of MHD probes is also given there. In §4 the results of the measurements and their interpretation are given and in §5 the main conclusions from the theory and the experiments are presented.

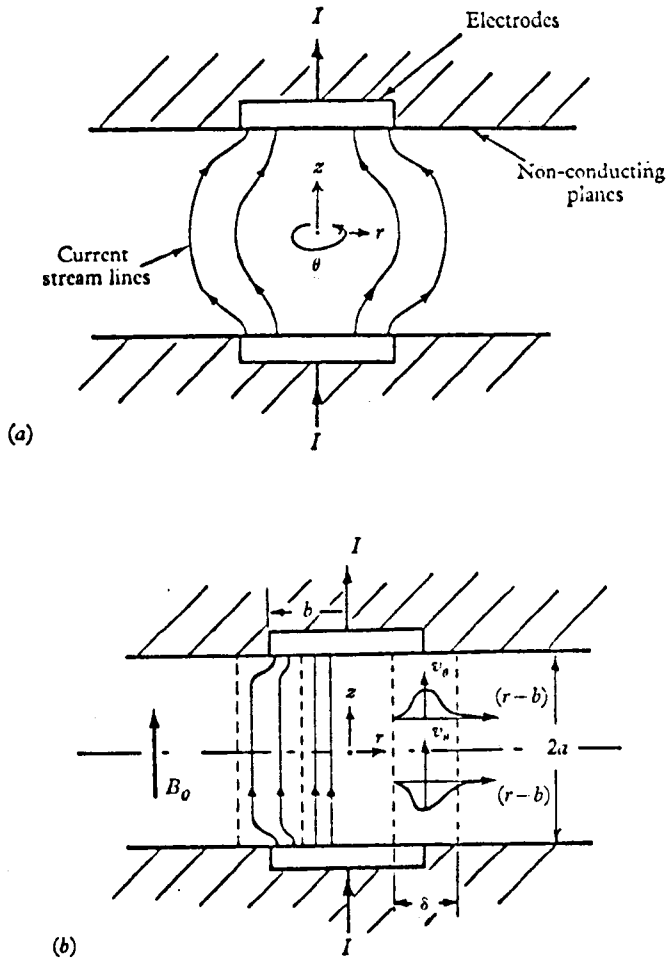

FIGURE 1. Electrically driven flow between circular electrodes. (*a*) Current streamlines when $M = 0$. (*b*) Current streamlines and velocity profiles when $M \gg 1$.

2. Asymptotic analysis of the flow between aligned circular electrodes when $M \gg 1$

In this section we analyse the flow induced by passing a current between two electrically conducting disks (the electrodes) placed opposite each other in non-conducting planes, their surfaces being flush with these planes. A uniform magnetic field of flux density B_0 is applied perpendicular to the planes. (See figure 2.) In our analysis we assume: (i) an incompressible, laminar flow with uniform fluid properties; (ii) a flow in which radial and axial velocities may be ignored (in appendix B we show by theoretical arguments and experimental results that this condition requires $|B_0|$ to be sufficiently great and the azimuthal velocity, v_θ, sufficiently small); (iii) the boundary conditions and the flow to be axially symmetric; (iv) that $|B_0|$ is great enough to satisfy the conditions that (*a*) $M^{\frac{1}{2}} \gg 1$,

and (*b*) $Ml \gg 1$, where $l = b/a$ is the ratio of the diameter of the electrodes to the distance between them; (v) the electrodes are perfectly conducting.

The first three of these assumptions were made in part 1 of this paper, where

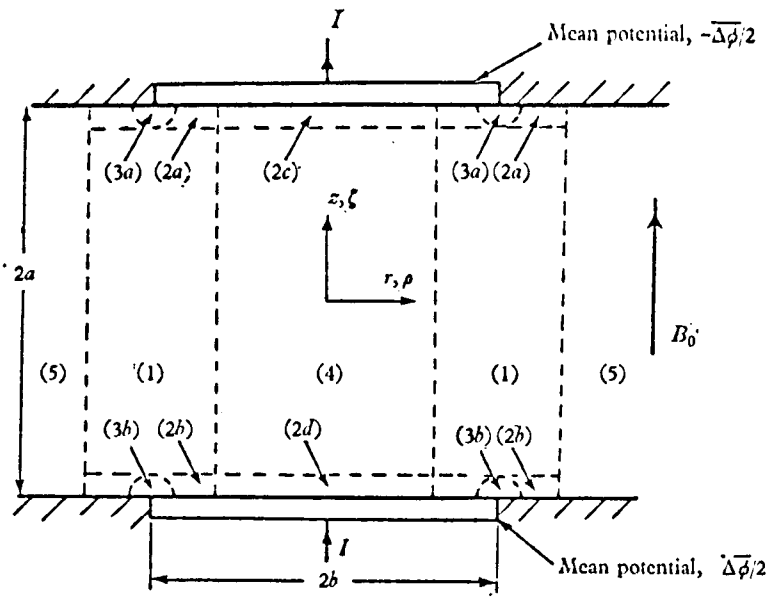

FIGURE 2. Circular electrodes with various regions for asymptotic analysis.

we showed that the relevant equations of MHD in cylindrical co-ordinates may be written in the non-dimensional form

$$0 = M\frac{\partial h}{\partial \zeta} + D_\rho(\rho v) + \frac{\partial^2 v}{\partial \zeta^2}, \tag{2.1}$$

$$0 = M\frac{\partial v}{\partial \zeta} + D_\rho(\rho h) + \frac{\partial^2 h}{\partial \zeta^2}, \tag{2.2}$$

where $$D_\rho = \frac{\partial}{\partial \rho}\left(\frac{1}{\rho}\frac{\partial}{\partial \rho}\right)$$

and $$v = \frac{v_\theta}{I/(2\pi a\sqrt{[\sigma\eta]})}, \quad h = \frac{H_\theta}{I/(2\pi a)}, \quad \rho = r/a, \quad \zeta = z/a,$$

$M = B_0 a(\sigma/\eta)^{\frac{1}{2}}$; I is the total current entering and leaving the electrodes and a is the half distance between them. If we express the electric potential ϕ as the non-dimensional parameter Φ, then $\Phi = \phi/(I/2\pi a\sigma)$ and

$$\partial\Phi/\partial\rho = \partial h/\partial\zeta + Mv, \tag{2.3a}$$

$$\partial\Phi/\partial\zeta = -(\partial h/\partial\rho + h/\rho). \tag{2.3b}$$

We take the potential of the two electrodes as $(-\Delta\phi)/2$ and $\Delta\phi/2$ at $\zeta = \pm 1$, respectively.

As in part 1 we shall be using the composite variable $(v+h)$ for which the governing equation is

$$\frac{M}{\rho}\frac{\partial}{\partial\zeta}(\rho(v+h))+\left(\frac{1}{\rho}\frac{\partial^2}{\partial\zeta^2}+D_\rho\right)(\rho(v+h)=0. \tag{2.4}$$

Boundary conditions. On the electrodes and the non-conducting walls at $\zeta=\pm1$, the first boundary condition is, of course,

$$\mathrm{v}=0. \tag{2.5}$$

The boundary condition on h at the non-conducting walls ($\rho>l$) is such that $j_z=0$, whence

$$\text{for}\quad \rho>l,\quad h=(1/\rho)\quad\text{at}\quad \zeta=\pm1. \tag{2.6}$$

On the surface of the perfectly conducting electrodes at $\zeta=\pm1$,

$$\text{for}\quad \rho<l,\quad \partial\Phi/\partial\rho=\partial h/\partial\zeta=0. \tag{2.7}$$

If $h=f(\rho)$ on the electrodes we can calculate the value of $f(\rho)$ when $\rho=l$:

$$I=\int_0^b 2\pi r\frac{1}{r}\frac{\partial}{\partial r}(rH_\theta)_{\zeta=\pm1}dr=\frac{Ib}{a}(f(l)-f(0)).$$

If we assume $f(0)=0$, then

$$f(l)=h(l,\zeta=\pm1)=1/l. \tag{2.8}$$

As in part 1, when $M\gg1$ we divide the space between the boundaries into different regions, as labelled in figure 2, and then analyse these regions in turn.

Region 4. In this region, lying between the electrodes, $\partial/\partial\rho\simeq l^{-1}$ and $\partial/\partial\zeta\simeq1$, whence as $M\to\infty$ (2.4) becomes

$$M\frac{\partial}{\partial\zeta}(v+h)=0. \tag{2.9}$$

Then since v is antisymmetric

$$v=\partial h/\partial\zeta=\partial\Phi/\partial\rho=0.$$

Thence it follows, since the potential is constant on the electrodes, that in region (4)

$$h=\lambda\rho/l^2\quad\text{and}\quad\Phi=-2\lambda\zeta/l^2, \tag{2.10}$$

where λ is a constant; as it turns out λ is a function of M.

Region 5. In this region, which extends outwards from the edge of the electrodes, the solutions for v and h which satisfy (2.1) and (2.2) and the boundary conditions at $\zeta=\pm1$, namely (2.5) and (2.6), are:

$$v=0,\quad h=1/\rho. \tag{2.11}$$

Matching regions. Now, although the values of h and v for regions (4) and (5) are continuous at $\rho=l$, their derivatives with respect to ρ are not. Therefore the higher derivatives with respect to ρ which were ignored in calculating $(v+h)$ in region (4) become singular and a matching layer must exist. We expect this layer to be of the same form as that analysed in part 1. Therefore we can assume that

the thickness of this layer is $O(M^{-\frac{1}{2}})$ and that, since in this case the current density on the electrode is not specified in regions (2*a*) and (2*b*), we can assume

$$v+h=f(\rho)=\frac{1}{\rho}+\frac{g(\bar{\rho})}{l^2M^{\frac{1}{2}}} \quad \text{at} \quad \zeta=\pm 1, \tag{2.12}$$

where $\bar{\rho}=(\rho-l)M^{\frac{1}{2}}$ and $g(\bar{\rho})$ satisfies the condition

$$g(\bar{\rho})=0 \quad \text{for} \quad \bar{\rho}>0. \tag{2.13a}$$

In order that regions (1) and (4) should match, $g(\bar{\rho})$ also satisfies the condition

$$g(\bar{\rho})\to 2\bar{\rho}+\bar{\lambda} \quad \text{as} \quad \bar{\rho}\to-\infty, \tag{2.13b}$$

on making the assumption that

$$\lambda=1+\bar{\lambda}/lM^{\frac{1}{2}}. \tag{2.14}$$

Using the same notation and the same approximations as in part 1 for the regions (1), (2) and (3), we find that in region (2*a*), where $1-\zeta\sim O(M^{-1})$,

$$(v+h)_{(2a)}=f(\rho),$$

and in region (1), where $\bar{\rho}\sim O(1)$ and $\zeta\sim O(1)$,

$$(v+h)_{(1)}=\frac{1}{\rho}+\frac{1}{2l^2M^{\frac{1}{2}}[\pi(1-\zeta)]^{\frac{1}{2}}}\int_0^\infty g(t)\exp\left(-(t-\bar{\rho})^2/4(1-\zeta)\right)dt. \tag{2.15}$$

In region (2*b*), the other Hartmann-type boundary layer, for

$$\left.\begin{aligned}
&\bar{\rho}<0, \quad (v+h)_{(2b)}=\frac{1}{\rho}+\frac{g(\bar{\rho})}{l^2M^{\frac{1}{2}}}e^{-M(1+\zeta)}+\left((v+h)_{(1)}-\frac{1}{\rho}\right)(1-e^{-M(1+\zeta)}),\\
&\bar{\rho}>0, \quad (v+h)_{(2b)}=\frac{1}{\rho}+\left((v+h)_{(1)}-\frac{1}{\rho}\right)(1-e^{-M(1+\zeta)}).
\end{aligned}\right\} \tag{2.16}$$

We can obtain some useful information from these very incomplete solutions. First, we can show that, if $f(\rho)$ is a function $\bar{\rho}$ near $\rho=l$, then in region (1) the distribution of Φ, for a given value of ζ, is *similar* for all values of $M\gg 1$. We first calculate v in region (1), using the fact that v is antisymmetric in ζ:

$$v_{(1)}=\frac{1}{4l^2M^{\frac{1}{2}}\sqrt{\pi}}\left\{\int_0^\infty \frac{g(t)\exp\left(-(t-\bar{\rho})^2/4(1-\zeta)\right)dt}{(1-\zeta)^{\frac{1}{2}}} - \int_0^\infty \frac{g(t)\exp\left(-(t-\bar{\rho})^2/4(1+\zeta)\right)dt}{(1+\zeta)^{\frac{1}{2}}}\right\}.$$

Thus we see that in region (1) $v=O(M^{-\frac{1}{2}})$. Also, since $\partial h/\partial\zeta=O(M^{-\frac{1}{2}})$ and $Mv=O(M^{\frac{1}{2}})$, it follows that

$$\frac{\partial\Phi}{\partial\rho}=Mv, \tag{2.17}$$

a result peculiar to shear layers like these, which was first noted by Moffatt

(1964). Thence, since $\Phi = 0$ when $\bar{\rho} \to \infty$,

$$\Phi = -\int_{\bar{\rho}}^{\infty} (M^{\frac{1}{2}} v)\, d\bar{\rho}, \tag{2.18}$$

and therefore, in our experiments, if we measure Φ as a function $\bar{\rho}$ at a given value of ζ, we should expect the results to be independent of M.

The second result we can deduce from our approximate analysis is the resistance, R, of the fluid between the electrodes, as $M \to \infty$. Since this result is not dependent on the electrodes being perfectly conducting we define R as

$$R = \overline{\Delta\phi}/I, \tag{2.19}$$

where

$$\overline{\Delta\phi} = -\frac{1}{\pi b^2}\int_0^b \left[\phi(r)\right]_{-a}^{+a} 2\pi r\, dr$$

is the mean value of the potential difference between the disks. From this definition and (2.3) we have

$$R = \frac{2}{\pi\sigma b}\int_{-1}^{+1} (h)_{\rho=l}\, d\zeta. \tag{2.20}$$

Now it follows from our solution (2.15) and the boundary conditions placed on $g(\bar{\rho})$ that

$$\lim_{M\to\infty} (v+h)_1 = \frac{1}{l}, \quad \text{when} \quad \rho = l.$$

Since $(v+h) = O(v+h)_1$ in regions (2) and (3),

$$\int_{-1}^{+1} (v+h)_{\rho=l}\, d\zeta = \int_{-1}^{+1} (v+h)_1\, d\zeta + O(M^{-1}), \tag{2.21}$$

and therefore, since v is antisymmetric in ζ, using (2.18),

$$\lim_{M\to\infty} R = R_\infty = \frac{2a}{\pi\sigma b^2}. \tag{2.22}$$

This result does not depend on the function $g(\bar{\rho})$; it depends only on the fact that $g(\bar{\rho}) = 0$ at $\rho = l$. From (2.15) and (2.21), we might expect the next approximation in M, as $M \to \infty$, to be

$$R = R_\infty\left(1 - \frac{k}{lM^{\frac{1}{2}}}\right), \tag{2.23}$$

where k is some constant. Clearly, if the electrodes are highly conducting, $\overline{\Delta\phi} = \Delta\phi$, and it follows then that $\bar{\lambda} = -k$, and that in regions (4), as $M \to \infty$,

$$\frac{\phi/I}{a/\pi\sigma b^2} = \frac{\Phi}{2/l^2} = -\tfrac{1}{2}(1 - k/lM^{\frac{1}{2}}). \tag{2.24}$$

The physical reason for the dependence of R on $(lM^{\frac{1}{2}})^{-1}$ is that since the thickness of the region (1) is always $O(M^{-\frac{1}{2}})$ the current density in the z direction, for a given value of I, is less by $O(lM^{\frac{1}{2}})^{-1}$ than if there were no 'bulging' of the current lines at all (i.e. the limiting case). This implies that $\partial\phi/\partial z$ and consequently the resistance are also reduced by $O(lM^{\frac{1}{2}})^{-1}$.

3. The experimental apparatus

Our experiments on electrically driven flows using mercury as the conducting fluid were performed in a rectangular duct which had originally been constructed as a prototype for a much larger duct, described by Hunt (1967), and which was then modified for examining electrically driven flows (see figure 3). For the first set of experiments two Perspex blocks, $\frac{1}{2}$ in. thick, were made with copper disks $\frac{3}{4}$ in. in diameter ($=2b$) and $\frac{1}{4}$ in. thick ($=t$) let into them, the surfaces

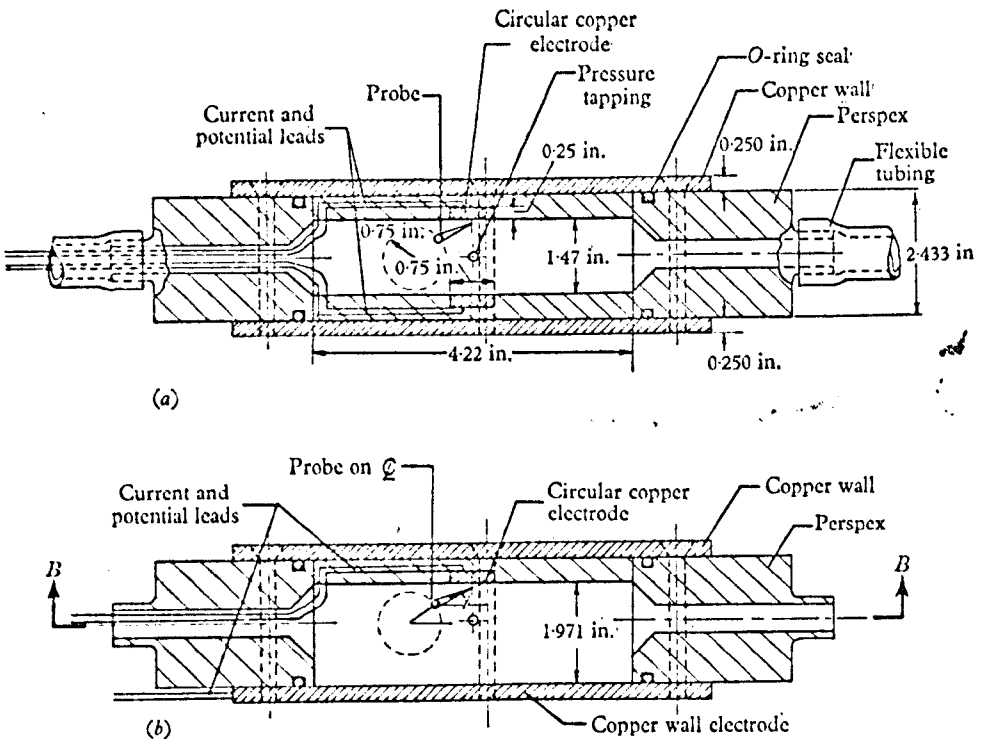

FIGURE 3. Apparatus for examining electrically driven flows. (*a*) Section of the first apparatus. (*b*) Section of the second apparatus. (*c*) Section *BB* through both.

of the copper disks being flush with those of the Perspex blocks (figure 3(*a*)). The blocks were placed either side of the duct with a gap of 1·47 in. ($=2a$) between them, so that $l = b/a = 0{\cdot}512$. (The copper side walls of the duct were isolated from its interior by rubber sheets to avoid any short circuits.) Each disk had two wires connected to it, one to supply the current and the other to measure the electrical potential of the disk. A fifth wire was placed in one of the tubes leading out of the duct, its purpose being to measure the potential far away from the electrodes.

We found that, with this first apparatus, the layers emanating from the disk edges were not sufficiently thick compared to the width of the probe. Also, since we were interested in examining the flow at a different value of l, we performed a

second set of experiments in which one of the Perspex blocks and the insulation on one of the duct's copper side walls were removed so that we were effectively examining only one half of the space between two disks. The distance from the disk to the copper face was 1·97 in. ($=a$), and thus $l = b/a = 0{\cdot}190$, as shown in figure 3*b*. In this case we attached two wires to the plate to measure potential and transmit the current.

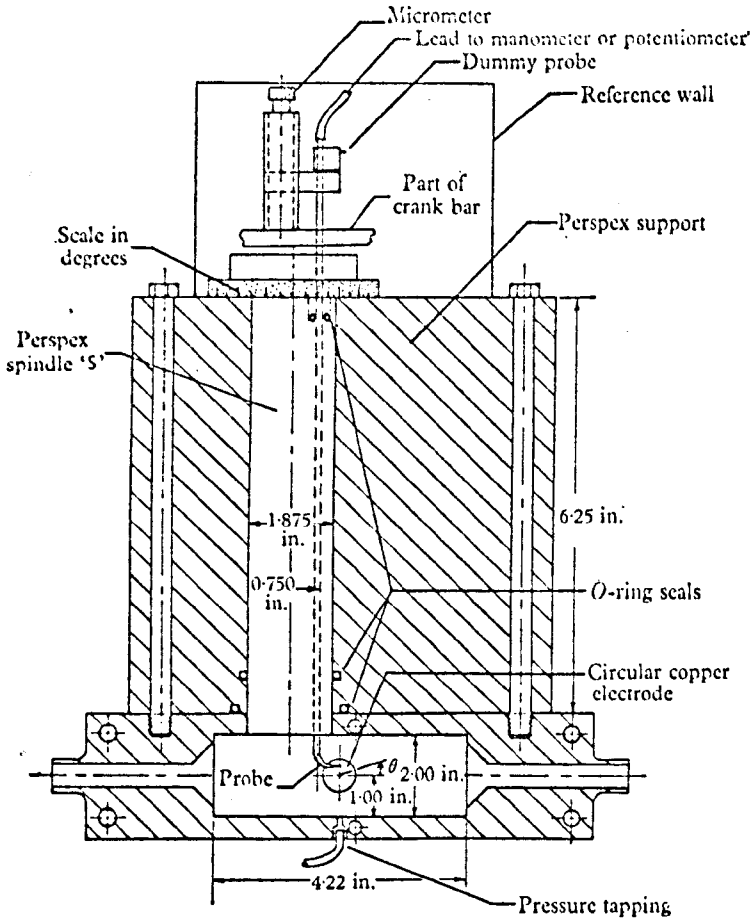

FIGURE 3(*c*). For legend see facing page.

With the duct placed in the electro-magnet in the first apparatus the maximum value of the Hartmann number, M, based on a was about 600 and in the second about 1600. In order that the flows developed were similar to those described in the asymptotic theory of § 2, two conditions had to be satisfied by the apparatus. The first was that any error in alignment of the two disks had to be very much less than the thickness of the regions (1); i.e. the layers emanating from the disk edges, which are $O(aM^{-\frac{1}{2}})$, $= O(0{\cdot}030$ in.). We can confidently say this condition was satisfied by the two disks; with the one disk of the second apparatus this condition did not apply. The second condition was that the thickness of region (1)

should be very much less than the radius of the electrodes, which required that

$$b \gg aM^{-\frac{1}{2}} \quad \text{or} \quad lM^{\frac{1}{2}} \gg 1.$$

The maximum values of $lM^{\frac{1}{2}}$ attainable in the two apparatus were 13 and 7·7 respectively, which shows that the first apparatus met the conditions of the theory better than the second. (We did not use larger electrodes for fear of the regions (1) touching the top and bottom walls of the duct.) We also note that, if σ_e is the conductivity of the electrodes and t is their thickness, $\sigma a/\sigma_e t$, the relative conductance of the fluid to the electrodes (~~where t is the electrode thickness~~), is 0·049 and 0·132 in the two cases.

The object of the experiment was first to measure (by means of a Pye potentiometer) the potential difference between the electrodes when a steady current (measured by an ammeter) was passed between them, as the magnetic field (evaluated from a calibration curve using the measured current in the magnet coils) was varied. The second object was to examine the distribution of the electric potential between the electrodes, which was achieved by the insertion of an

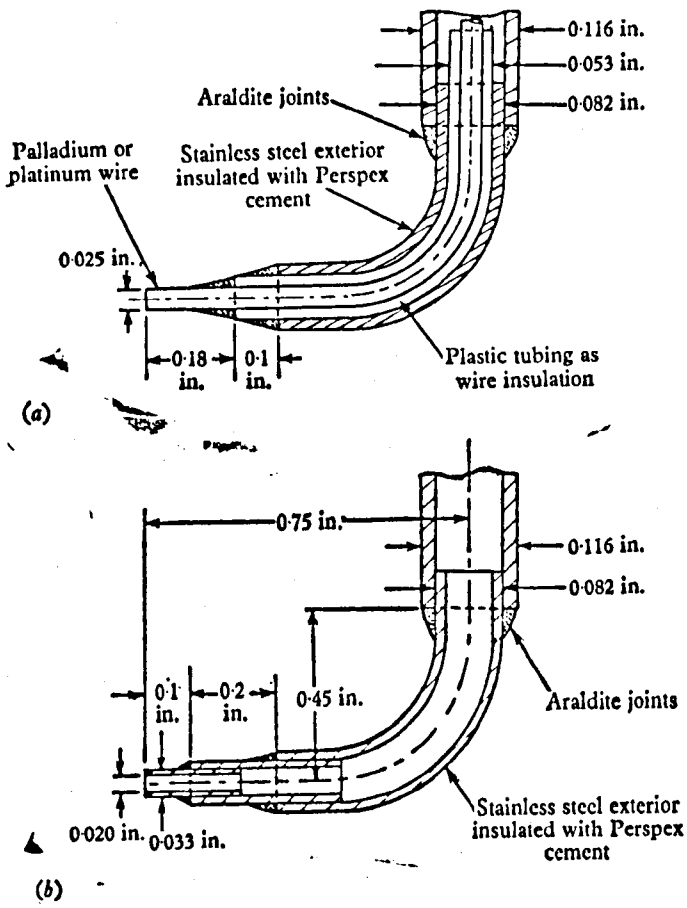

FIGURE 4. Sections through the experimental probes. (*a*) Electric potential probe. (*b*) Pitot tube.

electric potential probe, shown in figure 4*a*, into the fluid and by measuring the difference between the tip of the probe and one of the electrodes, as the probe was moved. The third aim was to examine the velocity in the shear layers existing between the rims of the electrodes by means of measuring the difference in pressure between that at the tip of a Pitot tube, shown in figure 4*b*, and the pressure tapping at the wall, shown in figure 3*c*.

In appendix A these two probes are described along with the mechanism for moving them across the duct.

4. Experimental results

4.1. *Electric potential measurements*

In the first part of the experiment we measured the mean potential difference between the disks, $\overline{\Delta\phi}$, and the difference in electrical potential, ϕ, between the probe and the plane $z = 0$, both as a function of I and M. (In the second apparatus we have calculated $\overline{\Delta\phi}$ by doubling the potential between the electrode and the wall.) In the first instance we wanted to see whether $\overline{\Delta\phi}$ and ϕ were proportional to I at a given value of M, at least for sufficiently small values of I, since all the theory of §2 was based on this assumption. The experimental results shown in figures 5 and 6 show this condition to be well satisfied. These figures also give us some understanding of how the magnetic field affects secondary flows, but this discussion is relegated to appendix B. An important practical point to note in figures 5 and 6 is that the values of $\overline{\Delta\phi}$ and ϕ in the linear regime were always below 100 μV and often below 10 μV. Since the potentiometer only measured to 1 μV and other errors, caused by fluctuations in the magnetic field, temperature effects, etc., were at least of the order of 1 μV, it follows that the errors to be expected were as much as 10 % in some places.

Having found the values of I below which it was necessary to operate to avoid the non-linear flow regime, we then measured the variation of $R, = \overline{\Delta\phi}/I$, with M, for the two apparatus. We showed theoretically in §2 that, whatever the distribution of current density across the electrodes,

$$\lim_{M\to\infty} R = R_\infty = 2a/\pi\sigma b^2.$$

We also demonstrated physically why we could expect R/R_∞ to be a linear function of $(lM^{\frac{1}{2}})^{-1}$ when $M \gg 1$. Therefore, in presenting our experimental results in figure 7 we plot R/R_∞ against $(lM^{\frac{1}{2}})^{-1}$ for the two electrode configurations in which $l = 0{\cdot}512$ and $0{\cdot}190$ respectively. The two main conclusions from these results are first that R/R_∞ is indeed a linear function of M, secondly that, to within the experimental error, the points for the two values of l fall approximately on the same straight line, and thirdly that to within 2 % $R/R_\infty = 1{\cdot}00$ when this line is extrapolated to the point where $M = \infty$. It is unfortunate that so few readings were taken for $l = 0{\cdot}190$ because it is hard to tell whether these are falling on a separate curve or are truly scattered about the straight line drawn in figure 7.

Having demonstrated that some of the external characteristics of the

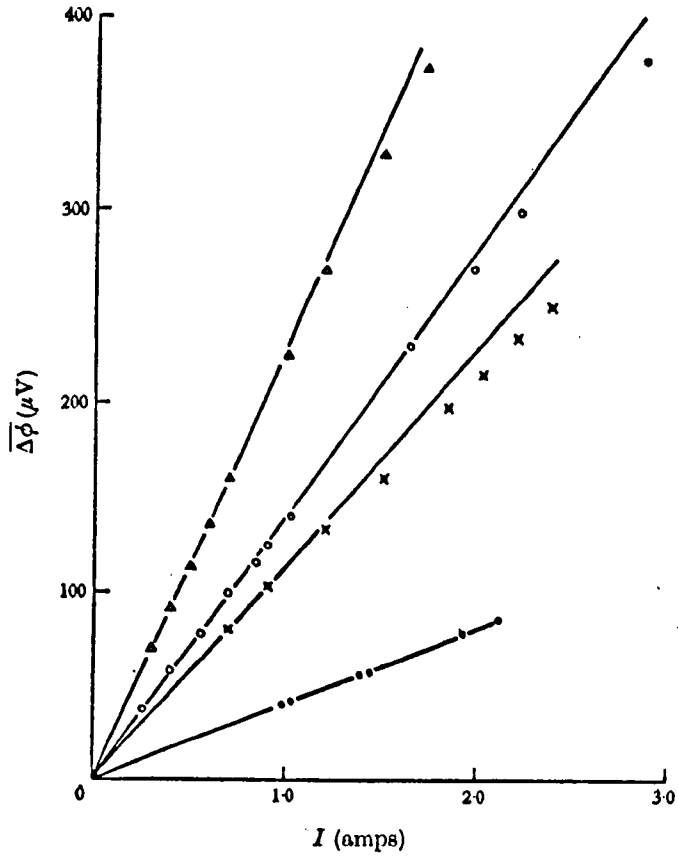

'IGURE 5. Experimental graph of potential between the disks, $\overline{\Delta\phi}$, against current, I, at 'arious values of M. △, $M = 1370$, $l = 0{\cdot}190$; ○, $M = 588$, $l = 0{\cdot}512$; ×, $M = 204$, $= 0{\cdot}512$; ●, $M = 0$, $l = 0{\cdot}512$.

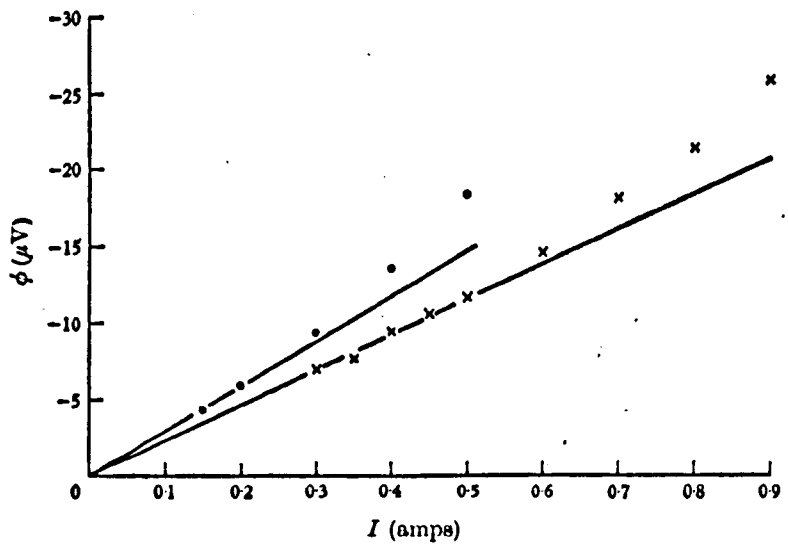

FIGURE 6. Graph of probe potential, ϕ, against I ($l = 0{\cdot}190$; probe positioned at $r/b = 0{\cdot}127$, $\zeta = 0{\cdot}054$). ●, $M = 855$; ×, $M = 1370$.

behaviour were approximately as predicted theoretically, we then examined the internal flow structure. In our theoretical discussion of § 2 we first postulated the existence of various separate regions and then made certain deductions about them, some of which we have been able to verify experimentally. In the central region between the electrodes, region (4), we concluded that when $M \gg 1$ the

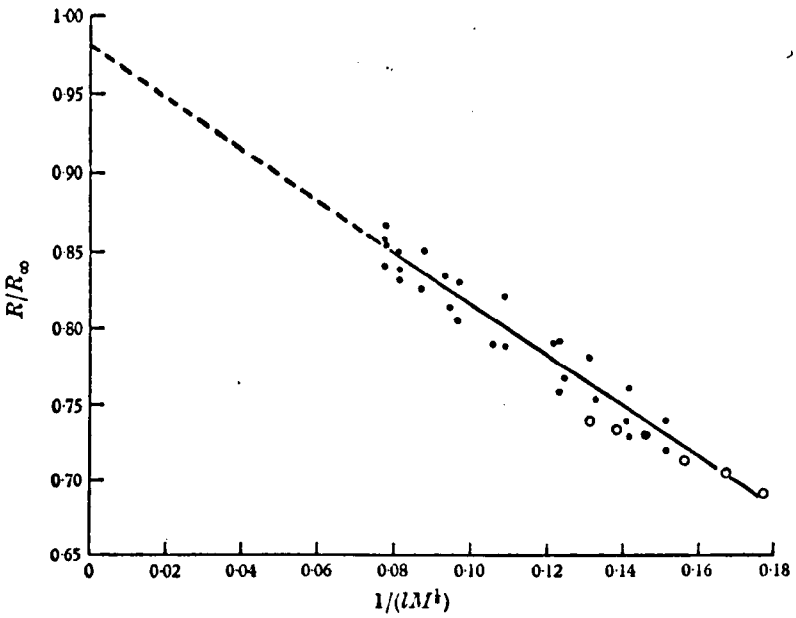

FIGURE 7. Variation of resistance between the electrodes, R/R_∞, with $(1/lM^{\frac{1}{2}})$. ○, $l = 0{\cdot}190$; ●, $l = 0{\cdot}512$.

velocity is zero and that the current density and electric field are uniform, provided the electrodes are perfectly conducting, a condition only approximately satisfied by our apparatus. In figure 8 we have plotted $(-\phi)\sigma\pi b^2/aI$ against ζ along the centre line ($r = 0$) when $M = 0$ and $M \gg 1$, since $(-\phi)\sigma\pi b^2/Ia = \phi/\phi_\infty$ where ϕ_∞ is the value of ϕ on the disk when $M = \infty$ at the same value of I. This figure shows that, when $M = 0$, the current density j_z is lower at $\zeta = 0$ than at $\zeta = 1$ because of the spreading of the current lines, and that, when $M \gg 1$, the curves become straight in this region, which is explicable in terms of our theory of § 2. Also we conclude that the spreading of the current streamlines is eliminated as shown in figure 1*b*. The slopes of the two straight lines for two different values of $(lM^{\frac{1}{2}})^{-1}$ are different, as we would expect from the graph of R/R_∞ against $(lM^{\frac{1}{2}})^{-1}$. We would also expect, as indeed we find, that the values of $(-\phi)\sigma\pi b^2/Ia$ are approximately equal to R/R_∞ for these two values of $(lM^{\frac{1}{2}})^{-1}$. We should note that the potential measurements in this region were only likely to be in error to order (d/a), i.e. less than 4%, owing to MHD effects (see appendix A, equation (A 1)), but the random errors were about 5%.

We now consider the results of the radial traverses of the electric probes in the region (1). Figure 9 shows the results of a potential traverse when $M = 0$, which

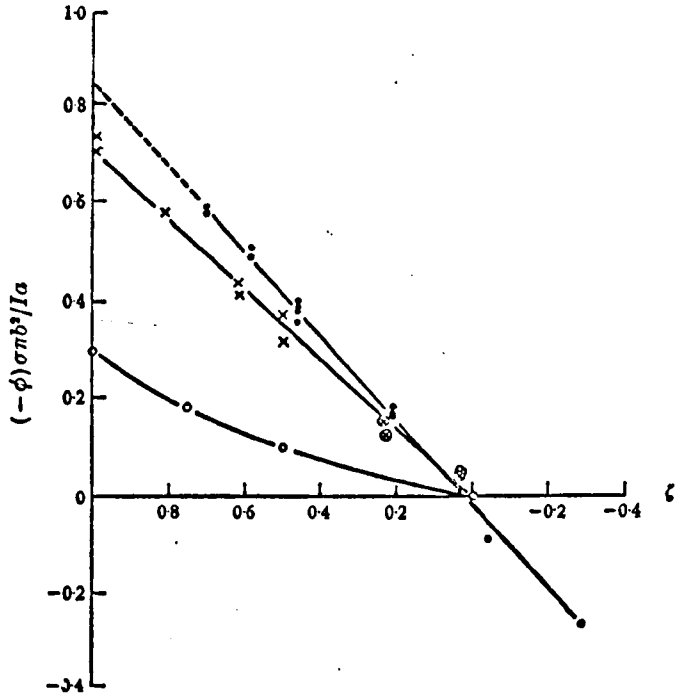

FIGURE 8. Variation of potential, $(-\phi\sigma\pi b^2/Ia)$, along the centre line of the electrodes when $M = 0$ and when $M \gg 1$. ●, $M = 595$, $l = 512$; ○, $M = 0$, $l = 0{\cdot}512$; ×, $M = 1550$, $l = 0{\cdot}190$, $\phi > 0$; ⊗, $M = 1550$, $l = 0{\cdot}190$, $\phi < 0$.

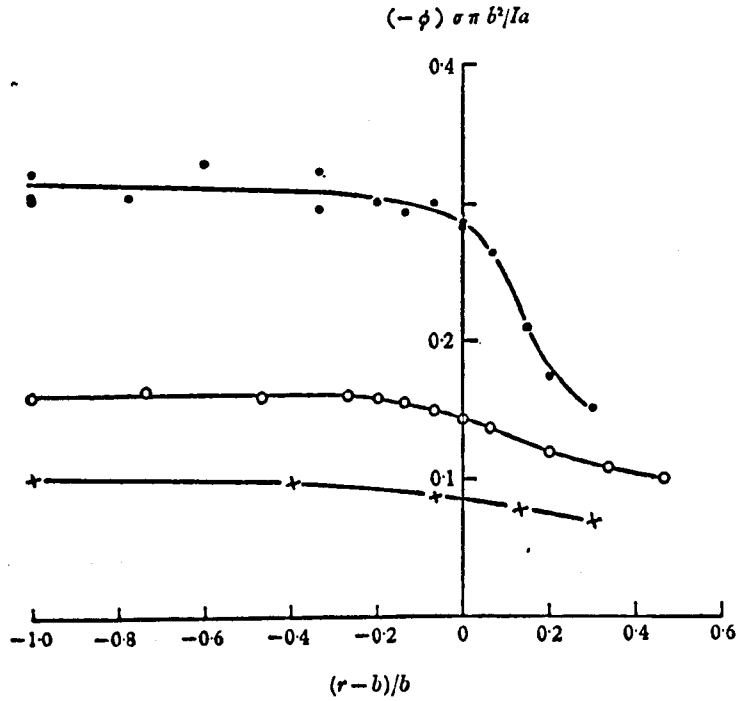

FIGURE 9. Graphs of potential $(-\phi\sigma\pi b^2/Ia)$, against radius, $(r-b)/b$, when $M = 0$. ●, $\zeta = +0{\cdot}97$, $l = 0{\cdot}512$; ○, $\zeta = +0{\cdot}99$, $l = 0{\cdot}190$; × , $\zeta = +0{\cdot}50$, $l = 0{\cdot}512$.

acts as a reference with which to compare the results for $M \gg 1$. We made three sets of measurements of ϕ in the first apparatus, i.e. the two disks, when $\rho = 0{\cdot}294$ and $M = 175{,}330$ and 610. (The notation we use is the same as that of figure 2, I being positive when parallel to the magnetic field.) In figure 10*a* we have plotted the results in the form of one graph of $(-\phi)\sigma\pi bl/I$ against $(r-b)/(aM^{-\frac{1}{2}})$ $(=\bar{\rho})$, in order to show firstly that the thickness of the region (1) is unquestionably of order $(aM^{-\frac{1}{2}})$, and secondly to show that the distribution of ϕ and therefore v_θ is similar for different values of M in these layers. We have drawn the best line through the experimental points, because they show only a small systematic departure from this line. Considering the randomness of many of the errors involved, the curves do not indicate any large-scale departure from similarity except where $(r-b)/(aM^{-\frac{1}{2}}) < -3$, when the values of $(-\phi)$ are lower for the lower values of M. This result is to be expected since in the central region, (4), $(-\phi)\sigma\pi b^2/aI$ varies linearly with $M^{-\frac{1}{2}}$, $(-\phi)$ increasing as M increases.

The results shown in figure 10*b* were taken in the second apparatus and were plotted in the same way as those in figure 10*a*. In this case the results were taken with the probe just touching the wall or very close to it, $\zeta > 0{\cdot}96$, and, as the figure shows, there is no detectable difference caused by moving the probe very slightly near the wall. As well as indicating the similarity of the ϕ profiles (in the sense of §2), these results also show that near the edge of the disk $(-\phi)$ decreases and the distance in which this drop occurs is $O(aM^{-\frac{1}{2}})$. Therefore the electrodes cannot be considered as resembling perfectly conducting electrodes, because, if they were, the probe would have recorded a constant potential across the electrode, at least to within a probe error of $O(d/a)$.

It is interesting that the thickness of the layers are approximately the same in all cases, being about $6aM^{-\frac{1}{2}}$ (~~This may indicate why the profiles are not completely similar and why the slopes of the two curves of R/R_∞ against $(lM^{\frac{1}{2}})^{-1}$ are different in figure 7, since, if $\delta \simeq 6aM^{-\frac{1}{2}}$~~) the ratio of the thickness of the layers to the radius of the electrodes is $\delta/b = 6(lM^{\frac{1}{2}})^{-1}$. For the maximum value of M in the first apparatus $\delta/b = 0{\cdot}46$ and in the second apparatus $\delta/b = 0{\cdot}78$. Therefore the approximation we made in §2 that $\partial/\partial\rho \gg 1/\rho$ is not really justifiable in analysing our experimental situation, and consequently we ought not to expect the degree of agreement that we find for the values of R/R_∞ against $(lM^{\frac{1}{2}})^{-1}$ in the two apparatus; nor should we expect the ϕ profiles to be the same, even if they had been measured at exactly the same value of ζ.

4.2. *Pitot tube measurements*

As with the electric potential probes, when we began to use the Pitot probe we first checked that we were measuring a velocity *low* enough to be in the required linear flow regime. With the Pitot tube we also had to ensure that the measured velocity was *high* enough for $(p_0 - p_s)$ to be proportional to the square of the velocity v_θ, where p_0 and p_s are the total and static pressure, respectively. Since in the flow regime examined in §2 v_θ is proportional to I and since it follows from (A 7) that p_0 is proportional to v_θ^2, if the MHD error is small, we had to find the values of I for which $\Delta p = p_0 - p_w$ was proportional to I^2, where p_w is the pressure at the tapping on the wall.

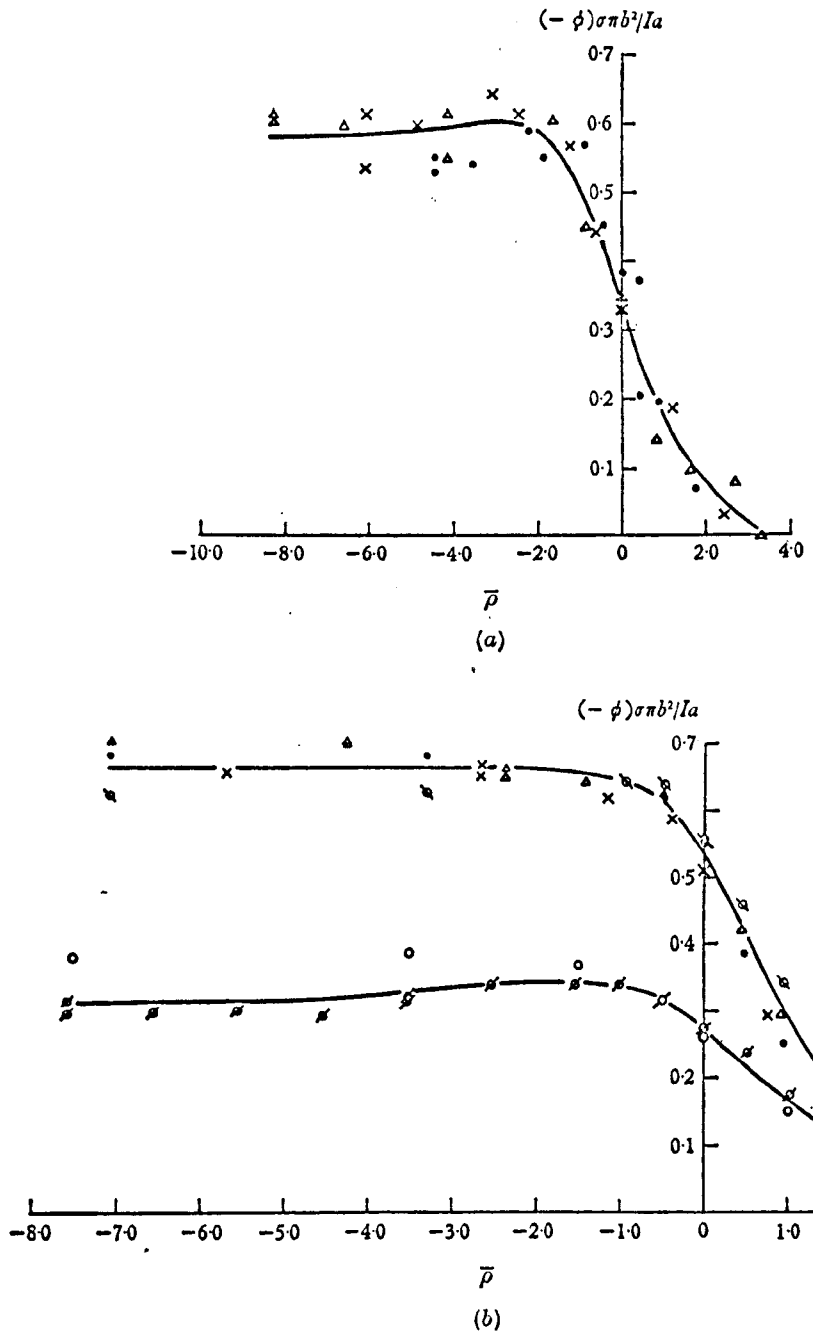

FIGURE 10. Variation of potential with radius in region (1) when M ≫ 1. (*a*) $(-\phi\sigma\pi b^2/Ia)$ against $\bar{\rho} = (r-b)/(aM^{-\frac{1}{2}})$; $l = 0{\cdot}502$, $\zeta = 0{\cdot}706$. ●, $M = 175$; ×, $M = 330$; △, $M = 610$. (*b*) $(-\phi\sigma\pi b^2/Ia)$ against $\bar{\rho}$; $l = 0{\cdot}190$. △, $M = 1367$, $\zeta = 0{\cdot}97$; ×, $M = 882$, $\zeta = 0{\cdot}99$; ●, $M = 1367$, $\zeta = 0{\cdot}99$; ⊗, $M = 1367$, $\zeta = 0{\cdot}96$; ○, $M = 1550$, $\zeta = 0{\cdot}50$; ⌀, $M = 1575$, $\zeta = 0{\cdot}50$.

In figure 11*a* we plot Δp against I^2 when $r = 0$, $M = 1370$, and when $r = 1{\cdot}33b$, $M = 855$, these and all subsequent readings being taken in the second apparatus, where $l = 0{\cdot}190$. Note that, when $r = 0$, $\Delta p < 0$ since $v_0 = 0$ and the static pressure is below the outside the disks due to the radial pressure gradient. When $r = 1{\cdot}33b$, $\Delta p > 0$, showing that in region (1) the rise in total pressure is greater than the fall in static pressure, which is, of course, to be expected.

Realizing that the most critical region for examining the onset of secondary flow was region (1), we then measured Δp at two values of M when $r = 1{\cdot}267b$. The results, plotted in figure 11*b*, show, first, that the velocity decreases as M increases for given I, as is to be expected from the theory of §2, and, secondly, that to operate in the required regime we needed to measure pressures of the order of 0·030 in. meths, which are about as low as can be measured with any degree of repeatability. This meant that we had to operate at high values of M, with the associated disadvantage of using the Pitot tube when the thickness of region (1) was least. We have to presume that, though the MHD probe error for these values of I was about 50 % of the measured value, the random errors preclude any conclusion as to the exact linearity of the Δp *vs.* I^2 relation.

We measured the radial distribution of Δp at $\zeta = 0{\cdot}991$ and $\zeta = 0{\cdot}972$ at only one value of M, 1370, since we could not lower M enough to obtain appreciably different yet repeatable readings and at only one value of I, 0·7 amps. From the radial distribution of Δp we calculated v_0 using the relations (A 9). Since Δp is positive in region (1) and negative in (4) it is zero on the boundary between these two regions and consequently it is impossible to calculate the velocity there at all accurately. We have plotted $v_0 b l^{\frac{1}{2}} M^{\frac{1}{2}} (\sigma\eta)^{\frac{1}{2}}/I$ against $(r-b)/(aM^{-\frac{1}{2}})$ in figure 12 so that if a suitable theory can be developed it may be compared with these results. We note that the velocity is greatest nearest the wall, which is predictable since the jump in potential across the layer is greatest when ϕ is greatest, i.e. near the disk. Also note that, as *r decreases*, v_0 *decreases* more sharply near the wall, which is to be expected since, if the wall is highly conducting, the current must leave the electrode at right angles, thus reducing the shear stress and consequently the velocity at the wall. We may note that the Hartmann boundary layer here was so thin, 0·001 in., as to be negligible.

4.3. *Discussion*

Having calculated the velocity from the Pitot tube readings, we can now compare these values found with those calculated from the electric potential distribution, using the relation,

$$-\frac{\partial \phi}{\partial r} + v_0 B_0 = 0. \tag{2.17}$$

Rewriting this in a non-dimensional form we have

$$-\frac{v_0 M a (\sigma\eta)^{\frac{1}{2}}}{I} = -\sigma a^2 \frac{\partial(\phi/I)}{\partial r}. \tag{4.1}$$

In figure 13 we have plotted $\sigma a^2 \partial(\phi/I)/\partial r$ and $v_0 M a (\sigma\eta)^{\frac{1}{2}}/I$ against $(r-b)/(aM^{-\frac{1}{2}})$,

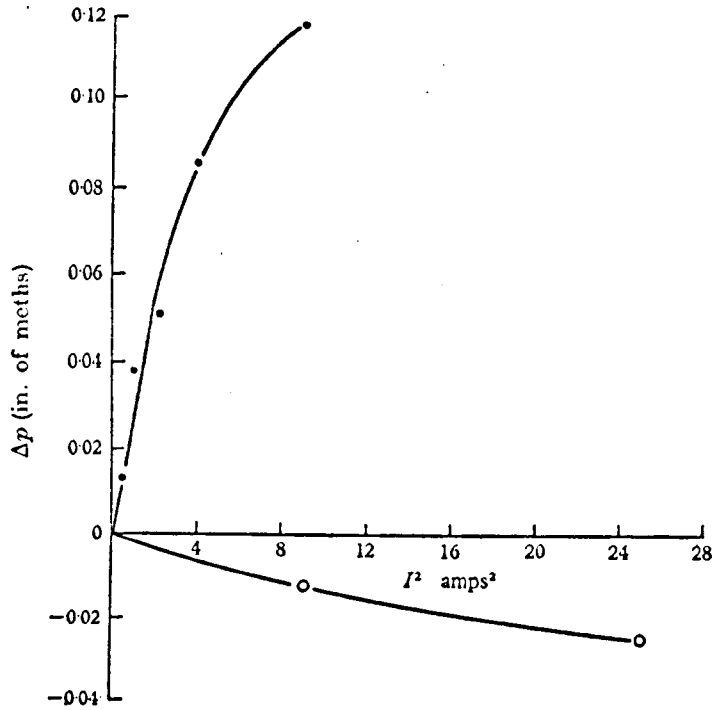

(a)

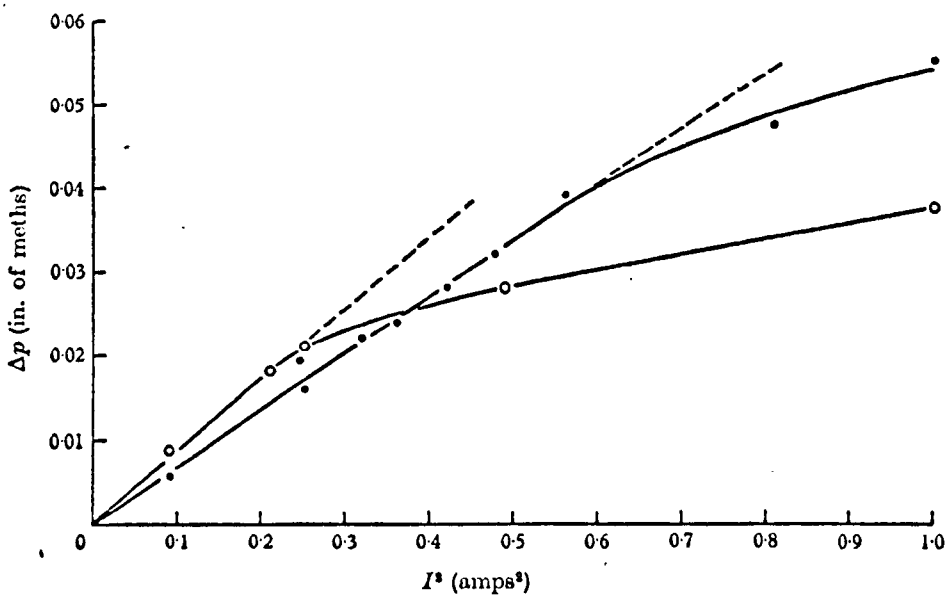

(b)

FIGURE 11. Variation of Pitot pressure, Δp, with I^2 when $M \gg 1$ and $\zeta \simeq -1$. (*a*) Large values of I. ○, $M = 1370$, $r/b = 0$; ●, $M = 855$, $r/b = 1{\cdot}33$. (*b*) Small values of I. ○, $M = 855$, $r/b = 1{\cdot}27$; ●, $M = 1370$, $r/b = 1{\cdot}27$.

using the uncorrected readings of the electric potential and Pitot probe. (With the latter we have corrected for the static pressure gradient.) We see that a discrepancy of $>100\,\%$ exists between the two curves. We then calculated $v_0 Ma(\sigma\eta)^{\frac{1}{2}}/I$ using the correction formula (A 9) (as we did for figure 12), and thence calculated the mean value of $kd^2\hat{c}^2/\hat{c}r^2\,[Mav_0(\sigma\eta)^{\frac{1}{2}}/I]$ across the probe

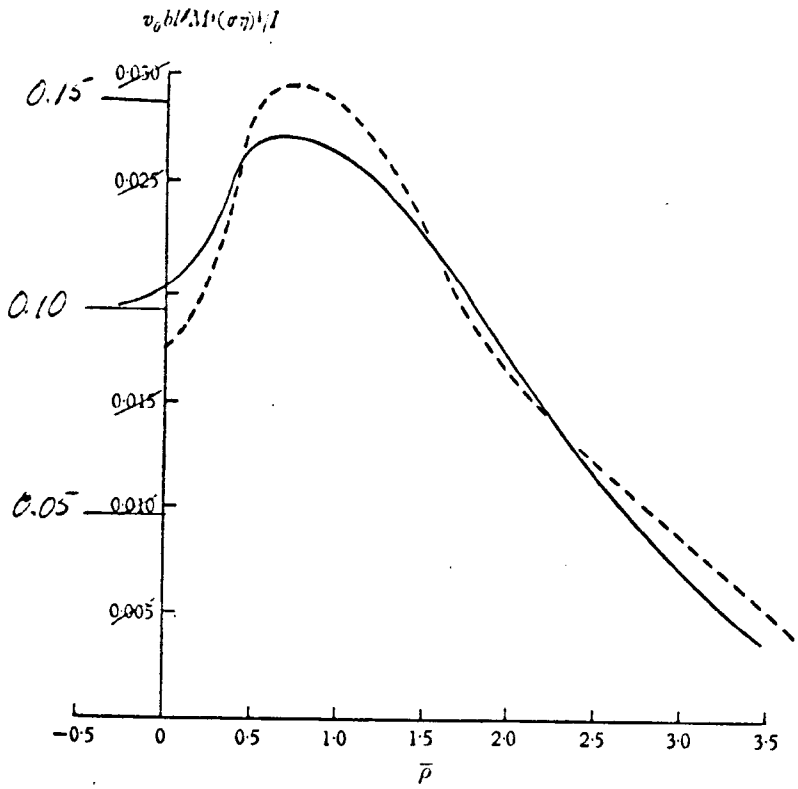

FIGURE 12. Variation of velocity, $v_0 b/aM^{\frac{1}{2}}(\sigma\eta)^{\frac{1}{2}}/I$, with radius, $\bar{\rho} = (r-b)/(aM^{-\frac{1}{2}})$, in region (1) ($M = 1365$, $I = 0{\cdot}7$ amps). ——, $\zeta = 0{\cdot}97$; — — —, $\zeta = 0{\cdot}99$.

face in order to use the correction formula (A 2) for ϕ_m. (We took $k = \frac{1}{4}$, being the value for the two-dimensional probe examined by Hunt (1967), chapter 4.) We note that, though $d^2M/a^2 \simeq 0{\cdot}1$, since $\hat{c}^2 v_0/\hat{c}\bar{\rho}^2$ was so great, the size of the correction term was sufficient to reduce the difference in the maxima to about $30\,\%$. We also note that the maximum of the uncorrected curve of the potential gradient is at a *lower* value of r than the velocity maximum and that, with the correction applied, the maximum moves to a *higher* value of r. We note from figure 13 that this displacement is approximately equal to the diameter of the probe.

The main reason for the difference in these two corrected curves is probably that the experimental situation did not sufficiently satisfy the condition that $\hat{c}/\hat{c}r \gg 1/r$ and that therefore the radial currents were sufficiently large to make (2.17) a poor approximation.

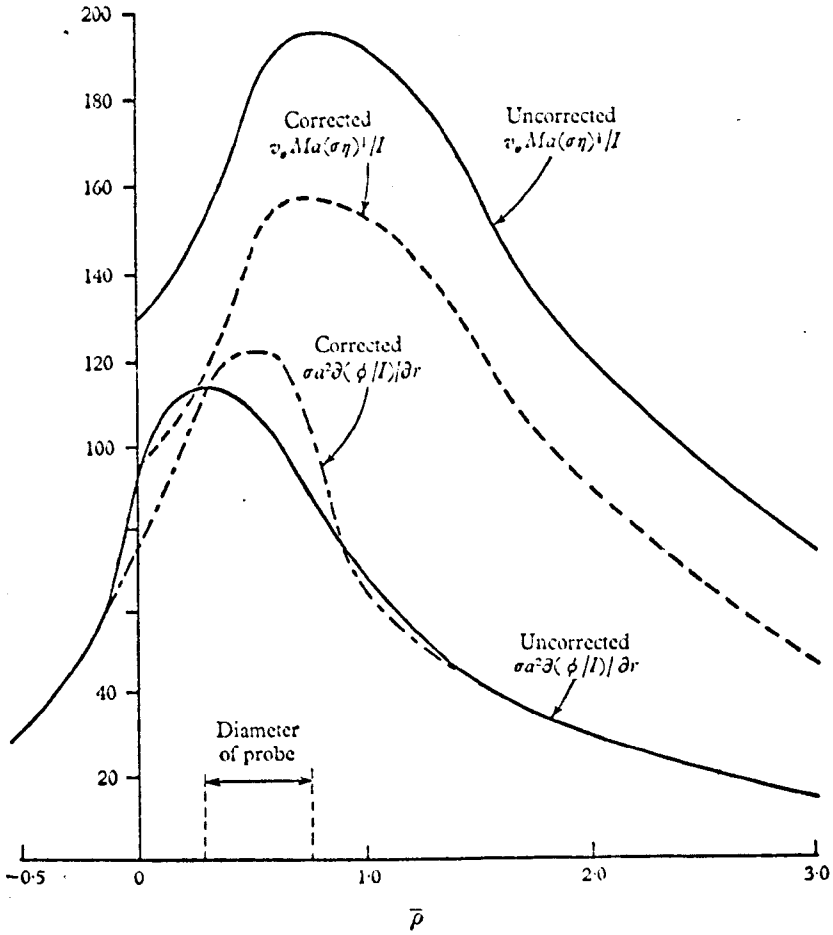

FIGURE 13. Comparison of the values of the velocity calculated from Pitot and electric potential probe readings, both corrected and uncorrected for MHD error ($\zeta = 0{\cdot}991$, $M = 1367$).

5. Conclusions

From our analysis in §2 of the flows induced between two highly conducting circular electrodes we concluded that the following *qualitative* phenomena are to be expected when $M \gg 1$. (i) The 'channelling' of current between the two electrodes. (ii) The existence of a thin layer joining the edges of the circular electrodes in which a large radial electric field and an azimuthal velocity are induced. In this layer the electric field increases and the velocity decreases as M increases. (iii) The variation of the potential distribution across the electrode as M varies, on account of the finite conductivity of the electrode.

Our main *quantitative* predictions are that: (i) If R is the resistance between the two electrodes,

$$\lim_{M\to\infty} R = R_\infty = \frac{2a}{\sigma\pi b^2}, \tag{2.22}$$

whatever the current distribution on the electrodes. From *physical* reasoning we

expect the variation of R with M to be given by

$$R/R_\infty = 1 - k/lM^{\frac{1}{2}}, \tag{2.23}$$

where k is a constant. (ii) If the relative conductance of the fluid to the electrodes is low enough, i.e. if $\sigma a/\sigma_e t \ll 1$, then, provided $(b-r)/(aM^{-\frac{1}{2}}) \gg 1$, $\partial\phi/\partial r = 0$ and $\partial\phi/\partial z$ is constant. (iii) On *physical* grounds we expect the current density distribution to be a function of $\bar{\rho} = (r-b)/(aM^{-\frac{1}{2}})$ on the electrodes. We are then able to conclude mathematically that, if this is so, ϕ is also a function of $\bar{\rho}$ at a given value of z.

It follows that, if the quantitative phenomena (i) to (iii) are shown to exist experimentally, then the qualitative phenomena (i) to (iii) also exist.

In our experiments, described in §4, we first showed that the relation between R/R_∞ and M took the form of (2.23), whence the result (2.22) follows. We demonstrated that $\partial\phi/\partial r = 0$ and $\partial\phi/\partial z$ is a constant in the region (4), thus confirming the second quantitative prediction, and the first qualitative one. We showed that a thin layer existed between the electrodes' edges and that, in this layer, $\phi\sigma\pi b^2/Ia$ was a function of $\bar{\rho}$, as predicted. In this layer the variation of the velocity with M agreed *qualitatively* with our predictions, though the agreement between the velocity and potential results was not satisfactory. Thus the main conclusions from our physical and mathematical analysis were confirmed experimentally.

The last important result from our experiments comes from the comparison of the results of the Pitot tube and the electric potential probe in an MHD flow and the application of some of the new theory of MHD probes, outlined in appendix A, to explain the differences in their results. (This is the first experiment in which such an exercise has been attempted.) The calculations of velocity in the region (1) deduced from Pitot probe measurements were between 100 % and 400 % higher than those made from electric probe measurements, when no corrections were applied for MHD probe errors. After applying such corrections we found that the differences between the two sets of measurements were reduced to between 30 % and 150 %; also the value of r at the maximum of the electric potential readings became closer to that of the Pitot readings. Thus we conclude that, though our error corrections are of some value, the large discrepancy remaining between the results demonstrates how little we understand the probes. (Some of the discrepancy may be due to the flows not satisfying the conditions of the asymptotic theory, by which we compared the results of the probes.)

We should like to thank Professor J. A. Shercliff for originally suggesting the work on electrically driven flows, and Mr A. E. Webb for constructing the apparatus and endlessly making and changing probes. J.C.R.H. acknowledges the generous support of the Central Electricity Generating Board in supporting this research at the University of Warwick and also acknowledges the support of the U.S. Army Research Office, Durham, North Carolina, at Cornell University, where some of the manuscript of this paper was written. D.G.M. gratefully acknowledges the support provided by the Royal Commission for the Exhibition of 1851 and in part by the National Research Council of Canada, in the form of an Overseas Scholarship.

Appendix A

1. *Electric potential probes*

We mention here a few of the considerations which led to the design of the electric potential probe used in our experiments. On the one hand such a probe needs to be as small as possible, when used in flows such as these where the gradients of velocity and electric potential are large, to avoid the MHD errors discussed by Hunt (1967); the probe size must also be minimized to reduce the size of the vortices shed by the probe which, being carried round, would tend to affect the potential at the probe tip. On the other hand the probe must be sufficiently rigid for its position to be determinate, particularly since in this experiment the probe was not always facing into the flow; also, the conducting region inside the probe must have a sufficient diameter for its resistance to be reasonably low and this wire has to be insulated from the probe's exterior, if this is made of metal.

The fact that the strongest small-diameter tubing easily available is made of stainless steel determined our choice of the material for the probe's exterior. We could either choose to have mercury or a wire inside the probe as our conducting region. The advantage of the wire is that it can be made to protrude from the end of the probe and thus present a small area to the flow. We chose to use palladium and platinum wires, the thermoelectric potential of these wires being close to that of mercury. The final design is shown in figure 4*a*. Note the two diameters of stainless-steel tubing used, the use of flexible plastic tubing as the insulator between the steel tubing and the wire, and the coating of the exterior of the probe with a thin layer of non-conducting Perspex cement.

We now consider the various regions of the flow between the disks, as discussed in § 2, in order to estimate the kind of errors to be expected when $M \gg 1$.

Region (4). In this region the current density is uniform and the velocity is zero so that, if the probe is at right angles to the current, i.e. $\gamma = 0$, from the symmetry result of Hunt (1967, chapter 4) no error would be induced. However, as we have explained, the probe could not always be at right angles to the plane $\theta = \frac{1}{2}\pi$, so that we could expect some error due to blocking the currents. Then the error in ϕ compared to $\Delta\phi$ is easily seen to be $O(d/a)$, where d is the probe diameter.

Region (1). In this region severe velocity and potential gradients exist and the equation,

$$-\frac{\partial\phi}{\partial r} + v_\theta B_0 = 0, \tag{2.17}$$

gives the approximate relation between ϕ and v_θ. Now, if the measured potential is ϕ_m and the true potential ϕ, since $\partial\phi/\partial\theta = 0$,

$$\phi_m - \phi = -\int_{-L}^{0} \frac{j_\theta}{\sigma} r\,d\theta - B_0 \int_{-L}^{0} v_r r\,d\theta, \tag{A 1}$$

where L is a large distance, relative to the probe diameter, in the azimuthal direction. (For further discussion of this and other aspects of electric potential probes see Hunt (1967).) Since $N = \sigma B_0^2 d/\rho v_0 \ll 1$, we can ignore the effect of the magnetic field on the flow over the probe to the first order and then (A 1) becomes

$$\phi_m = \phi + k d^2 B_0 \partial v_\theta/\partial r, \tag{A 2}$$

where k is some positive, dimensionless constant which may be assumed to be independent of v_0 since $R_d = \rho d v_0/\eta \gg 1$.

Using (2.17), (A 2) becomes

$$\phi_m = \phi + kd^2 \partial^2\phi/\partial r^2, \tag{A 3}$$

whence we deduce two results by considering a simple expression to represent the fall of ϕ through the regions (1), say $\phi = 1 - \mathrm{erf}(\bar{p})$, where $\bar{p} = (r-b)/(aM^{-\frac{1}{2}})$. We see that if k is large enough $\partial\phi_m/\partial r$ has two maxima for $\bar{p} \lesssim 0$, but that, if k is low enough, the maximum value of $\partial\phi_m/\partial\bar{p}$ is *less* than that of $\partial\phi/\partial\bar{p}$. To find the condition for the error term to be negligible in region (1), we write (A 3) in terms of $\bar{p}$:

$$\phi_m = \phi + \frac{kd^2}{a^2} M \partial^2\phi/\partial\bar{p}^2. \tag{A 4}$$

In our experiments $d^2M/a^2 = 0{\cdot}105$ and therefore we could expect one maximum for $\partial\phi_m/\partial r$ and with a value less than $\partial\phi/\partial r$.

In order to calculate ϕ from ϕ_m we could either integrate (A 4) or, as in fact we did, we could use the results of the Pitot tube readings for v_0 to find ϕ from (A 2). To calculate the error term we averaged the values of $\partial^2\phi/\partial r^2$ or $\partial v_0/\partial r$ across the face of the probe, 0·025 in. in diameter.

2. *Pitot tubes*

The considerations leading to the design of the Pitot tube were very similar to those leading to the design of the electric potential probe, the only difference being that the probe should not have too small an internal diameter because of the need to reduce the time for taking a reading of pressure. Again we used various sizes of stainless-steel non-magnetic tubing for the probe, each tube fitting inside the other. The tube was coated with Perspex cement in order to minimize the effects of the probe on the electric fields; however, this was not really necessary as the contact resistance of stainless steel is so large as to render it effectively non-conducting. The final design of Pitot tube is shown in figure 4*b*.

From the theory of Hunt (1967, chapter 4) and the experimental results of East (1964) we expected that the MHD probe errors could be calculated from the formula

$$p_0 = p_s + \tfrac{1}{2}\rho v_0^2 \left(1 + \alpha \frac{\sigma B_0^2 d}{\rho v_0}\right), \tag{A 5}$$

where p_0, p_s and ρ are the total pressure, the static pressure and density respectively. It turned out that $N = \sigma B_0^2 d/\rho v_0$ was about unity so that higher-order terms in the expansion should have been used. However, the experimental results of East (1964) gave $\alpha = 0{\cdot}39$ and the experimental results of Hunt (1967) gave $\alpha \simeq 0{\cdot}4$ for values of N of $O(1)$, so we assumed $\alpha = 0{\cdot}4$ in our calculations of velocity.

The other source of error to be expected was caused by measuring velocity in a shear flow, i.e. region (1), the length scale of which was somewhat smaller than the diameter of the Pitot tube. However, it was shown experimentally by Hunt (1967) that, if a Pitot tube is used to measure the velocity of a plane Poiseuille

flow in a duct the width of which is only four times that of the tube, the errors over the central half are negligible, but appreciable errors ($\sim 50\,\%$) occur when the centre line of the probe is within one diameter of the wall. However, even that shear flow was less steep than those measured here, so we could expect an appreciable and largely uncertain error in velocity in this highly asymmetric shear flow.

We decided to measure the velocity induced in the region (1) by means of a Pitot tube only, the pressure in the Pitot tube being measured relative to the pressure at a tapping in the wall of the duct, p_w. The static pressure was not measured in the layer, even though there was a small static pressure gradient through the layer caused by the rotating flow. However, this pressure gradient may be calculated from the equation

$$\partial p_s/\partial r = \rho v_\theta^2/r. \tag{A 6}$$

Leaving the error in p_0 for the moment, we have the usual relation between p_0 and p_s, the total and static pressures, i.e.

$$p_0 = p_s + \tfrac{1}{2}\rho v_\theta^2. \tag{A 7}$$

Eliminating p_s from (A 6) and (A 7) we have

$$\frac{\partial p_0}{\partial r} = \frac{\rho v_\theta^2}{r} + \tfrac{1}{2}\rho \frac{\partial v_\theta^2}{\partial r},$$

whence

$$v_\theta^2 = \frac{2}{\rho r^2}\int_\infty^r \left(r^2 \frac{\partial p_0}{\partial r}\right) dr. \tag{A 8}$$

Thus, by only measuring p_0, we could calculate v_θ. Since the static pressure effect is $O(\delta/b)$ ($\ll 1$), we could approximately allow for the MHD error, which was greater than the static pressure effect, by using successive approximations to calculate v_θ, viz.

$$v_{\theta(n)} \simeq 2\int_\infty^r \left(r^2 \frac{\partial p_0}{\partial r}\right) dr \Big/ \left\{\left(1 + \frac{0{\cdot}4\sigma B_0^2 d}{\rho v_{\theta(n-1)}}\right)\rho r^2\right\}. \tag{A 9}$$

(We needed to use two iterations at the most in our calculations.)

3. *The probe mechanism*

To examine the flow between two circular electrodes placed in non-conducting planes opposite each other with a magnetic field parallel to the line joining their centres, we only needed to examine the flow in one plane, $|\theta|$ = constant, because, for low enough velocities, the flow is axisymmetric. Since we wanted to use the mechanism and the probes designed for examining duct flows with the minimum number of alterations, we chose to examine the flows in the plane $\theta = \pm \frac{1}{2}\pi$. As a result of this decision we mounted the mechanism on the duct as shown in figure 3*c*. (This mechanism is similar to that of Lecocq (1964).)

The method of moving the probe in the plane, $\theta = \pm \frac{1}{2}\pi$, may be understood by referring to figure 3*a*, where the locus of the probe stem is shown in the (r, z)-plane ($\theta = 0$). To move the probe tip to a given value of z in the $\theta = \pm \frac{1}{2}\pi$ plane, the probe had to be twisted on its own axis and the probe spindle, S, also twisted.

To move the probe vertically, i.e. to vary r in the $\theta = \pm\frac{1}{2}\pi$ plane, a micrometer screw was used. As a consequence of this method of moving the probes, being $\frac{3}{4}$ in. from their tip to the centre line of their stem, the probes were only able to face into the flow at two positions: (1) $z \simeq +a$, $\zeta \simeq 1$ and (2) in the first apparatus at $z \simeq -a$, $\zeta \simeq -1$, and in the second at $z = 0{\cdot}25a$, $\zeta = 0{\cdot}25$. Therefore, without making new probes of differing lengths, the Pitot tubes could only be used near these values of z, such a probe being accurate to 1 % if it faces into the flow to within 10°. However, the electric probes could be used at all values of z, since they do not critically depend on pointing into the flow, or being at right angles to the current path. But, if γ is the angle between the line joining the probe's tip to the axis of its stem and the duct's axis (see figure 3*a*, *b*), it may be shown from the analysis of Hunt (1967, chapter 4) that the probe errors are reduced if γ is kept to a minimum. When the probe tip was on the duct's centre line, γ took its maximum value, about 45°.

Appendix B. Secondary flow

1. *Orders of magnitude*

As the velocity increases, the form of the flow generated between the electrodes must change in either or both of two basic ways. One possible change is caused by the fact that the azimuthal velocity, v_θ, varies in the radial direction such that $\partial v_\theta/\partial r \gg \partial v_\theta/\partial z$, so that the flow is expected to be unstable somewhat in the manner of a plane jet. Thus, when $v_\theta(aM^{-\frac{1}{2}})\rho/\eta = R_c$, where R_c is the critical value of the Reynolds number of that plane jet which corresponds to the variation of v_θ with r at the highest values of v_θ, we might expect the flow to become unstable to small disturbances, which eventually develop into non-axisymmetric eddies with the major component of the vorticity vector lying in the z direction, i.e. an unsteady flow similar to that found by Lehnert (1956). Since $v_\theta \propto I/M^{\frac{1}{2}}$ from the theory in § 2, it follows that

$$I_c \propto R_c M, \tag{B 1}$$

where I_c is the critical value of I. Thus, for a stable flow at a given value of M, I must be lowered so that $I < I_c$. If the flow becomes unstable in this way, $v_z \neq 0$ and/or $v_r \neq 0$, and in that case the inertial terms would have to be considered in the momentum equation. As a result v_θ, and consequently $\overline{\Delta\phi}$, would no longer be proportional to I.

The second change in the basic flow could be the onset of steady, or unsteady, secondary flow caused by the variation of the azimuthal velocity in the z direction so that $\partial p/\partial r$ $(= \rho v_\theta^2/r)$ varies significantly with z. Thence $v_r \neq 0$, $v_z \neq 0$, and v_θ is changed because the inertial terms in the momentum equation are no longer zero, e.g. $v_z \partial v_\theta/\partial z \neq 0$. It is again clear that when this occurs v_θ and $\overline{\Delta\phi}$ are no longer proportional to I.

Thus we conclude that when the basic flow changes, or becomes unstable, we should be able to detect this change by noting the departure from linearity in the variation of $\overline{\Delta\phi}$ with I. Whether a change should become evident at a particular value of I, as in the first instability, or becomes gradually more apparent as in the

gradual onset of a steady secondary flow, cannot be established without a more detailed investigation. Such an investigation of these interesting instability and secondary flow problems has recently been undertaken in which a quartz-insulated hot-film sensor is being used as a flow measurement device in liquid mercury. The results of this investigation will be reported in detail in a forthcoming paper by Malcolm (1968*b*), but one result will be mentioned briefly in § B 2 as it relates to equation (B 1).

2. *Secondary flow measurements*

Figure 5 shows the $\overline{\Delta\phi} - I$ curves for the two apparatus at various values of M. We note that $\overline{\Delta\phi} \propto I$ when $M = 0$, and that, when $M \neq 0$, the curve of $\overline{\Delta\phi}$ against I is a straight line for I sufficiently small, but as I increases the curve ceases to be a straight line.† From the two curves taken at $M = 588$ and $M = 204$ in the two-disk apparatus ($l = 0{\cdot}512$), we note that the value of I at which the linear regime ceases is higher when M is higher, thus showing that an increased magnetic field tends to suppress the onset of the flow in the non-linear regime. A simple examination of the equations would indicate this result for either of the two non-linear flows discussed in § B 1.

We continued this investigation of the onset of secondary flow by examining the relation between the current, I, and the difference in potential, ϕ, between that on the line $z = 0$ and that measured by the electric potential probe in the one-disk apparatus ($l = 0{\cdot}190$). The probe was placed at a radius of $1{\cdot}27b$ and at a value of $\zeta = -0{\cdot}95$, i.e. in the region (1), so that any secondary flow effects could be markedly demonstrated. As shown in figure 6, the ϕ against I curve becomes non-linear at a much lower value of I for the same value of M than in the $\overline{\Delta\phi}$ against I curve shown in figure 5. The most plausible explanation is that a secondary flow occurs in which the radial velocity tends to thicken the region (1), leading to a reduction at a given value of I of the current density in region (4) and thence $\overline{\Delta\phi}$, as we see in figure 5. However, as region (1) thickens, the potential gradients fall and therefore, if the probe's position is at a radius greater than that of the disk, $|\phi|$ rises, and, if at a lesser radius, $|\phi|$ falls. This explains why, when the curves in figure 6 become non-linear, $|\phi|$ *rises*.

Experimental studies of the stability of the primary flow which are presently under way using the hot-film anemometry technique (Malcolm 1968*a*) indicate that, in the two-disk apparatus ($l = 0{\cdot}512$), the critical current at which the primary flow first becomes unstable varies in the manner, $I_c \propto M$, for $M > 200$. The most interesting consequence of this result is that the critical Reynolds number, R_c, defined in (B 1) must be a *constant* and independent of M, for M sufficiently high. This implies that the magnetic field tends to stabilize the flow chiefly by affecting the primary flow, i.e. lowering its Reynolds number for given I. The other consequence is that, since $v_\theta \propto I/M^{\frac{1}{2}}$, the critical velocity, occurring when $I = I_c$, *increases* as $M^{\frac{1}{2}}$, which agrees qualitatively with the results of figure 11*b*.

† These readings for $M > 0$ were taken to examine the secondary flow, not to measure accurately $\overline{\Delta\phi}/I$ in the primary flow regime. The latter readings were taken later and are not shown.

REFERENCES

BRANOVER, G. G. & LIELAUSIS, O. A. 1962 *Vopr. Magn. Gidro. Akad. Nauk. Latv. SSR., Riga* **2**, 575–81.

EAST, D. 1964 The Pitot tube in magnetohydrodynamics. Ph.D. Thesis, Mass. Inst. Tech.

HUNT, J. C. R. 1967 Some aspects of magnetohydrodynamics. Ph.D. Thesis, Cambridge University.

HUNT, J. C. R. & STEWARTSON, K. 1968 To be published.

HUNT, J. C. R. & WILLIAMS, W. E. 1968 *J. Fluid Mech.* **31**, 705.

LECOCQ, P. 1964 Contribution à l'étude des pertes de charge et profils de vitesse en écoulement turbulent en magnéto-hydrodynamique. Ph.D. Thesis, Toulouse.

LEHNERT, B. 1956 *Proc. Roy. Soc* A**233**, 299.

~~MALCOLM, D. G. 1968 To be published~~

MOFFATT, H. K. 1964 *Proc. 11th Int. Cong. Appl. Mech., Munich*, p. 946.

MOREAU, R. 1966 *C. R. Acad. Sci.* **262**, 259.

Malcolm, D.G. 1968a Thermo-anemometry in magnetohydrodynamics Ph.D. Thesis, University of Warwick

Malcolm, D.G. 1968b To be presented at the 6th Symposium on Magnetohydrodynamics, Institute of Physics, Latvian Academy of Sciences, Riga, Sept. 3-6.

A.2 Some aspects of turbulence measurement in liquid mercury using cylindrical quartz-insulated hot-film sensors

by D.G. Malcolm

- as submitted to J. Fluid Mech., March, 1968.

Some aspects of turbulence measurement in liquid mercury using cylindrical quartz-insulated hot-film sensors.

by

D.G. Malcolm,
School of Engineering Science,
University of Warwick.

Abstract

This investigation demonstrates by theory and experiment methods for the measurement of low turbulence intensities in the flow of a low Prandtl number fluid using the constant-temperature hot-film technique. Simple formulae for the determination of turbulence intensity are derived from known theoretical relationships between the flow velocity and the heat transferred through forced convection by cylinders of infinite length and from calibration data for cylindrical quartz-insulated platinum hot-film sensors of finite length in mercury. Various difficulties associated with the application of hot-film anemometry to mercury flows are discussed. Of particular practical importance are the effects of small environmental temperature drift and the wetting characteristics of the insulating material surrounding the platinum film.

1. Introduction

This investigation was prompted by the need for a reliable method of measuring magnetohydrodynamic turbulence quantitatively in low Prandtl number fluids such as liquid mercury. The practical problems of protecting and insulating the measurement device from the hostile environment and establishing a precise calibration procedure are exceedingly difficult. Of the few measurement devices which could possibly be applied, the electrically heated thin-film sensor seems at present the most promising.

The earlier work of Sajben (1964, 1965, 1967) provided a basis for this study. He applied a lacquer-insulated tungsten hot-wire in the constant-current mode to measure turbulence intensity in a turbulent mercury jet subjected to an axial magnetic field. The present study was further prompted by advances in the area of constant-temperature hot-film anemometry by commercial firms such as Thermo-Systems Inc. (St. Paul, Minnesota, U.S.A.) and DISA Elektronik A/S (Herlev, Denmark). Sputtered-quartz coated platinum-film sensors now manufactured are more rugged than conventional hot-wires and offer sufficient frequency response when operated in the constant-temperature mode. The operation of thin-film sensors by the constant-current technique is not feasible because the thermal inertia of the boundary layer, protective coating and substrate material greatly impairs the frequency response and measurement accuracy. As discussed by Bellhouse and Schultz (1967) and by Bellhouse and Rasmussen (1968), situations also exist in which constant-temperature operation of the films fail to give acceptable results. Such effects are negligible for the cylindrical sensors considered in this discussion and in fluids such as water or mercury. It is noteworthy that Bellhouse and Schultz (1966) have been successful in manufacturing hot-film sensors in the laboratory from commercially available materials.

Sajben's work (1965, 1967) with hot-wires in mercury represents one of two known published accounts of quantitative turbulence measurement in low Prandtl number fluids. The other is by Branover, Slyusarev and Shcherbinin (1965) who related strain-gauge measurements of fluctuating drag on a tear-drop shaped probe immersed in mercury to turbulence intensity. This technique does not seem to hold much promise however, primarily because the size of the probe precludes the measurement of small scale turbulence.

Section 2 of this paper presents a brief theoretical study of the turbulence measurement problem. Section 2.1 presents a similar analysis to that of Sajben (1965). Section 2.2 proceeds from the results of this analysis to develop simple formulae for the measurement of low intensity turbulence using a constant-temperature anemometer system. Although Sajben found it necessary to use a special electronic circuit to linearize the voltage across the sensor with respect to the flow velocity, these formulae should eliminate the need for such elaborate treatment of the anemometer signal in the majority of cases where turbulence of low intensity is involved. In fact, with appreciable signal drift taking place continuously in some cases (for reasons which will be discussed), these formulae should prove more accurate than the alternative electronic operation because of their independence of any reference conditions such as the power dissipated at zero velocity.

Section 3 describes and discusses the results of the experiments which test the measurement procedures and Section 4 presents conclusions. The problem of environmental temperature drift effects and various noteworthy special problems concerned with the application of the hot-film technique to mercury flow are discussed in Appendices A and B.

2. Theory

2.1. Heat transfer relations

Let the hot-film sensor be considered as a very long, uniformly heated, composite cylinder which is placed in a flow of low Prandtl number fluid perpendicular to its axis. Figure 1(a) is a sketch of the actual sensor and Figure 1(b) shows a cross-section of this sensor. The platinum film is maintained at a constant temperature, T_s, which is above the temperature of its fluid environment, T_f. The equation for the rate of heat transfer in this case may be readily derived (see Chapman (1960) for example) as

$$Q = \frac{\Delta T}{\frac{1}{2\pi r_\ell L h} + \frac{1}{2\pi L k_c} \ln\left(\frac{r_c}{r_s}\right) + \frac{1}{2\pi L k_\ell} \ln\left(\frac{r_\ell}{r_c}\right)} , \quad \ldots\ldots (1)$$

where suffices s, c and ℓ refer to the platinum film surface, insulating coating and non-wetted thermal contact resistance layer, respectively. $\Delta T = (T_s - T_f)$ and h, k, r and L represent the convective heat transfer coefficient, thermal conductivity, cylinder radius and hot-film length, respectively. k_ℓ and r_ℓ are unknown and, for the case of mercury in particular, often change to an unknown extent with each passage of the sensor through the unavoidable free surface. These effects are discussed in detail in Appendix B.

Using the usual definition of the Nusselt number for a horizontal cylinder in convection, $Nu = h(2r)/k$, h may be replaced in equation (1) by $k_f Nu/2r_\ell$. If equation (1) is now rewritten in the form

$$\frac{\pi k_f L \Delta T}{Q} = \frac{1}{Nu} + \frac{1}{2}\frac{k_f}{k_c} \ln\left(\frac{r_c}{r_s}\right) + \frac{1}{2}\frac{k_f}{k_\ell} \ln\left(\frac{r_\ell}{r_c}\right),$$

the last two terms are observed to be independent of flow velocity. On the other hand Nu depends upon the forced convection velocity through PR (the Prandtl-Reynolds number product) which is usually

termed Pé, the Péclet number. The equation may be further rewritten as

$$\frac{\pi k_f L \Delta T}{Q(Pé)} = \frac{1}{Nu(Pé)} + K , \qquad \ldots\ldots (2)$$

where K represents the velocity independent terms. Because K depends upon the properties of the contact resistance layer it may take a markedly different value each time the sensor passes through the mercury free surface. As shown by Sajben (1965), it is possible to eliminate this changing K term by the following procedure,

$$F(Pé) = \pi k_f L \Delta T \left(\frac{1}{Q(0)} - \frac{1}{Q(Pé)}\right) = \left(\frac{1}{Nu(0)} - \frac{1}{Nu(Pé)}\right) \ldots\ldots (3)$$

It is necessary to note here that, in order to be evaluated, Pé must be based upon $2r_c$ rather than upon $2r_\ell$ which is unknown. Providing that the contact resistance layer is relatively thin the error in this evaluation should not be significant.

Equation (3) is observed to be strongly dependent on slight changes in ΔT due to normal environmental temperature drift during the course of an experiment. This important aspect is discussed in Appendix A. It is found that a small relative error in ΔT may be multiplied by a factor of ten in the relative error of F(Pé). The use of temperature compensation equipment to complement a conventional constant-temperature anemometer is therefore advisable in velocity measurement investigations of this type.

A theoretical solution for Nu(Pé) for cylinders of infinite length which applies to low values of Pé and to low R, allowing the use of the Oseen approximation, was derived by Cole and Roshko (1954) in the form,

$$Nu = \frac{2}{(\ln 8 - \Gamma) - \ln Pé} , \qquad \ldots\ldots (4)$$

where Γ is Euler's constant.

Grosh and Cess (1958) have assumed inviscid flow for the specific case of a low Prandtl number fluid to derive the following equation which should be most accurate at higher values of R.

$$Nu = 1.015\ Pé^{1/2}. \qquad \ldots\ldots (5)$$

2.2. Formulae for turbulence intensity measurement

Practical formulae for the direct calculation of low intensity turbulence from measurements obtained using a constant-temperature anemometer will now be developed. First, for the case of low R and low Pé, if Nu(Pé) is replaced by equation (4), equation (2) becomes

$$\frac{\pi k_f L \Delta T}{Q(Pé)} = \frac{(\ln 8 - \Gamma)}{2} - \frac{1}{2}\ln Pé + K. \qquad \ldots\ldots (6)$$

Let Q(Pé) be replaced by the ohmic dissipation in the hot-film, $E^2 R_s/(R_s + R^*)^2$. E is the voltage across both the hot-film resistance, R_s, and R*, a resistance in series with R_s. R* represents a resistance in the electronic circuit and/or the combined resistance of the current leads and the probe body. The only variable part of Pé in a constant temperature environment is the velocity component, U, perpendicular to the sensor. Equation (6) may now be rewritten as

$$\frac{\pi k_f L \Delta T (R_s + R^*)^2}{E^2 R_s} = -\frac{1}{2}\ln U + K', \qquad \ldots\ldots (7)$$

where K' includes all velocity independent terms. Differentiating equation (7) results in the relationship,

$$4\left[\frac{\pi k_f L \Delta T (R_s + R^*)^2}{R_s}\right]\frac{dE}{E^3} = \frac{dU}{U}. \qquad \ldots\ldots (8)$$

It is assumed that the turbulent velocity components perpendicular to the sensor, u' in the streamwise direction and v', are very small compared to the local mean velocity $\bar{u}$, i.e.,

$$u', v' << \bar{u} . \qquad \ldots\ldots (9)$$

Using this assumption, which is applicable to low intensity turbulence, it is seen in Figure 1(a), that $dU \sim u'$ and $U \sim \bar{u} + u'$. The following substitutions will be made in equation (8).

$$\begin{aligned} E &= \bar{E} + e, \quad dE = e, \\ U &= \bar{u} + u', \quad dU = u', \end{aligned} \qquad \ldots\ldots (10)$$

where e is the small deviation from the mean voltage, $\bar{E}$, caused by the turbulence. Substitution of equation (10) into equation (8), followed by a conventional root-mean-square operation in which fluctuation quantities of greater order than two are neglected, yields the desired simple relationship,

$$4\left[\frac{\pi k_f L \Delta T (R_s + R')^2}{R_s}\right]\frac{\sqrt{\overline{e^2}}}{\bar{E}^3} = \frac{\sqrt{\overline{u'^2}}}{\bar{u}} . \qquad \ldots\ldots (11)$$

In Section 3.2. it becomes evident that it is not always possible to ignore the interacting effects of free convection and conduction on the heat transfer by forced convection. Hence equations (4) and (5) are not expected to completely describe the actual situation in most cases. The present experiments, using a horizontal cylindrical hot-film of dimensions as shown in Figure 1(a), show that the slope of the 1/Nu(Pé) vs ln Pé curve may be considerably different from $-1/2$ for low values of Pé. If this experimental slope is given a value -s, a modified turbulence intensity formula results, i.e.,

$$\frac{2}{s}\left[\frac{\pi k_f L \Delta T (R_s + R')^2}{R_s}\right]\frac{\sqrt{\overline{e^2}}}{\bar{E}^3} = \frac{\sqrt{\overline{u'^2}}}{\bar{u}} . \qquad \ldots\ldots (12)$$

For higher values of Pé in mercury, in cases where free convection and conduction effects are proven negligible, a similar method may be applied using equation (5) as the Nu (Pé) function in equation (2). The resulting turbulence measurement equation is

$$4\left(1.015\,\overline{Pé}^{1/2}\right)\left[\frac{\pi k_f L \Delta T (R_s+R')^2}{R_s}\right]\frac{\sqrt{\overline{e^2}}}{\overline{E}^3} = \frac{\sqrt{\overline{u'^2}}}{\overline{u}}, \quad \ldots\ldots (13)$$

where $\overline{Pé}$ is the Péclet number at the mean velocity.

Equations (11) to (13) have the advantage of being independent of the changeable properties of the contact resistance layer which surrounds the sensor. Equations (11) and (12) possess the particular advantages of being independent of the Nu(0) reference and relatively free from the irritating effects of signal drift due to slight changes in ΔT (see Appendix A) or due to slowly varying properties of the contact resistance layer (see Appendix B). The only information required other than directly measured quantities is the slope of the $1/Nu\,(Pé)$ vs ln Pé curve which is obtained by calibration. Equation (13) on the other hand cannot be used where signal drift is a problem because both $1/Nu\,(Pé)$ and $1/Nu\,(0)$ must be readily available for every measurement in order to evaluate $\overline{Pé}$ from the calibration curve. Similarly, any attempt to use more sophisticated electronic linearization or digital computation techniques to allow for the very nonlinear dependence of E on U is hampered by drift problems.

The important questions to be answered experimentally are:
(i) at a point of measurement in a turbulent flow, will equation (12) give the same value for $\sqrt{\overline{u'^2}}/\overline{u}$ at different levels of operating temperature and ohmic dissipation?
(ii) are values of $\sqrt{\overline{u'^2}}/\overline{u}$ from equation (12) actually independent of the value of K' in equation (7), and therefore independent of the thickness and properties of the impurity layer on the sensor?

(iii) are values of $\sqrt{\overline{w'^2}}/\bar{u}$ from equation (12) actually independent of signal drift caused by the combined effects of normal small environmental temperature changes and slow timewise variations in the properties of the contact resistance layer?

3. Experiment

3.1. Apparatus and experimental methods

The apparatus used in this investigation is a mercury tow-tank facility constructed for the purpose of calibrating hot-film probes for use in magnetohydrodynamic experiments. The tow-tank itself is formed of rigid pvc sheet, 3/16 inch in thickness, to produce a trough of internal dimensions, 4 x 4 x ~~50~~ 54 inches. It is supported in a steel framework to eliminate deformation of the tank walls when filled with about 400 lb. of mercury.

The hot-film probes are suspended through the mercury free surface (with the sensors horizontal) from a 3 lb. brass trolley which runsabove the tow tank on two $\frac{3}{4}$ inch diameter stainless steel rails. The trolley has three wheels, approximately $2\frac{1}{2}$ inches in diameter, formed from pvc material to assist in the damping of vibrations in the mechanism. Two wheels on one side resemble V-pulleys and serve to guide the trolley on one of the round rails. The third wheel has a flat running surface and rides freely on the other rail. This arrangement of guide wheels minimizes wheel chatter and eliminates the need for accurate relative positioning of the rails.

The trolley is towed, via a system of pulleys and steel cables, by a hollow brass cylinder with a sharp-edged orifice at one end which descends under gravity in a vertical stainless steel tube through a mixture of water and common water-soluble machining lubricant. The rate of descent is fixed at about 0.9 cm/sec. by the pressure drop across the 0.1 inch diameter orifice. Slower speeds are obtained by adding counterweights to a restraining cable attached to the rear of the trolley. Higher speeds are obtained by adjusting a by-pass valve to regulate a by-pass flow from the bottom to the top of the stainless steel tube during the descent of the brass cylinder. The trolley is timed over a 50 cm. distance

by an electronic timer which is actuated by microswitches. A similar towing technique has been previously used by Lindgren and Chao (1967). These authors covered the complete speed range by using orifices of various sizes. In the present case the apparatus is capable of speed regulation from 0.3 to 14 cm/sec. with $\pm 0.5\%$ precision and with sufficiently low vibration in the mechanism to produce an equivalent turbulence intensity of 0.015. Most of this vibration apparently arises from harmonic oscillations in the towing cables.

A low intensity turbulence field was created by mounting a conventional square-mesh grid of round rods on the trolley ahead of the hot-film sensor and towing the whole assembly along the tow tank at constant speed. The grid was composed of 0.028 inch diameter brass rods in a brass frame (sprayed with pvc paint to prevent amalgamation) with a mesh length to rod diameter ratio of 5.36 and was situated at a 20 mesh length distance from the sensor.

Widely varying properties of the contact resistance layer around the sensor were obtained by repeated reimmersion through each of two types of interface, from air to mercury and from water to mercury. The water-mercury interface was obtained by pouring a layer of water on top of the mercury in the tow tank. As will be discussed in the experimental results, the differences in the heat transfer characteristics when passing through these two different interfaces are quite dramatic. Theoretically, the turbulence intensity as calculated from equation (12) should be unaffected however. This aspect is important from a practical point of view also, in that it is often desirable in experiments to minimize the amount of poisonous mercury vapour above mercury free surfaces by covering them with a layer of water.

The mercury free surface was cleaned periodically using a

vacuum skimming device. The sensor itself was not cleaned during the course of these experiments.

Figure 1(a) shows a sketch of the hot-film sensor specially manufactured by Thermo-Systems Inc. for work in mercury. It is 0.031 mm. in diameter and has a sensitive length of 0.495 mm. The platinum film and the sputtered-quartz coating have thicknesses as stated by the manufacturer of 0.1μ and 1.6μ respectively. The support needles are insulated by a coating of resin cement. The temperature coefficient of resistance was found experimentally to be $.00236^{o}C^{-1}$.

The hot-film probe was operated by a Thermo-Systems Model 1010 Constant Temperature Anemometer. ΔT was varied by adjusting the hot-film operating resistance, R_s, on this instrument. $\bar{E}$ was read from a digital voltmeter and $\sqrt{\overline{e^2}}$ was obtained using a Hewlett Packard Model H 12 - 3400A true rms voltmeter with frequency response down to 2 Hz, and with a 20 second averaging time on the d.c. output. The instantaneous anemometer signal and the d.c. output from the rms voltmeter were continuously followed by an oscilloscope. Because of random variation in the instantaneous value of $\sqrt{\overline{e^2}}$ during the course of each timed passage of the trolley it was found that direct readings of $\sqrt{\overline{e^2}}$ tended to be imprecise. The following photographic method was devised to overcome this problem. The time base of the oscilloscope was set at a sweep rate which allowed a large number of sweeps during the transit time of the trolley through its 50 cm. distance. A time exposure was then taken of the oscilloscope trace representing the d.c. output of the rms meter during this transit time. The result was a photograph showing a sweep band which represents the maximum variation in $\sqrt{\overline{e^2}}$. The more highly exposed line near the centre of this sweep band shows the rms value most often occurring during any one sweep. This line was taken to represent the best available average value of $\sqrt{\overline{e^2}}$ at the particular experimental conditions.

3.2. Results and discussion

Figure 2(a) shows calibration results for the hot-film sensor used in these experiments. Table 1. contains descriptive information for the various sets of data points included in the figure. These data were taken at intervals during a three week period and during a total run time in mercury of approximately 30 hours. Although a considerable amount of scatter is evident it should be emphasized that no special attention was given to cleaning the mercury free surface except to remove the thickest scum prior to each day's runs. The sensor itself was never cleaned. This lack of special care was purposely allowed since it was considered desirable to check the reproducibility of results under realistic operating conditions. One observes from Figure 2(a) that measurement precision decreases as $Pé \longrightarrow 1.0$.

The ratio, $\pi k_f L\Delta T/Q0)$, takes a different value each time the sensor crosses the free surface. The higher this ratio becomes, the greater is the insulating effect of the thermal contact resistance layer which surrounds the sensor.

In general, the use of the mercury-water free surface lessened the contact resistance. However, the increased sensitivity thus gained by improved wetting was lost because the water – impurity layer on the sensor seemed unstable and gave rise to random drift effects. The most satisfactory operation was experienced while using a mercury - air free surface and a high running temperature of about 30 °C. The best operating temperature must be chosen as a compromise between the higher temperatures, which give increased sensitivity and greater freedom from environmental temperature drift effects, and the lower temperatures, which ensure longer sensor life and lessen uncertainties in the calulation of physical properties of mercury at the mean temperature, $(T_s + T_f)/2$.

The calibration results are replotted in Figure 2(b) where

Legend	$\frac{\pi k_f L \Delta T}{Q(0)}$	Free surface type	ΔT °C
×	6.35	Hg - air	11.4
+	8.24	Hg - air	11.3
△	4.91	Hg - air	11.3
◇	5.49	Hg - air	10.8
⌀	4.82	Hg - air	22.1
•	3.34	Clean Hg - air	33.6
⌀	3.32	Hg - H_2O	33.0
o	3.86	Hg - H_2O	33.6

Table 1. Data for Figures 2(a) and 2(b).

it is observed that, for $0.3 \leq P\acute{e} \leq 1.0$, $F(P\acute{e})$ is a linear function of $\ln P\acute{e}$ with a slope of -0.31. This slope is considerably less numerically than the value of $-1/2$ predicted by the infinite length forced convection theories discussed in Section 2. A rigorous analysis of the modifying effects of conduction and free convection has not been attempted. For the range of ΔT used in these experiments $G P$, where G is the Grashof number, is as high as $O(10^{-3})$ so that free convection effects are likely to be significant at low $P\acute{e}$. Note that very small sensor diameters are desirable since G increases as d^3. A second constant-temperature anemometer set was brought into commission to ensure that the low slope of the $F(P\acute{e})$ vs $\ln P\acute{e}$ curve was not a result of equipment malfunction. This cross-checking procedure gave similar results.

From the point of view of accurately measuring turbulence intensity it is significant that, although descrepancies exist between the various sets of data in Figure 2(b), the slope of each set is very nearly the same.

On an occasion when the ambient temperature remained constant (within 0.2 °C) for a period of a few hours, the low speed calibration shown in Figure 3. was carried out. At these low speeds ($\bar{u} < 0.9$ cm/sec) $F(P\acute{e})$ is observed to vary linearly with $P\acute{e}$. The instrument can therefore be usefully employed to measure very low velocities providing that temperature drift effects are either absent or compensated for. On many occasions calibrations at low speed were unsuccessful because significant signal drift was instigated by a temperature difference from end to end in the tow tank of as little as 0.1 °C ! The scatter in Figure 2(a) for $P\acute{e} < 0.1$ is primarily due to the existence of these minute temperature gradients. These temperature drift effects are in accordance with the conclusions drawn in Appendix A.

Table 2 presents the results of experiments, using the trolley and turbulence grid apparatus, to test the turbulence measurement

Free surface type	$\frac{\pi k_1 L \Delta T}{Q(0)}$	$\bar{E}^3$	ΔT°C	$\sqrt{\overline{u^2}}/\bar{u}$	R
Hg - air	7.2	104	33.5	.041*	4650
Hg - H_2O	3.3	404	33.5	.041**	
	3.3	408	33.5	.040**	
Hg - air	---	48.6	10.8	.035	3050
	---	157	22.2	.035	
	---	290	33.1	.034	
	---	486	43.8	.034	
	---	185	32.8	.036	
	---	187	32.8	.039	
	---	319	33.0	.035	
	---	320	33.0	.033	
Hg - H_2O	---	65.4	10.8	.038	
	---	372	33.1	.036	
	---	591	43.8	.037	
	---	370	33.0	.040	
	---	370	33.0	.039	
	---	362	33.0	.041	
	---	366	33.0	.040	
	---	346	33.0	.038	
	---	346	33.0	.038	

Table 2. Turbulence measurements using the trolley and turbulence grid apparatus (horizontal lines indicate reimmersion of the probe through a free surface):

* Refer to Figure 4(a).

** Refer to Figure 4(b).

formula, equation (12). The value of s in equation (12) was taken from Figure 2(b) as 0.31.

It should be mentioned that Sajben's long (L/d = 100) hot-wire sensor (Sajben (1965)) performed in close accordance with the theoretical predictions for cylinders of infinite length. It is possible that with longer hot-film sensors it may be realistic to use the theoretical equations (11) and (13) directly to calculate turbulence intensity. It must be remembered, however, that the sensor length limits the measurement sensitivity for small scale eddies.

In Table 2 the comparison of $\bar{E}^3$ at the same ΔT yields qualitative information similar to that provided by $(\pi k_f L \Delta T)/Q(0)$ regarding contact resistance effects. All the turbulence intensities are observed to fall in the range, 0.033 - 0.041, and are uncorrelated with the wide variation in ΔT and the large changes in contact resistance which occur from one immersion to another through either of the two types of free surface. As was expected, no temperature drift effects were observed in these experiments. Since no correlation appears to exist between $\sqrt{\overline{u'^2}}/\bar{u}$ and $\pi k_f L \Delta T/Q(0)$, or $\bar{E}^3$ at corresponding ΔT, it is unlikely that the variations between values of $\sqrt{\overline{u'^2}}/\bar{u}$ are due to the changing properties of the contact resistance layer. Experience with the apparatus suggests that this variation could be due to a change from one run to another in the substantial contribution to $\sqrt{\overline{u'^2}}/\bar{u}$ made by the trolley vibrations.

From the results of many previous researches, one would expect the value of $\sqrt{\overline{u'^2}}/\bar{u}$ in grid turbulence alone, at a position 20 mesh lengths downstream from the grid, to be about 0.028. The values obtained for the trolley - grid combination are thus quite reasonable.

The dramatic effects of a substantial improvement in thermal contact are best appreciated by comparing the results in the first two entries in Table 2 with their related oscilloscope traces in

Figures 4(a) and 4(b). These traces have identical time and voltage scales and show typical e vs time variations for a mercury - air free surface with $(\pi k_f L \Delta T)/Q(0) = 7.2$ and for a mercury - water free surface with $(\pi k_f L \Delta T)/Q(0) = 3.3$, respectively. The oscillation amplitudes are much greater in the case of the mercury - water free surface. This is because, at constant ΔT, $\overline{e^2}$ must always increase in direct proportion to E^3 to yield similar values of $\sqrt{\overline{u'^2}}/\bar{u}$.

In Figure 4(b) it is observed that the shortest oscillation period, corresponding roughly to the smallest passing eddy within the sensor's sensitivity range, is about 0.005 sec. This corresponds to a frequency of 200 Hz. This value is quite reasonable since, if the maximum eddy sensitivity is based on the sensitive length of the sensor at $\bar{u} = 14$ cm/sec, a maximum frequency response in the region of 280 Hz would be expected. This illustrates the point that the maximum frequency response is governed by the sensor length in low speed mercury flow rather than by time varying heat transfer considerations.

4. Conclusions

From this investigation it is concluded that meaningful measurements may be obtained in a mercury flow using insulated cylindrical hot - film sensors providing that sufficient efforts are made to understand the physical and practical problems involved. Considerable attention must be paid to minimizing and compensating for drift in ambient temperature. The submerging of the sensor through the mercury free surface must be done with great care to avoid coating the sensor with a thick non-statio contact resistance layer. Since sensitivity is greatly increased by improving the wetting characteristics of the insulating coating, it is hoped that methods will be found to bring about such an improvement. In the present experiments a water - mercury interface was found to increase sensitivity, but with the unfortunate side effect of introducing a random drift effect.

It is concluded that it is possible to measure velocities as low as a few mm/sec quite accurately. Although the calibration method cancels out the effects of thermal contact resistance, the measurement precision decreases significantly for large $P\acute{e}$.

The turbulence intensity formula, equation (12), yields acceptable results over a wide range of operating parameters and over a large variation in contact resistance. This is so throughout the range of $P\acute{e}$ in which there is a linear dependence of $F(P\acute{e})$ on $\ln P\acute{e}$. The drift effects which hamper velocity measurement do not affect the measurement of turbulence intensity, as is expected from equation (12) which is dependent only on the knowledge of the correct slope of the $F(P\acute{e})$ vs $\ln P\acute{e}$ calibration curve. This slope is observed to be quite precise from one set of data to another in the present experiments so that the imprecision which exists in the calibration curve for large $P\acute{e}$ has no observeable effect on the turbulence measurement capabilities of equation (12).

I would like to thank Prof. J. A. Shercliff for originally suggesting this work, Dr. C. J. N. Alty for many helpful suggestions and Mr. A. E. Webb for his skilful construction of the apparatus. In particular, I would like to thank Mr. P. Bradshaw at the National Physical Laboratory and Dr. D. L. Schultz at the Engineering Laboratory, University of Oxford for very helpful discussions on various aspects of constant-temperature anemometry. This work has been made possible by an Overseas Scholarship from the Royal Commission for the Exhibition of 1851.

References

Bellhouse, B.J. and Rasmussen, C.G., D I S A Information, no.6, 3 - 10 (1968).

Bellhouse, B.J. and Schultz, D.L., J. Fluid Mech., 24, 2, 379-400(196

Bellhouse, B.J. and Schultz, D.L., J. Fluid Mech., 29, 2, 289-295(196

Branover, G.G., Slyusarev, N.M. and Shcherbinin, E.V., Magnitnaya Gidrodinamika, 1, 1, 33 - 36 (1965).

Chapman, A.J., Heat Transfer, The Macmillan Company, New York (1960).

Cole, J. and Roshko, A., Heat transfer from wires at Reynolds numbers in the Oseen range, Heat Transfer and Fluid Mechanics Inst., Univ. of California, Berkeley (1954).

Crosh, R.J. and Cess, R.D., Trans. A S M E, 80, 667 - 676(1958

Lindgren, E.R. and Chao, Junn - Ling, Phys. of Fluids, 10, 3, 667 - 668 (1967).

Sajben, M., Hot Wire Measurements in a Liquid Mercury Jet Subject to an Axial Magnetic Field, Sc.D. thesis, M I T, Cambridge, Mass. (1964).

Sajben, M., Rev. of Sci. Inst., 36, 7, 945 - 949 (1965).

Sajben, M. and Fay, J.A., J. Fluid Mech., 27, 1, 81 - 96(196

Appendix A. The effect of environmental temperature drift on measurement accuracy.

A calibration procedure for hot-film measurement of flow velocity in mercury was represented in the text by equation (3),

$$F(P\acute{e}) = \pi k_f L \Delta T \left(\frac{1}{Q(0)} - \frac{1}{Q(P\acute{e})} \right) = \left(\frac{1}{Nu(0)} - \frac{1}{Nu(P\acute{e})} \right) \quad \ldots\ldots (3)$$

It is quite possible that after a short time ΔT will have drifted by 1% due to environmental temperature changes. If a low ΔT is applied (0 (10) °C) to encourage long sensor life and minimize free convection, a 1% change will be 0 (10^{-1}) °C and near the limit of ordinary temperature measurement accuracy. If such a small change is apt to go unnoticed it is important to observe its effect on the value of F(Pé) in equation (3).

For a cylinder in free convection it is known that $Nu \propto (\Delta T)^{\frac{1}{4}}$ if fluid properties are constant. Therefore, very small changes in ΔT will not affect $1/Nu(0)$ significantly. From equation (2) in the text it is seen that

$$\frac{1}{Nu(0)} = \frac{\pi k_f L \Delta T}{Q(0)} - K .$$

Consequently,

$$\frac{\Delta T_2}{Q_2(0)} \sim \frac{\Delta T_1}{Q_1(0)} , \quad \ldots\ldots (A.1)$$

where ΔT_2 is slightly different from ΔT_1, because of temperature drift effect. Combining equations (3) and (A.1) yields the true value, $F_t(P\acute{e})$, at either ΔT_1 or ΔT_2,

$$F_t(P\acute{e}) = \pi k_f L \left(\frac{\Delta T_1}{Q_1(0)} - \frac{\Delta T_1}{Q_1(P\acute{e})} \right) \simeq \pi k_f L \left(\frac{\Delta T_1}{Q_1(0)} - \frac{\Delta T_2}{Q_2(P\acute{e})} \right) . \quad \ldots\ldots (A.2)$$

An accuracy error will arise on the rhs of equation (A.2) if ΔT_2 is mistakenly thought by the observer to have remained at ΔT_1. In this case, the apparent value, $F_a(P\acute{e})$, is

$$F_a(Pé) = \pi k_f L \left(\frac{\Delta T_1}{Q_1(0)} - \frac{\Delta T_1}{Q_2(Pé)} \right) , \quad \text{or}$$

$$F_a(Pé) = \pi k_f L \left(\frac{\Delta T_1}{Q_1(0)} - \frac{\Delta T_2}{Q_2(Pé)} \cdot \frac{\Delta T_1}{\Delta T_2} \right) . \qquad \ldots\ldots (A.3)$$

Let the respective relative errors in ΔT and F(Pe) be defined as

$$\epsilon_T = \frac{\Delta T_2 - \Delta T_1}{\Delta T_1} , \qquad \epsilon_F = \frac{F_a - F_t}{F_t} . \qquad \ldots\ldots (A.4)$$

In order to compare the values of the terms in equation (A.3), let the following ratio be defined at any Pé,

$$\left(\frac{\Delta T_1}{Q_1(0)} - \frac{\Delta T_2}{Q_2(Pé)} \right) \Big/ \left(\frac{\Delta T_1}{Q_1(0)} \right) = Z . \qquad \ldots\ldots (A.5)$$

Combining equations (A.2) to (A.5) results in the error equation,

$$\epsilon_F = \left(\frac{1}{Z} - 1 \right) \left(1 - \frac{1}{\epsilon_T + 1} \right) . \qquad \ldots\ldots (A.6)$$

From equation (A.6) it may be noted that an <u>increase</u> in ϵ_T or a <u>decrease</u> in Z brings about an <u>increase</u> in ϵ_F. The value of Z at a particular Pé depends upon the wettability (and hence upon the thermal contact resistance) of the sensor. In general Z increases as the contact resistance decreases. Suppose that, at a certain Pé, Z takes the value of 0.1. If ϵ_T is assigned a value of 0.01, it is easily calculated that $\epsilon_F = 0.09$. Thus a 1% error in ΔT has brought about a 9% error in F(Pé) which, when referred to the calibration curve, gives a correspondingly large error in Pé. As a consequence of this error propagation, it is advisable either to control the environmental temperature accurately or else to employ an electronic temperature compensator which follows T_f continuously and makes appropriate changes in R_s to keep ΔT constant. In any case, it is advisable to run at as high a level of ΔT as is practically feasible to minimize ϵ_T.

It is evident from equations (11) to (13), which are linearly dependent on ΔT, that the relative error in turbulence intensity due to temperature drift will be equal to ϵ_T.

Appendix B. Special operational problems

B.1. Thermal contact resistance

It was mentioned in the text that a contact resistance layer surrounds the sensor after immersion through a mercury free surface. This imperfect contact between the quartz coating and the liquid metal is thought to be primarily a result of surface tension effects and the effect of impurities which cling to the sensor whenever it passes through the unavoidable scum on the free surface. Each time the sensor is reimmersed an impurity layer of slightly different properties surrounds the sensor and the thermal contact resistance changes accordingly. Surface tension effects are important in two ways. First, the mercury does not wet the quartz coating and, second, the high surface tension at the free surface necessitates very careful insertion of the sensor through that surface in order to avoid trapping a thick, insensitive and non-static layer of air (or water, in the case of the water-mercury interface) around the sensor. This thick layer may be detrimental to frequency response and cause erroneous readings due to redistribution of the layer material around the sensor by drag forces.

The other detrimental effects of the contact resistance layer are to accentuate the considerable error caused by environmental temperature drift (see Appendix A) and to cause unknown error in the evaluation of fluid properties, especially if ΔT is high (i.e. the usually accepted procedure of evaluating properties at the mean temperature, $(T_s + T_f)/2$, becomes questionable).

In order to minimize contact resistance it is concluded that the free surface must be kept as clean as possible, that great care must be taken in submerging the hot-film sensor and that every possibility for increasing the wettability of the insulating quartz coating should be explored. It is evident from the results of Section 3.2 that the wettability of the coating is effectively increased by using a water-mercury interface in place of an air-

mercury interface. A certain lack of precision is introduced, however, especially at low flow speeds, since the water-impurity layer seems more unstable and more prone to cause drift problems than the air-impurity layer.

B.2. Sensor life

One of the unfortunate aspects of the application of hot-film anemometry to measurements in mercury is short sensor life. An average of about 50 hours of stable operation may be expected from a carefully manufactured sensor. The end of the useful lifetime of the sensor for quantitative measurements comes when the quartz coating either cracks or is worn away sufficiently to bring the mercury in contact with the platinum film, allowing an amalgamation process to begin. The sensor resistance is then observed to drift upwards until complete failure takes place by shorting of the electric current. Before shorting occurs the sensor may still be useful in qualitative work such as detecting flow instability. In the author's experience the useful lifetime of one sensor was extended to about 200 hours by employing it in this manner.

B.3. Drift problems

The effects of environmental temperature drift have been discussed in Appendix A. In addition, a slow drift in the properties of the thermal contact resistance layer may occur even if the fluid is stationary and at constant temperature. This necessitates a regular referencing procedure during the course of an experiment even if electronic temperature compensation is employed. Sajben (1965) experienced rapid signal drift and attributed it to minute amounts of impurity in the mercury. In the present work the most rapid signal drift rates seem rather to be a consequence of temperature drift rates of 0 (10^{-1}) ^{o}C/hr.

List of Figures

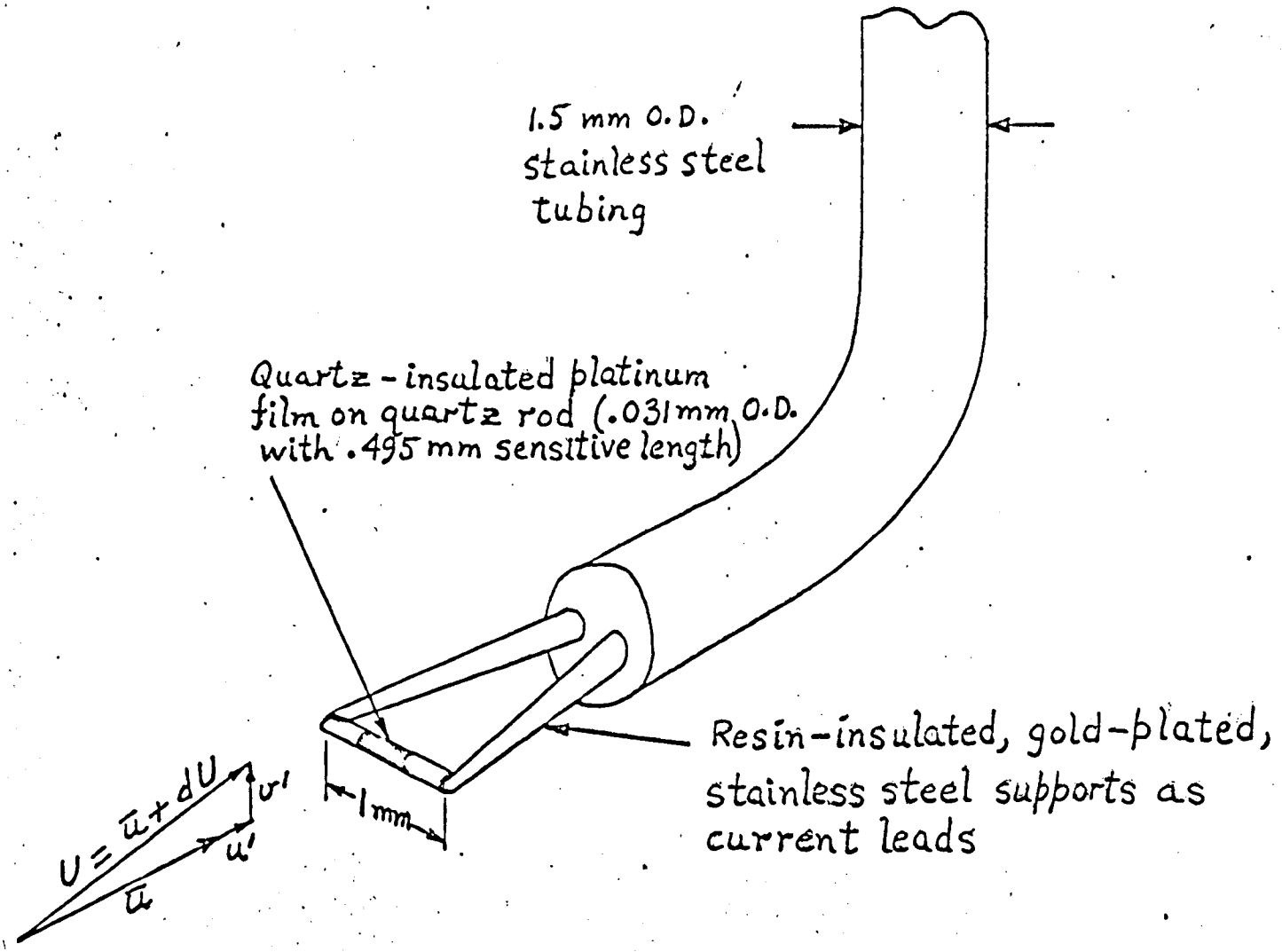
1.5 mm O.D.
stainless steel
tubing
Quartz-insulated platinum
film on quartz rod (.031mm O.D.
with .495 mm sensitive length)
Resin-insulated, gold-plated,
stainless steel supports as
current leads
1 mm
$U = \bar{u} + dU$
v'
u'
$\bar{u}$

Figure 1(a)

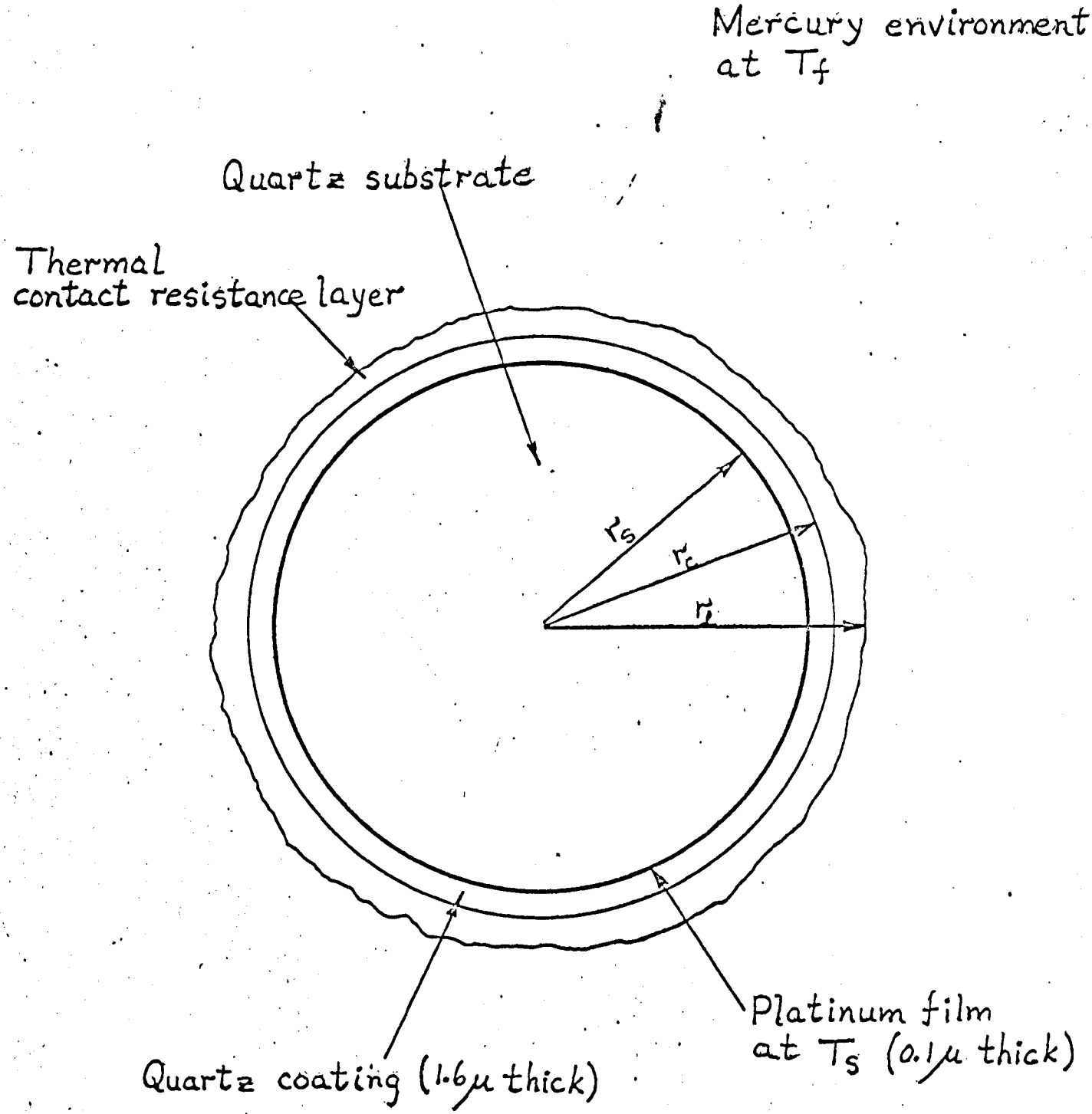
Mercury environment
at T_f
Quartz substrate
Thermal
contact resistance layer
r_s
r_c
r_i
Platinum film
at T_s (0.1μ thick)
Quartz coating (1.6μ thick)

Figure 1(b)

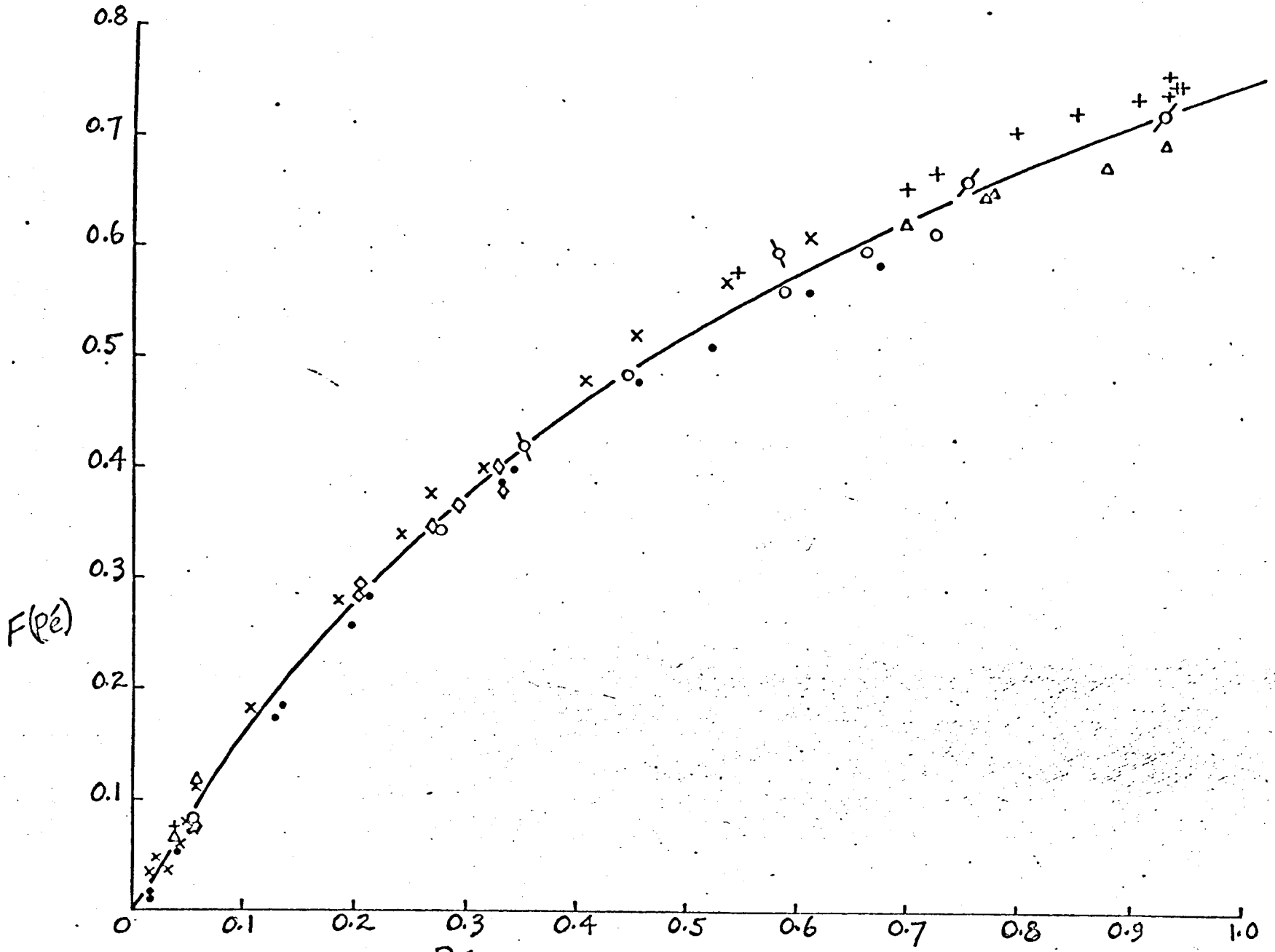

Figure 2(a)

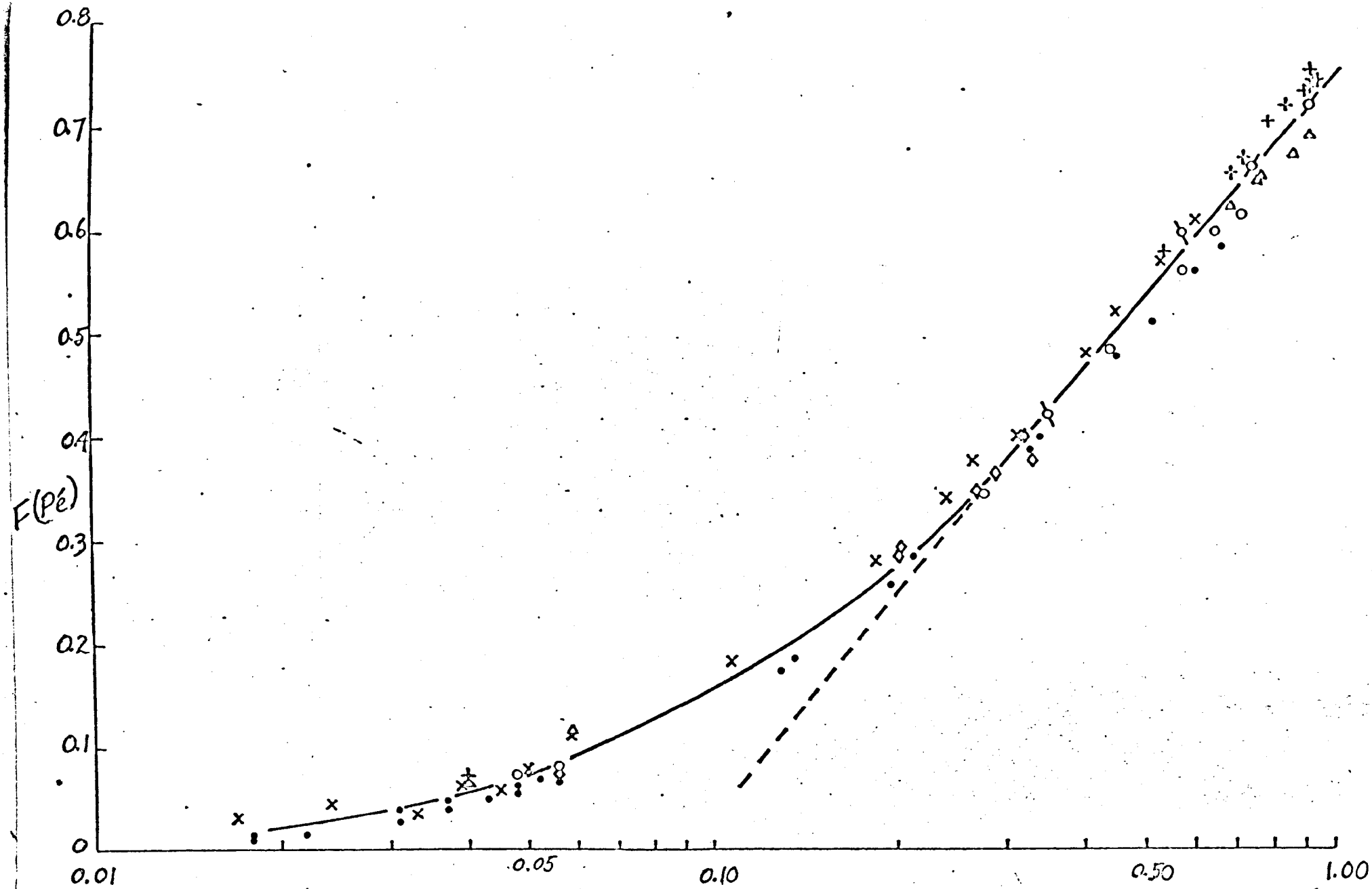

Figure 2(b)

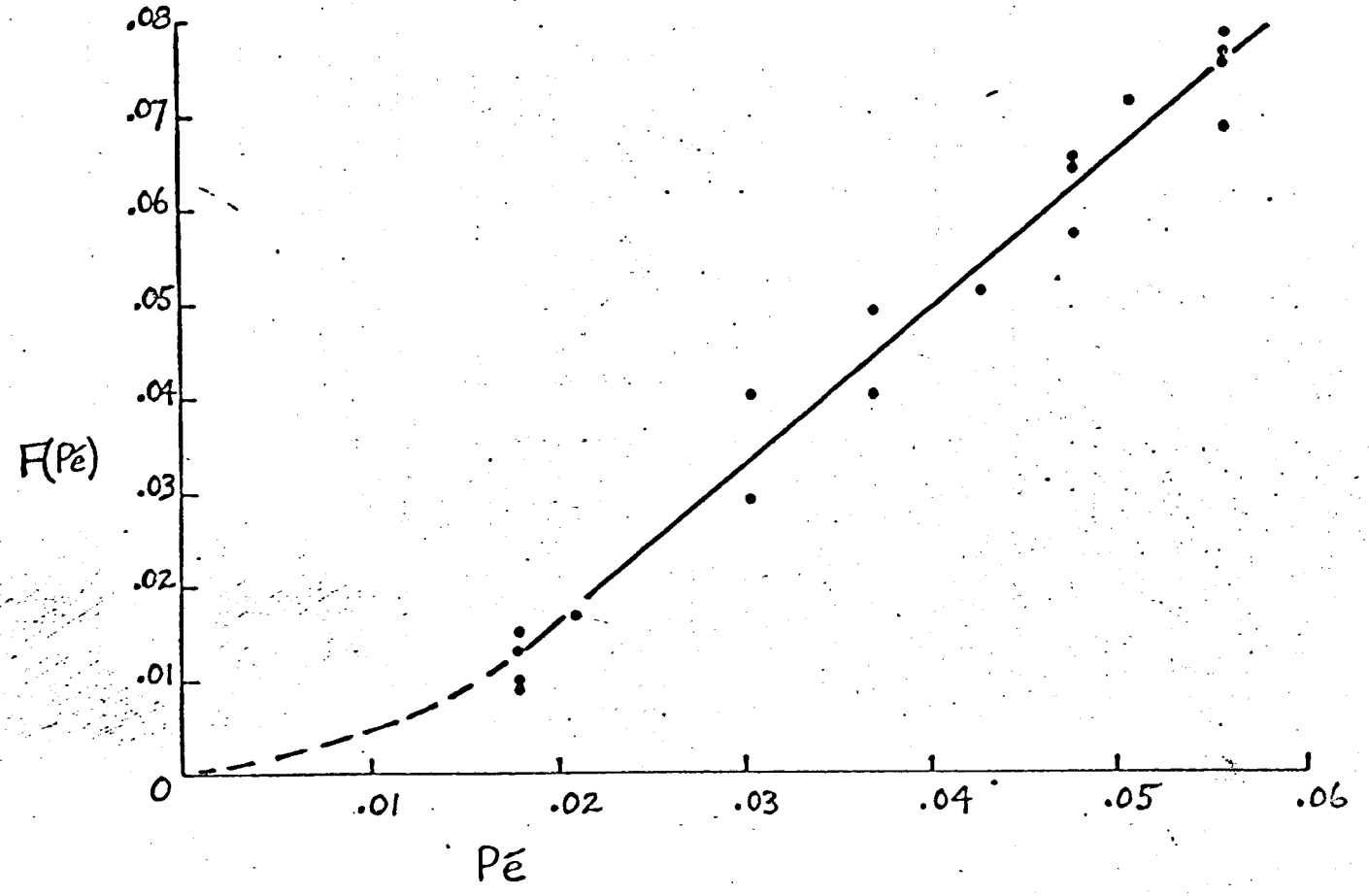

Figure 3

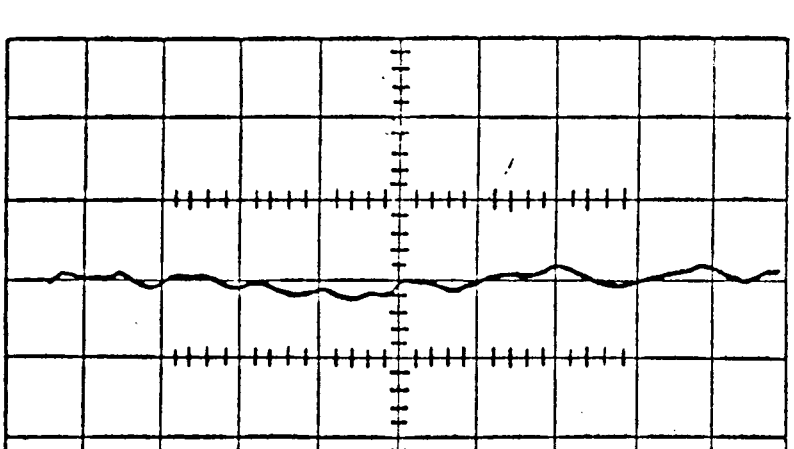

Figure 4(a)

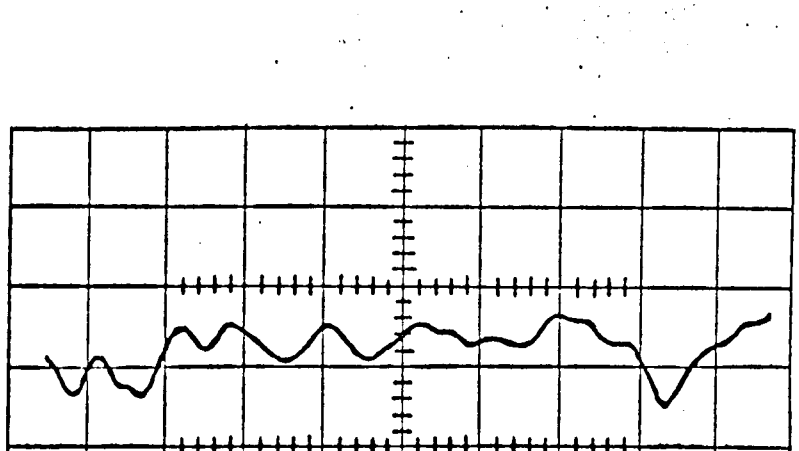

Figure 4(b)

A.3 Unsteady magnetohydrodynamic flow measurement in liquid metals using thermo-anemometry with applications of insulated platinum films in mercury

by D.G. Malcolm

- to be presented at:
Sixth Symposium on Magnetohydrodynamics, Inst. of Phys., Acad. of Sci., Riga, Latv. S.S.R., Sept. 3-6, 1968.

UNSTEADY MAGNETOHYDRODYNAMIC FLOW MEASUREMENT IN LIQUID METALS USING THERMO-ANEMOMETRY WITH APPLICATIONS OF INSULATED PLATINUM FILMS IN MERCURY.

By

David G. Malcolm,
Department of Mechanical Engineering,
University of Saskatchewan,
Saskatoon, Canada.

July, 1968.

To be presented at: Sixth Symposium on Magnetohydrodynamics, Institute of Physics, Academy of Sciences, Riga, Latvian S.S.R., September 3-6, 1968.

Abstract

This paper is concerned with research conducted by the author at the School of Engineering Science, University of Warwick, England. It begins with a discussion of the few previously published attempts to measure unsteady magnetohydrodynamic (MHD) phenomena quantitatively in liquid metals. It is concluded from this discussion that constant temperature anemometry using cylindrical, quartz-insulated, platinum film sensors comprises the best measurement system yet devised for such applications.

The main body of the paper consists of three sections. The first of these discusses various aspects of hot-film measurement in liquid metal MHD systems. One of these aspects concerns the presence of a non-wetting, thermal contact resistance layer at the sensor-fluid interface which changes in properties each time the sensor crosses a mercury free surface. The special calibration procedure of Sajben (1965) is necessary to cancel out this undesirable effect, viz,

$$F(Pé) = \pi k_f L \Delta T \left(\frac{1}{Q(0)} - \frac{1}{Q(Pé)} \right) .$$

For low aspect ratio sensors a plot of $F(Pé)$ versus $\ln Pé$ is observed to be linear for $Pé > 0.30$. From this calibration information a new formula is developed for the direct calculation of low turbulence intensities from measured variables, viz.,

$$\frac{\sqrt{\overline{w^2}}}{\overline{u}} = \frac{2}{S} \left[\frac{\pi k_f L \Delta T (R_s + R^*)^2}{R_s} \right] \sqrt{\frac{\overline{e^2}}{\overline{E}^3}}$$

The particular merits of this formula are that it is independent of slow signal drift and that it depends only on the measured variables at the investigated flow condition. It is successfully tested experimentally in a hydrodynamic turbulence field in mercury for various values of ΔT and thermal contact resistance.

The second section applies the hot-film techniques to a study of steady and unsteady electrically driven flows between circular electrodes in mercury. Circular copper electrodes are placed opposite one another in parallel, insulating planes with mercury between them in the presence of a uniform magnetic field, $B_z = B_0$, normal to these planes. When electric current passes between these electrodes and

the Hartmann number, M, is sufficiently large, steady shear layers having a velocity profile, $u_\theta(r, z)$, and a thickness, $\delta = O(M^{-1/4})$, join the edges of the electrodes. At the onset of instability in these layers, electromagnetic forces control the growth of the most unstable disturbances if the magnetic field is sufficiently strong. The instabilities grow until a steady, wave-like secondary flow is produced containing vorticity concentrations which are periodic in θ and which travel at constant speed in the θ-direction, the direction of the primary flow. The waves are observed to extend in a direction parallel to $\underset{\sim}{B}_o$.

The third section applies the hot-film technique to a preliminary experiment on the suppression of vorticity downstream from a square-array grid of circular tubes in a uniform, transverse magnetic field. The observed effects result from the well known tendency for a magnetic field to suppress the components of vorticity which are perpendicular to itself. If B_o is large enough, eddies are only allowed to separate from those wires in the square array which lie parallel to $\underset{\sim}{B}_o$. For smaller B_o, a non-homogeneous field of decaying turbulence exists.

1. Introduction

The problem of devising and applying a sensing element to measure instantaneous velocity within MHD flows has been the concern of many investigators during the past decade. In order for such a sensing element to respond quickly to changing events at its surface it must be very small. To withstand the high drag forces at relatively low velocities in liquid metals, this small element must also be of high strength. In addition, the chemically active nature of liquid metals and their high electrical conductivity severely limits the choice of materials from which a sensor can be constructed. Branover, Slyusarev and Shcherbinin (1965) made one of the first serious attempts to solve the problem by employing a strain gauge technique to measure the fluctuating drag on a 2.15 mm diameter teardrop probe in a turbulent mercury flow. The size of the probe precludes the measurement of small scale turbulence, however, and the signal-to-noise ratio is not very high. About the same time Sajben (1964, 1965) made a very important contribution. He employed the constant current thermo-anemometric technique to operate an enamel-insulated, tungsten wire (of dimensions 0.043 x 5 mm) in mercury with some success. The technique was used by Sajben and Fay (1967) to study the effects of an axial magnetic field on the growth of a turbulent mercury jet and by Fraim and Heiser (1969) to study the effect of an axial magnetic field on transition to turbulence in a circular duct flow of mercury.

Sajben (1965) developed a special calibration procedure in order to eliminate as nearly as possible the effects of the non-wetting, thermal contact resistance layer which surrounds a non-metallic element in mercury and which has extremely variable physical properties. This same calibration procedure is used in the present work. It is interesting to note that Lielpéteris (1960) attempted to develop an electrically heated sensor for mercury and that he also noted the changeable heat transfer effects at the sensor-fluid interface which, apart from using Sajben's method, frustrate any attempt to arrive at a

steady calibration. Sajben's hot-wire technique is somewhat unsatisfactory for quantitative measurements because of the large heating currents involved for the large diameter wire and because of the fluctuating heat transfer which occurs naturally under constant current operation and which causes rather severe lag in the thick thermal boundary layer.

The constant temperature thermo-anemometric technique has now been advanced to a very reliable state (see Freymuth (1967)) so that the operation of hot-film sensors in liquids has become feasible. An industrial firm, Thermo-Systems Inc., St.Paul, Minnesota, U.S.A., has been successful in depositing a thin insulating layer of quartz, of $O(10^{-3})$ mm in thickness, on cylindrical, platinum film sensors which are as small as 0.025 mm in diameter. A sketch of such a sensor is shown in Figure 1. These sensors have proved their reliability for measurements in mercury in the studies of Hill (1968) and Hoff (1968) as well as in the present work. Wedge-type, quartz-insulated hot-film sensors are also produced by Thermo-Systems Inc. and by DISA Elektronik A/S, Herlev, Denmark. However, the cylindrical sensors are preferable for probing thin shear layers and in low speed flows where MHD effects on heat transfer are considerable.

Hill (1968) has examined the directional sensitivity of a cylindrical hot-film in mercury without a magnetic field and has found this sensitivity to depend on the flow velocity. His work should be examined in detail before measurements with an X-array are attempted.

Hoff (1968) has increased the sensitivity of cylindrical sensors in mercury by depositing a thin film of copper or gold over the quartz insulation to improve the surface wetting. This technique has also eliminated some of the signal drift effects caused by the contact-resistance layer. He has successfully operated 0.150 mm diameter sensors at speeds up to 1.5 m/sec and wedge-type sensors up to about 4.5 m/sec.

As far as is known, no research has been seriously attempted yet in applying hot-film techniques to liquid metals other than mercury.

Water-cooled hot-film sensors are also produced by Thermo-Systems Inc. for work in combustion gases. Few results are yet available, except for the original work of Fingerson (1961), although some fundamental work has recently been completed by Fingerson and Ahmed

(1968) at McGill University, Canada. A qualitative study is in progress at Manchester University, England, by Stoneham (1968) who is attempting to operate a cooled sensor in the cylinder of a diesel engine.

One problem needing further study concerns the dynamic response of constant temperature hot-films in low Prandtl number fluids. It might be expected that the thermal inertia of the thick thermal boundary layer would be troublesome. Sajben (1965) reported a response time in mercury of about 10^{-3} sec for his constant current hot-wire. By applying the conventional square-wave test, the response time of the 0.030 mm diameter constant temperature hot-films used in this study is estimated to be less than 10^{-4} sec.

The details of the work described in this paper are to be found elsewhere (Malcolm (1968a)). The work on hot-film sensor calibration and turbulence measurement in mercury has been described, in detail, except for MHD effects on the heat transfer, by Malcolm (1968b).

The experimental techniques are developed in §2 of the paper and for demonstration purposes are applied to two MHD experiments in §3 and 4. Section 3 describes an experimental study of steady electrically driven flow between circular electrodes, the onset of instability in this flow and the subsequent development of secondary flow. For the theory involved in the steady flow case and for details of the electrically driven flow apparatus, refer to Hunt and Malcolm (1968). Interesting experiments using Pitot tubes and electric potential probes are also described there. Refer to Malcolm (1968a) and Malcolm (1969) for a discussion of a possible physical mechanism for instability which applies to this electrically driven, three-dimensional, MHD shear layer. Section 4 presents the results of a hot-film investigation of vorticity decay behind a square-array grid of wires in a uniform, transverse magnetic field.

2. Constant temperature hot-film anemometry in mercury.

As a first approximation, the hot-film sensor in Figure 1 may be considered as a uniformly heated, very long, composite cylinder which is placed in a mercury flow. The effect of a magnetic field will be discussed later. If the physical properties are constant an equation for the steady rate of heat transfer may be written as,

$$\frac{\pi k_f L \Delta T}{Q(P\acute{e})} = \frac{1}{Nu(P\acute{e})} + K, \qquad (2.1)$$

where k_f is the thermal conductivity of mercury, L is the film length, ΔT is the temperature difference, Q is the rate of heat transfer, Nu is the Nusselt number, P$\acute{e}$ is the Prandtl-Reynolds number product, PR, or P$\acute{e}$clet number and K is a velocity independent term which depends upon the physical properties of both the insulating coating and the thermal contact resistance layer which exists at the sensor-fluid interface. K will generally drift in value between calibrations or with each reimmersion of the sensor through a mercury free surface. Sajben (1965) found experimentally that the effects of large changes in K could be eliminated by the calibration procedure,

$$F(P\acute{e}) = \pi k_f L \Delta T \left(\frac{1}{Q(0)} - \frac{1}{Q(P\acute{e})}\right) = \frac{1}{Nu(0)} - \frac{1}{Nu(P\acute{e})} . \qquad (2.2)$$

Experiments have shown (Malcolm (1968b)) that the equation (2.2) yields similar calibration curves for a finite-length sensor ($L/d \simeq 20$) as ΔT varies over a range of $O(10)^\circ C$ and as $\pi k_f L \Delta T / Q(0)$ varies from 3.3 to 8.2 owing to changes in properties of the peculiar contact resistance layer. These latter changes were brought about experimentally by repeated reimmersion through both a water-mercury interface and an air-mercury interface. The similarity over a short range of temperature is reasonable since the forced convection Nusselt number, Nu(P$\acute{e}$), is expected to be a function of P$\acute{e}$ alone (see Cole and Roshko (1954) and Grosh and Cess (1958)) and since the Nusselt number at no flow, Nu(0), containing the combined effects of conduction (see Cole and Roshko (1954) for a discussion of finite length conduction) and free convection (the Grashof-

Prandtl number product, GP, was $O(10^{-3})$ in the experiments) is expected to be only weakly dependent on temperature.

The above-mentioned experiments have shown that $F(P\acute{e})$ is a linear function of $\ell n P\acute{e}$, at least over the range, $0.3 \leq P\acute{e} \leq 1.0$, where $P\acute{e}$ becomes sufficiently high for forced convection to completely overshadow the complicated heat transfer which occurs at $P\acute{e} = 0$. Although the conditions of their theory are not strictly applicable to the present experiments, it is noteworthy that Cole and Roshko (1954) predicted a linear dependence of $1/Nu(P\acute{e})$ on $\ell n P\acute{e}$, the slope of the curve being $-\frac{1}{2}$, as a result of a theory based on the Oseen approximation for low values of $P\acute{e}$ and R. The slope of the straight line portion of $F(P\acute{e})$ varies from sensor to sensor but is generally in the range, 0.2 to 0.3. Figures 2 and 3 show F vs $P\acute{e}$ and F vs $\ell n P\acute{e}$ curves, obtained in a tow tank calibration, for a typical 0.030 mm diameter sensor with $L/d \simeq 14.8$. Other calibrations have shown (see Malcolm (1968b)) that velocities as low as about 2 mm/sec, where $P\acute{e} \sim 10^{-2}$, can be measured with such hot-film sensors, providing that the environmental temperature is controlled or measureable to well within 10^{-1} °C or that electronic temperature compensation is built into the anemometer system.

Using the calibration curve in Figure 3, (2.1) can be rewritten in the form,

$$\frac{\pi k_f L \Delta T}{Q(P\acute{e})} = A - S \ln P\acute{e}, \qquad (2.3)$$

where A contains all effects which are independent of $P\acute{e}$. Equation (2.3) may be used to develop a simple formula for the measurement of low turbulence intensities in mercury. If $Q(P\acute{e})$ is replaced by the ohmic dissipation of the sensor, the turbulence equation may be developed by, firstly, differentiating (2.3) with respect to the instantaneous velocity, secondly, substituting the fluctuations in measured voltage and velocity for their respective differential quantities and, finally, taking the rms of the equation in the usual manner, ignoring third order infinitesimals. The resulting equation is,

$$\frac{2}{S}\left[\frac{\pi k_f L \Delta T (R_s + R^*)^2}{R_s}\right]\frac{\sqrt{\overline{e^2}}}{\overline{E}^3} = \frac{\sqrt{\overline{u^2}}}{\overline{u}}, \qquad (2.4)$$

where $\overline{E}$ is the mean voltage across the sensor resistance, R_s, and a resistance in series with it, R*(which represents probe body resistance, etc.), and $\sqrt{\overline{e^2}}$ is the rms of the random voltage fluctuations which

corresponds to the rms intensity of the velocity fluctuations, $\sqrt{\overline{u'^2}}$, about the mean velocity, $\bar{u}$.

Equation (2.4) possesses the unique advantage of being independent of any reference condition such as Q(0), so that the calculation of turbulence intensity is independent of signal drift, provided only that the drift is on a much slower time scale than that required to measure a corresponding pair of values, $\bar{E}$ and $\sqrt{\overline{e^2}}$. Since signal drift is very difficult to eliminate, it is expected that (2.4) will give more accurate results than more sophisticated techniques which allow for the linearization of E with respect to the instantaneous velocity, U. Since $\sqrt{\overline{u'^2}}/\bar{u}$ is linearly dependent on ΔT in (2.4), small drift in ambient temperature can be easily accounted for. However, the calibration equation, $F(Pé)$, is very susceptible to temperature drift error at low $Pé$. It may be shown that a 1% drift in ambient temperature ($O(10^{-1})$°C if ΔT is O(10) °C) can easily give rise to 10% errors in $F(Pé)$, and correspondingly high errors in $Pé$, if $F(Pé)$ is $O(10^{-1})$.

Equation (2.4) has been tested experimentally in a tow tank by mounting the sensor behind a square-mesh grid on the towing trolley. The conclusions were that (2.4) gave consistent results over a wide variation in ΔT (i.e., ΔT varied from 11 to 44 °C in the experiment) and over a wide variation in the properties of the contact resistance layer.

When the MHD experiments were begun it was expected that, if the tiny hot-film sensor were alighed with the applied magnetic field, $\underset{\sim}{B}_o$, so that the vorticity shed by the sensor was nearly all parallel to $\underset{\sim}{B}_o$, MHD effects on the heat transfer would be absent. It was found however that, owing to finite length effects, the free convection heat transfer was significantly altered in the presence of $\underset{\sim}{B}_o$. The MHD effects on the free convection of two hot-film sensors are shown in Figure 4. In order to use the two tank calibration curves it was necessary to make an approximate correction for these MHD effects on $\pi k_f L \Delta T / Q(0)$. The adequacy of the correction cannot be determined since no provision has been made for calibrating within a magnetic field. The correction procedure will now be described.

When electromagnetic forces are present, let the measured calibration function be,

$$F' = \pi k_f L \Delta T \left(\frac{1}{Q_B(0)} - \frac{1}{Q_B(Pé)} \right), \qquad (2.5)$$

when subscript B refers to the presence of a magnetic field. F' will not in general be equal to F, the calibration function outside the magnetic field. From the defining equations, (2.2) for F and (2.5) for F', the error in F is

$$\Delta F = F' - F = \pi k_t L \Delta T \left\{ \left(\frac{1}{Q_B(0)} - \frac{1}{Q(0)} \right) - \left(\frac{1}{Q_B(P\acute{e})} - \frac{1}{Q(P\acute{e})} \right) \right\} . \tag{2.6}$$

By definition, $F = 0$ and $F' = 0$ when $P\acute{e} = 0$ so that,

$$\Delta F = 0,$$

in (2.6).

For some value, $F \geq F_o$, where $P\acute{e}$ is high enough that free convection and MHD effects may be considered negligible, $Q_B(P\acute{e}) = Q(P\acute{e})$, so that from (2.6) the maximum ΔF is

$$(\Delta F)_m = \pi k_t L \Delta T \left(\frac{1}{Q_B(0)} - \frac{1}{Q(0)} \right) . \tag{2.7}$$

This is the equation expressing MHD effects in free convection alone and is easily evaluated experimentally for different values of B_o, as in Figure 4.

For the correction in the range $0 \leq F \leq F_o$, let

$$\Delta F = \gamma (\Delta F)_m , \tag{2.8}$$

where, according to an assumed first approximation,

$$\gamma \propto F. \tag{2.9}$$

Thus, the corrected calibration curve may be represented by the expression,

$$F' = F + \gamma (\Delta F)_m , \tag{2.10}$$

where
$$\gamma = 0 \text{ for } F = 0,$$
$$\gamma \propto F \text{ for } 0 \leq F \leq F_o ,$$
$$\gamma = 1 \text{ for } F \geq F_o .$$

The adequacy of (2.9) for the correction factor is unknown, although for $F \geq F_o$, the correction should be accurate. It should be adequate providing that $(\Delta F)_m / F_o$ is small. For the hot-films used in these experiments, if F_o is taken to be the value of F at the beginning of the

linear variation with $\ell n Pé$, $(\Delta F)_m/F_o \simeq 0.1$. From Figure 4, $(\Delta F)_m$ is about 0.035 for $B_o \geq 0.4$ wb/m^2. The F' curves in Figures 2 and 3 have been drawn on this basis.

3. Electrically-driven flow between circular electrodes

When two electrodes at different electric potentials are placed one in each of two parallel insulating planes, between which is an electrically conducting fluid, and when a magnetic field is applied normal to these planes, a flow is induced in thin layers which join the edges of the electrodes. This effect was first fully appreciated by Moffatt (1964). Some of the fluid mechanical and electrical phenomena which occur for different electrode geometries have been described in a paper in three parts by Hunt and Williams (1968), Hunt and Malcolm (1968) and Hunt and Stewartson (1969).

Of particular interest to the present research is part 2 by Hunt and Malcolm. This paper describes, both theoretically and experimentally, the case where the electrodes are circular and positioned directly opposite from one another. When the Hartmann number, $M = B_0 a \sqrt{\sigma/\eta}$, is large, i.e. $M >> 1$, it was found that the current was channelled or, in other words, confined to the cylinder of fluid joining the electrodes. This effect is accounted for by the action of the induced electric field, $\underset{\sim}{u} \times \underset{\sim}{B}$, through the velocity component, u_θ, which is induced by $\underset{\sim}{j} \times \underset{\sim}{B}$ forces in thin layers with thickness $O(M^{-\frac{1}{2}})$ at the circumference of the cylinder. Through the layers the electric potential, ϕ, falls and u_θ is induced in the manner shown in Figure 5. The azimuthal velocity, u_θ, falls to zero on the centreplane between the electrodes and is of opposite sign on either side of this plane.

The experimental examination of this situation by the hot-film technique was accomplished by inserting a hot-film sensor into the region of the flow between the copper electrodes in a uniform magnetic field as described in detail elsewhere (Malcolm (1968a)). The electrically-driven flow apparatus was positioned with the z-axis (see Figure 5) and the hot-film sensor horizontal. The sensor was traversed vertically through the layer at the top of its travel where u_θ was horizontal, so as to make use of an F' calibration curve similar to that shown in Figure 2. Applicable non-dimensional co-ordinates which describe the flow are, the radial direction, $\varrho = r/a$, and the axial direction, $\zeta = z/a$. The ratio of the diameter of the electrodes to the distance between them is $\ell = b/a$. The velocity profiles in the shear layers should be similar if they are plotted as $u_\theta M^{1/2} b \ell \sqrt{\sigma/\eta} / I$ against

$\bar{\rho} = (\rho - \ell) M^{1/2}$, where σ and η are electrical conductivity and viscosity, respectively, and where I is the driving current.

Some of the hot-film measurements are shown in Figure 6, for $f \simeq 0.90$ (i.e. quite near one of the electrodes), for three high values of M. The readings were very reproducible so that the effects of varying M are quite definite. It is expected that for the largest value of M, 588, the flow is approaching the asymptotic case for $M^{\frac{1}{2}} >> 1$, $\ell M^{\frac{1}{2}} >> 1$, which was predicted by Hunt and Malcolm (1968). Theoretically, $u_\theta M^{1/2} b \ell \sqrt{\sigma\eta}/I$ should fall to zero at about $\bar{\rho} = -1$. It is interesting in this respect that the values of the velocity term in Figure 6 decrease as M increases for $\bar{\rho} < 0$. The fact that the experimental curves level off when $\bar{\rho} < 0$ to a nearly constant, apparent value of $u_\theta M^{1/2} b \ell \sqrt{\sigma\eta}/I$ can probably be attributed to radial flow, which was ignored in the theoretical analysis because of the assumption $\ell M^{\frac{1}{2}} >> 1$. The largest value of $\ell M^{\frac{1}{2}}$ in the experiment is approximately 12.2, which cannot truly be said to be very large, so that measureable radial flow is expected. This radial flow phenomenon also points out a basic weakness of the hot-film technique in that it is sensitive to all velocity components normal to itself and cannot therefore differentiate between u_r and u_θ.

A similar experimental profile at $f = 0.50$ is shown in Figure 7. Also shown in this figure are some provisional theoretical values which have been calculated according to the complete asymptotic analysis of Hunt and Stewartson (1969) and have been kindly provided by Hunt. The agreement is seen to be quite good except for $\bar{\rho} < 0$ where, again, non-zero components, u_r and u_z, are likely to exist. It is unfortunate that, because of these secondary flow components, the theoretically predicted negative velocity region for $\bar{\rho} \simeq -1.0$ could not be detected. The hot-film sensor was called upon to measure velocities lower than 0.8 cm/sec to obtain each of the experimental points in Figure 7. It is evident then, that the hot-film technique is a powerful one at low velocities.

In order to study stability and secondary flow in the electrically-driven shear layer the driving current was increased while holding the magnetic field constant, for each of a large range of magnetic field values, until critical conditions were reached. The onset of instability was observed by positioning the hot-film sensor in the outer, low velocity region of the shear layer and following the anemometer output signal on the oscilloscope while the current was being increased. The determination

of a critical current, I_c, was very tedious because of the necessity of approaching critical conditions very slowly and not forcing the onset of instability. When the current value was near critical it was necessary to observe the system for about three minutes before making the next very small increase.

At the onset of instability, interesting phenomena observed on the oscilloscope were recorded using Polaroid film. From the information contained in these oscillograms at various probe positions, and from the measured values of I_c and M, it was possible to describe the phenomena involved in instability and secondary flow both qualitatively and quantitatively and to substantiate the physical mechanism proposed in Malcolm (1968a). This stability study is continuing and will be published by Malcolm (1969).

Figure 8 shows the I_c vs M results, from which it appears that the data may be adequately described by the following empirical relationships:

$$I_c = 2.07M \times 10^{-3}, \quad 150 \leq M \leq 350, \tag{3.1}$$

and

$$I_c = 2.95M^{4/3} \times 10^{-4}, \quad 350 \leq M \leq 650. \tag{3.2}$$

In Hunt and Malcolm (1968) some preliminary hot-film results were given as:

$$I_c \propto M, \quad M > 200.$$

The data plotted in Figure 8 have been obtained in more carefully controlled expriments over a much wider range of M. The result stated in the paper, i.e. $I_c \propto M$, still appears to hold, although over a more limited range of M. In the same paper it was reasoned by order of magnitude arguments that the critical Reynolds number, $R_c = u_{0c}\delta\rho/\eta$, is related to I_c and M by,

$$R_c \propto I_c/M, \tag{3.3}$$

By combining (3.1) and (3.2) with (3.3) it is seen that,

$$R_c = \text{a constant}, \quad 150 \leq M \leq 350, \tag{3.4}$$

and

$$R_c \propto M^{1/3}, \quad 350 \leq M \leq 650. \tag{3.5}$$

The fact that R_c is a constant, independent of M, in (3.4) suggests that the magnetic field is not strong enough to have an observable effect on the growth of the most unstable three-dimensional disturbances which occur naturally in this three-dimensional shear layer. Its effect on the stability is through changing the shape of the velocity profile, i.e., at constant I, $u_0 \propto M^{-\frac{1}{2}}$ and $\delta \propto M^{-\frac{1}{2}}$, so that R decreases as M increases.

On the other hand, the dependence of R_c on M in (3.5) suggests that when the magnetic field becomes sufficiently high, it has an observable, direct effect on the growth of the most unstable disturbances.

The critical Reynolds numbers in (3.4) and (3.5) may be approximately evaluated from the following definition of R_c, viz.,

$$R_c = u_{\theta c}(6aM^{-1/2})\ell/\eta , \tag{3.6}$$

where $u_{\theta c}$ is the critical velocity which occurs near the electrode edge in the region of highest velocity and $6aM^{-\frac{1}{2}}$ is the approximate shear layer width as shown previously in the velocity profiles (e.g., see Figure 7). Although it was not possible to come close enough to the walls to measure velocities in the region of highest velocity with the hot-film sensors, since that region occurs at a distance of approximately aM^{-1} away from the wall, use can be made of a theoretical prediction by Hunt and Stewartson (1969) that the maximum velocity in the shear layer occurs near $\zeta = 1.00$ and is given by:

$$u_0 M^{1/2} b\ell\sqrt{\sigma\eta}/I \simeq 0.226 .$$

From this information, and the fact that Figure 7 showed reasonable agreement between theory and experiment, the critical velocity can be determined as follows,

$$u_{\theta c} = \left(\frac{0.226}{a\ell^2\sigma^{1/2}\eta^{1/2}}\right)\frac{I_c}{M^{1/2}} . \tag{3.7}$$

Now, (3.7) can be substituted in (3.6) to give,

$$R_c = \left(\frac{1.36\,\ell}{\ell^2\sigma^{1/2}\eta^{3/2}}\right)\frac{I_c}{M} . \tag{3.8}$$

If I_c in (3.8) is replaced by (3.1) or (3.2) the critical Reynolds numbers can be calculated and are given as follows, using properties of mercury at 20°C,

$$\left.\begin{aligned} R_c &= 2420 \quad , \quad 150 \leq M \leq 350, \\ R_c &= 345M^{1/3} \quad , \quad 350 \leq M \leq 650 . \end{aligned}\right\} \tag{3.9}$$

The observed oscillograms at the onset of instability confirmed qualitatively the results of Figure 8. When M was less than about 300 it was observed that the onset of instability proceeded in an erratic and non-reproducible manner, corresponding qualitatively to the wide

scatter in the I_c vs M results of low M. For $M \geq 300$, however, instability was always observed to occur in the same controlled, reproducible manner and ultimately to produce a wave-like secondary flow which was periodic in θ with a wave-number which varied with M. The analysis of this secondary flow is continuing and will be reported by Malcolm (1969) (also see Malcolm (1968a)). The physical mechanism by which the magnetic field controls the stability is connected with the fact that the amplitude of the disturbances varies in the γ-direction. It has been found to date, using the hot-film technique, that the secondary flow waves are symmetrical about their peaks and lie parallel to $\underset{\sim}{B}_o$, that their amplitudes decrease as γ decreases until they disappear on the centre plane, that the maximum fluctuation intensity compared to the mean flow speed is about 5%, and that the waves travel in the flow direction with a speed that is proportional to u_{oc}, as calculated from 3.7, and is approximately 15% of u_{oc} in value. There are from 4 to 8 waves around the circumference of the flow, the number increasing as M increases.

This experiment on steady and unsteady electrically driven flow, as well as being interesting in itself, has made use of the cylindrical hot-film's major advantages, good spatial resolution and small flow blockage. The MHD error effects caused by the interaction of electromagnetic forces with the convective heat transfer of the sensors needs more thorough investigation.

4. Vorticity suppression by electromagnetic forces in the wake of a square-array grid

This experiment was attempted to study further the application of the hot-film techniques in MHD and to examine the effect of a uniform, transverse magnetic field on vorticity decay behind a square-array grid of approximate overall dimensions, 5 x 7.5 cm, which was constructed from lengths of 0.071 cm diameter stainless steel tubes and had a mesh dimension of 0.38 cm. This grid of tubes was mounted in a plastic framework which was in turn inserted into a rectangular duct, having non-conducting walls of internal dimensions 5 x 7.5 cm, ahead of the hot-film sensor. The details of the duct and flow circuit are described in Malcolm (1968a). The hot-film sensor could be traversed in all three orthogonal directions.

The procedure was simply to traverse the hot-film probe downstream from the square-array grid in a steady mean flow while applying various magnetic field strengths.

The experiment showed how discomfiting the presence of signal drift can be during startup and shutdown, owing simply to temperature drift of $O(10^{-1})^{\circ}C/min$. This problem was so acute as to make the measurement of Q(0) very imprecise. Consequently the mean flow rate as determined from the F' calibration curve was also very imprecise. For further work it is strongly recommended either that a good temperature compensation circuit be added to the anemometer system or else that a reference velocity be always available in the test section (such as the reference jet used by Sajben (1964, 1965)). It is appropriate at this point to point out a contradiction with the conclusions drawn by Sajben as a result of severe signal drift in his experiment. He experienced severe, erratic signal drift during a period of about two hours after startup and found that temperature drift effects could not account for the phenomenon. He concluded that minute amounts of impurities present in the mercury, which might arise from chemical action between mercury and the stainless steel walls of his system, could change the heat transfer coefficient significantly. This conclusion is contradicted in the present experiment where there was enough chemical action between the mercury and the pvc tubing, perspex channel walls and stainless steel apparatus to give

rise to a continual fresh collection of dark scum on the surface of the mercury in the reservoir tanks. Because the stainless steel pump had only recently been installed, oil droplets also continued to appear on the free surfaces. In contrast to Sajben's experience, a period of about thirty minutes was sufficient in the present experiment for signal drift to be reduced to a low level, which could easily be accounted for by small temperature drift. It may be that the differences between the sensor insulation used in the two cases, i.e. enamel vs quartz, has a significant effect on the complicated heat transfer characteristics of the contact resistance-impurity layer surrounding the sensor.

The mean velocity downstream from the grid was measured to be about 3.2 ± 0.5 cm/sec for the vorticity suppression tests. Although not accurately determined, the flow rate was very constant during any set of conditions. The magnetic field strengths used, 0.275 to 1.22 wb $/m^2$, kept the duct flow smooth and stable.

The qualitative results will be discussed first, followed by the few quantitative results.

When the highest magnetic field was applied, $B_o = 1.22$ wb $/m^2$, the interaction parameter based on the wire diameter was very high, viz., $N_d \cong 2.6$. As expected from the work of Kalis, et al (1965) and Leibovich (1967), no measureable flow separation was allowed from those grid wires which were orientated vertically, perpendicular to $\underset{\sim}{B}_o$. The wake of the grid was then filled with the combined oscillating wakes of the field-parallel grid tubes. At a distance of about 8 tube diameters downstream of the grid, no trace could be detected of any effects on the flow caused by the vertical tubes. The sensor was then traversed in the stream direction to see how the maximum fluctuation intensity of the vortex system decayed with time. As will be seen in the quantitative results this vortex system decayed quite rapidly, whether due to MHD effects at the vortex ends or to intense viscous action in the close-packed vortex array is not certain.

When the magnetic field was lowered to 0.50 wb $/m^2$, with N_d now falling to 0.43, the present of the vertical tubes could just be detected at the 8-diameter station downstream. Also, the velocity fluctuations in the oscillating grid wake were more intense. The decay of this wake system was also examined.

When B_o was still lower, 0.275 wb $/m^2$, N_d had fallen to 0.13 and, as expected, the wakes of the two sets of wires now combined strongly

enough to produce some turbulence. This turbulence had a maximum intensity at $x/L_o \simeq 1.3$, where L_o is the mesh length, and at the centre of a mesh square. The distance x was measured in the direction of flow from the rear edge of the field-parallel tubes which were nearest to the hot-film sensor. The sensor was traversed in the flow direction, along a line through a mesh-square centre, to study the decay of this turbulent vorticity. The oscillograms in Figure 9 show the suppression qualitatively.

The turbulence intensities were calculated using the measurement techniques described in section 2 of the paper.

The vorticity decay results are plotted as $\sqrt{\overline{u'^2}}/\bar{u}$ vs x/L_o in Figure 10. Note that the fluctuation intensities, $\sqrt{\overline{u'^2}}/\bar{u}$, are highest when B_o is lowest, indicating that both y and z-vorticity are present in the grid wake. Accordingly, the $\sqrt{\overline{u'^2}}/\bar{u}$ values are lowest when B_o is highest and only z-vorticity is present. It seems rather strange, as already mentioned, that the vorticity decays so quickly in this situation. The intensity of the vortex trail decays to approximately zero at $x/L_o \simeq 5.0$.

The most interesting curve in Figure 10 is the upper one, since it represents the only part of the study which could be termed "MHD turbulence decay". The interaction parameter of the eddies, N_L, based on the mesh length, L_o, is equal to 70, i.e., $N_L >> 1$. The characteristic suppression time, $(\sigma B_o^2/\rho)^{-1}$, is in this case approximately 0.18 sec. For comparison, the characteristic "eddy turnover time", $L_o/\sqrt{\overline{u_o^2}}$ is about 1.2 sec (where $\overline{u_o^2} \simeq \overline{u'^2}$ at $x/L_o = 1.3$). Consequently, each turbulent eddy newly formed behind the grid may be expected to decay in a time which is much less than the time taken for it to revolve and interact with surrounding eddies. The appropriate data plotted in Figure 10 are obviously not varying linearly with time as in the case of the largest B_o. The presence of such large scatter and the small number of data points requires caution in interpreting the results. The results are plotted as $\ln\left(\sqrt{\overline{u'^2}}/\bar{u}\right)$ vs time, $t = x/\bar{u}$, in Figure 11 and they appear to follow a straight line. Zero time is taken to be at $x/L_o = 1.33$ where $\sqrt{\overline{u'^2}}/\bar{u}$ was observed to be greatest. The equation of the line, drawn in by eye is,

$$\frac{\sqrt{\overline{u'^2}}}{\bar{u}} = 0.10\, e^{-2.44t} = 0.10^{-0.44\left(\frac{\sigma B_o^2}{\rho}\right)t}.$$

It is seen therefore that the turbulent eddies which are newly formed behind the grid seem to decay as $e^{-\beta t}$ and that the damping time is indeed $O(\sigma B_o^2/\rho)^{-1}$.

The results of this experiment indicate that it should be possible to use the hot-film technique to good advantage in measuring turbulence quantities in an MHD duct flow. Turbulent vorticity suppression has been examined both qualitatively and quantitatively in the wake of a square-array grid. In calculating the calibration function, F(Pé), the use of a reference velocity other than no flow is strongly recommended to avoid signal drift effects during startup and shutdown of a flow system.

I wish to thank Professor J.A. Shercliff for originally suggesting the study of thermo-anemometry in MHD, Dr. C.J.N. Alty for many helpful discussions, Dr. J.C.R. Hunt and Professor K. Stewartson for supplying the theoretical curve used in Figure 7 and, finally, Mr. A.E. Webb for his invaluable assistance in the construction and modification of apparatus. I would also like to thank the Royal Commission for the Exhibition of 1851 for making my studies at the University of Warwick possible through an Overseas Scholarship and the University of Saskatchewan who have provided a generous travel grant to enable me to attend the Sixth Symposium on Magnetohydrodynamics.

References

Branover, G.G., Slyusarev, N.M. and Shcherbinin, E.V. (1965). Some results of measurements of turbulent velocity pulsations in a mercury flow in the presence of a transverse magnetic field, Magnetohydrodynamics, 1, 1, 23.

Cole, J. and Roshko, A. (1954). Heat transfer from wires at Reynolds numbers in the Oseen range, Heat Transfer and Fluid Mechanics Institute, University of California, Berkeley.

Fingerson, L.M. (1961). A Heat Flux Probe for Measurements in High Temperature Gases, Ph.D. thesis, University of Minnesota, U.S.A.

Fingerson, L.M. and Ahmed, A. (1968). Private communication.

Fraim, F.W. and Heiser, W.H. (1968). The effect of a strong longitudinal magnetic field on the flow of mercury in a circular tube, to be published in J. Fluid Mech.

Freymuth, P. (1967). Feedback control theory for constant-temperature hot-wire anemometers, Rev. Sci. Inst., 38, 5, 677.

Grosh, R.J. and Cess, R.D. (1958). Heat transfer to fluids with low Prandtl numbers for flow across plates and cylinders of various cross section, Trans. A.S.M.E., 80, 667.

Hill, J.C. (1968). The Directional Sensitivity of a Hot-Film Anemometer in Mercury, Ph.D. thesis, University of Washington, Seattle, Wash.

Hoff, M. (1968). Grumman Res. Memo., Grumman Aircraft Engineering Corp., Bethpage, New York.

Hunt, J.C.R. and Malcolm, D.G. (1968). Some Electrically driven flows in magnetohydrodynamics. Part 2. Theory and experiment, accepted for publication in J. Fluid Mech.

Hunt, J.C.R. and Stewartson, K. (1969). Some electrically driven flows in magnetohydrodynamics. Part 3. The asymptotic theory for flow between circular electrodes, to be published.

Hunt, J.C.R. and Williams, W.E. (1968). Some electrically driven flows in magnetohydrodynamics. Part 1. Theory, J. Fluid Mech., 31, 4, 705.

Kalis, Kh. E., Tsinober, A.B., Shtern, A.G. and Shcherbinin, E.V. (1965). Flow of a conducting fluid past a circular cylinder in a transverse magnetic field, Magnetohydrodynamics, 1, 1, 11.

Leibovich, S. (1967). Magnetohydrodynamic flow at a rear stagnation point, J. Fluid Mech., 29, 2, 401.

Lielpéteris, J.J. (1960). Electromagnetic and Hydrodynamic Processes in the Channel of the Induction Pump, Thesis, Moscow Power Institute.

Malcolm, D.G. (1968a). Thermo-Anemometry in Magnetohydrodynamics, Ph.D. thesis, University of Warwick, England.

Malcolm, D.G. (1968b). Some aspects of turbulence measurement in liquid mercury using cylindrical quartz-insulated hot-film sensors, submitted for publication to J. Fluid Mech.

Malcolm, D.G. (1969). An experimental investigation of the stability of a magnetohydrodynamic shear layer, to be published.

Moffatt, H.K. (1964). Electrically driven steady flows in magnetohydrodynamics, Proc. 11th Int. Cong. Appl. Mech., Munich, 946.

Sajben, M. (1964). Hot Wire Measurements in a Liquid Mercury Jet Subject to an Axial Magnetic Field, D.Sc. thesis, Mass. Inst. Tech., Cambridge, Mass.

Sajben, M. (1965). Hot wire anemometer in liquid mercury. Rev. Sci. Inst., 36, 7, 945.

Sajben, M. and Fay, J.A. (1967). Measurement of the growth of a turbulent mercury jet in a coaxial magnetic field, J. Fluid Mech., 27, 1, 81.

Stoneham, M. (1968). Private communication.

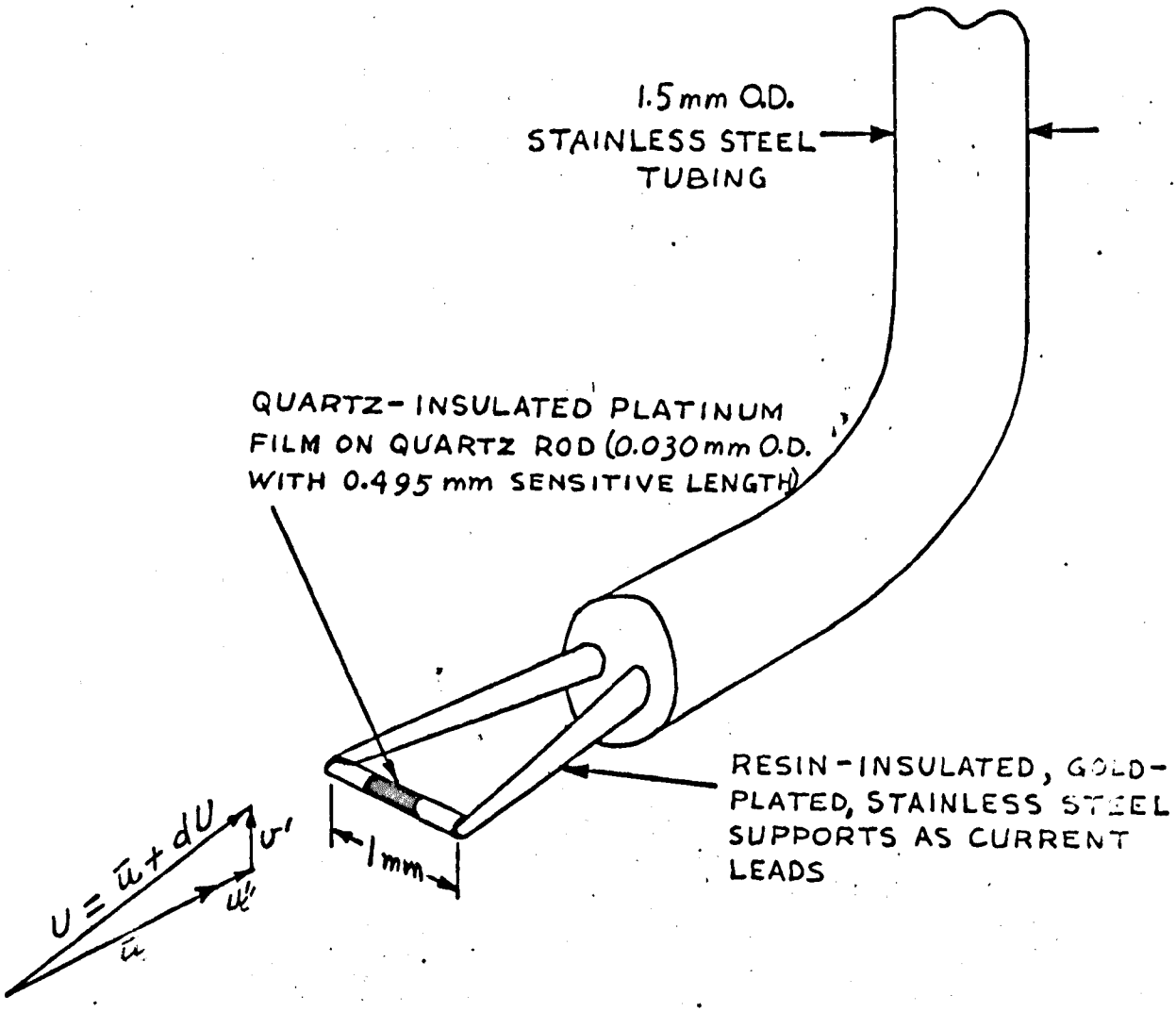

Figure 1 A typical hot-film probe for use in mercury.

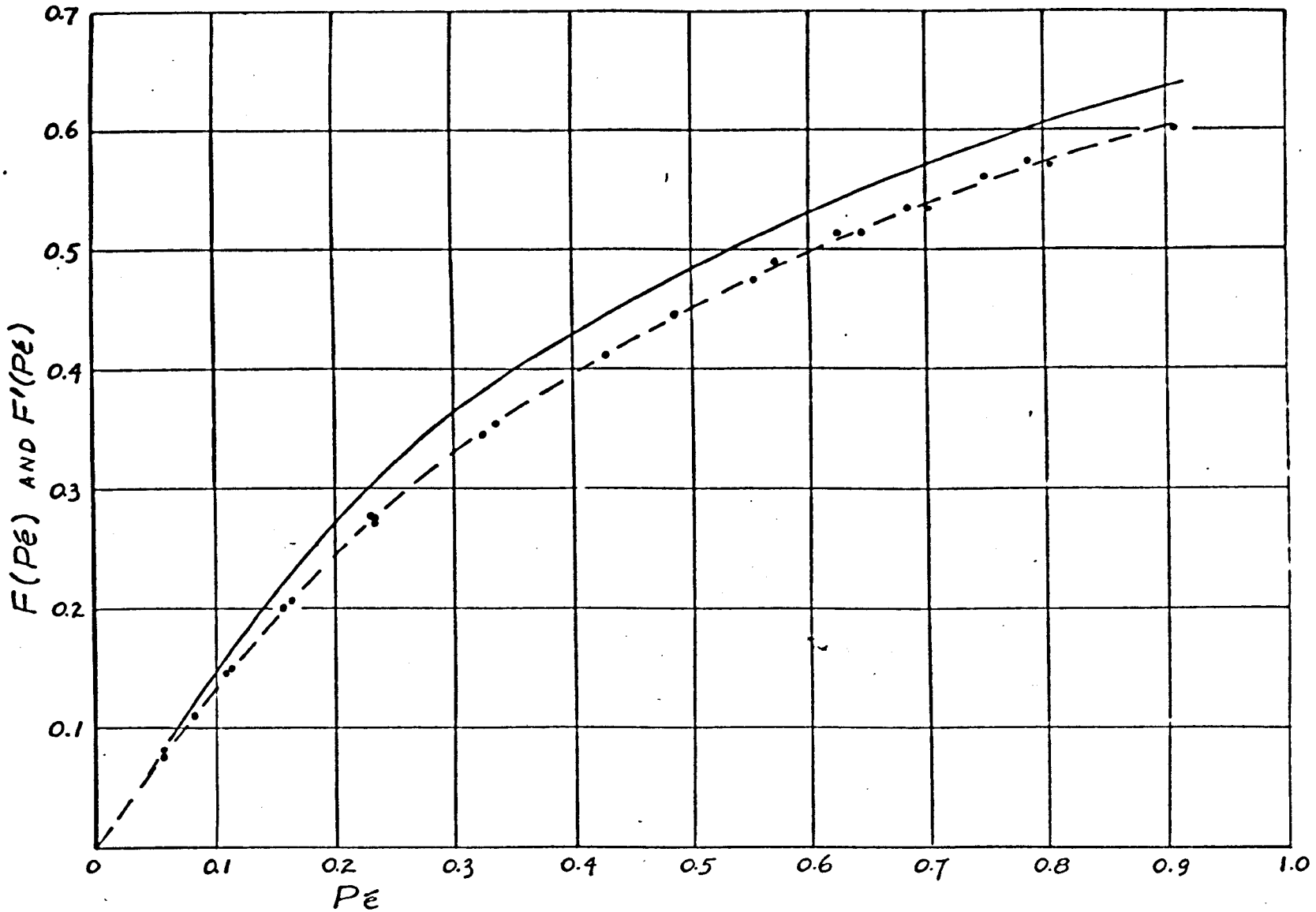

Figure 2 Hot-film probe no. 1 calibration curves: F(Pé) and F'(Pé) versus Pé (• — —, F vs Pé; ———, F' vs Pé).

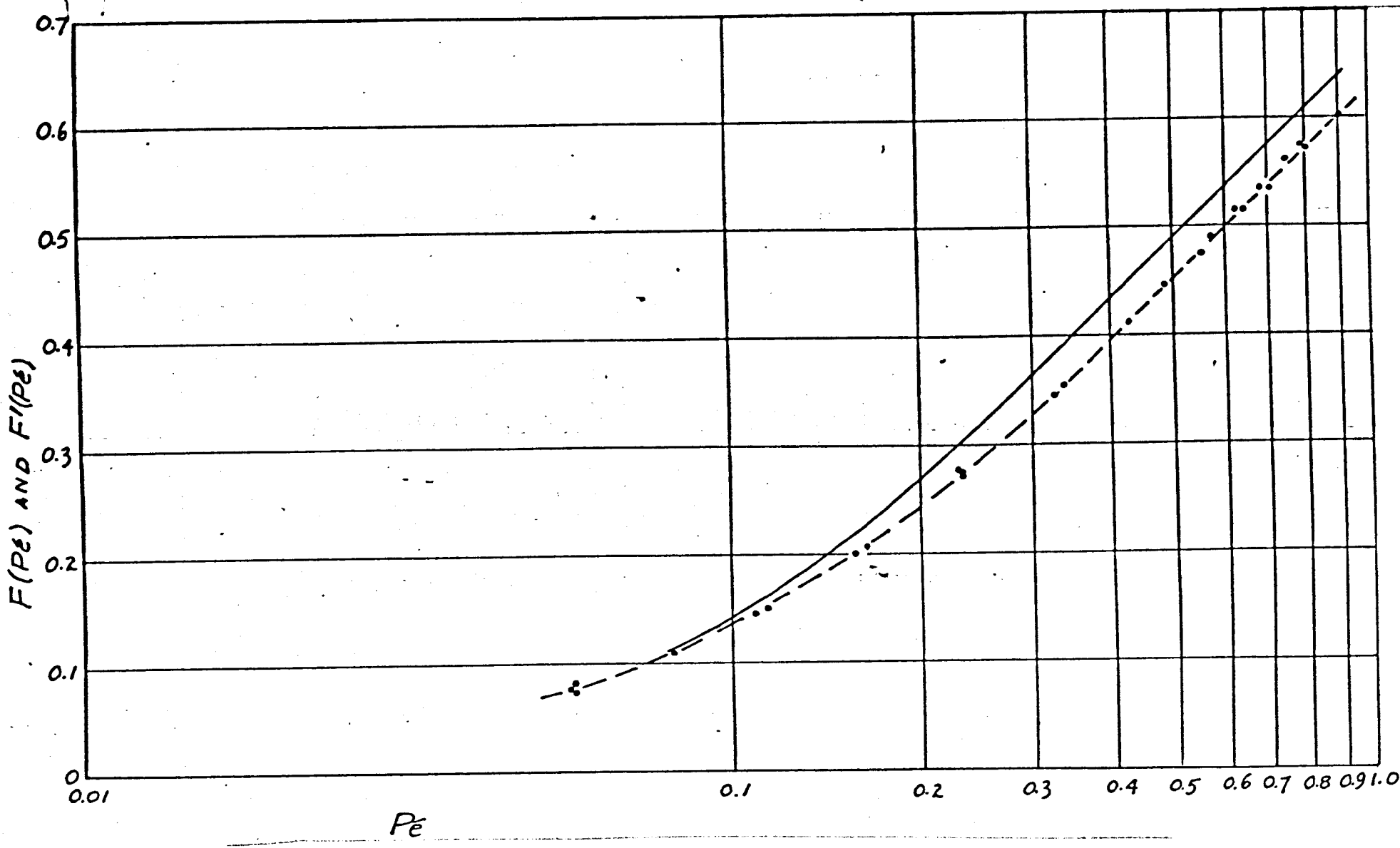

Figure 3 Hot-film probe no. 1 calibration curves: F(Pé) and F'(Pé) versus lnPé (• — —, F vs lnPé; ———, F' vs lnPé).

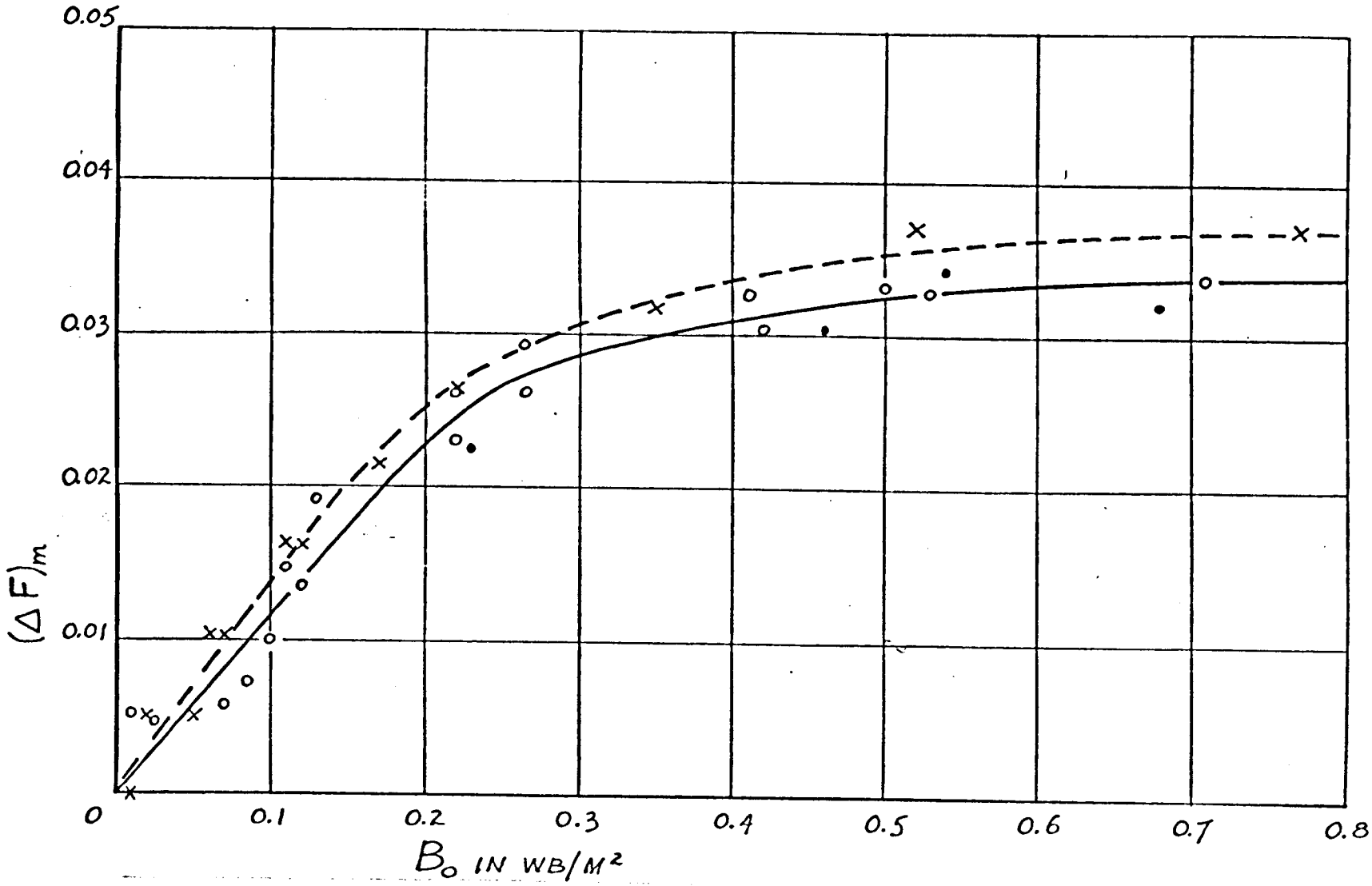

Figure 4 The effects of a magnetic field on free convection from field-aligned sensors (o• ———, sensor no.1, L/d = 15; x – – – –, sensor no.6, L/d = 17).

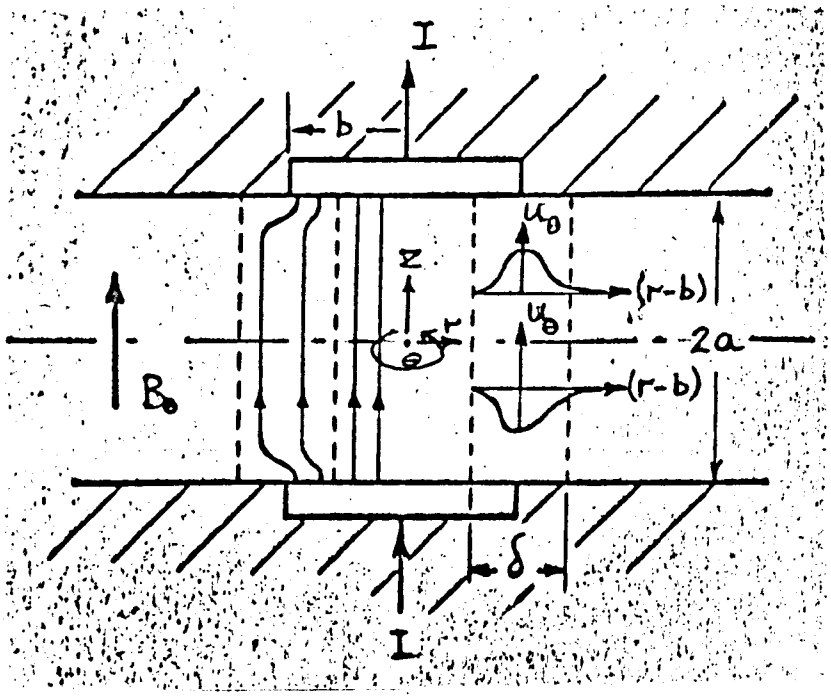

Figure 5 Electrically driven flow between circular electrodes showing current streamlines and velocity profiles when M >> 1 (b = 0.952 cm, a = 1.90 cm).

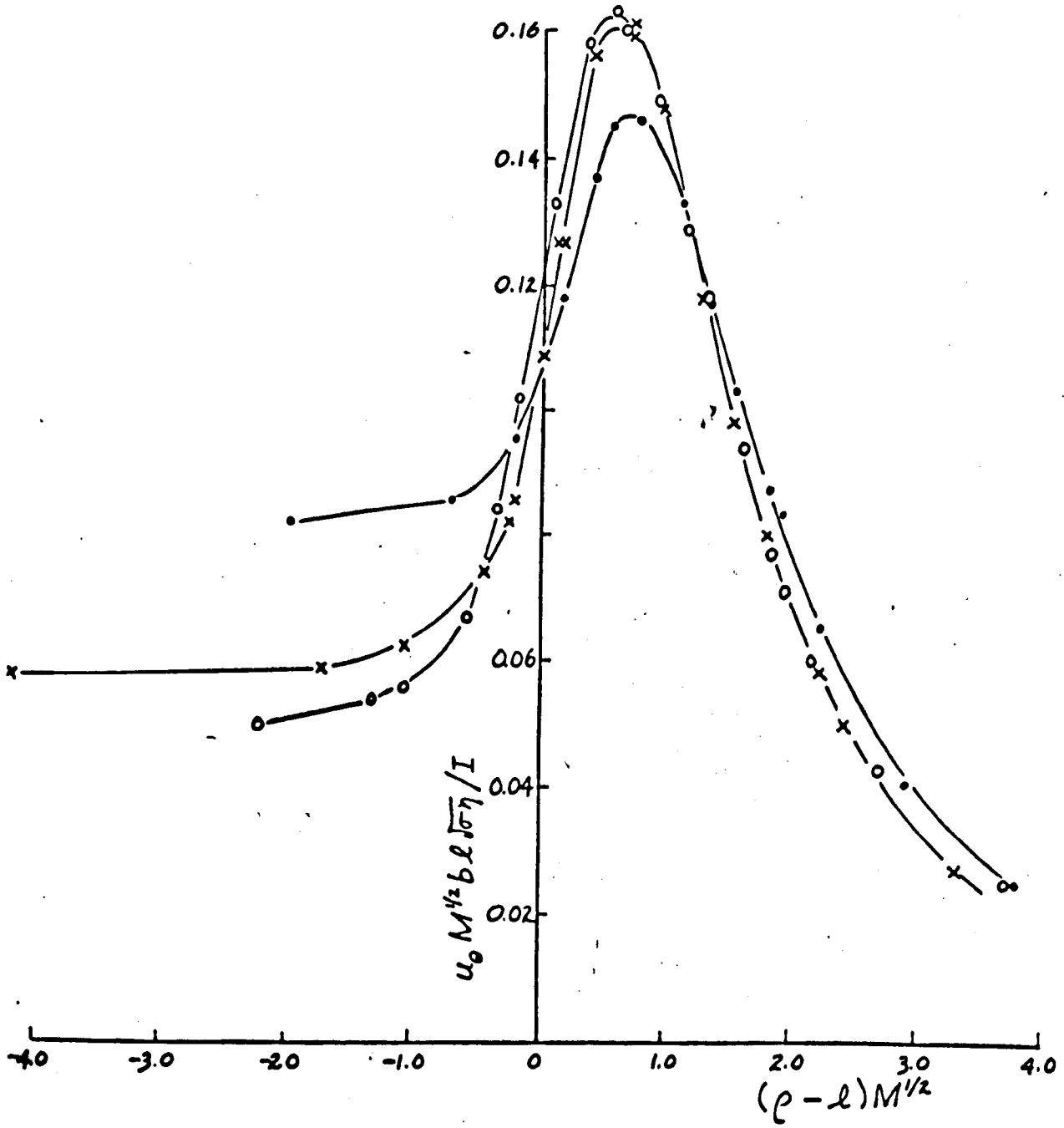

Figure 6 Radial profiles of azimuthal velocity, $\mathcal{J} \approx 0.9$ (•, M = 212, $\mathcal{J}$ = 0.922; ×, M = 390, $\mathcal{J}$ = 0.922; ○, M = 588, $\mathcal{J}$ = 0.905).

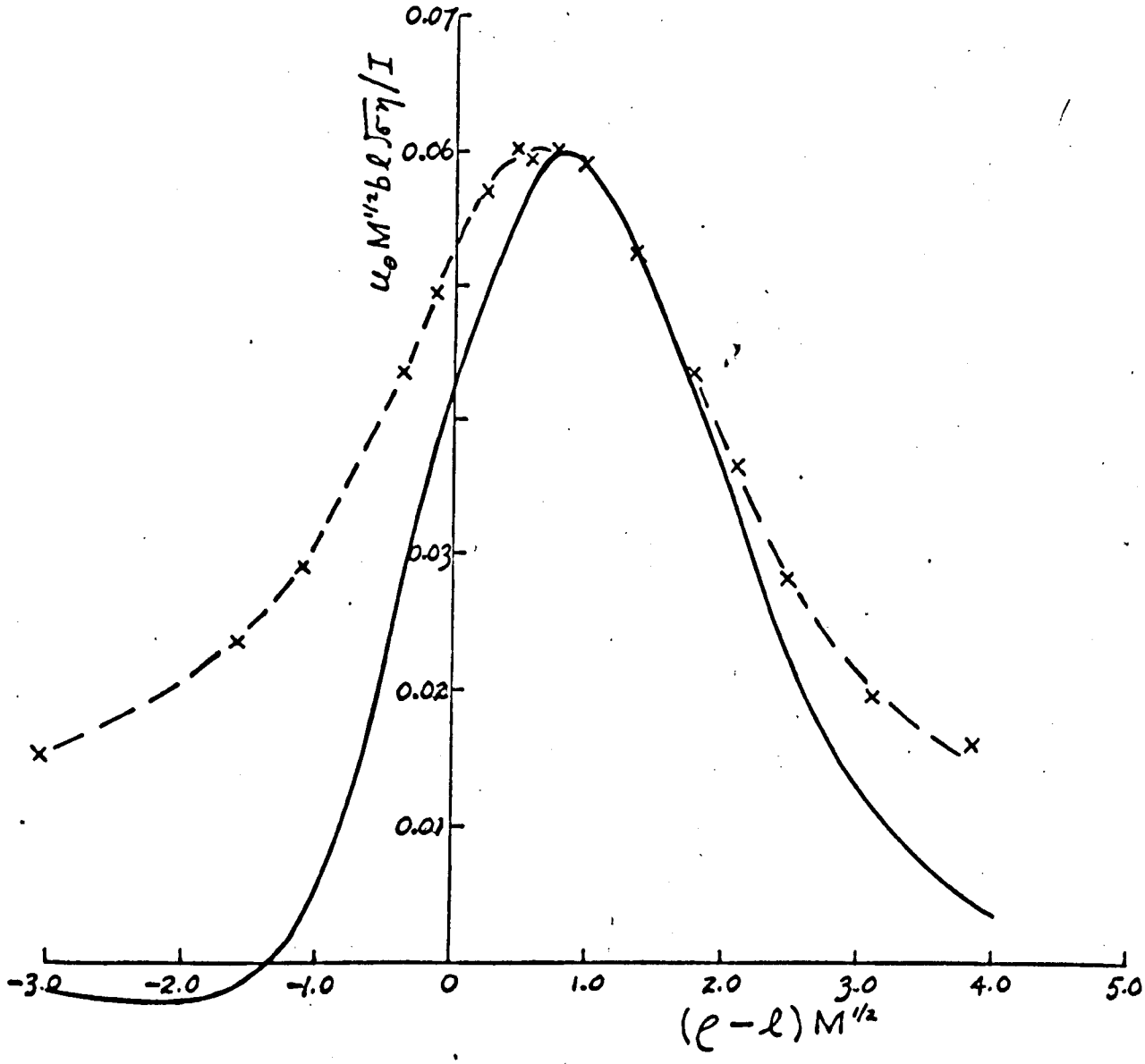

Figure 7 Radial profiles of azimuthal velocity: experimental versus theoretical, $\mathcal{P} = 0.50$, $M = 390$ (× — —, hot-film measurements; ————, theoretical results of Hunt & Stewartson).

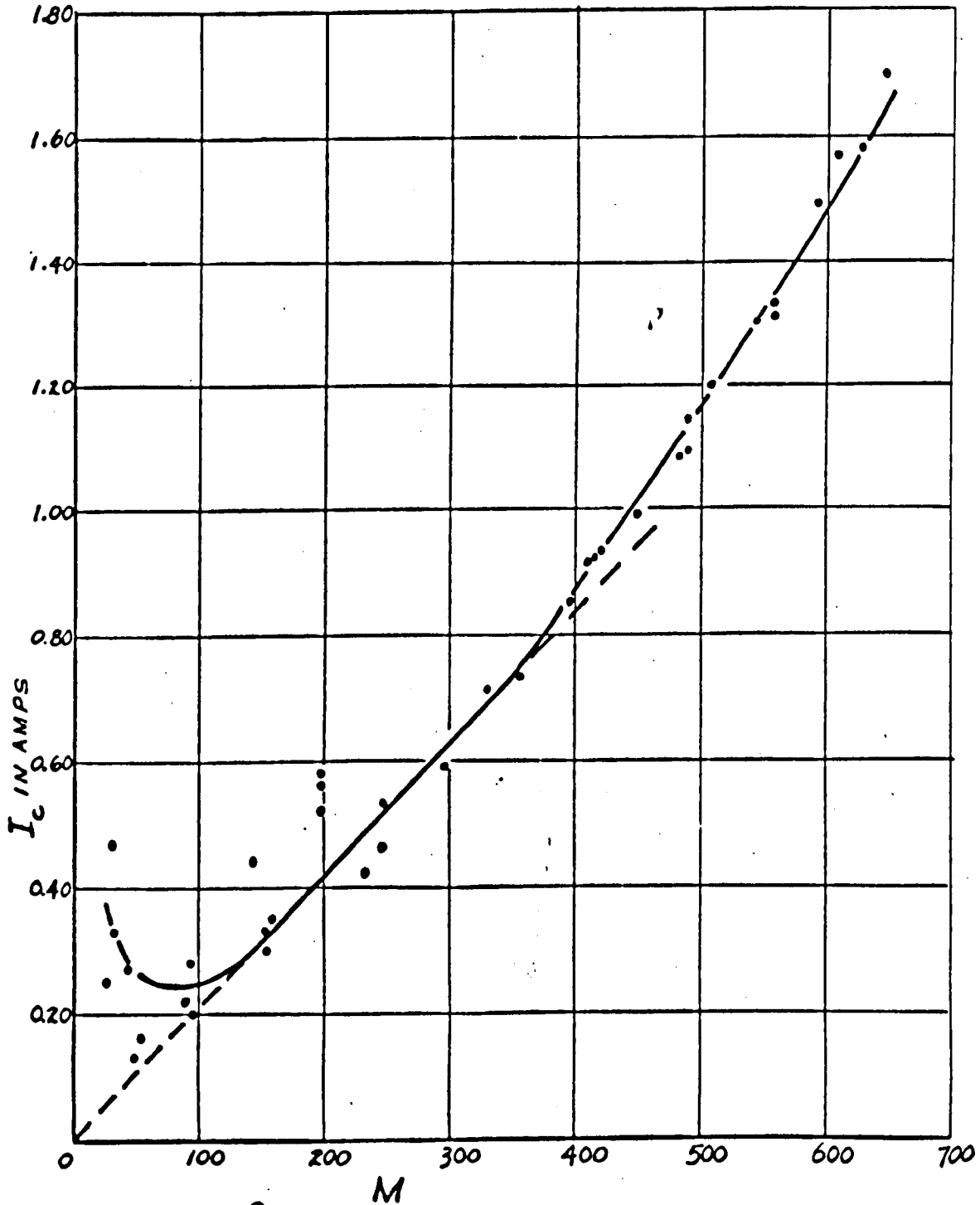

Figure 8 The dependence of critical driving current on Hartmann number in circular electrically driven flow, $\ell = 0.502$.

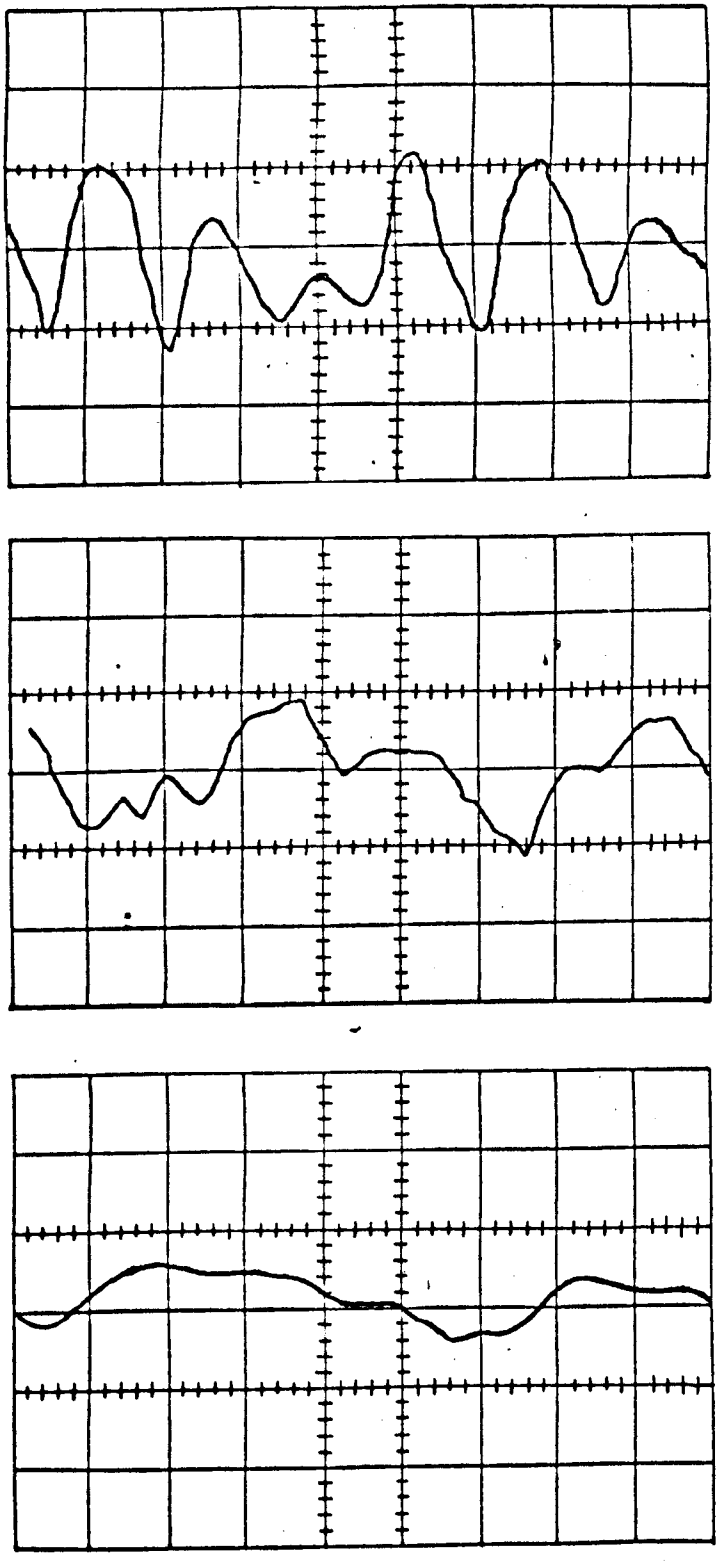

Figure 9 Vorticity suppression behind a square-mesh grid of circular cylinders, $N_d = 0.13$, $N_L = 70$.

Top to bottom: $x/L_o = 1.3$, 3.3 and 6.0.

Scales: 0.1 sec/division, 5 mv/division.

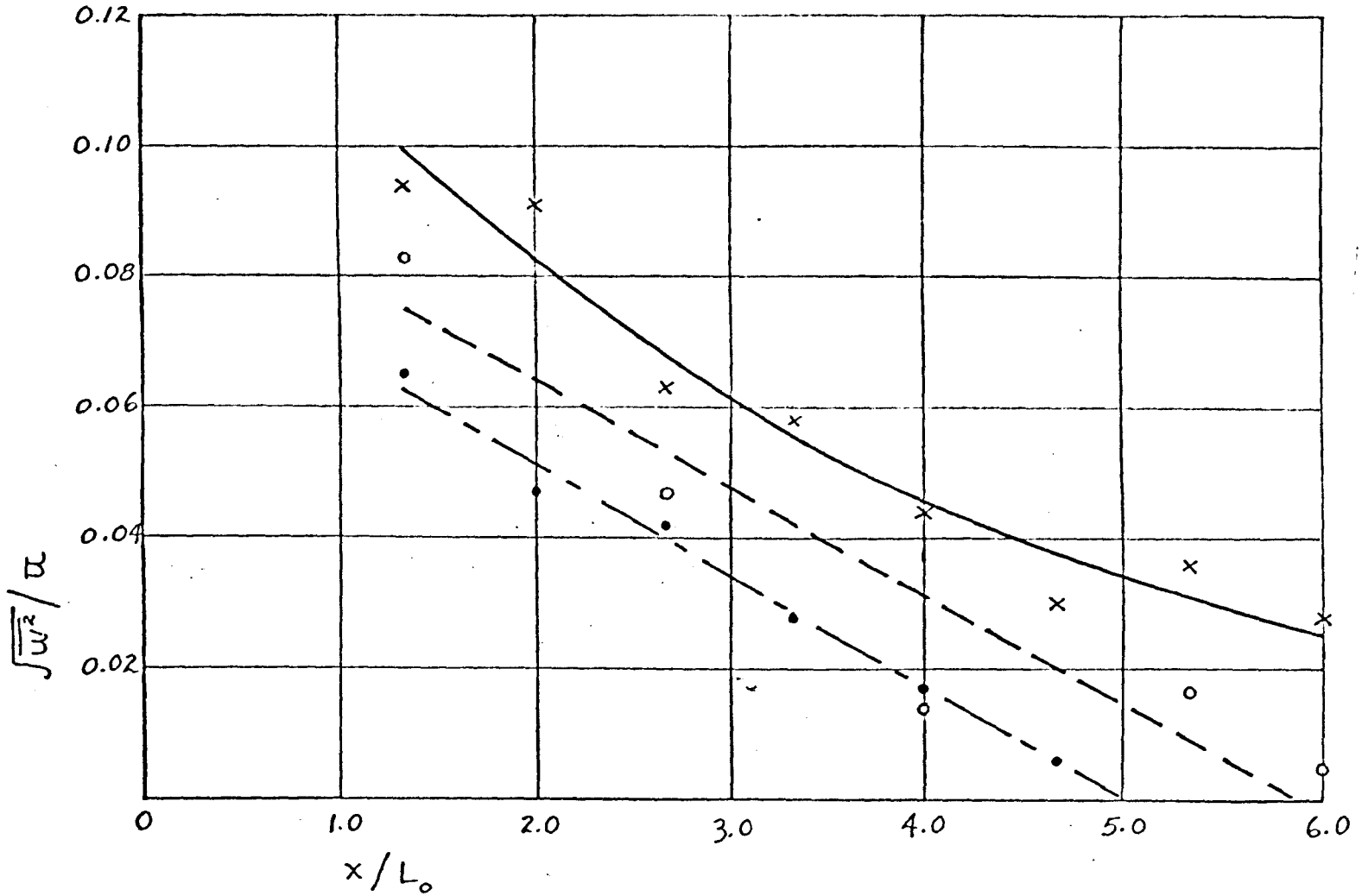

Figure 10 Vorticity suppression behind a square-mesh grid of circular cylinders ($\bar{u}$ = 3.2 cm/sec, L_o = 0.38 cm; • ——— –, B_o = 1.22 wb/m^2; ○ — — —, B_o = 8.50 wb/m^2; × ———, B_o = 0.275 wb/m^2).

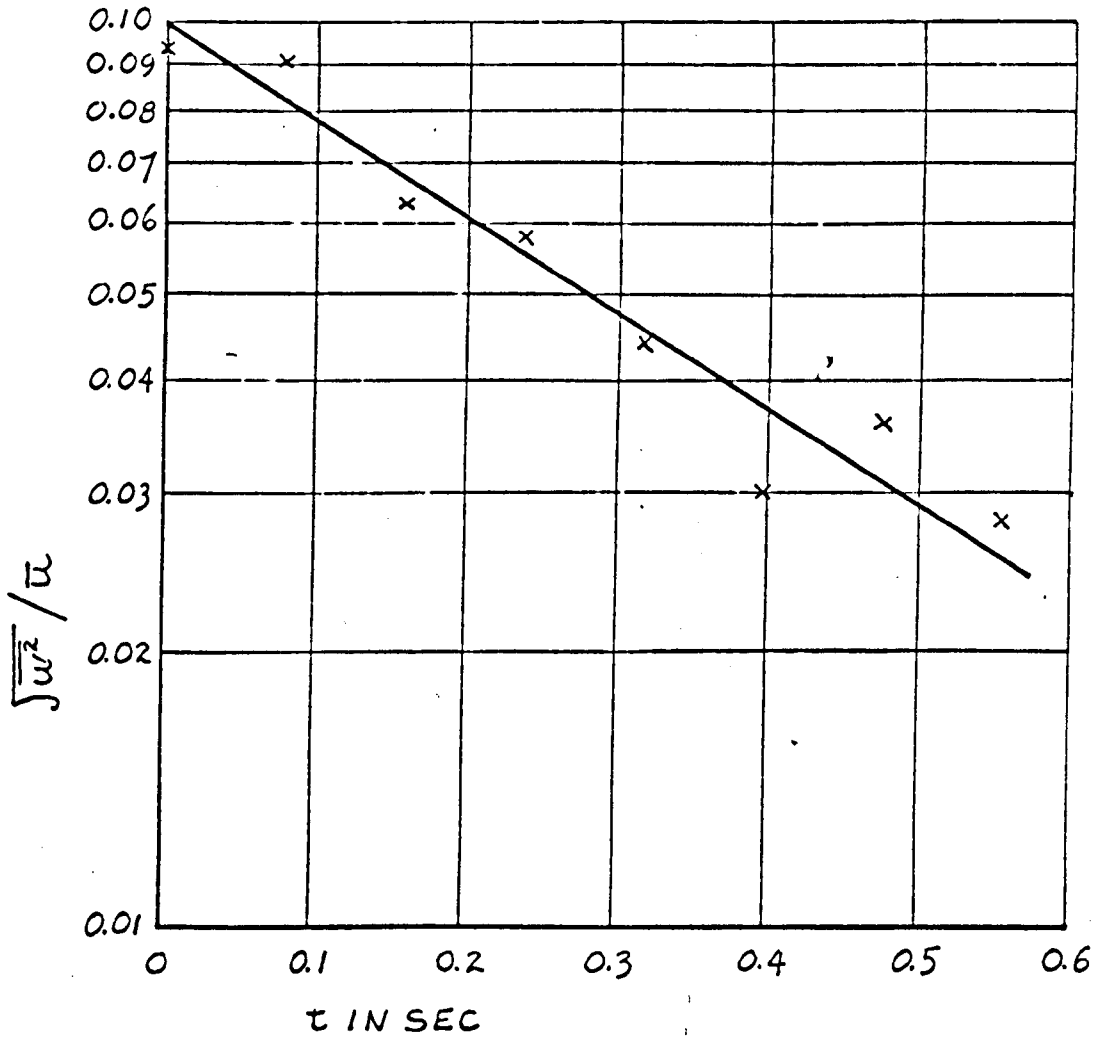

Figure 11 Turbulent vorticity suppression behind a square-mesh grid of circular cylinders, $N_L = 70$, $t = 0$ at $x/L_o = 1.3$.

APPENDIX B. Notes on the design and manufacture of cylindrical hot-film sensors in the laboratory.

Some progress has been made here at the School of Engineering Science in our attempts to produce small cylindrical hot-films for constant temperature operation in mercury. The design work has been done by the author and the manufacture has been carried out by Mr. A.E. Webb. In this endeavour we were able to benefit from discussions with Dr. D.L. Schultz, Dr. B.J. Bellhouse and Mr. F. Bellhouse of the Department of Engineering Science, University of Oxford, who have had considerable experience in making wedge-type hot-film probes for use in air and water.

This far, we have been successful in producing uninsulated, cylindrical, platinum film sensors as small as 0.05 mm in diameter and 2.5 mm long which operate well in air at temperatures of about 300°C.

The problem of insulating these sensors in an acceptable manner for work in mercury has not yet been solved. We have tried insulating varnish and various mixtures of thinned araldyte with little success due to the seeming impossibility of achieving a uniform coating. However, it has been possible, no doubt to the detriment of good frequency response, to insulate the sensors with a thick coat of araldyte (i.e. with an average thickness equal to about half the film radius) so that they remain insulated when submerged in mercury for long periods of time. Such sensors may prove reliable for taking measurements in steady mercury flows where frequency response is unimportant. A calibration has not yet been carried out.

By far the best technique known to date for insulating hot-films is radio frequency quartz sputtering, as evidenced by the superior performance of the Thermo-Systems quartz-insulated sensors.* A quartz sputtering unit is currently in the design stages here at the School of Engineering Science so that the insulation of our home-made sensors by this technique should be possible in the near future.

---

* DISA Elektronik will also be producing similar quartz-insulated sensors in the near future.

A typical home-made hot-film probe is shown in Figure B.1. Non-magnetic stainless steel tubing is used for both the sensor mounting prongs (0.4 mm O.D.) and the probe body (3 mm O.D.). The manufacture of such a probe will now be briefly described.

The sensor is based upon a quartz fibre which may be fairly easily drawn to as small as 0.03 mm diameter from a larger quartz rod. In this drawing process the quartz rod is heated by an oxygen-acetylene flame.

The next step, and the most critical one, is the application of approximately ten very thin coats of platinum paint (Englehard Industries, Hanovia Liquid Bright Platinum, grade 05-X), using a fine brush, onto a length of quartz fibre which is somewhat longer than the finished length required. The coats must each be applied as thin as possible and heat cured for ½ hour at about 680°C in a clean atmosphere to ensure a bright, uniform film surface. No cleaning is necessary prior to the painting process providing that the quartz fibre has been drawn just previously. If necessary, the fibres can be cleaned before painting or between coats by boiling them for about 15 min. in dilute nitric acid, followed by thorough rinsing in distilled water. Examination of the sensor under a low power microscope after each application of platinum reveals the quality of the film. The final thickness of the film will generally be less than 1 μ.

While the platinum fibre sensor is being prepared a probe body can be manufactured from a stainless steel tube of convenient size. The sensor mounting prongs may be stainless steel needles instead of the short lengths of hypodermic tubing used here. Two lengths of insulated wire are threaded through the probe body to protrude some distance beyond the open ends, and are soldered at one end to two ready prepared prongs. The soldered joints and prongs are insulated from each other and from the probe body by coating them with thinned araldyte (the araldyte may be cured rapidly by applying low heat). A thick, pasty coat of ordinary araldyte is then applied around the soldered joints. These are then drawn into the probe body by pulling on the current lead wires from the other end of the probe. As the prong joints are thus drawn in, the araldyte should completely seal the end of the probe. While the araldyte is tacky the prongs may be orientated parallel to one another. This orientation is advisable to prevent subsequent breakage of a sensor by thermal expansion of the prongs. After curing, the araldyte holds the support prongs firmly in position. The resistance of the leads and

prongs may now be obtained if desired by the usual procedures while shorting the bare ends of the prongs.

The platinum film sensor may be attached to the prongs by the following simple procedure. A piece of the painted quartz fibre is broken off to somewhat longer than the finished length and is laid on a clean, flat surface. The prong tips are then dipped into a silver preparation (Johnson, Matthey & Co., grade FSP 409), which bonds well to both platinum and stainless steel, and are brought in contact with the platinum film sensor. The silver preparation is sticky enough to bond to the film on contact. To ensure good contact all round the ends of the sensor, some extra silver is then daubed on the joints. The probe is subsequently heated in an oven for an hour at low temperature (e.g. about 80°C) to dry the silver preparation. This produces highly conducting joints which have so far proved strong enough to support the sensor. After trimming off the excess length, the sensor is ready for operation in air. To operate the sensors in a steady mercury flow, the sensor and its supports may be insulated, as discussed previously, by dipping into thinned araldyte. This process must often be repeated four or five times to achieve complete insulation. If possible, sputtered quartz insulation should be applied instead to form a uniform insulation with a thickness of 2 to 3μ. A sensor so insulated will have a sufficiently rapid response to allow turbulence measurement in liquids.

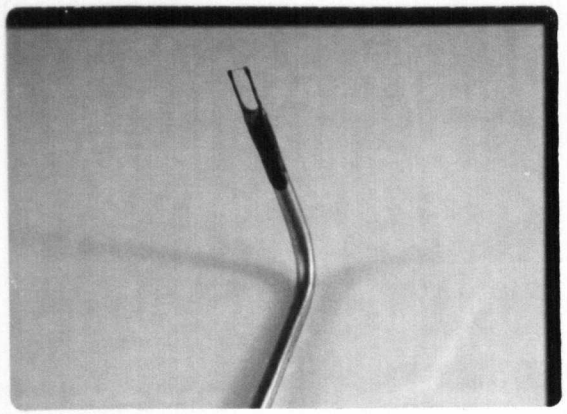

Figure B.1 A typical home-made platinum film sensor, $d \simeq 0.060$ mm.

APPENDIX C: Experimental details

C.1 Operating procedure

In general the operation of the Thermo-Systems anemometer with the insulated hot-film sensors in mercury is in accordance with the step by step operating procedures given in the instruction manual (see Thermo-Systems Inc. (1966)). In this section a few special considerations will be emphasized which apply specifically to the operation of sensors in mercury.

It is very important to measure the temperature of the mercury in the vicinity of the sensor often and accurately during a run so that appropriate corrections may be made to ΔT during subsequent calculations. The operating temperature difference and the operating sensor resistance are related by the formula,

$$\Delta T = \frac{1}{\alpha} \frac{(R_{op} - R_e)}{(R_e - R_p)}, \qquad \text{(C.1)}$$

where α is the temperature coefficient of resistance of the sensor (see Table 2.1), Re is the resistance of the sensor at ambient temperature, Rop is the operating resistance at the operating film temperature and Rp is the resistance of the connecting cable and probe body.

A digital voltmeter must be used in place of the panel meter on the anemometer to measure $\overline{E}$ sufficiently accurately in low speed calibration or measurement. It is always advisable to follow the instantaneous anemometer output continuously on an oscilloscope. Many equipment malfunctions can be diagnosed immediately in this way.

If the mean flow velocity is $O(10^2)$ cm/sec (i.e. when fluctuation frequencies are low) it is not possible to measure $\sqrt{e^2}$ accurately on the panel meter of the Hewlett-Packard H12-3400A true rms voltmeter. The 0-1 volt d.c. output from the back of the instrument must be measured and averaged over a short period (with the damping switch in the 20 sec position), either using a digital voltmeter with sufficient filtering facilities or else the following photographic technique in which the d.c. output of the rms meter is displayed on a d.c. - coupled oscilloscope and photographed using a scope camera and Polaroid film. The time base of

the oscilloscope is first set to a sweep rate which is sufficiently rapid to allow a large number of sweeps during an averaging time of a few seconds. The trace is photographed by holding the shutter open for the desired averaging time. If screen illumination has been correctly adjusted, the resulting oscillogram shows a sweep band which represents the maximum variation of $\sqrt{\overline{e^2}}$, above an arbitrarily chosen datum, occurring during the averaging time. The more highly exposed line near the centre of this band represents the average value of $\sqrt{\overline{e^2}}$. An example oscillogram is shown in Figure C.1.

The rms voltmeter can be used to measure the electronic noise at the no flow condition. This noise level can be minimized, when low turbulence frequencies are of interest, by using the 1 KC low-pass filter in the anemometer to condition the output signal.

If it is desired that ΔT should be maintained constant, the bridge must be balanced at every flow condition. This procedure is very tedious and is unwarranted unless the exact value of ΔT is desired. Throughout this work the bridge has been balanced at no flow only. It is important that the anemometer be sufficiently warmed up (1 hr. warmup is advisable) before balancing is attempted; otherwise, signal drift may be troublesome.

To avoid shorting problems, it is advisable to fix the split pin connector (which mates with the split pin contacts on the probe) in position once a good contact has been achieved.

The calibration function $F(Pe')$ is calculated from the measured variable as follows:

$$F(Pe') = \pi k_t L \Delta T\left(\frac{1}{Q(0)} - \frac{1}{Q(Pe')}\right) = \pi k_t L \Delta T \frac{(R_{ob}+40)^2}{(R_{ob}-R_b)}\left(\frac{1}{\bar{E}(0)^2} - \frac{1}{\bar{E}(Pe')^2}\right), \qquad \text{(C.2)}$$

where the 40 Ω resistance is that which is built into the anemometer bridge in series with the sensor.

Turbulence intensities may be calculated directly from the formula,

$$\frac{\sqrt{\overline{u'^2}}}{\bar{u}} = \frac{2\pi k_t L \Delta T}{S} \frac{(R_{ob}+40)^2}{(R_{ob}-R_b)} \frac{\sqrt{\overline{e^2}}}{\bar{E}(Pe')^3} \qquad \text{(C.3)}$$

Properties of mercury may be obtained from heat transfer texts such as Chapman (1967) and evaluated at the mean temperature $T_m = T_e + \Delta T/2$.

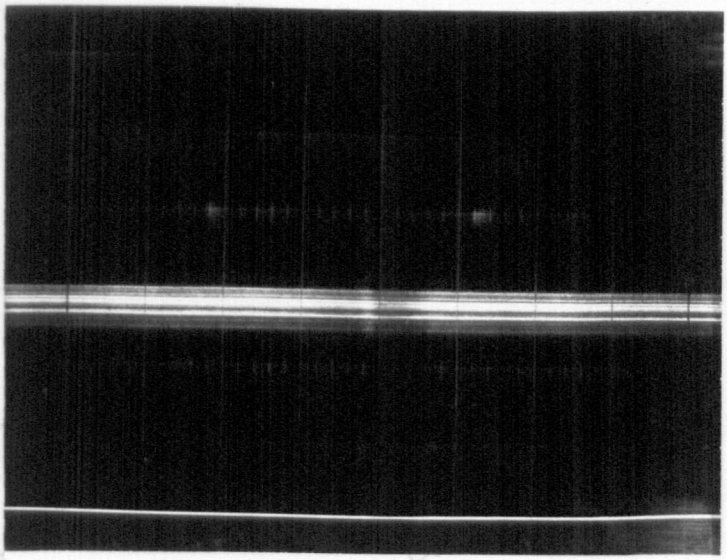

Figure C.1 A typical record of the average rms voltage which corresponds to turbulent fluctuations.

C.2 Tables of Data

As examples of the data taken during the experiments, tables are now presented to include a calibration run for each of the three sensors and the steady electrically driven flow results for M=588. To show the presence of secondary flow, results are also tabulated for r=0, M=212.

Hot-film sensor no.1 was used for the electrically driven flow experiment. In order to process the data, the appropriate value of Rp is 0.51Ω.

TABLE C.1 Unprocessed probe calibration data.

Probe No.	Te (°C)	Rp (Ω)	Re (Ω)	Rop (Ω)	E(0) (volts)	E(Pe) (volts)	Trolley time for 50 cm (sec)
1	20.6	0.44	6.035	6.49	6.208	6.276	56.61
					6.193	6.291	39.57
					6.200	6.336	28.05
					6.197	6.380	20.34
					6.198	6.453	13.68
					6.196	6.522	9.84
					6.195	6.627	6.58
					6.195	6.673	5.59
					6.194	6.698	5.12
					6.195	6.723	4.67
					6.180	6.733	4.26
					6.178	6.744	4.05
					6.165	6.236	56.05
2	20.75	0.31	7.56	8.13	5.504	5.563	56.74
					5.504	5.591	35.35
					5.504	5.567	49.42
					5.500	5.746	10.39
					5.498	5.676	15.46
					5.496	5.813	7.20
					5.494	5.865	5.65
					5.493	5.902	4.84

Probe No.	Te (°C)	Rp (Ω)	Re (Ω)	Rop (Ω)	E(0) (volts)	E(Pé) (volts)	Trolley time for 50 cm (sec)
					5.493	5.923	4.42
					5.491	5.945	4.05
	21.1		7.56		5.493	5.983	3.54
6	18.85	0.52	8.73	9.39	3.878	3.900	56.24
					3.859	3.902	22.64
					3.855	3.925	12.40
					3.854	3.959	6.38
					3.853	3.968	5.14
					3.851	3.977	4.03
					3.850	3.958	5.86
					3.849	3.945	7.48
					3.849	3.934	9.12
					3.849	3.918	12.27
					3.848	3.896	20.43
					3.848	3.884	28.14
					3.846	3.865	56.38
					3.844	3.973	3.54

TABLE C.2 Steady electrically driven flow.

Te (°C)	Re (Ω)	Rop (Ω)	E(Pé) (volts)	Probe co-ordinates r(in.)	z(in.)	I (amps)	B_o (wb/m^2)
17.7	6.06	6.51	7.851	. 0	0	0.80	1.19
			7.860	.308			
			7.872	.335			
			7.883	.380			
			7.868	.410			
			7.860	.472			
			7.851	.564			
			7.847	.659			
			7.850	0			
17.9	6.07	6.51	7.841	0	.203	0.80	1.19
			7.864	.309			
			7.885	.331			
			7.922	.357			

Te (°C)	Re (Ω)	Rop (Ω)	E(Pé) (volts)	Probe co-ordinates r(in.)	z(in.)	I (amps)	B_{o_2} (wb/m^2)
			7.935	.373			
			7.941	.378			
			7.939	.392			
			7.904	.420			
			7.879	.437			
			7.853	.484			
			7.848	.557			
			7.836	.657			
			7.839	0			
18.1	6.08	6.54	8.061	0	.390	0.80	1.19
			8.089	.306			
			8.107	.325			
			8.138	.341			
			8.177	.356			
			8.211	.366			
			8.233	.376			
			8.248	.384			
			8.248	.396			
			8.326	.406			
			8.211	.415			
			8.165	.431			
			8.126	.445			
			8.094	.462			
			8.067	.511			
			8.061	.557			
			8.045	.664			
			8.244	.387			
			8.049	0			
18.1	6.08	6.54	8.047	0	.576	0.80	1.19
			8.059	.280			
			8.069	.306			
			8.089	.329			
			8.114	.342			
			8.151	.353			
			8.191	.361			
			8.268	.373			

Te (°C)	Re (Ω)	Rop (Ω)	E(Pē) (volts)	Probe co-ordinates r(in.)	z(in.)	I (amps)	B_o (wb/m^2)
			8.327	.383			
			8.346	.390			
			8.340	.401			
			8.321	.407			
			8.298	.412			
			8.252	.421			
			8.214	.428			
			8.155	.440			
			8.099	.458			
			8.059	.484			
			8.038	.532			
			8.017	.635			
			8.033	0			
18.1	6.08	6.54	8.060	0	.676	0.80	1.19
			8.078	.307			
			8.091	.334			
			8.101	.342			
			8.140	.359			
			8.194	.365			
			8.245	.370			
			8.332	.378			
			8.405	.386			
			8.419	.394			
			8.379	.403			
			8.320	.411			
			8.289	.415			
			8.154	.436			
			8.174	.432			
			8.114	.443			
			8.224	.425			
			8.050	.459			
			7.982	.490			
			7.955	.528			
			7.943	.580			
			7.926	.659			
			8.413	.395			
			8.045	0			

Te (°C)	Re (Ω)	Rop (Ω)	E(Pé) (volts)	Probe co-ordinates r(in.)	z(in.)	I (amps)	B_o (wb/m^2)
17.4	6.06	6.51	7.960	0	.690	0.25	0.43
			7.903		.610		
			7.917		.660		
			7.908		.635		
			7.904		.610		
			7.901		.560		
			7.901		.510		
			7.902		.410		
			7.904		.210		
			7.906		.010		
			7.956		.690		